

# POLITECNICO DI TORINO

Dipartimento Energia

**Corso di Laurea Magistrale in  
Ingegneria Energetica e Nucleare (Energy and Nuclear Engineering)**

**EIT InnoEnergy Masters in Environmental Pathways for Sustainable  
Energy Systems (SELECT)**

Tesi di Laurea Magistrale

**System Evaluation with Experimental Analysis of Two-Step  
Chemical Looping Syngas Production Integrated with  
Conventional Power Plants**



## **Relatori**

Prof. Massimo Santarelli

Dott. Azharuddin E. Farooqui

Dott. Domenico Ferrero

**Candidato**

Archishman Bose

Luglio 2018 (July 2018)

## Abstract

The present work focuses on both Solar and Methane Driven Two-Step Chemical Looping (CL) syngas production with splitting of CO<sub>2</sub> and H<sub>2</sub>O. For the solar-driven cycle, a kinetic moving bed reactor model in the commercial software ASPEN Plus was developed using kinetics available in the literature, for both reduction and oxidation. Results, including sensitivity studies, were performed, with good agreement to literature data. Thereafter, a CL unit integrated combined cycle power generation layout (SCLP-OXY-CC) was proposed, to be retrofitted to a 100 MW Oxyfuel NGCC with CCS. A maximum power output of 12.9 MW at a solar to electricity efficiency of 25.4% was obtained while working with CO<sub>2</sub> recycling. This would reduce the efficiency penalty suffered by NGCC with CCS from 11.3 to 6 percentage points. Nevertheless, the reduction reactor would be needed to operate at 1600°C and 10<sup>-7</sup> bar vacuum pressure to obtain the maximum output, which would limit the applicability of the cycle to only a few hours during the day without storage integration. Subsequently, methane reduction of ceria as an alternative to thermal reduction was considered and studied in detail. At first, analyses were performed to obtain the optimum operating condition of the methane driven redox cycle from a thermodynamic point of view. ASPEN Plus was used in this regard. Operation between 900 and 950°C with 50% excess of methane than stoichiometry would result in the optimal system performance. A system efficiency of 62% was obtained with an optimum yield of CO and H<sub>2</sub>, while at the same time ensuring avoidance of complete oxidation of methane and carbon deposition. The oxidation reactor yielded a highly exothermic complete oxidation of ceria, whereby a high outlet temperature would considerably benefit the energetic efficiency of the complete redox cycle. The variation of H<sub>2</sub>/CO ratio at the output with respect to varying input parameters including the composition of the gas to the oxidation reactor was studied to specify the necessary operating conditions, while combined to subsequent chemical production from the generated syngas. Since no comprehensive solid-state kinetic model exists in literature to describe the methane reduction of commercial Ceria, experiments were performed in a packed bed reactor within a temperature range of 900-1100°C. CO<sub>2</sub> splitting, being a more complex reaction than water splitting was chosen to be studied for kinetic development as well, while water splitting kinetics was obtained from the literature. The Avrami-Erofeev 3 (AE 3) model was found to fit best to both the cases, with respective activation energies being obtained as 283 kJ/mol and 59.687 kJ/mol. The order of the reaction was found as a relation between temperature and concentration of the reactants. Acknowledging the drawbacks of the SCLP-OXY-CC add-on unit, a new power plant layout using NGCC and oxyfuel combustion, with subsequent CCS was developed by integrating the CL unit with methane reduction (MCLP-OXY-CC). A 500 MW scale plant was designed and comparative system performance with state of the art NGCC and Oxyfuel NGCC with carbon capture was performed using idealistic (thermodynamic) approach as a proof of concept. A system efficiency of 50.7% was obtained, which could be improved to 61.5%, subject to system optimization with pinch analysis. Exergetic efficiency was 47.4%. A comprehensive sensitivity analysis was also performed to evaluate the impact of operating conditions on the overall

system output. A detailed techno-economic assessment revealed a specific overnight capital cost of 2455\$/kW, the levelized cost of CO<sub>2</sub> savings of 96.25 \$/tonneCO<sub>2</sub>, and an LCOE of 128.01 \$/MWh. However, with carbon credits of 6 \$/tonneCO<sub>2</sub>, the LCOE would drop below 50 \$/MWh. To improve upon the proof of concept, the moving bed reactor model with the experimentally obtained methane and CO<sub>2</sub> splitting kinetics was incorporated to evaluate the proposed MCLP-OXY-CC layout. A drop of 20% in the efficiency of the CL unit was observed. However, due to thermal balance within the system, a similar thermal efficiency of the overall plant was achieved as 50.9%. with only 3.8% energy penalty with CCS. However, unlike the thermodynamic layout, no excess heat was available to improve the system efficiency further. Besides CO<sub>2</sub> savings, the land and water footprint as a sustainability assessment criterion for the MCLP-OXY-CC unit was found to increase by 2.5 times with respect to a state of the art NGCC.

## Acknowledgements

I would like to start by sincerely thanking my thesis advisor Dr. Massimo Santarelli of Department of Energy (DENERG) at the Politecnico di Torino. Even though extremely busy, he was always there, whenever I ran into a trouble spot or had a question about my research or writing.

Next, I want to mention my grateful indebtedness to my immediate thesis supervisor, Azharuddin Ehtesham Farooqui, PhD Candidate, DENERG, Polito. Not only was he always there to guide me in the right direction throughout the work, but also treated me as a colleague in his research. This led to constant interchange of ideas and group work that increasingly enhanced the net output of the thesis. Also, in times of struggle during the thesis, whether experiments or analyses of results, his words of motivation provided the necessary driving force required to complete this comprehensive work.

I would also like to acknowledge Dr. Domenico Ferrero of DENERG at Politecnico di Torino as the second reader of this thesis. I am most obliged for his constant support and consultations, as well as his very valuable comments on this thesis.

Subsequently I must express my very profound gratitude to my parents and the almighty for providing me with unfailing support and continuous encouragement throughout my years of study and through the process of researching and writing this thesis. I would also be failing in my duty if I do not acknowledge the help and support I had from my colleagues Felice di Tomaso and Angal Prudwee Raj during the entire course of the thesis. This accomplishment would not have been possible without them.

The research presented has been performed within the framework of the InnoEnergy Master Program-SELECT, ‘Environomical Pathways for Sustainable Energy Systems’ and funded with support from the Education, Audiovisual, and Culture Executive Agency (EACEA) of the European Commission. The research presented reflects only the views of the author, and the Commission cannot be held responsible for any use, which may be made of the information contained therein.

Thank you all

Archishman Bose

14.07.2018

Turin, Italy

## Contents

Abstract.....	i
Acknowledgements.....	iii
List of Tables .....	vii
List of Figures.....	ix
1 Introduction.....	1
2 Chemical Looping Technology.....	2
2.1 Background .....	2
2.2 Chemical Looping Technology for CO <sub>2</sub> /H <sub>2</sub> O Splitting .....	4
2.3 Prospective oxygen carriers .....	6
2.3.1 Volatile carriers.....	6
2.3.2 Non-volatile carriers .....	6
2.3.3 Perovskites .....	9
2.3.4 Spinel Structured Oxygen Carriers .....	9
2.4 Reactors for Chemical Looping CO <sub>2</sub> /H <sub>2</sub> O Splitting .....	10
2.4.1 Reactors for Solar Thermochemical Chemical Looping Splitting Cycles.....	10
2.4.2 Reactors for Chemical Looping Splitting Cycles with Carbonaceous Fuels.....	22
2.5 Modelling of Reactors.....	23
2.5.1 Fluidized Bed Reactors .....	23
2.5.2 Moving Bed Reactors .....	25
2.6 System Modelling .....	26
3 Reactor and System Modelling of Thermochemical dissociation of CO <sub>2</sub> /H <sub>2</sub> O Using Non-stoichiometric Ceria .....	27
3.1 Reaction Kinetics .....	27
3.1.1 Reduction kinetics.....	30
3.1.2 Oxidation kinetics .....	32
3.2 Modelling of Reactors.....	34
3.2.1 Moving Bed Reactor Model.....	35
3.3 Evaluation Methodology .....	38
3.4 Results and Discussions .....	39
3.5 Solar Thermochemical Power Generation .....	50
3.5.1 Plant Layout and Configuration.....	51
3.5.2 System Modelling in ASPEN Plus .....	53
3.5.3 Energy Performance Evaluation .....	57
3.5.4 System Evaluation .....	58
3.5.5 Comments and Discussions .....	71

3.6	Conclusions .....	71
4	Thermodynamic Analysis of the Chemical Looping Cycle with Methane reduction of Ceria .....	73
4.1	Introduction .....	73
4.2	Thermodynamics method .....	75
4.3	Results and discussion .....	77
4.3.1	Reduction reactor .....	77
4.3.2	Oxidation reactor .....	79
4.3.3	Heat balance .....	82
4.4	Efficiency Assessment .....	83
4.4.1	Definition .....	83
4.4.2	Efficiency Evaluation .....	84
4.5	Pinch Analysis .....	87
4.6	Conclusion .....	88
5	Kinetic Modelling of POM with Commercial Ceria followed by CDS .....	89
5.1	Reaction Mechanism .....	90
5.1.1	Model-Free Method .....	92
5.2	Experimental Section .....	93
5.3	Reactivity results .....	96
5.3.1	Effect of temperature .....	97
5.3.2	Effect of concentration .....	99
5.4	Kinetic study .....	100
5.4.1	Model fitting method .....	101
5.5	Kinetic Parameter Evaluation .....	102
5.5.1	Reduction of $CeO_2$ by $CH_4$ .....	102
5.5.2	Oxidation of $CeO_{2-\delta}$ by $CO_2$ .....	104
5.6	Discussions and Conclusions .....	105
6	System Evaluation of Novel Oxy-fuel NGCC Integrated with Chemical Looping Cycle and CCS .....	107
6.1	Process Description and Plant Configuration .....	107
6.2	Process Simulation and Assumptions .....	111
6.3	Thermodynamic Assessment Methodology .....	115
6.3.1	Energy Analysis .....	116
6.3.2	Exergy Analysis .....	116
6.4	Economic Performance .....	119
6.5	Environmental Performance .....	122
6.6	Thermodynamic Evaluation of the MCLP-OXY-CC Unit .....	123

6.6.1	Energy Analysis of MCLP-OXY-CC .....	123
6.6.2	Exergy Analysis of MCLP-OXY-CC .....	124
6.6.3	Effect of key operating parameters .....	126
6.7	Comparative Performance Evaluation of State of the Art NGCC, Oxyfuel NGCC with Carbon Capture and MCLP-OXY-CC unit.....	130
6.7.1	Thermodynamic Performance.....	130
6.8	Economic Analysis.....	132
6.8.1	Capital Cost and Operational Expenses .....	132
6.8.2	LCOE and LCOA Calculations .....	134
6.9	Pinch Analysis.....	135
6.10	Thermodynamic and Kinetic Evaluation of MCLP-OXY-CC .....	136
6.11	Environmental Evaluations.....	140
6.11.1	Water Footprint Analysis .....	140
6.11.2	Land Footprint Analysis .....	141
6.12	Conclusions .....	142
7	Conclusions.....	143
8	References.....	145

## List of Tables

Table 3-1 Ceria reduction rate equation coefficients presented by Bulfin et al [51].....	31
Table 3-2 Kinetic parameters of the oxidation reaction of reduced ceria obtained by Arifin [124].....	33
Table 3-3 Design assumptions used for developing the process flowsheet models in ASPEN plus.....	55
Table 3-4 Comparative performance evaluation of the proposed SCLP-OXY- CC add-on unit with varying gas compositions to the OXI at equivalent operating conditions of 1600°C and 10 <sup>-7</sup> bar reduction temperature and pressure respectively, metal and gas inlet temperature to the OXI of 800°C, 275 mol/s flow of CeO <sub>2</sub> and gas flow to the OXI of 66 mol/s .....	69
Table 3-5 Comparative performance evaluation of the proposed CL unit of the proposed SCLP-OXY-CC with varying gas composition to the OXI at equivalent operating conditions of 1600°C and 10 <sup>-7</sup> bar reduction temperature and pressure respectively, metal and gas inlet temperature to the OXI of 800°C, 275 mol/s flow of CeO <sub>2</sub> and gas flow to the OXI of 66 mol/s .....	70
Table 5-1 Rate and integral expressions for different solid-state kinetic models [172] based on $\alpha$ , which indicates the conversion, $f(X)$ represents the differential form of the kinetic model, and $g(X)$ is the integral form of the model. ....	92
Table 6-1 Design assumptions used for developing the process flowsheet models in ASPEN plus.....	112
Table 6-2 NG Composition Assumed.....	113
Table 6-3 Syngas composition from the Reduction Reactor (RED) and the Oxidation Reactor (OXI) of the Chemical Looping Unit.....	115
Table 6-4 Summary of the Different Plant Component Scale Factors [115,195,202,203]....	120
Table 6-5 Basic economic assumptions [195,204,205] .....	121
Table 6-6. Global Energy Flow and Energetic Efficiency of the Proposed MCLP-OXY-CC Unit .....	123
Table 6-7. Global Exergy Flow and Efficiency of the MCLP-OXY-CC unit.....	124
Table 6-8. Exergy balance in MCLP-OXY-CC break-down by component.....	125
Table 6-9. Plant performance indicators for State of the Art NGCC, oxy-fuel NGCC, and the oxyfuel NGCC with CL unit (MCLP-OXY-CC) processes obtained by ASPEN plus simulations .....	130

Table 6-10. CO <sub>2</sub> Captured per unit energy and efficiency penalty with reference to conventional Oxyfuel NG Power Plant .....	132
Table 6-11. Capital Cost Breakdown of the proposed MCLP-OXY-CC unit .....	133
Table 6-12 Comparison between the Thermodynamic and Kinetic Evaluation of the CL unit of the MCLP-OXY-CC unit .....	137
Table 6-13 Plant Data Comparison of the MCLP-OXY-CC unit based on Thermodynamic and Kinetic Evaluation of the CL unit .....	138
Table 6-14. Summary of Water footprint analysis of the MCLP-OXY-CC unit.....	140
Table 6-15. Comparative Land Area Requirement in m <sup>2</sup> for NGCC, Oxy-CC and MCLP-OXY-CC unit for a net power output of 500MW .....	141

## List of Figures

Figure 2-1 Chemical looping diagram as an example of the three-reactor set-up for fuel decarbonization.....	2
Figure 2-2 FCC process chemical loop with indicated recirculation of part of the catalyst in the regenerator .....	3
Figure 2-3 Conceptual scheme of the chemical looping Syngas production through methane reduction with subsequent splitting of water and carbon dioxide.....	5
Figure 2-4: Schematic representations of i) Stationary monolith cavity (SMC) reactor by Chueh et al. [72] for H <sub>2</sub> O-CO <sub>2</sub> dissociation; ii) Sectional view of the Spherical Stationary monolith cavity (SMC) reactor as proposed by Houaijia et al [73] and iii) the rotating piston reactor as proposed by Chambon et al [74].....	12
Figure 2-5: CR5 reaction proposed by Diver et al.[77]. .....	14
Figure 2-6: The SurroundSun reactor design proposed by Melchior et al. [79].....	14
Figure 2-7: Schematic representation of i) Honeycomb multi-channels Solar Reactor as proposed by Roeb et al. [41]; ii) multi-chambers reactor proposed by Roeb et al. [81] (a) and lamellae shutter for temperature regulation (b). .....	15
Figure 2-8: a) Rotary reactor concept proposed by Kaneko et al. [83], b) pilot scale rotating reactor. ....	16
Figure 2-9: tubular packed bed solar reactor for H <sub>2</sub> production proposed by Tamaura et al. [84]. .....	17
Figure 2-10 i) The Rotating particle flow reactor proposed by Muller et al. [85].....	18
Figure 2-11: The schematic representation of i) aerosol reactor, as proposed Scheffe et al. [89]; ii) internally circulating bed proposed by Gokon et al. [90]; Moving Packed Particle Bed Reactor, proposed by Ermanoski et al. [91].....	20
Figure 2-12 The proposed solar thermal particle flow reactor (not scaled) by Muhich et al [70], .....	21
Figure 2-13 Schematic of the proposed solar particle-transport reactor by Welte et al [28] showing both counter current and co-current gas-solid flow configurations. ....	22
Figure 2-14 Proposed Hydro-dynamic and kinetic model of a Circulating Fluidized Bed Reactor in ASPEN Plus as proposed by Legros et al, 1998 [102].....	24
Figure 3-1 Different behaviours for the reacting solid particles [120] .....	29
Figure 3-2 Schematic Diagram of a Generic Moving Bed Reactor.....	35

Figure 3-3 Logic diagram of moving bed reactor model in ASPEN Plus hooked with user kinetics written in an external FORTRAN Code .....	37
Figure 3-4 Iterative calculation procedure for determining the number of RCSTRs in series, n. ....	40
Figure 3-5 Relative changes in the output from increasing the number of RCSTRs in series for (a) Reduction Reactor (b) Oxidation Reactor .....	41
Figure 3-6 Variation of (a) Non-Stoichiometry ( $\delta$ ) and (b) the heat requirement of the reduction reactor (Q) with the temperature and reactor volume of the reduction reactor at a constant reactor vacuum pressure of $10^{-7}$ bar, $CeO_2$ molar flow of 285.71 mol/s and a constant metal oxide inlet temperature of $1300^\circ C$ .....	41
Figure 3-7 Variation of Non-Stoichiometry ( $\delta$ ) at $1600^\circ C$ and $1000^\circ C$ with the reduction reactor volume at a constant reactor vacuum pressure of $10^{-7}$ bar, the $CeO_2$ molar flow of 285.71 mol/s and a constant metal oxide inlet temperature of $1300^\circ C$ .....	42
Figure 3-8 Variation of non-stoichiometry ( $\delta$ ) generated in the reduction reactor with temperature and reactor vacuum pressure at a constant reactor volume of $0.5\ m^3$ , $CeO_2$ molar flow 285.71 mol/s and a constant metal oxide inlet temperature of $1300^\circ C$ . Symbols represent experimental results of Bulfin et al [51], lines represent the moving bed model results.....	43
Figure 3-9 Variation of Non-Stoichiometry ( $\delta$ ) along the length of the reactor at a constant reduction reactor volume of $1\ m^3$ , a constant $CeO_2$ flow of 285.71 mol/s and a constant reactor temperature and a vacuum pressure of $1600^\circ C$ and $10^{-7}$ bar respectively. ....	44
Figure 3-10 Variation of the heat of reaction ( $Q_{red}$ ) with metal oxide inlet temperature to the reduction reactor ( $T_{oc, inlet}$ ) and reactor pressure for a constant reduction temperature of $1600^\circ C$ for a constant reactor volume of $0.5\ m^3$ and $CeO_2$ molar flow 285.71 mol/s.....	45
Figure 3-11 Impact of variation of the reactor volume on the Solid Conversion (X) in the oxidation reactor (OXI) with a variation of the inlet gas mixture composition, all other parameters and molar flow being constant. ....	46
Figure 3-12 (a) Impact of variation of the reactor volume and the flow of steam (Stoichiometric excess) on the Solid Conversion (X) and (b) the variation of the metal oxide outlet temperature ( $T_{oc, outlet}$ ) with the flow of steam (Stoichiometric excess) on the Solid Conversion (X) in the oxidation reactor (OXI) for water splitting for an inlet non-stoichiometry of 0.35, completely oxidized $CeO_2$ flow rate of 285.71 mol/s and pressure of 2 bar. ....	47
Figure 3-13 Variation of the Solid Conversion (X) (left) and metal temperature (right) in the oxidation reactor with variable inlet gas mixture composition, at a constant oxidation reactor	

volume of 2 m<sup>3</sup>, a constant non-stoichiometry factor of 0.35 and a constant molar flow of 110 mol/s of gas in the oxidation reactor, with a fixed metal and gas inlet temperature of 800°C....48

Figure 3-14 Variation of (a) metal outlet temperature from the oxidation reactor and (b) solid conversion (X) in the oxidation reactor with variable gas inlet temperature; Variation of (c) metal outlet temperature from the oxidation reactor and (d) solid conversion (X) with variable metal oxide inlet temperature (T<sub>OC, inlet</sub>) in the oxidation reactor for a variable gas mixture composition at a constant oxidation reactor volume of 4 m<sup>3</sup>, a constant inlet metal non-stoichiometry factor of 0.35 and a constant molar flow of 105 mol/s of gas in the oxidation reactor. ....49

Figure 3-15 Solar Thermochemical plant Conceptual layout with CO<sub>2</sub> and/ or H<sub>2</sub>O recycling for power generation, integrated as add-on unit to an existing Oxyfuel NGCC with CCS.....52

Figure 3-16 Conceptual layout of the SCLP-OXY-CC add-on unit utilizing CO<sub>2</sub> and/or H<sub>2</sub>O splitting with thermal reduction of ceria recycling for power generation via fuel-air combustion .....56

Figure 3-17 Impact of the variation of the oxidation reactor volume with water splitting (Solid Lines) and CO<sub>2</sub> splitting (Dashed Lines) on the specific system performance of the proposed SCLP-OXY-CC add-on at a constant RED temperature and pressure of 1600°C and 10<sup>-7</sup> bar respectively, a constant molar flow rate of CeO<sub>2</sub> and CO<sub>2</sub>/H<sub>2</sub>O of 275 mol/s and 66 mol/s respectively, and a constant metal oxide and gas inlet temperature of 800°C to the OXI.....59

Figure 3-18 . Impact of the variation of the reduced metal inlet temperature to the OXI on the operating parameters of the SCLP-OXY-CC at a constant RED temperature and pressure of 1600°C and 10<sup>-7</sup> bar respectively, a constant molar flow rate of CeO<sub>2</sub> and gas to the OXI of 275 mol/s and 66 mol/s respectively and a constant gas inlet temperature to the OXI of 800°C...61

Figure 3-19 . Impact of the variation of the reduction temperature on the operating parameters of the SCLP-OXY-CC at a constant RED temperature and pressure of 1600°C and 10<sup>-7</sup> bar respectively, a constant molar flow rate of CeO<sub>2</sub> and gas to the OXI of 275 mol/s and 66 mol/s respectively and a constant gas inlet temperature to the OXI of 800°C .....63

Figure 3-20 . Impact of the variation of the reduction vacuum pressure on the operating parameters of the proposed SCLP-OXY-CC add-on unit at a constant RED temperature of 1600°C, a constant molar flow rate of CeO<sub>2</sub> and gas of 275 mol/s and 66 mol/s respectively and a constant gas and metal oxide inlet temperature to the OXI of 800°C.....64

Figure 3-21 . Impact of the variation of the water flow rate (% H<sub>2</sub>O to CL) on the parameters of the proposed SCLP-OXY-CC unit working with only water at a constant molar flow rate of

CeO <sub>2</sub> and water of 120 mol/s, a constant gas and metal inlet temperature of 800°C to the OXI and a constant reduction temperature and pressure of 1600°C and 10 <sup>-7</sup> bar.....	66
Figure 3-22 . Impact of the variation of the CO <sub>2</sub> flow rate (% CO <sub>2</sub> to CL) on the parameters of the proposed SCLP-OXY-CC unit working with only water at a constant molar flow rate of CeO <sub>2</sub> and water of 120 mol/s, a constant gas and metal inlet temperature of 800°C to the OXI and a constant reduction temperature and pressure of 1600°C and 10 <sup>-7</sup> bar.....	67
Figure 4-1 Process simulation flowsheet of interconnected reduction and oxidation reactors. ....	76
Figure 4-2 Impact of the variation of the CH <sub>4</sub> /CeO <sub>2</sub> ratio and temperature on the yield of the following chemical species as molar fractions of outlet streams within the reduction reactor: a) unreacted methane; b) CO; c) H <sub>2</sub> ; d) Ce <sub>2</sub> O <sub>3</sub> (solids).....	77
Figure 4-3 Impact of the variation of the CH <sub>4</sub> /CeO <sub>2</sub> ratio and temperature on the yield of the following unwanted chemical species as molar fraction of the outlet product streams within the reduction reactor: a) CO <sub>2</sub> ; b) H <sub>2</sub> O; c) elementary carbon (solids).....	78
Figure 4-4 H <sub>2</sub> /CO ratio at the exit of the reduction reactor for different reduction temperatures for various CH <sub>4</sub> /CeO <sub>2</sub> .....	79
Figure 4-5 Impact of the variation of the waste gas (equimolar mixture of CO <sub>2</sub> and H <sub>2</sub> O) flow rate and temperature on the yield of the a) CO and b) H <sub>2</sub> as the molar fraction of the product gas of the oxidation reactor.....	80
Figure 4-6 Impact of the variation of the waste gas flow parameters and temperature on the H <sub>2</sub> /CO yield ratio in the oxidation reactor: a) variation of flow of waste gas with an equimolar mixture of CO <sub>2</sub> and H <sub>2</sub> O; b) variation of the composition of the waste gas at a constant waste gas feed rate of 1kmol/hr .....	81
Figure 4-7 Heat need/release from the reduction and oxidation reactions as per: a) with a variation of CH <sub>4</sub> /CeO <sub>2</sub> feed ratio and temperature in the reduction reactor; b) with a variation of the waste gas flow at an equimolar mixture composition and temperature in the oxidation reactor. ....	83
Figure 4-8 Variation of system efficiency considering syngas from both the reactors (h <sub>1</sub> ) based on the parametric variations within the oxidation reactor, at a constant CH <sub>4</sub> /CeO <sub>2</sub> flow ratio of 0.8 in the reduction reactor based on: a) variation of waste gas flow rate at a constant equimolar mixture of CO <sub>2</sub> and H <sub>2</sub> O and temperature; b) variation of waste gas composition and temperature. ....	85

Figure 4-9 Impact of the CH <sub>4</sub> /CeO <sub>2</sub> molar feed ratio and temperature, based on an isothermal system operation and a constant flow of 2 kmol/hr of waste gas at equimolar composition within the oxidation reactor on a) the system efficiency, $\eta_1$ b) net H <sub>2</sub> and CO yield from the redox cycle, considering both the oxidation and reduction reactors.....	86
Figure 4-10 Impact of the CH <sub>4</sub> /CeO <sub>2</sub> molar feed ratio and temperature, on the system efficiency considering only the yield from CO <sub>2</sub> and H <sub>2</sub> O splitting ( $\eta_2$ ), based on an isothermal system operation and a constant flow of 1 kmol/hr of waste gas at equimolar composition within the oxidation reactor. ....	87
Figure 4-11 Pinch Analysis of the Methane driven chemical looping cycle at an isothermal temperature of 950°C .....	87
Figure 5-1. Kinetic models with corresponding reaction mechanisms (a) Reaction order model (b) Geometrical contracting model (c) Diffusion model (d) Avrami-Erofeev (Nucleation) model applicable for Ceria-based oxygen carrier. ....	91
Figure 5-2 Experimental set-ups for developing reaction kinetics in micro-reactor configuration .....	94
Figure 5-3. a) H <sub>2</sub> and b) CO production rate from the reduction of CeO <sub>2</sub> over 50% CH <sub>4</sub> and c) oxidation of the reduced metal oxide with 50% CO <sub>2</sub> over five cycles each. Operating conditions: $m_{\text{CeO}_2}$ : 250 mg; $\dot{V}_{\text{gas}}$ : 120 Nml/min (balance Argon); Isothermal redox cycling temperature: at 1000°C (1273 K); for all cases, the baseline reactor pressure: 1 atm. ....	96
Figure 5-4. Variation of yield rates of CO in a) reduction and b) oxidation of CeO <sub>2</sub> in redox cycle of methane reduction followed by oxidation with CO <sub>2</sub> with the variation of temperature in the range 900°C and 1100°C at the following conditions: $m_{\text{CeO}_2}$ : 250 mg; $\dot{V}_{\text{gas}}$ : 120 Nml/min (balance Argon); Methane concentration during reduction: 30%; CO <sub>2</sub> concentration during oxidation: 50%, baseline reactor pressure: 1 atm. ....	98
Figure 5-5. CO production and the maximum non-stoichiometry ( $\delta_{\text{max}}$ ) during reduction as a function of temperature at the following conditions: $m_{\text{CeO}_2}$ : 250 mg; $\dot{V}_{\text{gas}}$ : 120 Nml/min (30% CH <sub>4</sub> , balance Argon); baseline reactor pressure: 1 atm. ....	99
Figure 5-6. Variation of yield rates of CO in a) methane reduction of ceria at 1000°C and b) oxidation of reduced ceria at 1100°C with the variation of concentration of the gaseous reactants at the following conditions: $m_{\text{CeO}_2}$ : 250 mg; $\dot{V}_{\text{gas}}$ : 120 Nml/min (balance Argon); reactor pressure: 1 atm.....	100

Figure 5-7. (a) $\ln(K)$ vs $(1/T)$ Arrhenius plot of the reduction reaction for AE3 model; (b) $\ln(AP^m)$ vs $\ln(P)$ plot for reduction reaction order determination. ....	102
Figure 5-8. Comparison of the kinetic model and the experimental data for methane reduction of ceria (a) with the variation in temperature, 1000°C, 1050°C, 1100°C and (b) with the concentration of CH <sub>4</sub> of 30%, 40% and 50% for reactor pressure of 1 atm. The symbol represents experimental data and lines represent the kinetic model .....	103
Figure 5-9. (a) $\ln(K)$ vs $(1/T)$ Arrhenius plot of the reduction reaction for AE3 model; (b) $\ln(AP^m)$ vs $\ln(P)$ plot for reduction reaction order determination .....	104
Figure 5-10. Comparison of the kinetic model and the experimental data for oxidation of reduced ceria with CO <sub>2</sub> (a) with the variation in concentration of CO <sub>2</sub> of 50%, 30% and 20% (b) with temperature of 1000°C, 1050°C, 1100°C for reactor pressure of 1 atm and a constant non-stoichiometric extent of reduced ceria of 0.22. The symbol represents experimental data and lines represent the kinetic model.....	105
Figure 6-1 Block Diagram of NGCC, OXY-CC and the novel MCLP-OXY-CC process ...	109
Figure 6-2 Process simulation flowsheet of MCLP-OXY-CC unit.....	114
Figure 6-3 Methodology for Techno-economic and Sustainability Assessment.....	116
Figure 6-4. Impact of the variation of a) pressure of the CL unit and b) molar flow rate of Cerium Oxide (CeO <sub>2</sub> ) at a constant natural gas flow and on the power generating components, the net power produced and the efficiency of the MCLP-OXY-CC power plant. ....	127
Figure 6-5. Impact of the variation of a) fraction of the exhaust gas from GT1-1 recirculated into the oxidation reactor (OXI) of the CL unit for production of syngas and b) temperature of the CeO <sub>2</sub> at the inlet of the reduction reactor (RED) of the CL unit at constant natural gas flow on the power generating components, the net power produced and the efficiency of the MCLP-OXY-CC power plant. ....	128
Figure 6-6. Impact of the variation of a) GT1-1 inlet pressure and b) Turbine Inlet Temperature (TIT) for both the turbines (GT1-1 and GT2) at constant natural gas flow on the power generating components, the net power produced and the efficiency of the MCLP-OXY-CC power plant.....	129
Figure 6-7. Impact of the variation of the natural gas flow rate on the system capacity (net power produced) and the efficiency of the MCLP-OXY-CC power plant.....	129
Figure 6-8. Comparison between GT, ST, gross, parasitic and net power output for base NGCC, OXY-CC and MCLP-OXY-CC.....	131

Figure 6-9. Impact of Carbon Tax on the Levelized Cost of Electricity of the proposed MCLP-OXY-CC unit.....	134
Figure 6-10. Comparative Evaluation of the Levelized Cost of Carbon Capture between MCLP-OXY-CC and post-combustion capture at new NGCC power plants.....	135
Figure 6-11. Pinch Analysis of the proposed MCLP-OXY-CC unit.....	135
Figure 6-12. Pinch Analysis of the proposed MCLP-OXY-CC unit based on a Kinetic assessment of the CL unit .....	139
Figure 6-13. Comparison of specific water need of power production of the proposed MCLP-OXY-CC and commercial technologies with cooling tower-based cooling.....	141

# 1 Introduction

Burning fossil fuels, resulting in anthropogenic carbon dioxide (CO<sub>2</sub>) emissions are presently recognised as the primary contributor to climate change, with 36.2 Gt being emitted in 2015 [1,2]. Notwithstanding substantial investment and decline in prices of renewable energy, fossil fuels continue to play an indispensable role in the world's energy landscape [3]. Indeed, even though the trend is on a decline, such technologies continue to play a major role as the primary energy source, especially in developing countries [4]. Hence, it is expected that the relevance of fossil fuels in the primary energy mix will continue to a significant extent in the considerable future.

Carbon capture and storage (CCS) technologies have been shown to have considerable potential to reduce such anthropogenic CO<sub>2</sub> emissions as part of the global transition towards a low carbon energy system [2,5,6]. These technologies are typically categorized into three categories: pre-combustion, post-combustion, and oxy-combustion [7,8], the common idea being the capture and subsequent storage of CO<sub>2</sub> from the complete or partial combustion of fossil fuels in either the power or industrial sectors. The captured high purity CO<sub>2</sub>, nevertheless, needs to be subsequently compressed to approximately 110 bar prior to transportation via pipeline to a storage site [2,9,10]. Sequestration of CO<sub>2</sub> is the process of injecting and depositing CO<sub>2</sub> into deep oceans or in the earth shells. An already proven, it is implemented in some countries, able to successfully store a considerable amount of CO<sub>2</sub>. Moreover, such CO<sub>2</sub> injections into earth shells in oil/gas reservoirs can also be utilized for activities like enhanced oil recovery (EOR) and other industrial activities. Nonetheless, technical limitations of the CCS technology, like high costs for the long-distance transportation, and high deposition of CO<sub>2</sub> related to the risk of abrupt release, is dangerous for marine or terrestrial life. Water and marine life quality around the deposits sites are also widely debated.

Therefore, in recent studies, recycle and re-use of the captured CO<sub>2</sub> via innovative methods, as an alternative to storage has also received much interest via chemical formation for subsequent use [11–13]. Indeed, CO<sub>2</sub> conversion to fuels or other chemicals components requires high energy density, leading to the need for the development of efficient conversion techniques. Use of renewables in such conversions is important as well, due to the need for decarbonization of the future energy sector.

Synthesis of non-fossil fuels from carbon dioxide (CO<sub>2</sub>) has received significant research interest in recent years as an alternative to the mitigation of fossil carbon emissions. Use of recycled carbon dioxide as a reactant to prepare hydrocarbons is one of the options [14]. Multiple pathways for CO<sub>2</sub> recycling exist through thermochemical and electrochemical processes [15–17]. Thermochemical redox cycles driven by concentrated solar power systems (CSP), are a promising route to simultaneously split H<sub>2</sub>O and CO<sub>2</sub> for syngas (a mixture of H<sub>2</sub> and CO) production [18,19], that can be further processed to hydrocarbons for multiple applications via established industrial processes.

## 2 Chemical Looping Technology

### 2.1 Background

Due to the limitation of electrochemical or photochemical or other modes of conversions of  $\text{CO}_2$ , thermochemical conversions of  $\text{CO}_2$  are being currently studied as cheaper alternatives. There are primarily two methods for such thermochemical conversions of  $\text{CO}_2$ , namely:

- a. Direct disassociation
- b. Chemical Looping

Direct disassociation of  $\text{CO}_2$  at extremely high temperatures of  $1900^\circ\text{C}$ - $2400^\circ\text{C}$  has been investigated via a prototype by Traynor and Jensen in USA [20]. The process yielded around 6 % of  $\text{CO}$  into  $\text{CO}_2$ . Multiple other studies have been conducted to define the working parameters of such thermo-chemical conversions [21,22]. However, due to the requirements for high reaction temperatures and extra quenching processes, direct disassociation of  $\text{CO}_2$  have so far been considered as difficult and unprofitable.

Chemical looping process is based on the principle of a set of chemical reactions occurring in multiple reactors, whereby, one of the reactants constantly circulates between reactors forming a closed loop as shown in Figure 2-1.

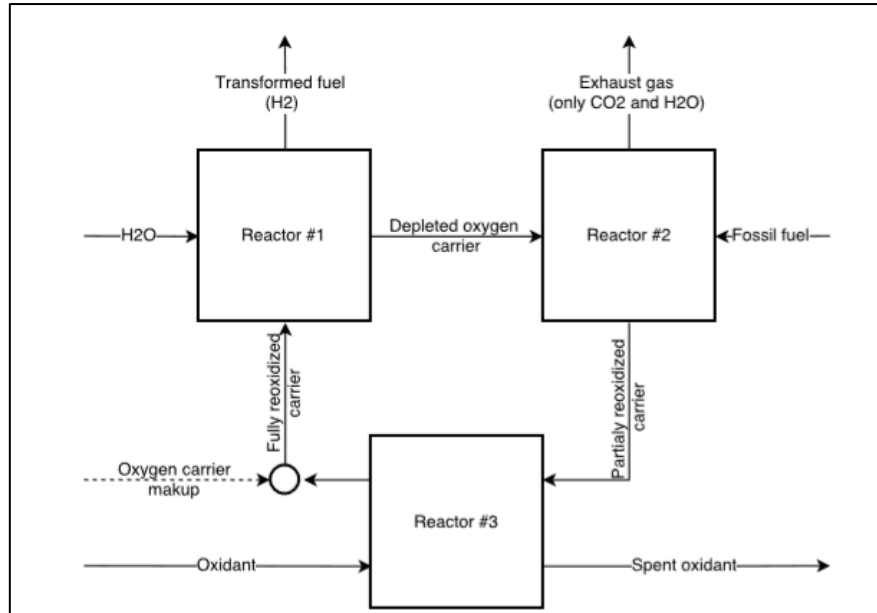


Figure 2-1 Chemical looping diagram as an example of the three-reactor set-up for fuel decarbonization.

Indeed, for practical application, losses occur, requiring make-up of the reactants into the closed-loop system, as indicated by the dashed lines in Figure 2-1. In general, depending on the individual reactions being either endothermic or exothermic, such systems do not operate

in isothermal conditions. Temperature swing between the reactors often over hundreds of degrees, requiring regenerative heat exchangers to be frequently incorporated into the system.

A wide variety of processes in the power engineering and petrochemical engineering currently use chemical looping as their main principle of operation, one of the most mature processes being the Fluid Catalytic Cracking (FCC). In this process, the catalyst is first used in the cracking reactor to break up higher order hydrocarbons to shorter chains, however, by losing its own potential, requiring regeneration. Therefore, it is sent to regeneration reactor and back to the cracking process, thereby completing a chemical loop. In this process, the regenerator reactor is of a circulating fluidized bed type, whereby the catalyst resides for a couple of cycles in the regenerator (Figure 2-2). This configuration of the system helps in temperature control of the regeneration process which otherwise is highly exothermic [23].

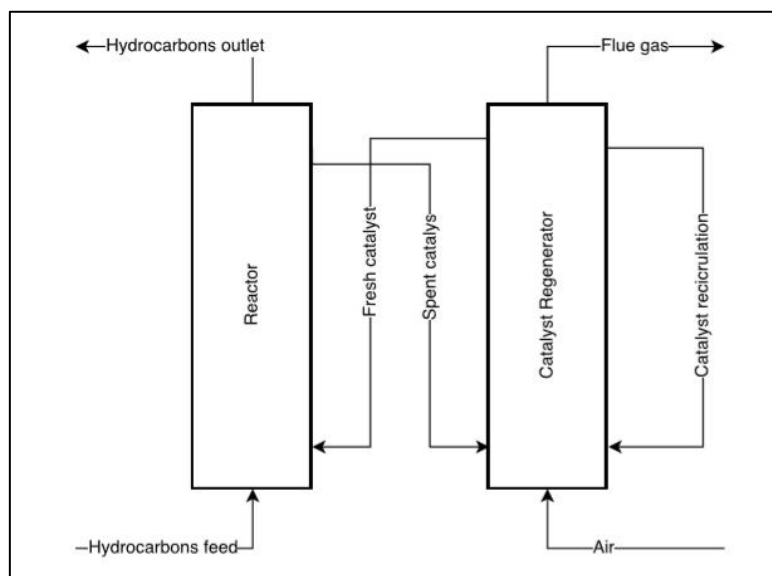


Figure 2-2 FCC process chemical loop with indicated recrystallization of part of the catalyst in the regenerator

Another example of an industrial chemical looping process is Monoethanolamine (MEA) reactor for Carbon Capture and Storage (CCS) systems. Though used in relatively small scale due to primary reason of lack of economic feasibility of the CCS process in current market condition, the technology is well developed. In this process, the exhaust gas is rinsed with chilled Monoethanolamine in the counterflow reactor, where the amines absorb the  $\text{CO}_2$ ,  $\text{SO}_2$  and other oxides available in the flue gas. Later the lean mixture is heated up, releasing the absorbed gases. Amines leaving the desorption reactor are cooled down, first in the regenerative heat exchanger and in the additional cooler and then they are directed into the scrubber. The MEA system is used as a post-combustion method of the  $\text{CO}_2$  separation, by which existing plants can be retrofitted to incorporate it.

However, new approaches are being developed for carbon capture, one of the recent developments being the separation of the exhaust gases from the oxidant through the Chemical Looping Combustion (CLC) process [24,25]. In such a system, as opposed to the oxidant and

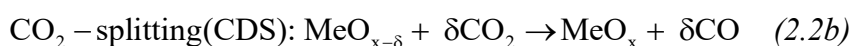
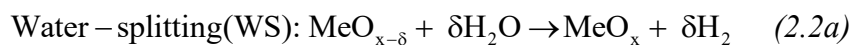
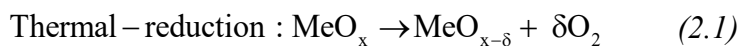
fuel to be in direct interaction with each other, the oxygen required for the combustion process is transported in between them by metal oxides. In fact, Figure 2-1 represents diagrammatically a CLC system layout. Even though it is not necessary to have the three-reactor set-up, some of the oxygen carriers might not be re-oxidized to their initial state within the first oxidation reactor (reactor #2, Figure 2-1) thus requiring additional oxidation reactor, fed with air or pure oxygen. Such a process has also been proposed to be used for fuel decarbonization.

In the CLC, the chemical energy of the carbonaceous fuel (coal, hydrocarbons, etc.) is converted to chemical energy of hydrogen, as reported in processes studied by Chiesa et al. [26]. In the study by Chiesa, iron oxide-based redox pair (hematite–wustite–magnetite) was considered as the oxygen carrier in three reactors configuration as can be visualized from Figure 2-1. The complete reaction chain is exothermic, allowing the production of high-quality steam. Chemical looping CO<sub>2</sub> or H<sub>2</sub>O splitting investigated in this work has similar configuration, though energy required to drive the process is not strictly limited to being from fossil fuel combustion but can from absorption of the solar irradiation or reduction via methane.

## 2.2 Chemical Looping Technology for CO<sub>2</sub>/H<sub>2</sub>O Splitting

Chemical-looping (CL) syngas production is an innovative fuel production technology based on splitting CO<sub>2</sub> and H<sub>2</sub>O, for production of platform chemicals CO and H<sub>2</sub> respectively. In the most common two-reactor set-up of the CL, two interconnected reactors (reduction reactor and oxidation reactor), containing powders of metal oxides, form a closed loop of circulating metal, being alternately reduced and oxidized respectively. The principle of its operation is based on the spontaneous release of oxygen from the metal oxide’s crystalline lattice either by thermal reduction at high temperatures (above 1300°C) or by fuel reduction, which leads to the creation of oxygen vacancies in the material. Subsequently, this reduced metal oxide is re-oxidized in the low-temperature oxidation reactor (below 1000°C) with use of water vapour or carbon dioxide.

Indeed, as mentioned, two fundamentally different pathways of the reduction are possible. Thermal reduction using concentrated solar energy is one of the most studied processes. The energy required to sustain the otherwise endothermic reduction reaction and to maintain such high temperatures is derived from the concentrated solar radiation. The complete reaction chain occurring via thermal reduction of metal oxide can be presented as per equations (2.1-2.2).



However, an intriguing approach to operating the cycle at a lower temperature, thereby decreasing the temperature swing between reduction and oxidation, is to combine the redox cycle with the methane reforming [27,28] according to the equations (3 and 2). Apart from lowering the temperature of the entire cycle, this approach also enables the production of parallel streams of syngas from both the reduction and the oxidation reactors steps as shown in

Figure 2-3, together with the possibility of the system to operate round the clock, without the need of the fluctuating renewable resource like the sun. Several sources of methane, a primary constituent of natural gas can be identified. Besides the abundant supply of locally available natural gas, increased access to natural gas reserves, through technological innovations like hydraulic fracturing (Fracking) has resulted in an increased access to methane for multiple industrial processes [29]. Additionally, current development in power to grid (P2G) technologies, with a well-established natural gas network can be speculated to provide an abundant supply of methane in future. Moreover, with an increase in the research of power to gas and the importance of biomethane in the renewable energy mix, the utility of methane would increase in the future.



As can be seen in both the processes, in the reduction step (eq. 2.1 and 2.3), the metal oxide is reduced either thermally or in the presence of methane, often up to a non-stoichiometric extent,  $\delta$ . The  $\delta$  moles of oxygen released from the  $\text{MeO}_x$  forms CO and  $\text{H}_2$  by partial oxidation of  $\text{CH}_4$ . In the subsequent reaction steps, usually exothermic, (eq. 2.2),  $\text{MeO}_{x-\delta}$  reacts with  $\text{CO}_2$  and/or  $\text{H}_2\text{O}$  to reincorporate oxygen into the metal oxide lattice, while reducing the  $\text{CO}_2$  and/or  $\text{H}_2\text{O}$  into a stream of syngas (CO or  $\text{H}_2$  respectively).

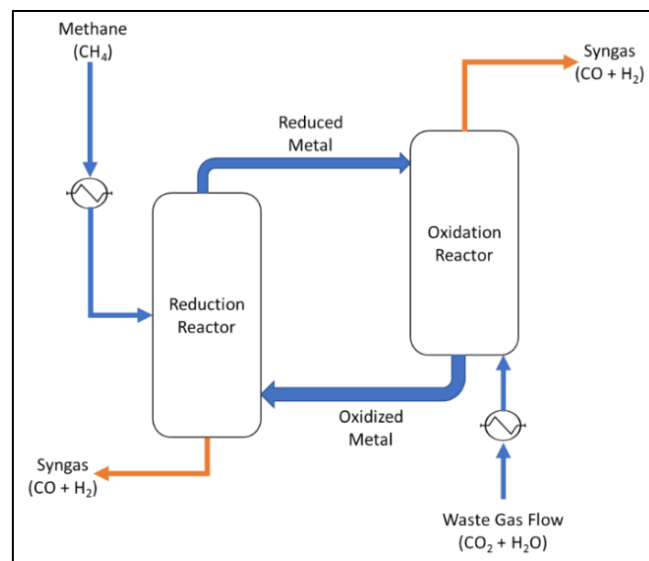


Figure 2-3 Conceptual scheme of the chemical looping Syngas production through methane reduction with subsequent splitting of water and carbon dioxide.

In addition, the chemical looping partial oxidation of methane over metal oxide provides multiple benefits listed as follows:

- a. It provides an alternative to the current high energy-intensive industrial process of steam reformation of methane (SRM) for syngas generation for subsequent chemical production.
- b. It also provides an alternate to catalytic partial oxidation of methane (CPOM), which, even though advantageous compared to SRM, suffers from the drawback of direct

contact of fuel and oxidant near the auto-ignition temperature of the fuel, raising safety concerns [30]

- c. It also negates the need for a separate Air separation Unit for pure oxygen requirement in the CPOM process, whereby, the oxygen is supplied by an oxygen carrier directly during the partial oxidation process, simplifying the entire chemical cycle greatly.

## 2.3 Prospective oxygen carriers

Oxygen carriers are essentially the species of metal oxides which has at least two states of oxidation or one metallic and oxidized state. Example include  $ZnO/Zn$ ,  $Fe_3O_4/FeO$ , etc., that has the ability to release oxygen during high-temperature reduction process [17]. Numerous studies exist on the determination of the suitable metal oxide for the chemical looping splitting cycle, the overview of which can be found in multiple literatures [17,19,24,31]. Such wide variety of metal oxides require them to be categorized specifically, based on the temperature of the reduction and oxidation reactions, the potential for oxygen storage or whether the metal oxide undergoes phase transformation during the redox cycle.

### 2.3.1 Volatile carriers

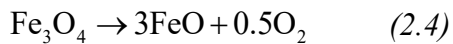
Among the different categories that exist, the oxygen carriers for the two-step chemical looping applications can be technically classified into volatile and non-volatile metal oxides. Volatile redox usually exhibits a phase transition in the reduction step, especially during thermal reduction. The metal produced due to the reduction of the metal oxide is usually in a vapour state, due to the lower boiling temperatures than the corresponding metal oxides, thus requiring rapid cooling to avoid recombination oxygen [31]. The most common volatile oxygen carriers (OCs) includes  $ZnO/Zn$ ,  $GeO_2/GeO$ ,  $CdO/Cd$  and  $SnO_2/SnO$  as metal oxide/ metal redox pair. The thermal dissociation of the volatile metal oxides is usually highly endothermic, with the  $\Delta G$  of reaction going below zero only at temperatures above 2000K. For zinc dissociation from zinc oxide, the temperature is 2253 K [31]. However, at this high temperature, the recombination of the reduced volatile metals with the released oxygen is the major problem. Therefore, a quenching process to fast cool the metal is an indispensable step for such redox pairs. Nevertheless, during the quenching process, a certain amount of oxygen recombines with the metal oxide reducing the overall effectiveness and efficiency of the cycle [17]. On the other hand, the hydrolysis reactions are usually highly exothermic and are favourable at lower temperatures. Multiple studies have focussed on the research and development of working with the volatile metal oxides [32–34]. However, the drawback of the quenching remains as the measure issue for such redox pairs. Hence, this type of metal oxide/metal redox pairs were not further considered in the present study.

### 2.3.2 Non-volatile carriers

Non-volatile oxygen carriers, unlike the volatile solids, do not undergo phase transformation upon reduction, either thermally or chemically, i.e., they remain solid during the entire

thermochemical cycle. Hence, no quenching step is necessary. Most often, specifically for thermal reduction, the non-volatile carriers are carried out from the reactor via sweep gases only as solids. Therefore, the separation of the reduced metals, usually in a cyclone is much easier, lowering the system complexity and also system losses. Nevertheless, non-volatile cycles usually utilize those metal oxides having a lower storage capacity than their volatile counterparts [17]. It is also to be mentioned that due to the lower molecular weights of the volatile materials, they tend to have a bigger share of oxygen atoms by weight. Thus, often, the storage capacity of the volatile metal oxides are 2 to 5 times higher than in the case of Magnetite/Wustite or Ceria/Cerium Oxide (III) pairs.

Several non-volatile metals were and are investigating in literature including ferrites with different valences,  $\text{Co}_3\text{O}_4$ ,  $\text{Nb}_2\text{O}_5$ ,  $\text{WO}_3$ ,  $\text{SiO}_2$ ,  $\text{Ir}_2\text{O}_3$ ,  $\text{CdO}$  to name few [35–39]. The magnetite/wustite redox cycle was firstly proposed in 1977 by Nakamura [40], while Roeb et al., in 2006, was one of the first to propose the same metal pair for the water dissociation [41]. In this cycle, the magnetite was first thermally reduced to wustite by simultaneously releasing oxygen, while the following oxidation with water of wustite ( $\text{FeO}$ ) resulted in the formation of magnetite ( $\text{Fe}_3\text{O}_4$ ) and  $\text{H}_2$ , as per the following equation (2.4 and 2.5).

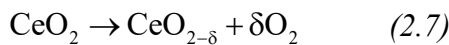
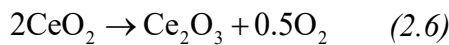


Iron oxides have been historically investigated as oxygen carriers for Chemical Looping Combustion (CLC), as described in Section 2.1. However, unlike the three-step CLC, the iron oxide-based cycles used for water and carbon dioxide splitting are two-step cycles, whereby, the Oxygen Carrier (OC) goes through the magnetite/wustite cycle, without being fully reoxidized to hematite. In his work, which essentially was a thermodynamic analysis, Nakamura developed the reaction system for alternate reduction and oxidation at temperatures of  $2200^\circ\text{C}$  and  $1000^\circ\text{C}$  respectively. The thermal reduction was evaluated to occur in air. However, the thermal reduction temperature, being higher than the melting point of the component metal oxides, limited the applicability of this process. Multiple strategies, however, can be used to improve the benefit of the cycle that included: decreasing the cycle operation pressure [42]; doping of the iron solid with transition metal such as manganese (Mn), cobalt (Co), nickel (Ni) or zinc (Zn) forming a ferrite oxide ( $\text{Fe}_{1-x}\text{M}_x$ ) $_3\text{O}_4$  or with a reduced form ( $\text{Fe}_{1-x}\text{M}_x$ ) $_{1-y}\text{O}$  reduces the reduction temperature [17,43]. All the alternatives were studied with relative advantages and disadvantages and have been extensively reported in the literature [32,41,44–46]. However, as can be noticed from the reactions (4) and (5), this redox pair OCs essentially operates between two thermodynamically stable stoichiometric conditions ( $\text{FeO}$  and  $\text{Fe}_3\text{O}_4$ ). Hence such non-volatile oxygen carriers can be also be referred to as stoichiometric oxygen carriers as a sub-category.

Indeed, there exists one other sub-category within non-volatile OCs. This is formed by those oxygen carriers, which usually release oxygen, often up to a non-stoichiometric extent. One of the most studied metals in this category is Cerium Oxide. Cerium (IV) oxide ( $\text{CeO}_2$ ) is widely investigated in literature for its structural, chemical and optical properties, making it a

promising material in several fields of applications, such as fuel cells, catalysis, CO<sub>2</sub> adsorbing materials, nanofluids etc. [47]. Furthermore, the crystallographic stability of CeO<sub>2</sub>, even after several runs of thermal processes is well documented [48,49]. Rapid kinetics, together with the very minimal effect of sintering at high temperature with good attrition resistance and mechanical strength makes ceria one of the most interesting materials for the chemical looping CO<sub>2</sub>/H<sub>2</sub>O splitting applications [28].

Temperature plays one of the most crucial roles in determining the stoichiometric extent of reduction. Abanades and Flamant have reported almost stoichiometric reduction of Cerium (IV) Oxide to cerium (III) oxide at very high temperatures of around 2000°C, however, often leading to problems of sublimation of the reduced metal [50]. Nevertheless, the focus in the later stages of material development was shifted to much lower temperatures, around 1300 to 1500°C, even though this yielded non-stoichiometric reduction of ceria. Both the stoichiometric and non-stoichiometric thermal reduction reactions, followed by the splitting with CO<sub>2</sub> and H<sub>2</sub>O, under non-stoichiometric reduction conditions are shown in the following equations (2.6) through (2.9).



As can be understood, at lower temperatures and at non-stoichiometric conditions, the removal of the oxygen by thermal or chemical reduction is essential while ensuring no change in the crystalline structure. This, therefore, results in a limiting non-stoichiometric parameter,  $\delta$ , which has been reported in the literature to be 0.35 by Bulfin et al. [51] and Kümmerle et al [52]. The corresponding maximum available oxygen storing capacity of CeO<sub>2</sub>, therefore, can be calculated as 0.033 kgO<sub>2</sub>/kgCeO<sub>2</sub> before the material loses its lattice configuration.

The performance of pure and doped ceria has been extensively studied in the literature. Gokon et al. [53] evaluated the comparative performance of ceria and the NiFe<sub>2</sub>O<sub>4</sub>, both supported and unsupported on m-ZrO<sub>2</sub>. Results showed a superior thermal stability and yield rates of Ceria over six consecutive cycles. Better ceria oxygen was reported with a non-stoichiometric coefficient varying between 0.034 to 0.11 at a thermal reduction temperature of 1450°C. However, no significant improvement was observed as the temperature was raised to 1550°C in the same study [53].

Doping ceria has been investigated for improving the extent of reduction by increasing the intrinsic vacancies that affect its electronic structure which in turn influences the ionic conductivity resulting in the redox cycle to be achieved at lower temperatures. Abanades et al. [54], in their 2010 study, reported significant improvements in the thermal reduction behaviour of Zirconia doped Ceria, Zr<sub>0.5</sub>Ce<sub>0.5</sub>O<sub>2</sub> powder in comparison to pure Ceria. It was obtained that the reduction started already at 900°C in comparison with 1150°C for pure ceria with a 70%

increase in yield of oxygen release from the doped OC. However, this increases the oxidation temperature, with water splitting reactions starting in temperatures above 800°C [54]. In a second study performed in 2011, the same research group reported the rapid decrease in the performance of the doped metal oxide for re-oxidation [55]. Sheffe et al. [56] carried out thermodynamic analyses for CO<sub>2</sub>/H<sub>2</sub>O splitting on differently doped ceria oxides. The general trend showed the initiation of reduction reaction at temperatures of 930°C with simultaneous enhancement of oxidation reactions with an increase in the dopant concentration. Results from the evaluation of thermochemical cycles for CO<sub>2</sub> dissociation utilizing doped ceria were also reported by Jiang et al. [57]. Similar improvement to the thermal reduction as obtained by Abanades et al. [58] [54], was reported utilizing Ce<sub>0.75</sub>Zr<sub>0.25</sub>O<sub>2</sub> [57]. A doubling of the CO yield from splitting of CO<sub>2</sub>, from 4.5 ml/g for CeO<sub>2</sub> to 10.6 ml/g for Ce<sub>0.75</sub>Zr<sub>0.25</sub>O<sub>2</sub> was obtained [57].

### 2.3.3 Perovskites

Besides metal oxides, perovskites, as alternatives for the OCs have gained significant research interest in the recent years. Even though the most significant share of the research for the applicability of such OCs have focused on their applicability in the CLC and methane reforming processes [17], [56], many studies have reported the outcomes of the use of perovskite in chemical looping CO<sub>2</sub>/H<sub>2</sub>O splitting [60]. Much better oxygen capacities at lower temperatures in comparison to both pure and doped metal oxides have been reported.

Using Sr<sub>0.4</sub>La<sub>0.6</sub>Mn<sub>0.4</sub>Al<sub>0.6</sub>O<sub>3</sub>, McDaniel et al. obtained an increase of 8 times the yield of hydrogen at 1350°C than pure Ceria, with a subsequent higher yield of H<sub>2</sub> and CO from the H<sub>2</sub>O/CO<sub>2</sub> split reactions respectively [61]. No noticeable drop in the performance of the perovskite was reported after 80 redox cycles, confirming the high cyclic stability of the same. These results were subsequently confirmed through the studies by Jiang et al., in 2010, where, the performance of lanthanum–ferrite based perovskites doped with Co and Mn on the ferrite side were evaluated [62]. Experimental results, on the thermal reduction of both LaFe<sub>0.7</sub>Co<sub>0.3</sub>O<sub>3</sub> and LaFe<sub>0.7</sub>Mn<sub>0.3</sub>O<sub>3</sub>, revealed the high oxygen carrying capacity of such materials. However, a poor performance of the CO<sub>2</sub> splitting was reported, which were considerably improved by the addition of supporting materials like SiO<sub>2</sub>[62]. Another study by Galinsky reported significant improvements to the reduction rate utilizing iron oxide supported La<sub>0.8</sub>Sr<sub>0.2</sub>FeO<sub>3-d</sub> (LSF) as a supplement to iron oxide [63].

### 2.3.4 Spinel Structured Oxygen Carriers

Recent studies have also focused on the development and applicability of the spinel structured oxygen carriers for the chemical looping splitting application through the modification of physical and chemical properties. The selection of the right cation enables the synthesis of an OC, optimized for the selected application, with a high structural and mechanical stability under high-temperature operations [64,65].

Aston et al reported the performance of two mixed metal spinels, NiFe<sub>2</sub>O<sub>4</sub> and CoFe<sub>2</sub>O<sub>4</sub>, prepared by incipient wetness method, with ZrO<sub>2</sub> as substrate [66]. Results indicated a high - yield of hydrogen through water splitting (7-9 times per mass of metal than iron oxide),

however, at a much lower rate than with that of iron oxide. Cocchi et performed studies  $\text{CoFe}_2\text{O}_4$  [67]. Even though a faster reaction rate was seen, there was significant carbon deposition, which would often limit the applicability of the tested material over several cycles. Also, due to the corresponding oxidation and reduction reactions, the applicability of this metal oxide to a two-step cycle is limited, with a three-step cycle being a more preferred solution [60].

## 2.4 Reactors for Chemical Looping $\text{CO}_2/\text{H}_2\text{O}$ Splitting

Based on the type of reduction mechanism, the reactor design can be fundamentally different between for the concentrated solar driven cycle and the methane driven cycle. Also, based on the two reactors or three reactor design (splitting or CLC cycle), the reactor designs change significantly. In order to present a state of the art of the reactor designs, studied and/or operated for chemical looping  $\text{CO}_2/\text{H}_2\text{O}$  splitting for the two-reactor design model, the typology is divided between solar thermochemical cycles and fuel reduction cycles.

### 2.4.1 Reactors for Solar Thermochemical Chemical Looping Splitting Cycles

The most commonly used technique to achieve the high temperature required for thermal reduction is the use of concentrated solar energy. Most often, the conventional forms of concentrated solar power generation systems, as used for electricity generation, are employed, which includes, the Linear Fresnel (line focus), Parabolic Trough (line focus), Heliostat Field (point focus) and the Parabolic-Dish (point focus) Solar Concentrators [68].

As can be observed from the mentioned list, the four technologies have been mentioned in the increasing order of achievable concentration ratio and thereby achieving maximum operating temperatures. Obviously, the concentrators with line focus are unable to generate a high temperature due to a much lower concentration ratio. Since, as per the previous discussion, a temperature of over  $1000^\circ\text{C}$  is usually employed for thermal reduction of OCs, Heliostat Field or Central Tower Systems and Parabolic Dish technologies are the preferred choice. However, due to the limitation of the scale of parabolic dishes, state of the art of solar concentrators for thermal reduction of OCs have focused on the Central Tower as the most suitable technological alternative as a solar concentrator. In addition to the type of concentrators, many other categories of reactors exist and are discussed below.

Based on the mechanism of heat transfer from the concentrated solar heat generated to the working fluid and the reactor, the solar received configurations can be categorized as *a)* Direct Process and *b)* Indirect Process [69]. For the direct process, the reactor forms a single unit with the receiver. They are the so-called volumetric receivers, and volumetrically absorb the solar radiation on the oxides. On the other hand, the Indirect Process employs an additional thermal fluid that exchanges heat with the receiver (usually in a tubular receiver).

Since the primary reaction occurs on a solid (the OC) in presence of a gas (usually sweep gas to remove the oxygen), reactor classification can be based on the arrangement of the metal oxide between the reactor. Accordingly, two reactor types can be defined [69]:

- a. **Structured reactors** – In the structured reactors, the metal oxides are most often arranged in a particular ordered structure within the reactor. The reactor design ranges from a single reactor chamber to a modular dual chamber reactor for the simultaneous production of O<sub>2</sub> and H<sub>2</sub> [70]. The most common type of reactors belonging to this category is the honeycomb, foam or membrane reactor [69].
- b. **Non-structured Reactors** – In these type of reactors, the metal oxide is distributed randomly without a particular order, with a fluidized bed, moving bed and packed bed reactors being the most common reactors of this category [69].

Indeed, yet another classification exists for the reactor based on the possibility to perform the two-step cycle in a single reactor or separate reactors for the reduction and the oxidation reactions. As mentioned, structured reactors can usually be designed to perform simultaneously, the two reactions of the two-step cycle.

The efficiency of the reactor is one of the most crucial parameters, which might limit the productiveness of the entire cycle, even with a very active OC. To maintain optimal thermodynamics, kinetics, and durability, together with economic and efficient design for production of desired product, the reactor must be able to deliver solar heat and reactant gases to the reactive materials without dissipating unnecessary energy or requiring significant amounts of external work, while also being resistant to structural failure [70]. Efficient thermal management and minimization of heat losses are essential for a high-temperature process with heat loads. The primary necessities to ensure an adequate system design while minimizing system heat losses can be summarized as follows [71]:

- a. To limit the number of solar reflections, due to the limited efficiency of commercially available reflectors.
- b. To limit heat loss by re-radiation or convection from the light absorbing material.
- c. A rapid transfer of heat from the solar radiation to the active material.
- d. By avoiding unnecessary temperature changes of the reactive material and reactor system due to an inefficient heat recuperation between solids.
- e. By ensuring that the gas mass transport maintains the thermal efficiency and minimizes the electrical work and efficient removal of all reactants and products to ensure that there is no back reaction.
- f. By ensuring an effective transport of solids and at the same time maintaining the structure of active solid materials.

Besides efficient management of parasitic losses from heat and mass transport, several other key design considerations play a crucial role to ensure adequate system performance of the entire cycle. These factors can be summarized after Muhich et al. as follows [70]

- a. The reactor should be modular and scalable, thereby eliminating the need for many small reactors. This also ensures the economy of scale and prevents higher heat losses because of their small volume to surface area ratios, for smaller reactors.
- b. The reactors should be able to effectively decouple the reduction and oxidation reactor times, since, most often the kinetics and reaction rates are not identical.

- c. The reactors should be able to effectively decouple the reduction and oxidation steps, both spatially or temporally, to separate the  $O_2$  and the product gases ( $H_2$  and  $CO$ )
- d. The design should minimize moving parts, thereby also preventing the high-temperature operation failure of the reactors.
- e. Reactor materials should be compatible with the OCs, as well as be stable under the high temperature operating conditions.

Based on such design goals, significant work has been performed and the reactors can be broadly classified into monolithic (structured) or particle systems based (non-structured) reactors. A brief discussion on some of the developed reactors for the solar thermochemical cycle for two-step  $CO_2/H_2O$  splitting syngas production follows.

### 2.4.1.1 Monolithic or Structured Reactors

The basic design feature of this type of solar thermal reactors is based on a self-supported active material. In addition to this, the reduction and the oxidation steps are spatially separated [70]. This is made possible either by mechanical motion (e.g., rotation) of the material or redirection of the solar beam. Many designs of monolithic reactor designs have been proposed.

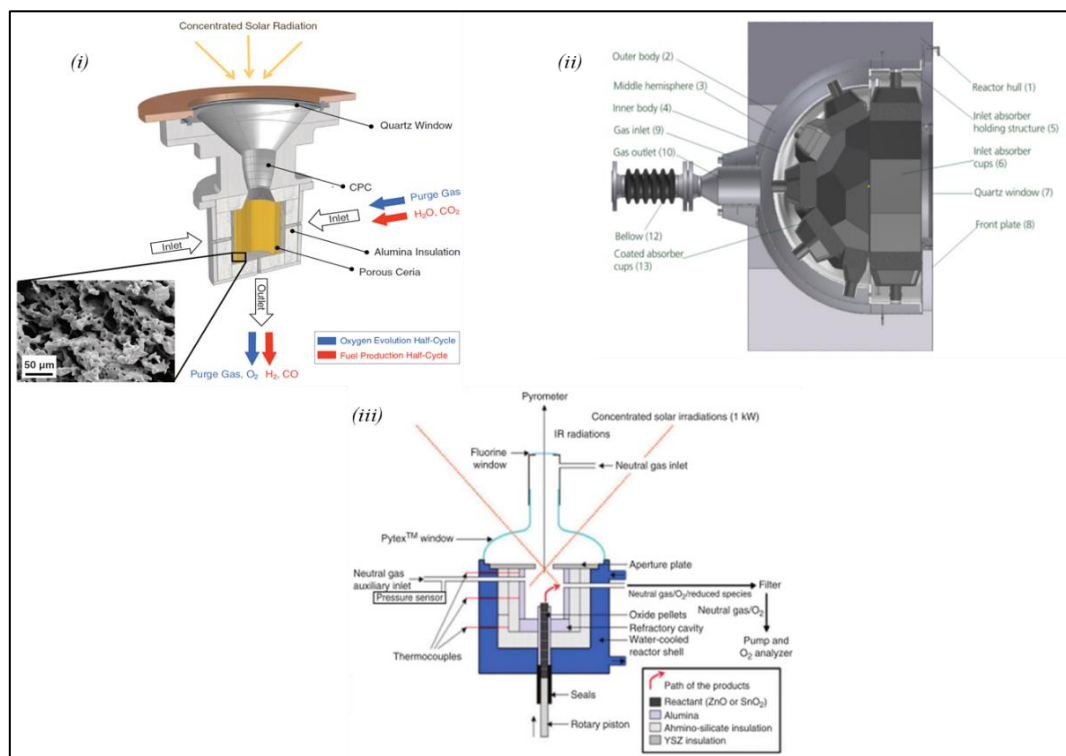


Figure 2-4: Schematic representations of i) Stationary monolith cavity (SMC) reactor by Chueh et al. [72] for  $H_2O-CO_2$  dissociation; ii) Sectional view of the Spherical Stationary monolith cavity (SMC) reactor as proposed by Houaijia et al [73] and iii) the rotating piston reactor as proposed by Chambon et al [74]

The simplest of the monolithic or structure reactors is the Stationary monolith cavity (SMC), as proposed by Chueh et al in 2010 [72], a schematic representation of which is provided in

Figure 2-4 (i). Here, the active material present in a porous cavity was irradiated from the top through a quartz window. The gases were proposed to be introduced radially, flowing through the OCs and exiting from the bottom. The tested metal oxide was monolithic porous ceria collected in cylinder form. The peak solar to fuel efficiency obtained was 0.8%, without any heat recovery [72]. In further experiments by Furler et al [75] the monolithic ceria was replaced by porous ceria felt, which led to the doubling of the solar to fuel efficiency. An energy balance was performed to evaluate the efficiency of the proposed reactor. It was found that around 50% of the energy losses came from conduction through the reactor wall, while 41% from the re-radiation of the windows [72]. Even though the first loss can be decreased by improving the reactor insulation, the losses through the windows are limited by the current technology of window materials. However, a good cyclability of the reactor was obtained, where, the reactor was able to operate continuously for 500 cycles, the steady state being achieved after 200 cycles.

Other types of monolithic cavity reactors have been proposed with one or more reaction chambers for the alternate reactions of the redox cycle occur [73]. Houaijia et al. [73] proposed a multi-cavity reactor, while at the same time aiming to improve the thermal performance of the reactor. A modular reactor design for 1MW thermal output was proposed with conical and spherical geometries being obtained as the most promising absorber geometries. However, spherical geometry was simulated as the most suitable and the design of the reactor developed is presented in the following Figure 2-4 (ii). A net cycle efficiency of 0.88% was obtained for the complete solar receiver-reactor system including hydrogen production. Radiation losses predominated the overall losses, contributing to over 50% of the net thermal losses, close to 100 kW. Windows continued to play a major role in the overall system losses, resulting in the poor system efficiency of such reactor designs.

Depending on the design of the solar cavity reactors, the reactive material is either free-standing or supported on a scaffolding, like a honeycomb structure [76]. In addition, the active metal can also be directly heated by the concentrated sunlight through a quartz window or indirectly heated using a containment structure. Even though the simplicity of design makes such cavity reactors less prone to mechanical failure, they lack in having an inherent way to recuperate the heat released during the temperature swing between the reduction and oxidation steps, unless the reduction and oxidation reactors are contained within a single cavity. This leads to lowering of the system losses. Additionally, the use of a quartz window to introduce solar radiation into the reaction chamber limits the potential size of the reactor, which means that these reactor types cannot fully exploit the economies of scale.

As opposed to a cavity reactor, the rotating piston reactor has been proposed, as shown in Figure 2-4 (iii). Even though the primary principle of the reactor design is same as that of the cavity reactor, this reactor design particularly suits well for application to volatile stoichiometric reaction chemistries [74]. For volatile metals, as the material reduces and volatilizes, it is swept by an inert gas into a quenching chamber, while the fresh material is continuously fed into the reactor. The rotating monolith reactors have similar advantages and disadvantages as SMC reactors, however, enabling the use of volatile chemistries [70].

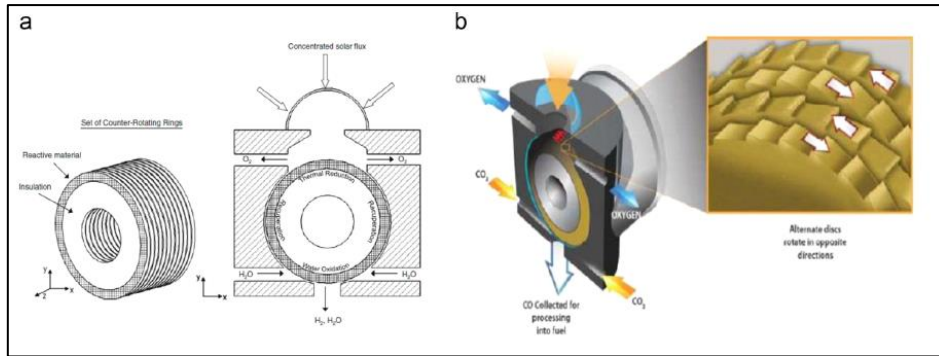


Figure 2-5: CR5 reaction proposed by Diver et al.[77].

The Counter-Rotating-Ring-Receiver-Reactor-Recuperator (CR-5) was proposed by Diver et al. [77], where, a stack of counter-rotating rings with metal oxide fins along the circumference will be irradiated in the upper part by solar beams. In this design, the pellets of the active material are fed into the hot zone of the reactor by a piston as shown in Figure 2-5. For volatile metals, as the material reduces and volatilizes, it is swept by an inert gas into a quenching chamber, while the fresh material is continuously fed into the reactor [74]. Each ring rotates in the opposite direction to that of its neighbour at a speed less than 1 RPM to enhance the heat recovery. As the ring rotates, the metal oxide alternately passes from the high-temperature reduction zone to the lower temperature oxidation regime and back again to form a continuous cycle. The calculated solar to fuel efficiency was 29% [77]. The scalability of such reactors was also evaluated, as Kim et al. proposed the use of the CR5 reactor for H<sub>2</sub>O/CO<sub>2</sub> splitting for liquid fuel generation within the “Sun to Petrol” (S2P) project [78].

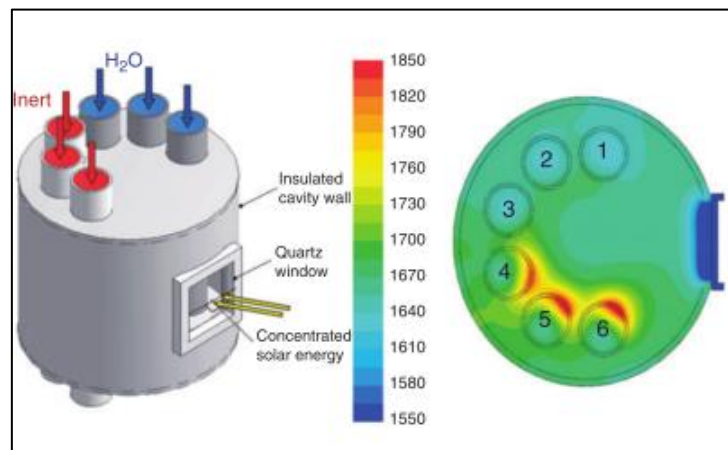


Figure 2-6: The SurroundSun reactor design proposed by Melchior et al. [79]

Yet another reactor design for structured reactors was developed. The SurroundSun reactor, using a ‘tube within a tube’ design, could potentially avoid the use of a quartz window, which by far was found to be one of the most inefficient components of such solar reactors [70]. As proposed by Melchior et al. [79], and followed by other studies by Martinek et al. [80], one or more tubular reactors would be packed with reactive material and housed within an insulated cavity. The concentrated sunlight would enter through an open aperture and the overall operation would occur in a temperature swing mode. While half of the tubes would be subject

to concentrated solar energy, thereby undergoing reduction, the other half would be exposed to steam or CO<sub>2</sub> to undergo oxidation. The reactor operation and geometry are pictorially depicted in Figure 2-6. Additionally, the reactor can also be operated in an isothermal mode, where, all the tubes are continually illuminated, and the reduction and oxidation cycles are subject to controlling the respective sweep and reactant gas flow. Not having a transparent material, in the form of a window, nor having rotating mechanical parts have significant advantages in such reactor designs, allowing them to be potentially scalable subject to the availability of that suitable containment materials are available [70]. However, one serious drawback of this type of reactor design is the uneven radial illumination of reactor [80] and poor thermal transport within the bed which results in lower redox reaction rates and, thus, lower production throughput [79]. Other problems like pumping gases through the packed bed, development of hot spots within the reactor bed, poor heat conductivity, etc. poses challenges to the commercial scale development of this type of reactors [70].

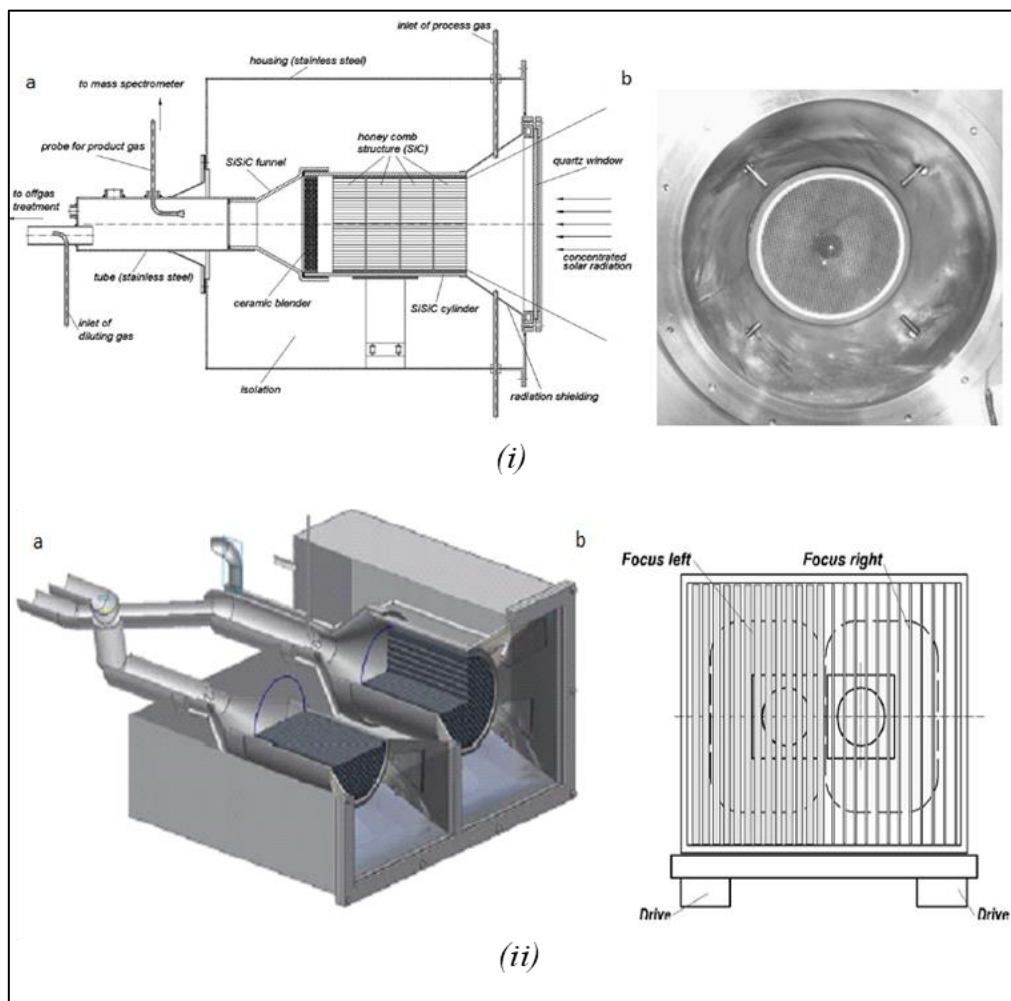


Figure 2-7: Schematic representation of i) Honeycomb multi-channels Solar Reactor as proposed by Roeb et al. [41]; ii) multi-chambers reactor proposed by Roeb et al. [81] (a) and lamellae shutter for temperature regulation (b).

Different prototype reactors incorporating fixed coated ceramics in a structured reactor form have been developed within the HYDROSOL project. Roeb et al. [41], proposed a structured solar reactor for simultaneous reduction and dissociation, implementing a honeycomb monolith

reactor made by a plurality of channels. As can be seen from Figure 2-7(i), each of the channels was coated by a surface of the active metal oxide compound and comprises a SiSiC ceramic coating with ferrite oxide. The metal oxide has been chosen to be directly irradiated by the concentrated sun rays. The reactor was tested within a solar furnace, under a reduction temperature of 1200°C, and the corresponding water dissociation temperature of 800-1200°C for six cycles [41]. A better output from oxidation reactions was obtained at a high temperature of 1200 °C, which, nevertheless, results in precipitation, leading to a faster degradation of the support material. Around 80% productivity of the water-splitting reaction was obtained, at an efficiency of 40%, however, producing hydrogen intermittently.

To improve on the discontinuity in the production of hydrogen, due to the application of the same reactor for alternate reduction and oxidation Roeb et al. 2009 [81] further proposed a quasi-continuum reactor for hydrogen synthesis. The honeycomb structures, as developed in their previous study was used, however, by employing two parallel chambers, that made it possible to perform both reductions and splitting together (Figure 2-7.(ii.a)). Similar to the previous study, they were assessed at 1200°C and 800°C for reduction and oxidation, utilising a lamellae shutter to regulate the different temperatures in the respective reactors, as shown in Figure 2-7.(ii.b).

A further scale up plant of 100 kW<sub>th</sub>, based on the multi-chamber reactor design with the honeycomb structure, as proposed by Roeb et al. [81] with a solar tower as a concentrator was installed on the Plataforma Solar de Almeria [82]. About 35 g per cycle of H<sub>2</sub> was measured which resulted in the production of around 500 grams of hydrogen per day, even though the objective was set at a daily production of 3 kg. Deactivation of the metal oxide during the cycles and non-homogeneous temperature distribution inside the coated channels were some of the challenges observed [81].

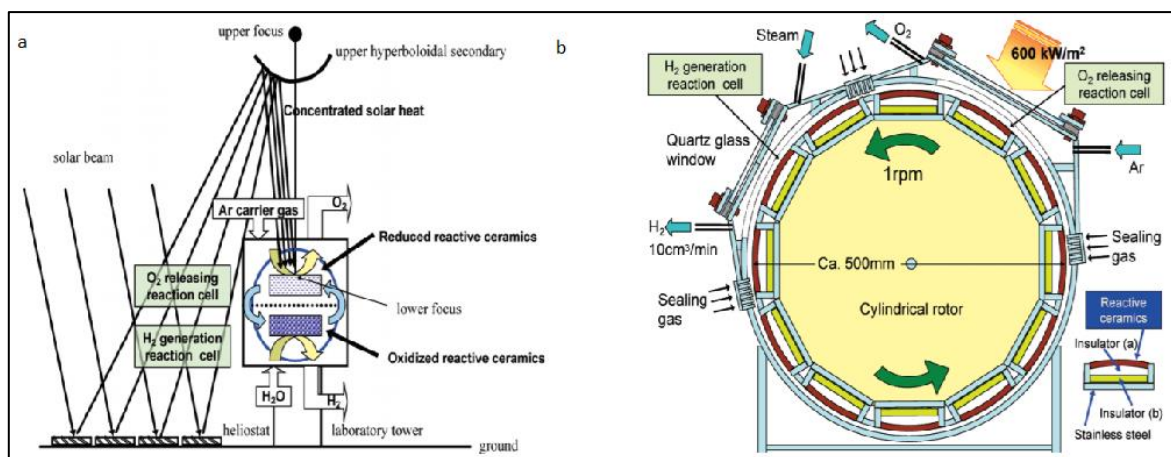


Figure 2-8: a) Rotary reactor concept proposed by Kaneko et al. [83], b) pilot scale rotating reactor.

An alternative to the design of Roeb et al. [81], for the continuous production of hydrogen in a honeycomb monolith structure, Kaneko et al.[83] proposed a rotary reactor which would be able to perform both reduction and oxidation continuously. A rotating reactor between two chambers was proposed, where, water splitting was simultaneously performed in one reactor,

to that of reduction in another, as shown in Figure 2-8. Like the previous study by Roeb et al [81], both lab and pilot scale applications were studied using a Ni-ferrite oxide coated reactor [83]. At the reported optimum temperatures for oxidation and reduction (900°C and 1200°C respectively), 2.1 cm<sup>3</sup> of O<sub>2</sub> was produced in 30 minutes [83].

#### 2.4.1.2 Particle or Non-Structured Reactors

This category of reactors essentially utilizes the movement of particles (i.e., the OCs), rather than the reactor itself. This results in the reactors to be non-structured, in relation to the arrangement of the metal oxides within the reactor [69,70]. Such movement of the OCs enables easy decoupling between the oxidation and reduction reactions, which, often have much dissimilar reaction kinetics.

One of the first reactors to be proposed of this kind was a tubular packed bed reactor in 1995 by Tamaura et al. [84]. It comprised a 2 cm diameter quartz tubular packed bed reactor heated by a solar furnace. As can be seen from Figure 2-9, a secondary concentrator was placed behind the solar reactor to ensure a uniform irradiation of the external surface. The performance of the reactor was evaluated by using an OC that comprised 5 grams of Ni<sub>0.5</sub>Mn<sub>0.5</sub>Fe<sub>2</sub>O<sub>4</sub> powder mixed with 7.5 grams of Al<sub>2</sub>O<sub>3</sub>. Alternate streams of Argon and water was used for reduction and oxidation respectively. Low amount of oxygen produced, together with the limitations with respect to use of oxygen free atmosphere for reduction step was obtained as significant disadvantages [84].

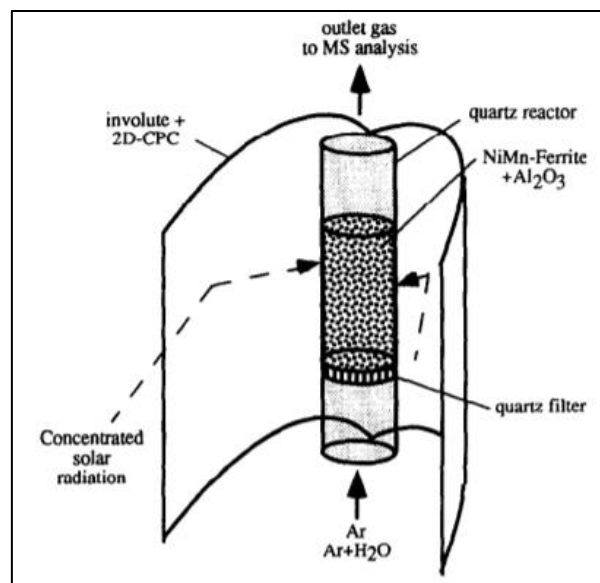


Figure 2-9: tubular packed bed solar reactor for H<sub>2</sub> production proposed by Tamaura et al. [84].

A comprehensive reactor design, overcoming multiple challenges of the non-structured class of reactors is the rotating cylinder type reactor by Müller et al. [85]. In this reactor design, sunlight would enter the rotating cylinder, where the OCs are contained along the main axis, as shown in Figure 2-10 (i). The design of such reactors has specifically focused on the use of volatile stoichiometric cycles. Therefore, the reduced material is removed via a vacuum pump

and transported to the quenching and oxidation units. Screw feeders are employed for the feeding in fresh OCs [86]. Even though a good mass and heat transport properties are obtained, due to the use of direct radiation, these types of reactors often suffer from scale limitations with the use of quartz windows. Moreover, the presence of the rotary elements at high temperatures of more than 1500°C creates significant operational challenges to the proposed design. Nevertheless, a reactor efficiency of 14% and a process efficiency of 12% was obtained by employing ZnO as the OC. Optimal operating conditions and feed conditions were also studied and reported in the same study [85].

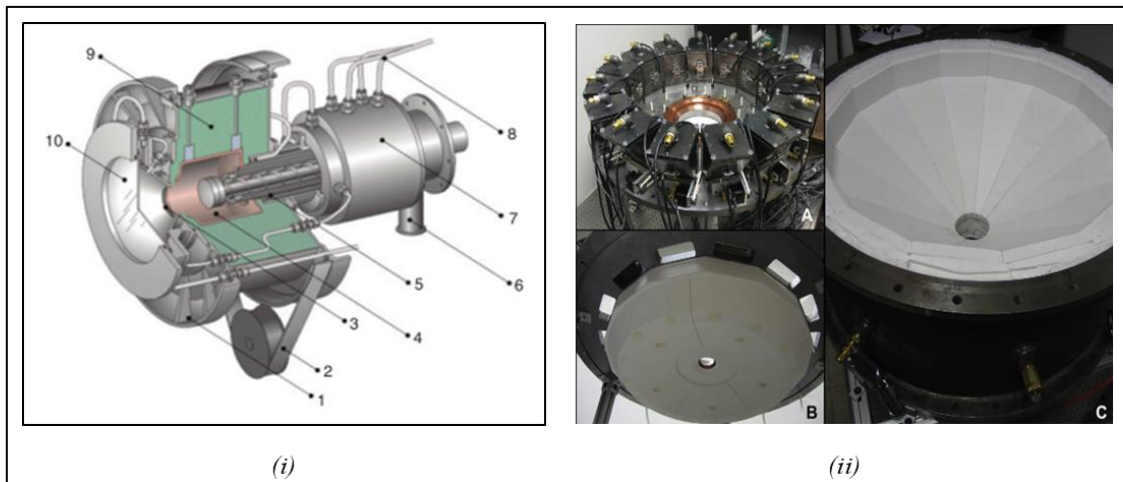


Figure 2-10 *i*) The Rotating particle flow reactor proposed by Muller et al. [85] . The labels in the schematic are as follows (a) point out: (1) rotating drum, (2) actuation, (3) aperture, (4) cavity, (5) screw feeder, (6) product outlet port, (7) rotary joint, (8) working fluids, (9) insulation, (10) quartz window and labels in (b) point out: (1) water-cooled window mount and vortex-flow generation, (2) water-cooled cavity aperture, (3) BOP and data-acquisition cavity access ports, (4) alumina-tile reaction surface, (5) annular solid ZnO exit, (6) bulk insulation and cavity-shape support, (7) central product-vapor and gas exit; *ii*) The proposed beam-down solar thermochemical reactor by Koepf et al. [87]: (A) hopper assembled and water-cooled window mounted reactor top (B) segmented and alumina pin suspended reaction cavity ceiling, (C) inverted-cone reaction cavity, lined with alumina tiles, backed by three layers of ceramic insulation.

To overcome the issues of a mechanically moving reactor, several different reactor designs, especially relating to material feeding has been proposed. Initially, a simple beam down reactor was developed on an experimental scale, which was further aimed to improve by incorporating vortex flow in a two-chambered solar beam down thermochemical reactor by Koepf et al. [87,88]. Abbreviated as the GRAFSTRR (Gravity-Fed Solar-Thermochemical Receiver/Reactor), it features an inverted conical-shaped reaction surface, as shown in Figure 2-10 (ii). The OCs were fed from the top and gravitationally transported the particles through the incident concentrated solar radiation, essentially forming a moving bed, undergoing a thermochemical reaction at high temperature upon exposure to highly concentrated sunlight within the reaction cavity. A good reactor design and stability with ZnO as the OC was demonstrated.

Particle reactors, essentially focusing on non-volatile metal oxide redox pairs have also been developed in recent years. Scheffe et al. [89] proposed an aerosol-based reactor design, in which the particles were proposed to be loaded at the top of a long tubular reactor, which would subsequently gravity fed through the hot zone of the reduction chamber, as shown in Figure 2-11(i). It essentially resembles a moving bed reactor. The inert sweep gas in the reduction reactor is fed from the bottom, that flows counter to the reducing particles and can be used to increase residence time and/or mass transfer [70,89]. For volatile metal oxide redox pairs, the released oxygen and metal vapour are collected at the top of the reactor for quenching. However, for non-volatile OCs, the reduced metal particles are collected from the bottom and subsequently fed to the oxidation reactor [89]. This reactor type essentially employs the indirect heating of metal oxide particles, where the heat is conducted and radiated on to the metal oxide particles from the walls of the reactor, which directly absorb the concentrated solar radiations. Ceria was employed as the OC and the complete set up was tested at a temperature range of 1723 to 1873 K and under vacuum conditions of oxygen partial pressures between  $5 \times 10^{-5}$  and  $1.2 \times 10^{-4}$  atm. A very high, almost thermodynamic yield of ceria reduction was obtained, with a very limiting mass flow being with respect to the reactor size for maximum yield. An isothermal operation of the reactor has been envisaged, and together with effective decoupling of the reduction and oxidation reactors, would result in a potential twenty four hour syngas generation from CO<sub>2</sub>/H<sub>2</sub>O splitting [89].

Even though the above model of reactor design would benefit significantly from low mass transfer limitations and the lack of a quartz window, the essential drawbacks lie in the lack of a direct connection between the reduction and the oxidation reactor leading to difficulties in metal handling, especially from the oxidation to the reduction reactor and inadequate solid-state heat recuperation [70]. To overcome such barriers, the internally circulating fluidized bed reactors were proposed by Gokon et al. [90] combined with a beam-down solar concept, as shown in Figure 2-11(ii). This reactor design attempts to retain the low mass transfer limitations of the aerosol reactor while simultaneously enabling both reduction and the oxidation reaction steps to occur in a single chamber [90]. As can be seen from Figure 2-11(ii), the OCs are loaded into a reaction chamber containing a centre draft tube, while the inert sweep gases are fed from the bottom of the reactor below the draft tube. This fluidizes the particles and forces them to rise through the centre and afterwards, fall through the annulus. A quartz window at the top of the reactor bed is employed to directly irradiate the particles from the top, while the circulating bed facilitates the heat transfer along the entire length of the fluidized bed.

The reactor performance was evaluated with unsupported NiFe<sub>2</sub>O<sub>4</sub> and supported NiFe<sub>2</sub>O<sub>4</sub>/ZrO<sub>2</sub> on a lab scale, using a high-powered sun-simulator equipped with three 6 kW Xenon lamps. Non-uniform heat distribution within the reactor was obtained, with only the upper part of the draft tube measuring sufficient temperatures required for the reduction step [90]. On an overall 30 minutes cycle, a 35% reduction of the supported ferrite oxide was obtained, however, with a subsequent complete re-oxidation for H<sub>2</sub> production from WS. The need for a quartz window, and presence of the oxidation reactor within the same chamber,

limiting the space for reduction reactor reduction and unequal heat distribution are primary disadvantages for efficient use of concentrated sunlight.

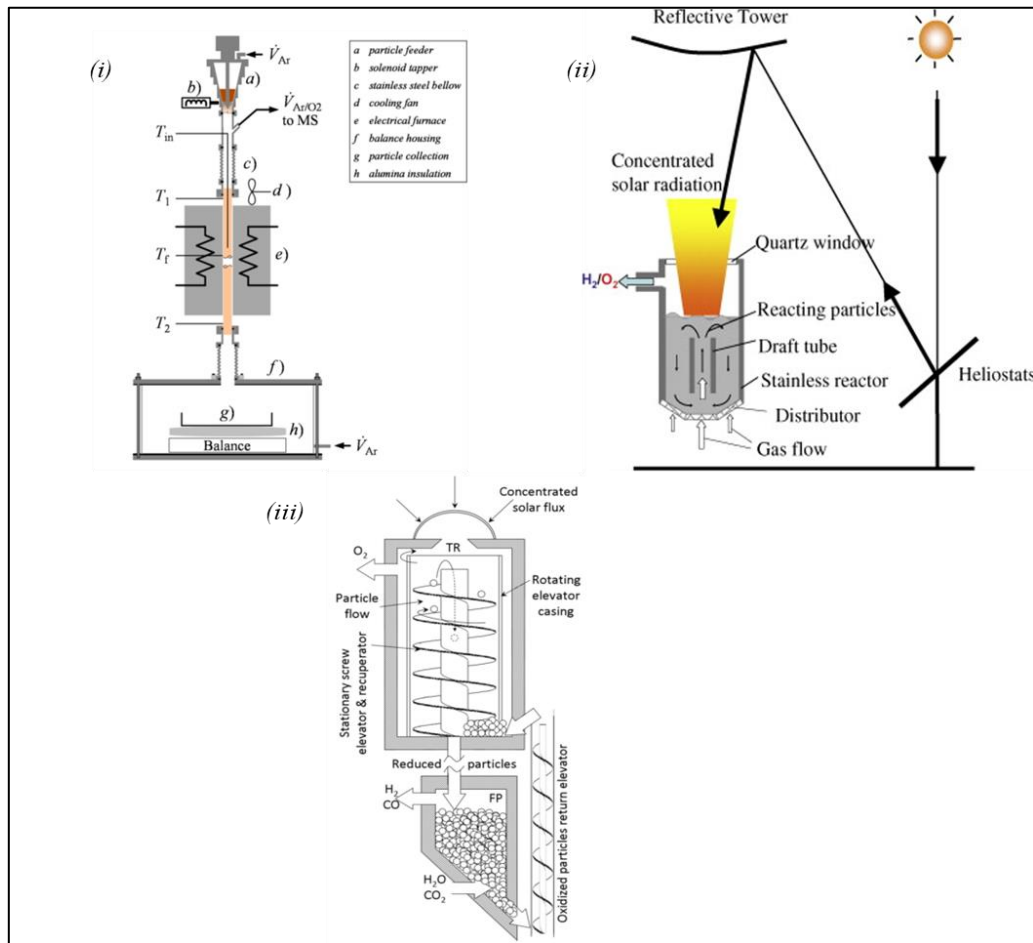


Figure 2-11: The schematic representation of i) aerosol reactor, as proposed Scheffe et al. [89]; ii) internally circulating bed proposed by Gokon et al. [90]; Moving Packed Particle Bed Reactor, proposed by Ermanoski et al. [91]

In another reactor design, a Moving Packed Particle Bed Reactor, Ermanoski et al [91] attempted to decouple the reduction and oxidation reactions, while maximizing the solid-solid heat recuperation. The reactor comprises a directly illuminated reduction chamber, at the top of a hollow ceramic screw located above an oxidation chamber. A schematic diagram of the proposed configuration is shown in Figure 2-11(iii).

The fully oxidized OCs are lifted to the bottom of the reduction chamber via a screw elevator, after which a rotating casing pushes the particles up to a stationary ceramic screw which also serves as a heat exchanger. The reduction step occurs at the top of the reactor, where the particles are irradiated with the concentrated solar light before dropping through the hollow centre of the screw elevator [91]. The generated  $O_2$  would be removed by vacuum pumping. As the reduced particles fall through the centre of the stationary screw they would be able to exchange heat with the oxidized particles moving up the outer section of the reactor. The oxidation zone is roughly atmospheric, while the reduction zone would operate at a low pressure, the screw acting as a pressure buffer between the two. The oxidation chamber forms

a secondary moving bed through which  $\text{H}_2\text{O}/\text{CO}_2$  can be pumped, thus re-oxidizing the OC, thereby generating syngas. While decoupling the oxidation and reduction reactions, this reactor design also simplifies the solid-solid heat transfers, provides co-location of both the redox steps and enabling continuous reaction. A design update has also been proposed by Ermanoski [92], whereby a staged pressure reduction has been proposed to facilitate oxygen removal while de-emphasizing the solid/solid heat recuperation. However, the use of the quartz window presents the familiar drawback, which, in addition to limiting the reactor size based on the size of available quartz windows would also increase the probability of attracting fines through thermophoretic deposition. This could potentially result in a diminished window transparency or catastrophic window failure if the deposited particles produce hot spots on the window. Additionally, large rotating parts at high temperatures are also a negative aspect, straining the vacuum seals and stressing the materials of construction [70].

Another recent development in reactor configuration was the Solar Thermal Particle Flow Reactor proposed by Muhich et al [70]. The design is based on a beam-up approach and comprises multiple reduction/oxidation chambers arranged in an inner and outer circle. The reduction chambers have been designed to form the inner ring of the reactor, while the oxidation chambers are on the outside. The reactor is proposed to be placed on a central tower, with concentrated sunlight being directed up through the gap in the bottom of the receiver, as illustrated in Figure 2-12. Due to the need of only one reflection by the downward-facing cavity receiver, a minimal convective heat loss from the hot gas rising out of the aperture is envisaged.

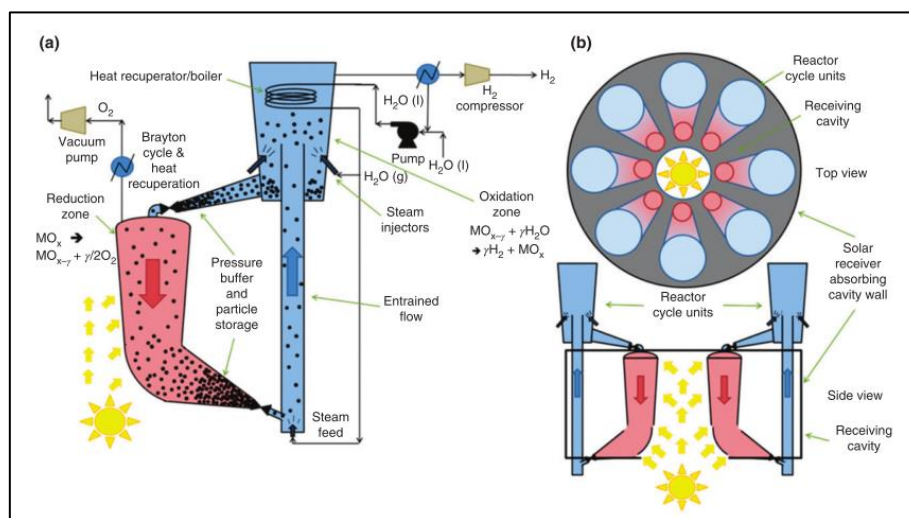


Figure 2-12 The proposed solar thermal particle flow reactor (not scaled) by Muhich et al [70], where (a) represents the individual reduction/oxidation reactor unit and (b) shows the receiver configuration containing multiple individual reduction/oxidation reactor units

The reduction reactor forms a moving bed reactor, indirectly heated through the reactor wall, and oxygen using vacuum pumping. The reduced particles, forming a pseudo packed bed, before entering the oxidation reactor would also provide a pressure buffer, enabling simultaneously a low pressure in the reduction reactor and a high steam partial pressure in the oxidation reactor [70]. The oxidation reactor is essentially a fluidized bed reactor, the particles being transported up by steam entrainment, enabling the oxidation time to be decoupled from

the height of the steam conveyance tube. The design claims the possibility to run the reduction and oxidation reactions at near-isothermal temperatures, reducing the need for solid-solid heat recuperation and lowering thermal stresses on the reactor due to cooling and reheating. Use of the fluidized bed results in a better heat distribution and gas/solid heat recuperation, resulting in a potential increase in the overall reactor and system efficiency. However, key challenges like the development of high-temperature ceramic heat exchangers for steam/steam heat exchange, high-temperature and thermally shock resistant reactor containment materials compatible with active materials, robust flowable active particles, and tower/receiver/heliostat designs allowing for efficient beam-up solar heating remain [70]. It is worth noting that the selectivity of the products in these types of reactors are limited to the fluidization regime in which the reactor operates and the downstream usage of the product gas.

## 2.4.2 Reactors for Chemical Looping Splitting Cycles with Carbonaceous Fuels

Experimental set-up using fixed bed reactors for studying the behaviour of methane partial oxidation using metal oxides have been performed and reported in multiple studies in the literature [29,30]. Solar aided methane reforming using ceria as the OC has been proposed and studied by Welte et al [28]. The reactor design concept is a particle transport reactor, whereby the heat required for the endothermic reaction has been proposed to be supplied via a solar concentrator. The schematic of the reactor, as proposed by Welte et al is shown in the following Figure 2-13. Both counter and co-current configurations have been proposed and evaluated. The maximum non-stoichiometry obtained was 0.25 with a solar to fuel efficiency of 12%. Indeed, the primary concept of the reactor was to use methane as an aid to enhance the thermal reduction and not as a primary reactant. The authors also reported the simultaneous upgrading of the calorific value of methane by 24% using concentrated solar energy.

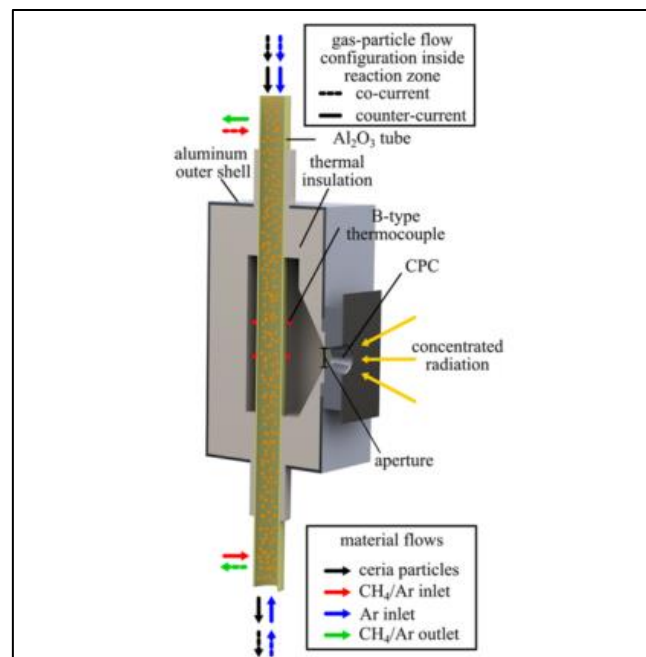


Figure 2-13 Schematic of the proposed solar particle-transport reactor by Welte et al [28] showing both counter current and co-current gas-solid flow configurations.

However, unlike thermal reduction of metal oxides for chemical looping cycles, no commercial-scale reactor design exists for methane partial oxidation coupled to CO<sub>2</sub> and H<sub>2</sub>O splitting. Multiple reactor designs based on fluidized or moving bed have proposed reactors for three-step chemical looping combustion cycles with complete combustion of methane aiming to produce CO<sub>2</sub> and H<sub>2</sub>O [60]. However, being a fundamentally different process to what the present study aims to explore, such reactors have not been further elaborated in detail.

## 2.5 Modelling of Reactors

Fundamental to the efficiency and reliability of the Chemical Looping process, irrespective of the type of reduction, is the type, behaviour and performance of both the reduction and oxidation reactors. This is necessary to not only determine the possible losses and limitation of the reactor design but also improve the understanding of the selection of the reactor design based on downstream applications of the generated products. Therefore, the modelling of the reactor would aid the design, optimization, and scale-up of the process, to obtain high metal reduction and gas conversion rates in both the reactors, together with identifying the challenges from scale-up of such proposed reactor systems. Most of the advanced reactor design modelling has been performed for chemical looping combustion [93,94]. As mentioned, non-structured reactors have shown the highest potential for scale-up, of which moving bed and fluidized bed reactors are the most commonly studied [95].

### 2.5.1 Fluidized Bed Reactors

Fluid bed reactors is an industrially advanced technology being used in the industry for many years now [96], with the first industrial scale devices was for coal gasification, known as the Winkler's coal gasifier. Since then, the concept has been expanded to different catalytic processes and synthesis of the hydrocarbon-based fuels in the Fischer–Tropsch process [96]. A significant development in scaling up of the reactor has taken place, especially for coal combustion and metallurgical processes. Commissioned at the end of the 2000s, the newest unit of Łagisza power plant in Poland uses the Circulating Fluidized Bed (CFB) boiler that supplies supercritical steam to the 480MWe turbine.

Modelling of fluidized bed reactors can be categorized into three categories after Abad et al [93], based on the fundamental principles followed for the respective design and evaluation.

- a. Simplistic models neglecting the complex fluid dynamic behaviours taking place in the fluidized [97,98];
- b. Macroscopic models based on empirical correlations for the fluid dynamics of a fluidized bed [99]; and
- c. Multiphase computational fluid dynamic (CFD) models [100,101]

Each of the different principles followed have their individual advantages and disadvantages. While the simplistic models lack accuracy, they provide relatively faster results in comparison to CFD models that are restricted from the large computational power necessary for evaluating the same.

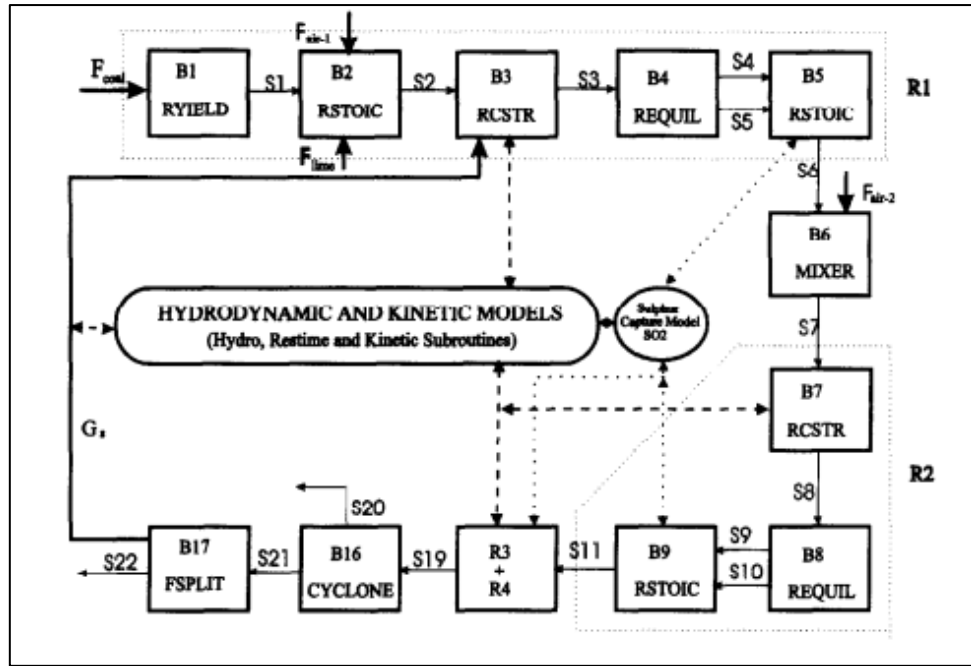


Figure 2-14 Proposed Hydro-dynamic and kinetic model of a Circulating Fluidized Bed Reactor in ASPEN Plus as proposed by Legros et al, 1998 [102]

To reduce the complexity of the mechanistic modelling approaches, the development of simplistic models incorporating the principles of the chemical reactions taking is necessary. Such an approach may be conveniently realized using the process simulator ASPEN Plus, a chemical design tool. It is widely used and accepted in the industry for its versatility, ease of use and ability to simulate a wide range of steady-state processes ranging from single unit operation to complex processes involving many units [102]. Legros et al [102] studied the modelling of circulating fluidized bed reactors for coal combustion in ASPEN Plus, by essentially utilizing the first principle of the reactor modelling stated above. Since no in-house fluidized bed model existed at that time in the ASPEN Plus reactor directory, a model of a circulating fluidized bed, using conventional reactor models of ASPEN PLUS integrating Fortran blocks and user kinetic subroutines were used to develop the desired model with satisfactory results. The proposed model is shown in Figure 2-14. Similar models have been extensively used for modelling coal and biomass gasification or combustion processes, with results being reported in the literature [103].

However, with the addition of the in-house fluidized bed model to the ASPEN Plus directory (v8.8), the need to develop own model to replicate fluidized bed hydrodynamics would no longer be there. Of course, kinetic modelling for reactions in the reactor is essential to be included to obtain accurate results. Indeed, the present in-house fluidized bed model in ASPEN Plus, that is simulated as a series of stirred reactors (RCSTR), utilizes the second principle of modelling fluidized bed reactors using empirical relations for the hydrodynamics of the fluidized bed [104].

## 2.5.2 Moving Bed Reactors

Similar to the fluidized bed, moving bed reactors have been extensively used in the chemical industry. One of the most used is the countercurrent packed bed reactor, also called the moving bed reactor, comprising two different phases moving countercurrent to each other and thereby transferring mass and/or energy between the phases accompanied by a chemical reaction in one or both phases [105]. The most famous example is the blast furnace, followed by calcination of limestone, etc. [105]. In spite of the simplicity of operations and major economic advantages of moving-bed operations, the main aspects of heat and mass transfer in these systems have received less attention in comparison with the fixed or fluidized bed reactors due to the absence of a general model and numerical techniques in solving the governing equations [106].

Most of the studies for modelling moving bed reactors have focussed on selecting the ideal reaction mechanism to increase the accuracy of prediction of the products from the designed reactors [106]. While Parisi and Laborde [107] and Negri [108] studied the applicability of the shrinking core reaction model, Dussoubs et al [109] extensively analysed the additive characteristic times model for formulating accurately the gas-solid reaction rates. Another kinetic model, the extended grain model was adopted and extended for the moving-bed reactor introduced by Niksiar and Rahimi [106]. Nonetheless, Rahimi et al [106] developed and reported a comprehensive numerical model of a moving bed reactor for reduction of  $\text{Fe}_2\text{O}_3$  pellets via an in-house methodology developed using fundamental principles of thermodynamics and chemical kinetics. An average error of 1.2% was reported from the obtained results of the simulation [106].

Reactor modelling using commercial software ASPEN plus provides multiple benefits and advantages, as already mentioned earlier. Since no moving bed reactor model exists in ASPEN Plus, similar to past modelling of Fluidized bed reactors, the development of a comprehensive model using the available in-built reactor models of ASPEN Plus is necessary. Benjamin, 1985 [110] proposed a built-in model for a counter-current moving bed coal gasifier. However, the results showed that the solution was time-consuming and an analysis of the proposed model can be found in the ASPEN guide to moving bed gasifier modelling [111]. An alternative, as proposed by ASPEN Plus [111], to utilize multiple RCSTRs in series, results in a considerably simple model. This also allows the direct use of the built-in algorithms of ASPEN Plus.

Such a reactor model for thermodynamic assessment of the moving bed reactor was assessed by Tong et al [112] for a moving bed in a chemical looping combustion cycle with  $\text{Fe}_3\text{O}_4/\text{Fe}$  redox pair and methane as fuel. Five RGIBBS reactors were modelled in series to replicate the counterflow moving bed reactor model, employing minimization of the Gibbs Free Energy for thermodynamic analysis. A good match for both the solid and gas conversion was obtained with respect to the experimental results conducted and reported in the same literature [112].

Chang et al [113] developed a steady state kinetic model of a Moving bed gasifier using a similar technique in ASPEN Plus, however, to model a Lurgi Coal Gasifier for Synthetic Natural Gas (SNG) production. In the same study, he went on to demonstrate the methodology

of optimizing the number of RCSTRs in series, necessary to provide a convergence to the obtained results. The results were also compared with industrial data, with good agreement.

## **2.6 System Modelling**

Besides generating CO or H<sub>2</sub> from splitting CO<sub>2</sub> or water respectively, system modelling for further use of the proposed chemicals is crucial to not only study the probable integration of the individual units like the chemical looping unit but also to identify the need of advancement for the balance of plant for effective integration. Integrating the chemical looping unit effectively for power or chemical production has been studied mostly for utilizing the chemical looping combustion technology [114,115].

Nevertheless, two-step water and CO<sub>2</sub> splitting cycles have been simulated for integration into industrial-scale processes by Gencer et al [116], whereby the Fe<sub>3</sub>O<sub>4</sub>/FeO redox pair was used for water splitting in a solar-driven cycle for round the clock power generation. An average efficiency of 35% was obtained including energy storage. Besides water splitting CO<sub>2</sub> splitting provides considerable opportunities for carbon dioxide utilization (CCU) as an alternative to CCS with potential system integration for chemical or electricity productions.

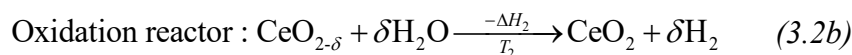
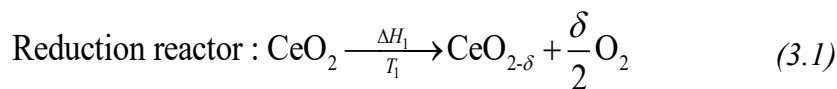
Such schemes have been proposed and modelled in detail in the respective chapters of the present report.

### 3 Reactor and System Modelling of Thermochemical dissociation of CO<sub>2</sub>/H<sub>2</sub>O Using Non-stoichiometric Ceria

Solar thermochemical cycles are much matured and studied than the corresponding methane driven cycles for two-step chemical looping splitting applications. Diverse types of proposed solar thermochemical reactors have been briefly discussed in the previous chapter. As per the most promising of such technologies, are essentially the particle type reactors with higher achievable efficiencies and ease of scale-up. Even though such reactor designs are each very specific to their own concept, a generic distinction, based on industrial technologies for commercial chemical reactors can be made. These include the moving packed bed type of reactors and fluidized bed reactors. Numerical modelling, specific to individual reactors proposed in literature have been made with some reported results [117–119]. In this study, however, a generic modelling layout, applicable to different reactors of similar classification has been tried to be obtained. Commercial software ASPEN Plus has been chosen to be utilized for this purpose. Nevertheless, a detailed analysis of the reaction kinetics is first essential as per previous discussions to develop a successful overall reactor model.

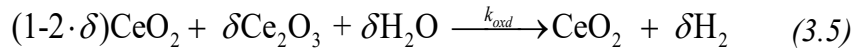
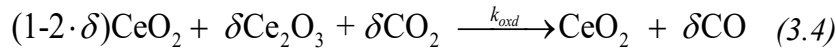
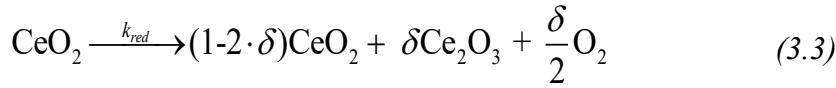
#### 3.1 Reaction Kinetics

As has been discussed in the previous section 2.3, multiple materials of distinct categories have been studied to develop the most the most suitable OC. However, no one material has yet been recognized as the most ideal. Non-stoichiometric Ceria has shown higher oxygen storage capacity at relatively lower reduction temperatures, with added advantages of good mechanical and physical properties. The typical reactions taking place in the reduction and the oxidation reactors are shown below in equations (3.1) and (3.2), in which, ceria releases oxygen and undergoes thermal reduction, in turn, to be oxidized by carbon dioxide and water producing carbon monoxide and hydrogen in the two reactors respectively.



It needs to be mentioned that both the reactions are heterogeneous and non-catalytic. As with other metal oxides, the reduction and oxidation reactions are fundamentally different from the energy perspective, with the former being endothermic and the later, an exothermic reaction. Hence, the two reactors are essentially operated at different temperature levels, with the reduction reactor being at a higher temperature than the oxidation reactor.

Due to the limited availability of the thermodynamic properties of non-stoichiometric ceria, a different approach was used using the fully reduced and stable form of Ceria,  $\text{Ce}_2\text{O}_3$ , widely available in the literature. The above reaction set (3.1-3.2) was therefore alternatively written as follows:



The non-stoichiometry factor ( $\delta$ ) has been proposed to be defined as the ratio between the still-unreacted ceria and the completely reduced form,  $\text{Ce}_2\text{O}_3$ . Equation (3.3) represents the reduction reaction, while the CDS and WS reactions can be modelled as per the equations (3.4) and (3.5) respectively. The  $\delta$  can hence be evaluated from equation (3.3) and can be written as per the following equation (3.6), whereby the value of  $\delta$  can ideally be between 0 and 0.5, the latter corresponding to a fully reduced state of  $\text{CeO}_2$ .

$$\delta = \frac{\dot{n}_{\text{Ce}_2\text{O}_3}}{2 \times \dot{n}_{\text{Ce}_2\text{O}_3} + \dot{n}_{\text{CeO}_2}} \quad (3.6)$$

where,  $\dot{n}$  is the molar flow of the respective components.

Nevertheless, a complete removal of all the available oxygen would cause the fluorite phase of  $\text{CeO}_2$  to destabilize, making phase transition inevitable beyond a certain degree of reduction [51]. Bulfin et al [51] reported the maximum achievable  $\delta$  without changing the fluorite structure of  $\text{CeO}_2$  for redox recycling of ceria as limited to 0.35.

Proceeding accordingly, due to the limited availability of the thermodynamic properties of non-stoichiometric ceria, the degree of advancement of the reaction has been fundamentally used in the kinetics model developed instead of the non-stoichiometry coefficient. Therefore, a separate  $\alpha$  parameter, indicating the degree of advancement of the reaction was defined for all the reactions in terms of the relative content of  $\text{Ce}_2\text{O}_3$  and  $\text{CeO}_2$  in the solid mixture after respective reactions.

For the reduction of  $\text{CeO}_2$ , the degree of advancement of reaction  $\alpha_{red}$  primarily describes the performance of the reduction reaction in terms of degree of reduction of the ceria powder and is represented by equation (3.7). The equation is based on its relationship with the non-stoichiometry coefficient  $\delta$ , whereby a maximum extent of reaction is obtained at  $\delta_{max}$  of 0.35. The numerator represents the current non-stoichiometry after reduction, while the denominator indicates the maximum possible non-stoichiometry.

$$\alpha = \alpha_{red} = \frac{\delta}{\delta_{max}} \quad (3.7)$$

A detailed discussion on the calculation of the degree of advancement of reaction is done in the following subsections. Indeed, such formulation of the degree of advancement of thermal reduction reaction ( $\alpha_{red}$ ) agrees with the reduction kinetic model developed by Bulfin et al [51]. On the other hand, the oxidation of the reduced ceria inherently moves in the opposite direction to reduction, whereby, the extent of oxidation ( $\alpha_{oxi}$ ) can be written according to the following equation (3.8).

$$\alpha_{oxd} = 1 - \alpha_{red} \quad (3.8)$$

Before delving in detail at the individual reaction kinetics, the pathways of reaction are worth discussing. Two primary pathways of reaction for the solid-gas systems have primarily been used in the literature [120]. In one method, the solid particle decreases in size as the reaction moves forward and leaves only a small portion of itself that contains impurities that are not able to react. An example being coal combustion, where the unreacted fraction of the initial fuel remains as ash. Another example of such mechanism might be a reduction of volatile OCs, whereby the metals get vaporized after the removal of oxygen by thermal reduction. The second mechanism assumes a constant reaction particle size during the entire reaction, even though the composition changes. The non-volatile OCs can essentially be considered to follow this reaction approach when the temperatures are low enough not to cause sublimation of the outer layers of the solid [121,122]. The schematic of the two different reaction model types is shown in the following Figure 3-1.

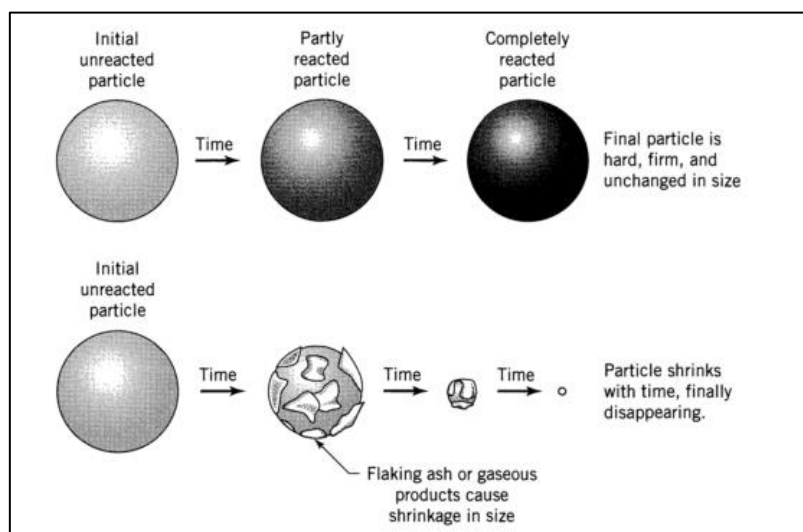


Figure 3-1 Different behaviours for the reacting solid particles [120]

As can be seen from the above Figure 3-1, the first mode of reaction, also called the Progressive Conversion Model (PCM), assumes that the concentration of unreacted solid in the particle is distributed quasi-uniformly during the reaction. However, the second, or the Shrinking Core Model (SCM) assumes that the front of the reaction advances into the solid as the reaction progresses, leading to gradual consumption of the unreacted material. Levenspiel [120] commented that the SCM represents reality much better than the PCM, though the PCM can be simplified under certain conditions to the SCM. Mainly such situation can be observed when

the surface reaction rate is the rate determining step of the process and the diffusion rates in solid and in gas film are much faster.

The thermal reduction of metal oxides comprises several reaction steps. Of the five reaction steps of thermal reduction of ceria, as proposed by Levenspiel [120], these steps can be limited to three, since there is no additional reactant transport towards the reaction surface. The steps can be elaborated as *i)* the release of oxygen particles from the surface of the ceria; *ii)* the diffusion of oxygen vacancies towards the particle core and *iii)* the diffusion of oxygen particles through the gas film

Like the reduction reaction, the oxidation reaction can also be fully described through four steps as *i)* the transport of oxygen vacancies towards the reaction surface, *ii)* the diffusion of oxidant through the gas film towards reaction surface, *iii)* the filling the vacancies with oxygen and *iv)* the diffusion of the spent oxidant through the gas film

The additional step of oxidant ( $\text{CO}_2/\text{H}_2\text{O}$ ) diffusion towards reaction surface needs to be considered. The second and the fourth steps of the oxidation reaction are much faster with respect to the other reactions. Literature reveals that the primary focus on studies in the related field focuses on expanding the reaction mechanism associated with filling the vacancies of the OC by oxygen (Step 3) through multiple reaction pathways [123,124] and on the transport of oxygen vacancies in the particle [125].

SCM can be used to model the redox kinetics of ceria, though not often used due to its higher complexity. Most of the studies focused on the kinetics of the OCs tend to describe possible reaction pathways for the material and later try to fit experimental data into various reaction models, based on the rate-limiting step in the reaction. Thus, the rate-determining step of the reaction pathway is included in the general formulation of the reaction rate. Between the two reactions, the reduction reaction is inherently slower, resulting in the reduction reaction to be the rate-determining step for the entire cycle, also directly influencing the yield from the oxygen reactor. Therefore, based on the above discussions, as well as the consideration that the crystal structure of the OC, especially for non-volatile and non-stoichiometric ceria remains constant throughout the redox cycle, a simplified approach was considered for modelling the reaction kinetics for the solar thermochemical cycle as described in the following sub-section.

### 3.1.1 Reduction kinetics

Bulfin et al [51] investigated ceria reduction kinetics at a wide range of temperature, between  $1000^\circ\text{C}$  and  $1900^\circ\text{C}$  and a wide range of oxygen partial pressures of  $10^{-2}$  to  $10^{-8}$  bar. The partial pressure of oxygen is developed from the presence of removable oxygen produced by the reduction of  $\text{CeO}_2$  as per equation (3.3).

The proposed reduction kinetic model by Bulfin et al [51] is essentially based on the Arrhenius equation, assuming an equilibrium reaction. This causes both forward and backward reactions from the release of oxygen and recombination of the released oxygen respectively, to occur together ( $\text{CeO}_2 \leftrightarrow \text{CeO}_{2-\delta} + 0.5\delta\text{O}_2$ ). Unlike the previous argument of measuring the extent of non-stoichiometry, the authors proposed moles of oxygen vacancies per mole of cerium per

second or simply per second to be used as the measure of the non-stoichiometry of the reduced ceria, as shown in the following equation (3.9).

$$\frac{[O_{vac}]}{[Ce]} = \delta \quad (3.9)$$

The forward reduction reaction is driven by the concentration of removal of oxygen, while the backward recombination (or oxidation) reaction is influenced by the concentration of both the vacancies and the oxygen gas [51]. Thus, the rate of the total change of the non-stoichiometry, which in other terms is also the rate of change of the oxygen vacancy concentration can be written as difference of the rate at which oxygen leaves CeO<sub>2</sub> (reduction) and the rate at which it recombines (oxidation) as per the following equation (3.10)

$$\frac{d\delta}{dt} = (\delta_{max} - \delta) \cdot A_{red} \cdot \exp\left(-\frac{E_{red}}{RT}\right) - \delta \cdot P_{O_2}^{n_r} \cdot A_{ox} \cdot \exp\left(-\frac{E_{ox}}{RT}\right) \quad (3.10)$$

Where A represents the Arrhenius constant, E is the activation energy in kJ/mol-K, P<sub>O<sub>2</sub></sub> is the partial pressure of oxygen, n<sub>r</sub> is the reaction order, R is the universal gas constant and T is the absolute temperature in kelvin with subscript f and b as forward and backward reaction respectively.

Assuming ideal gas behaviour, the concentration of O<sub>2</sub> is directly proportional to the partial pressure of O<sub>2</sub> (P<sub>O<sub>2</sub></sub>) or the vacuum pressure of the total reactor, as applicable based on the reactor design. Based on the works of Panlener et al. [126] and Dawicke et al. [127] and through the plotting of log(δ) against log(P<sub>O<sub>2</sub></sub>) with certain assumptions, the authors developed a reaction kinetic model for the net thermal reduction reaction of ceria. To fit the developed kinetic model with the experimental results, the shrinking core model was used. Considering a surface reaction to be the rate-determining step there would be a shrinking sphere of vacancies resulting in a restriction on the reaction rate with the advancement of the reaction. A third order model for the rate equation was found to be the best fit and the overall rate equation for the reduction reaction, based on X<sub>red</sub> is obtained as per the following equation (3.11). The values of the parameters of the rate equation are summarized in Table 3-1.

$$\frac{d\alpha_{red}}{dt} = \frac{d\delta}{dt} (1 - \alpha_{red})^{-1/3} \quad (3.11)$$

Table 3-1 Ceria reduction rate equation coefficients presented by Bulfin et al [51]

Parameter	Value
δ <sub>max</sub>	0.35
n	0.218 ± 0.0013
E <sub>red</sub> (kJ/mol)	232 ± 5
E <sub>ox</sub> (kJ/mol)	36 ± 4
A <sub>red</sub> (s <sup>-1</sup> )	720,000 ± 360,000
A <sub>ox</sub> (s <sup>-1</sup> bar <sup>-n</sup> )	82 ± 41

However, the transition from the rate equation to the reaction rates of the concerned chemical species is done as per the equations (3.2) and (3.11) together with the available chemical species. Three distinct chemical species take part in the above reaction. For each mole of cerium (III) oxide ( $\text{Ce}_2\text{O}_3$ ) generated, two moles of ceria (IV) oxide ( $\text{CeO}_2$ ) are consumed and half a mole of oxygen gets released. Aside from stoichiometric coefficients, knowledge of reaction time step is important. In the discrete kinetic model, the particle residence time is used as the time parameter, in terms of  $\Delta t$ , as can be seen from equations (3.12) through (3.14). The thermal reduction reaction rates for the three species taking part in the reaction are shown below.

$$k_{\text{redCeO}_2} = -2 \cdot \dot{n}_{\text{CeO}_2} \frac{d\alpha_{\text{red}}}{dt} \Delta t \quad (3.12)$$

$$k_{\text{redCe}_2\text{O}_3} = 1 \cdot \dot{n}_{\text{Ce}_2\text{O}_3} \frac{d\alpha_{\text{red}}}{dt} \Delta t \quad (3.13)$$

$$k_{\text{redO}_2} = 0.5 \cdot \dot{n}_{\text{CeO}_2} \frac{d\alpha_{\text{red}}}{dt} \Delta t \quad (3.14)$$

### 3.1.2 Oxidation kinetics

The oxidation kinetics for ceria for  $\text{H}_2\text{O}$  and  $\text{CO}_2$  splitting has been investigated for reactivity by different research groups [49]. The initial reduction state of the sample has been reported to strongly influence the subsequent oxidation reaction. Significant drop in the reaction rates were noticed when non-stoichiometry factor exceeded 0.18-0.2 values in the temperatures below  $820^\circ\text{C}$  [49]. It is reported that high variations in the reaction activation energies with non-stoichiometry of the sample in higher concentrations of the oxidizing gas. As reported, the activation energy varied in range of 160-200 kJ/mol for non-stoichiometry between 0.01 and 0.09. For oxidation, the kinetics developed by Arifin [124], and Arifin and Weimer [128], who investigated redox kinetics of ceria for water and carbon dioxide splitting reaction. The reaction mechanism has been proposed in the general formulation for the reaction rate as equation (3.15) with the corresponding coefficients being listed in Table 3-2.

$$\frac{d\alpha_{\text{oxd}}}{dt} = A_{\text{oxd}} \cdot \exp\left(-\frac{E_{\text{oxd}}}{RT}\right) y_i^{n_o} (1-\alpha_{\text{oxd}})^\psi \quad (3.15)$$

Where  $A_{\text{oxd}}$  is the Arrhenius constant,  $E_{\text{oxd}}$  is the activation energy degree and  $n_o$  is the order of the oxidation reaction and  $y_i$  is the oxidant molar fraction,  $\psi$  represents the reaction model exponent.

The oxidation reaction of the reduced ceria with  $\alpha_{\text{red}}$  water vapour and  $\text{CO}_2$  splitting was found to behave similarly to a homogeneous reaction, i.e. its rate decelerates proportionally to the depletion of the reactants ( $1-\alpha_{\text{oxd}}$ ). More so, the kinetics of the water splitting reaction are quite fast due to the relatively small activation energy of 29 kJ/mol. However, similar analyses revealed the dependence of the rate-determining step of the carbon dioxide splitting reaction on the on the temperature of the process [124]. It was also observed that with the increase in

temperature, carbon site blocking, and subsequent surface recombination stops. At 875°C only reaction pathway is direct desorption of carbon monoxide from the particle surface, which might result in significant changes to the reaction coefficients  $\psi$  and  $n_o$  as indicated in Table 3-2. It is worth noticing that in the discussed research, ceria sample was constantly cycled and reused in different conditions. Nevertheless Arifin [124], noted that the overall production of the fuel from the sample remained almost constant, though reaction times varied because of varying temperatures and molar fractions of reactants.

Table 3-2 Kinetic parameters of the oxidation reaction of reduced ceria obtained by Arifin [124]

Oxidant	Temp (°C)	$A_0$ (1/s)	$E_0$ (KJ/mol)	$\psi$ (-)	$n_o$ (-)
CO <sub>2</sub>	750-950	1.0	29	0.89	1.0
	650-725	4.2	47	0.53	1.0
H <sub>2</sub> O	750-800	3.4	45	0.65	1.2
	825-875	2.5	41	0.7	1.7

To determine the reaction rates for splitting reactions, the degree of advancement of oxidation reaction was calculated as per mentioned in equation (3.8). Following the aforementioned equation, independent to the use of CO<sub>2</sub> or H<sub>2</sub>O, when one mole of each is consumed, it leads to simultaneous consumption of each mole of Ce<sub>2</sub>O<sub>3</sub> with the corresponding generation of two moles of Ceria and one mole of CO and H<sub>2</sub> respectively. Taking this into account, the reaction rates for each species, in terms of the available solid reactant quantity (molar flow) are listed as per the following equations (3.16-3.21)

$$k_{\text{oxdCeO}_2} = 2 \cdot \dot{n}_{\text{Ce}_2\text{O}_3} \left\{ \frac{d\alpha_{\text{oxdH}_2\text{O}}}{dt} + \frac{d\alpha_{\text{oxdCO}_2}}{dt} \right\} \Delta t \quad (3.16)$$

$$k_{\text{oxdCe}_2\text{O}_3} = -1 \cdot \dot{n}_{\text{Ce}_2\text{O}_3} \left\{ \frac{d\alpha_{\text{oxdH}_2\text{O}}}{dt} + \frac{d\alpha_{\text{oxdCO}_2}}{dt} \right\} \Delta t \quad (3.17)$$

$$k_{\text{oxdH}_2\text{O}} = -1 \cdot \dot{n}_{\text{Ce}_2\text{O}_3} \frac{d\alpha_{\text{oxdH}_2\text{O}}}{dt} \Delta t \quad (3.18)$$

$$k_{\text{oxdH}_2} = 1 \cdot \dot{n}_{\text{Ce}_2\text{O}_3} \frac{d\alpha_{\text{oxdH}_2\text{O}}}{dt} \Delta t \quad (3.19)$$

$$k_{\text{oxdCO}_2} = -1 \cdot \dot{n}_{\text{Ce}_2\text{O}_3} \frac{d\alpha_{\text{oxdCO}_2}}{dt} \Delta t \quad (3.20)$$

$$k_{\text{oxdCO}} = 1 \cdot \dot{n}_{\text{Ce}_2\text{O}_3} \frac{d\alpha_{\text{oxdCO}_2}}{dt} \Delta t \quad (3.21)$$

## 3.2 Modelling of Reactors

As discussed in Section 2.4, both moving bed and fluidized bed reactors have received significant interests for the two-step chemical looping splitting cycle. Indeed, the selection of the reactor type and configuration can be directly followed from the literature discussions of Section 2.4, as well as the reaction kinetics of the complete redox reaction. Furthermore, the material plays a crucial role, if not the most significant, in the discussion of the selection of the reactor design for reduction and oxidation.

Based on work of Panlener et al [126] and following the kinetics developed by Bulfin et al [51], which has also been used in the present study, it can be concluded that to have an acceptable reduction of ceria, a very low partial pressure of oxygen is necessary, often to levels of lower than  $10^{-5}$  bar [51], working at temperatures of around 1300°C and above. This can be achieved either by operating the reactor in vacuum conditions or by sending sufficiently high sweep gas flow to maintain the desired level of oxygen partial pressure in the reduction reactor. The later, however, is often limited by the scale of the amount of inert gas flow. The moving bed aerosol reactor, proposed by Scheffe et al [89], acknowledges this fact, which would lower the effectiveness of the entire cycle. Indeed, such requirement of low pressure for reduction direct limits the use of sweep gas for reduction, which in turn would limit the application of fluidized bed reduction reactors. On the other hand, non-structured reactors working under vacuum can essentially be referred to as equivalent to moving bed reactors, where the particles undergo reduction while moving through the reactor. Reactor design concepts by Muhich et al and Ermanoski are essential of this type [70,129].

On the other hand, it is essential to maintain higher pressure to perform the oxidation. With CO and H<sub>2</sub> being the primary products of the two-step, this would considerably decrease the work needed from the compression of the products, especially H<sub>2</sub>, essentially for use in downstream industrial applications. In this regard, both fluidized bed and moving bed reactor configurations can be applicable, both with relative advantages and disadvantages. While fluidized bed configuration solves one of the major problems of metal oxide transport in a redox cycle, considerable disadvantages also exist related to the selectivity of the products and fluidization regime the reactor operates. Fan et al. [95] studied and reported the relative advantages of a moving bed reactor over a fluidized bed reactor for reduction of oxygen carriers with methane reduction. Besides a more homogeneous reduction of the OCs, reactions in a moving bed reactor result closer to thermodynamic states, rather than fluidized bed reactors.

In fluidized bed reactor, due to the requirement of desired flows for fluidization, this often results in a low gas or metal oxide conversion (transport reactors for smaller configurations) or would require sufficiently large reactors with a very high oxygen carrier inventory (bubbling bed reactors). Additionally, for transport reactors, the relative gas conversion is very low. This would then require downstream purification before the use of the generated product for the subsequent industrial application. However, the effectiveness of the cycle decreases thus. Moving bed reactors, on the other hand, do not experience such limitations, providing a greater design flexibility, as well as in operations.

Hence, following the above discussion relating to both the reduction and the oxidation reactors, moving bed reactors are considered in the present study. While the reduction reactor would operate at vacuum, the oxidation reactor would operate at near atmospheric conditions. This resembles the reactor concept proposed by Muhich et al [70], with the only essential difference being that the oxidation reactor is a moving bed reactor instead of a circulating fluidized bed reactor. The transport of the oxidized metal oxide particle can be performed by a screw conveyer.

However, the present study has been focused on the development of the reactor model using commercial software ASPEN Plus to predict the results reported in literature and to investigate the performance of each reactor for different operating conditions to have a high selectivity of the syngas produced and to see the effect of composition of mixture ( $\text{CO}_2$  and  $\text{H}_2\text{O}$ ) on the conversion within the oxidation reactor. The following section details the development of such reactor models with the obtained results.

### 3.2.1 Moving Bed Reactor Model

Different numerical models have been developed for simulating chemical reactions in the moving bed model reactor utilizing the unreacted core shrinking model [107,130], already described and detailed in section 2.5.2. A general schematic of the counter current moving bed reactor is shown in the following Figure 3-2.

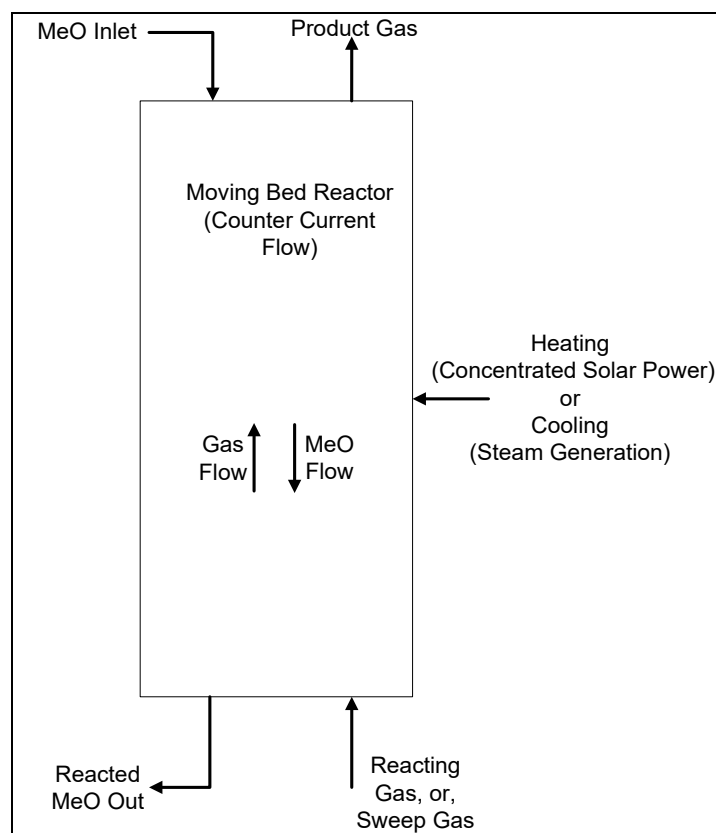


Figure 3-2 Schematic Diagram of a Generic Moving Bed Reactor

As can be seen from Figure 3-2, a vertical counter-current reactor is the most widely accepted and technically mature moving bed reactor configuration in industry. In the reduction reactor, the metal oxide is thermally reduced, as it is fed from the top operated in a vacuum. Hence, there exists no gas inlet. However, the generated oxygen flows up to the top of the reactor in a counter flow with respect to the metal oxide, wherefrom it is connected to a vacuum pump that drives away it away and maintains the necessary vacuum (not shown). In the oxidation reactor, the reduced metal oxide is fed from the top as well and reacts with the gas ( $\text{CO}_2/\text{H}_2\text{O}$ ) moving up. Since the splitting reaction is exothermic, a temperature gradient exists along the length of the reactor for non-isothermal operations. The reduced metal oxide is removed from the bottom by a rotating grate (not shown), while the produced gas exits the reactor from the top. The oxidized metal oxide is transported back to the reduction reactor. The pressure change between the two reactors for the metal is performed through constrictions as proposed by Muhich et al in their reactor design [70]. However, since it is a physical process, it would not lead to additional work being expended and accordingly was not modelled separately.

A counter-current reactor model was therefore simulated for the thermal reduction and CDS and WS reactions respectively. Following the discussion of moving bed reactor modelling using ASPEN Plus in Chapter 2.5.2, a similar reactor model incorporating RCSTR reactors in series have been used in the present study as well. The RCSTR reactor has the characteristic that all phases have the same temperature, which means the temperatures of solid and gas phases in the reduction and oxidation processes are equal in each RCSTR model. Also, it is modelled so that each RCSTR has the same volume, equal to the whole gasifier volume divided by the number of RCSTRs in series. The reaction kinetics described in section 3.1 was written in an external user kinetic subroutine in Fortran and hooked up with the RCSTR model. Specific assumptions with respect to the oxidation and reduction reactors were individually considered and summarized below:

- a. All the RCSTRs in the reduction reactor were at the same temperature, to simulate an isothermal reactor for the reduction.
- b. All the RCSTRs in the oxidation reactor were simulated as adiabatic reactors, and the heat loss factor was set as zero. This drives the temperature of the products and the reactor in some cases quite high. If not controlled, this might lead to the change of crystal structure of the oxygen carrier in actual practice. However, such considerations were not taken during the present simulation.
- c. A single-entry counter-current moving bed reactor was simulated for the oxidation reactor, where the oxygen carrier is fed from the top and the reactant gas flows upward from the bottom inlet as shown in Figure 3-2. However, the scope for optimization to enhance the reaction rates, together with performing temperature control within the reactor by multiple gas inlets is possible. Nevertheless, it was not included in the present study.
- d. The residence time in the reactors was calculated based on the bed volume with respect to the inlet oxygen carrier volumetric flow rate neglecting the changing volume flow due to change in composition from reactions.

- e. No change in oxygen carrier structure and hence the change in reactions kinetics was considered during the reactions.

Indeed, the higher the number of RCSTRs in series, higher is the accuracy of the estimation of the respective yields from the reactor. But this would increase the iterative calculations resulting in a time-consuming simulation. Also, such configurations exhibit slow solution convergence because the form of the mathematical model of counter-current moving bed reactor gasifier is a two-point boundary value problem [113]. Hence, the selection of the number of RCSTRs in series is crucial to the net evaluation of the system for minimization in simulation errors, and at the same time, to decrease the computation time as much as possible.

The hook-up logic between the in-built ASPEN Plus model and the external FORTRAN code for user kinetics, together with the use of calculator blocks for calculating the necessary external heat requirement for the isothermal reduction reactor is shown in Figure 3-3. Each RCSTR block is linked up with the user kinetic model and the resulting output is fed to the successive reactor. Unlike the reduction reactor, it is interesting to note that for the oxidation reactor, since two inlets at two different points in the reactor system is provided, the convergence is essentially a two-point convergence. This often requires the need to provide an estimation of the yields in each stream to facilitate convergence. Estimations too far off from the results often lead to increased convergence time and in some cases, failure of convergence.

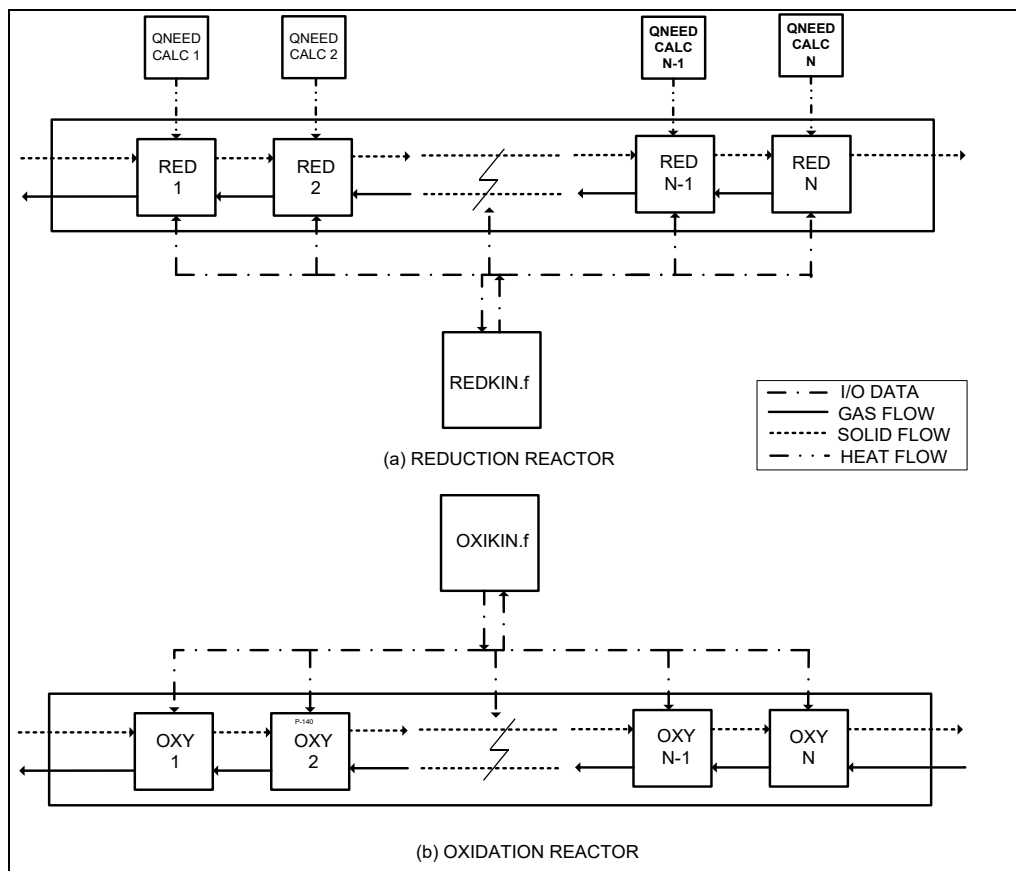


Figure 3-3 Logic diagram of moving bed reactor model in ASPEN Plus hooked with user kinetics written in an external FORTRAN Code

As for the reduction reactor, calculator blocks were added to calculate the heat need of each reactor. In fact, besides the heat requirement, the need to calculate the non-stoichiometry ( $\delta$ ) generated in each reactor together with other parameters might necessitate the addition of more calculator blocks for both the reactors. Indeed, based on the following Figure 3-3, the need to optimize the number of RCSTRs in series to predict well the net output from the RCSTR is essential and is conducted accordingly. The Broyden Solver Model was used as per the suggestion of ASPEN plus model already developed for moving bed coal gasifier and 500 iterations were provided for both the mass and energy solvers. The relative tolerance of errors was set at 0.0001 to decrease the computation time while minimizing errors in the overall results of the simulation. Usually, for gas processing, it is recommended to use the PR-BM method which utilizes the Peng-Robinson cubic equation of state with the Bostone Mathias alpha function [131]. Therefore, in all the three processes, the PR-BM method was selected for the simulations.

The temperature profile for an adiabatic reactor (Oxidation) can be obtained through the results of each reactor, retrieved by calculator blocks. The corresponding non-stoichiometry of the input and the output metal to the reactors are also evaluated via calculator blocks, incorporated with each RCSTR as per the coupling the equations (3.6).

### 3.3 Evaluation Methodology

Industrial scale evaluation is essential to understand the design perspectives and evaluate the fundamental areas necessary for future focus for practical application of any chosen technology. In this regard, application of the chemical looping technology for CO/H<sub>2</sub> generation, coupled to an industrial scale source of the CO<sub>2</sub> or water has been evaluated. The reactor model has been evaluated based on the common aim to provide a 100 mol/s of syngas from either CO<sub>2</sub> or H<sub>2</sub>O or CO<sub>2</sub>/H<sub>2</sub>O mixture. The value suits well with the amount of CO<sub>2</sub> or water available from the state of the art carbon capture power plants [5,132]. As per equations (3.6), the equivalent amount of CeO<sub>2</sub> to be circulated for generating a non-stoichiometry of 0.35 is 285.71 mol/s. This results in an equivalent Ce<sub>2</sub>O<sub>3</sub> generated on reduction to be 100 mol/s following the above-mentioned equations.

The reduction temperature was varied between 1000°C and 1600°C following the arguments by Bulfin et al [51], to allow comparison of the results of the model developed with theoretical experimental results available in literature c. The maximum temperature of 1600°C was selected considering limitations of reactor size and the performance of the industrial state of the art solar concentrators. However, for the base case assessment, a temperature of 1600°C was selected. The base reduction reactor vacuum pressure was selected as a 10<sup>-7</sup> bar to obtain acceptable reduction extent, while the oxidation reactor was considered to operate at a pressure of 2 bar to decrease the compression work associated with H<sub>2</sub> and CO compression for downstream, applications. The gas flow rate was varied according to the need of the reactor design. This also results in the assessment of the product purity in the generated stream from the splitting reactor, better known as the selectivity. The selectivity of CO and H<sub>2</sub> via three

different splitting reactions (only CO<sub>2</sub>, only H<sub>2</sub>O and CO<sub>2</sub>/H<sub>2</sub>O mixture) is written as per the following equations below (3.22a and 3.22b)

$$SC_{CO} = \frac{n_{CO}}{n_{CO_2} + n_{CO}} \quad (3.22a)$$

$$SC_{H_2} = \frac{n_{H_2}}{n_{H_2O} + n_{H_2}} \quad (3.22b)$$

Where  $n$  represents the molar flow of the components in the outlet product gas from the splitting reactor (oxidation reactor) and the subscript represents the components for which the molar flows are considered.

In addition, the metal inlet temperature for the base case scenario was fixed at 1300°C to the reduction reactor. As for the oxidation reactor, the metal and gas inlet temperature were fixed at 800°C for base case simulations. Further sensitivity studies to evaluate the impact of the variation of these temperatures have been carried out and commented accordingly. Based on such assumptions and considerations, the following section details the results and the design aspects of the moving bed reactor for application to an industrial scale solar CO<sub>2</sub>/H<sub>2</sub>O splitting using Ceria as the OC.

## 3.4 Results and Discussions

### 3.4.1.1 Model Convergence

To evaluate the number of RCSTRs in series that would result in the minimization of error from approximation, an iterative calculation procedure was adopted after He et al [113]. The reduction and the oxidation reactors have been considered separately for the optimization. Each RCSTR have been sequentially arranged along the height of the reactor, with an equivalent volume of 0.5 m<sup>3</sup> and 4 m<sup>3</sup> for the reduction and the oxidation reactor respectively. An iterative procedure, with increasing the number of the RCTRs is carried out till the relative change in the results by increasing an RCSTR in series would result in a lower than 0.25% change of the output of the moving bed reactor. The value 0.25% was considered a good approximation to the reactor convergence while ensuring minimization of computation time by unnecessarily increasing the number of reactors in series. The schematic of the algorithm followed for the iterative study is shown in Figure 3-4.

Figure 3-5 shows the relative changes of the outputs from the reduction and the oxidation reactors respectively while varying the number of RCSTRs in series ( $n$ ). To evaluate the following the oxygen released from reduction of ceria was considered for an isothermal reduction reactor at 1600°C and a vacuum pressure of 10<sup>-7</sup> bar. The amount of CeO<sub>2</sub> sent for reduction was 285.71 mol/s. As can be seen beyond  $n = 4$ , the relative change in the results

drops to lower than 0.0025% and beyond  $n = 7$ , the relative change becomes negligible. Therefore, the optimum number of RCTRs in the reduction zone is considered as  $n = 7$ .

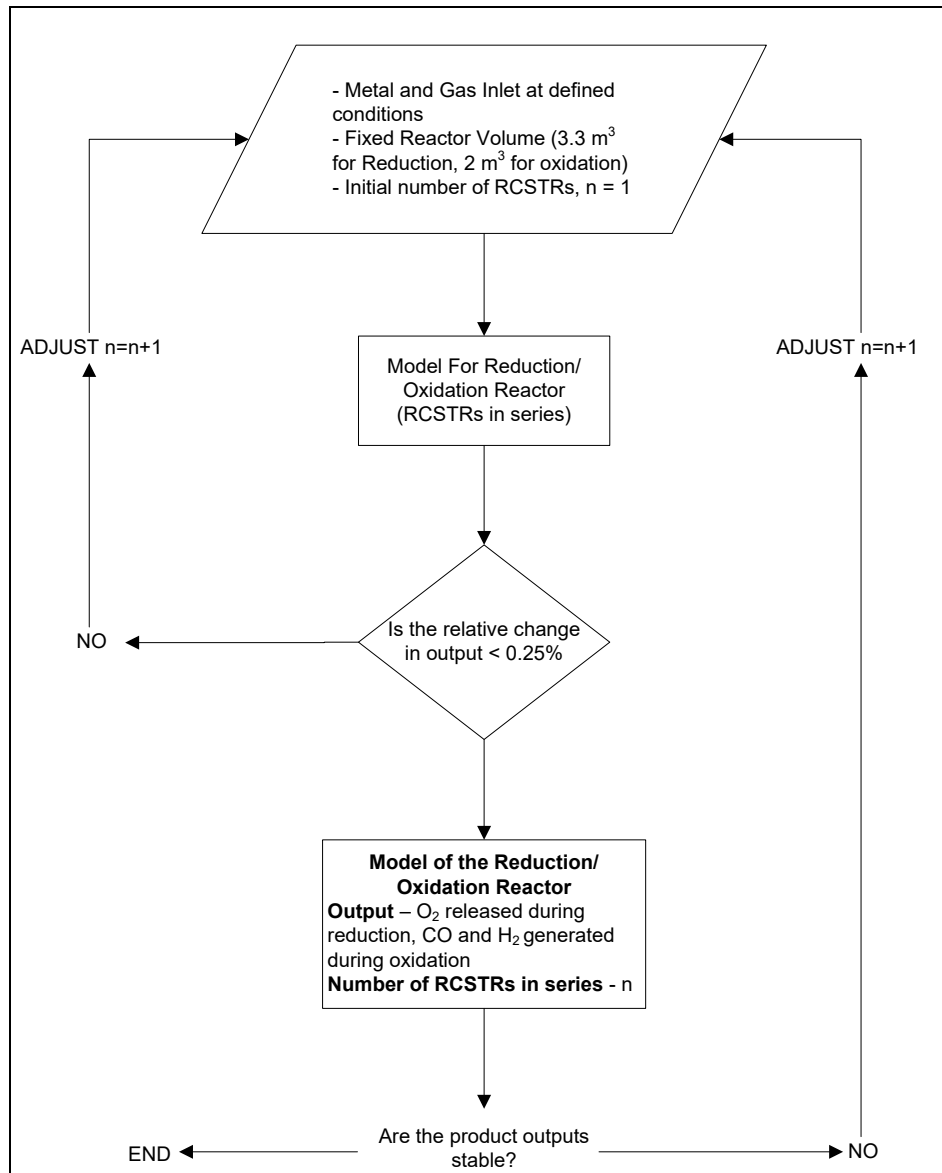


Figure 3-4 Iterative calculation procedure for determining the number of RCSTRs in series,  $n$ .

On the other hand, for the oxidation reactor, the  $H_2$  and CO yield was considered to evaluate the convergence of the number of RCTRs. An equimolar mixture of  $CO_2/H_2O$  was sent to oxidize the reduced ceria with a non-stoichiometric factor of 0.35, at a constant gas and metal oxide inlet temperature of  $800^\circ C$ . The reactors were considered adiabatic. As can be seen from the results shown in Figure 3-5b, due to slower  $CO_2$  splitting kinetics, a larger number of RCSTRs in series is required to obtain the necessary convergence. Hence, while after 8 RCSTRs in series, the relative change in  $H_2$  yield drops below 0.0025, the corresponding value is obtained with 10 RCSTRs in series for the CO yield. Hence, an  $n = 10$  was found to result in minimal relative error while simulating the Oxidation reactor.

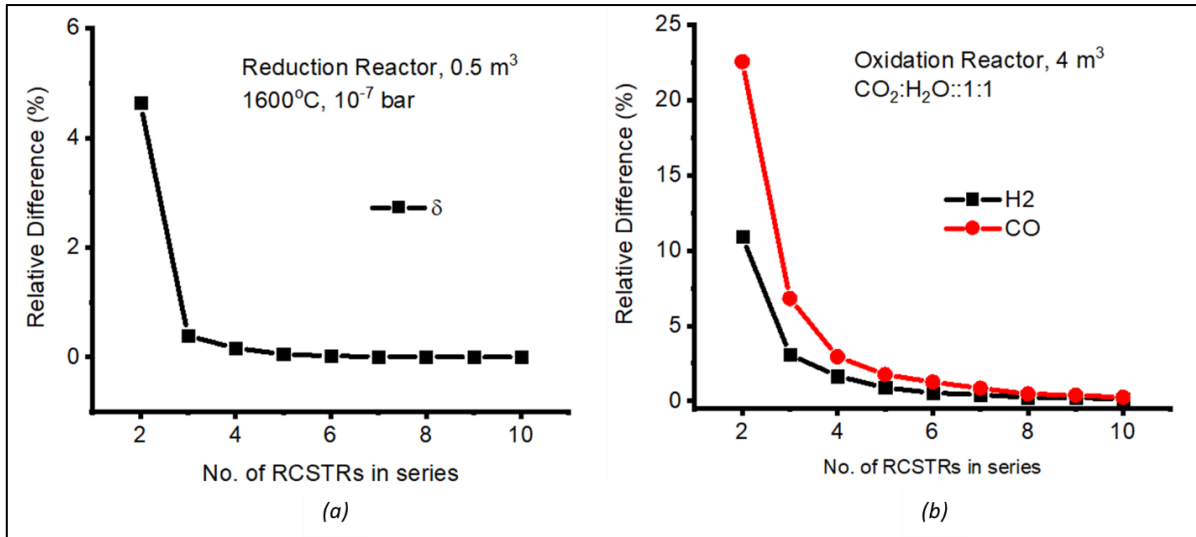


Figure 3-5 Relative changes in the output from increasing the number of RCSTRs in series for (a) Reduction Reactor (b) Oxidation Reactor

### 3.4.1.2 Reduction Reaction

The impact of the different operating parameters on the performance of the reduction reactor for a moving bed reactor design is described in the following section.

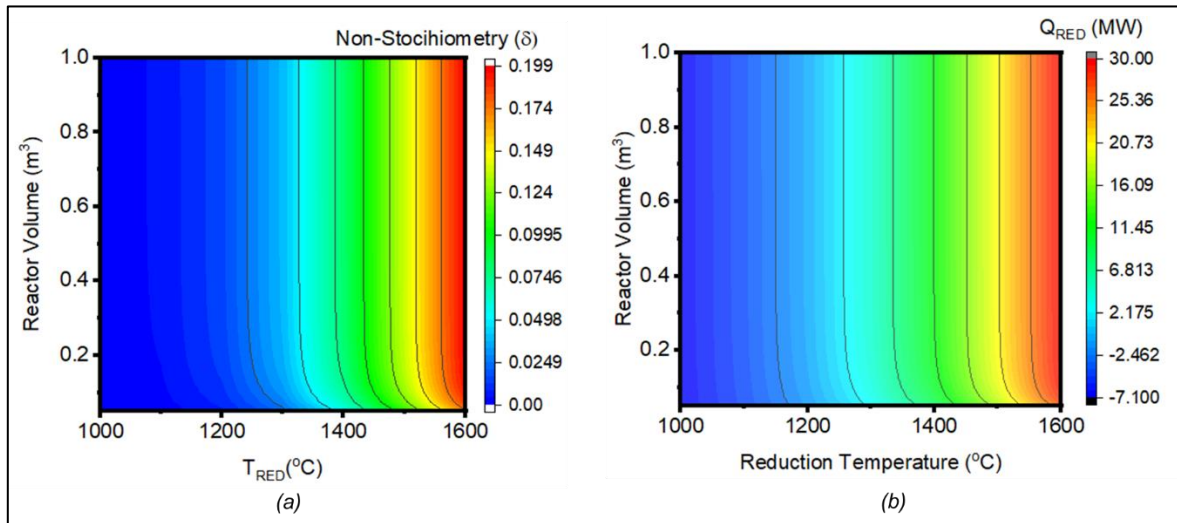


Figure 3-6 Variation of (a) Non-Stoichiometry ( $\delta$ ) and (b) the heat requirement of the reduction reactor ( $Q$ ) with the temperature and reactor volume of the reduction reactor at a constant reactor vacuum pressure of 10<sup>-7</sup> bar, CeO<sub>2</sub> molar flow of 285.71 mol/s and a constant metal oxide inlet temperature of 1300°C

The first set of sensitivity was performed to evaluate the variation of the non-stoichiometry ( $\delta$ ) with respect to both the reactor volume and temperature of the reactor and shown in Figure 3-6a. Due to the increased rate of oxygen recombination reaction with an increase in the non-stoichiometry factor, a fast initial reaction is seen, especially at higher temperatures. However, the increase rate is slower for lower temperatures, where, the kinetics of the global reduction

reaction is considerably slow. Nevertheless, to comment on the reactor volume to suffice for the complete reduction regime, between 1000°C and 1600°C, the relative change in the non-stoichiometry factor based on the two temperature regimes is plotted in Figure 3-7. As can be followed thus, no change in the reduction extent of ceria from a non-stoichiometry factor of 0.1982 is noticed at 1600°C beyond a reactor volume of 0.4 m<sup>3</sup>, also signifying an approximate residence time of the metal oxide of 1.2 minutes within the reactor. Nonetheless, even though much smaller, the reduction continues to occur for 1000°C with an increased volume of the reactor up to 1 m<sup>3</sup>. This corresponds to an approximate metal oxide residence time in the reactor is of 3 minutes. Beyond 0.4 m<sup>3</sup> however, the relative increase in yield is significantly small as well.

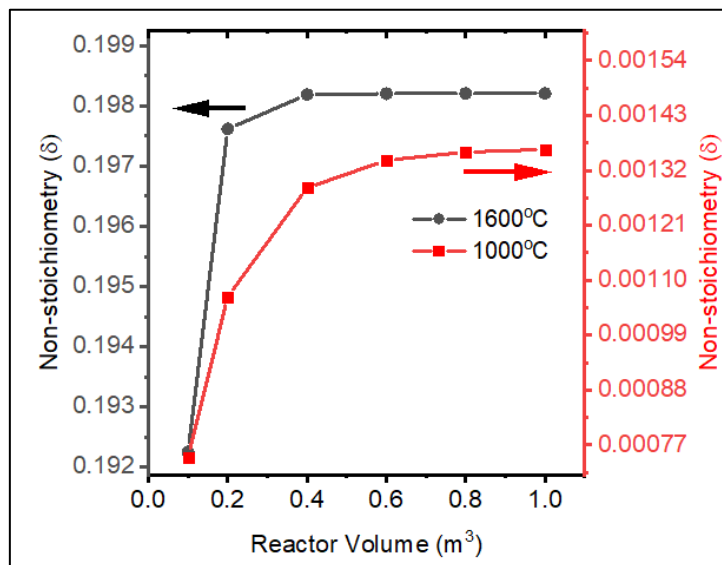


Figure 3-7 Variation of Non-Stoichiometry ( $\delta$ ) at 1600°C and 1000°C with the reduction reactor volume at a constant reactor vacuum pressure of  $10^{-7}$  bar, the CeO<sub>2</sub> molar flow of 285.71 mol/s and a constant metal oxide inlet temperature of 1300°C

On the other hand, a higher reduction extent would result in a higher heat of reaction ( $Q_{red}$ ) in the reduction reactor. This is clearly depicted in Figure 3-6b, whereby a maximum  $Q_{red}$  of 30 MW is needed to ensure the maximum yield of ceria reduction. Interesting to note, however, is the heat required for operating at lower temperatures for an assumed constant metal oxide inlet temperature of 1300°C. Since the metal oxide inlet is at a higher temperature and no significant reaction is observed, a net cooling effect can be seen within the reactor below 1200°C. However, above that with higher reaction extent, with high endothermicity, this results in the net heat requirement for the reaction to occur to increase. Nonetheless, an unnecessarily high reactor volume would require excess heating to the reactor, with minimal increase in the ceria yield. This would not only ensure an almost maximization in the desired yield over a wide range of temperature but at the same time optimize the heat requirement of the reactor.

Hence, based on the above discussions a reactor volume of 0.5 m<sup>3</sup> was selected to perform the subsequent sensitivity studies. Accordingly, the temperature of the reduction reactor was varied between 1000°C and 1600°C, while the vacuum pressure was varied between  $10^{-3}$  and  $10^{-7}$  bar

to study the impact of temperature and pressure on the reduction of pure ceria. Figure 3-9 shows the obtained results, plotted together with the experimental data obtained from Bulfin et al [51]. As can be seen, a good agreement is obtained between the experimental results and the developed moving bed model in ASPEN Plus. Thus, a validation of the present model in predicting the non-stoichiometric reduction of ceria is obtained.

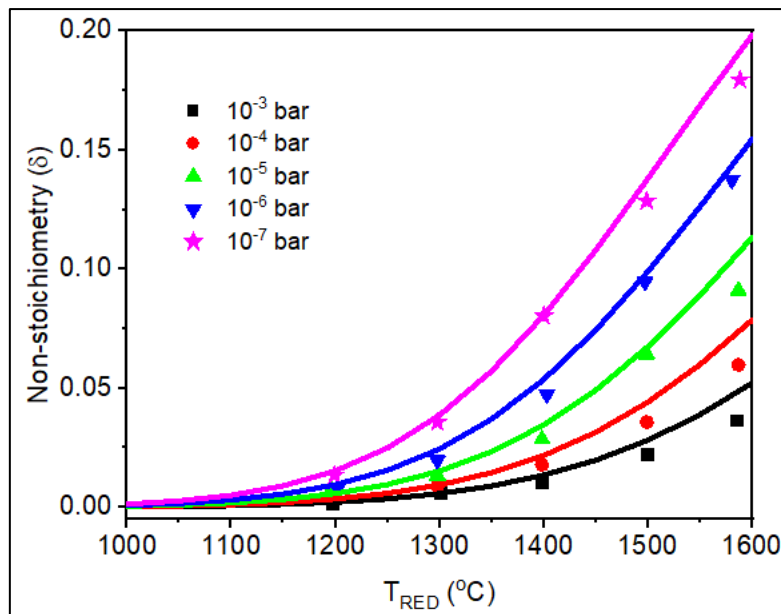


Figure 3-8 Variation of non-stoichiometry ( $\delta$ ) generated in the reduction reactor with temperature and reactor vacuum pressure at a constant reactor volume of  $0.5 \text{ m}^3$ ,  $\text{CeO}_2$  molar flow  $285.71 \text{ mol/s}$  and a constant metal oxide inlet temperature of  $1300^\circ\text{C}$ . Symbols represent experimental results of Bulfin et al [51], lines represent the moving bed model results.

Proceeding thus, a similar profile of the non-stoichiometry ( $\delta$ ) with temperature can be seen irrespective of the pressure variation, while for below  $1200^\circ\text{C}$  no significant reduction of ceria is noticed, even at a vacuum pressure of  $10^{-7}$  bar. A steep increase in the non-stoichiometry ( $\delta$ ) of the reduction reaction is only noticed beyond  $1300^\circ\text{C}$ . However, the rate of increase is enhanced at higher pressures, whereby the non-stoichiometry obtained at  $1400^\circ\text{C}$  and  $1500^\circ\text{C}$  being around 0.08 and 0.138 respectively for a pressure of  $10^{-7}$  bar. Indeed, at the same two temperatures, the non-stoichiometry drops to 0.05 and 0.09 respectively at a lower vacuum pressure of  $10^{-6}$  bar. The maximum non-stoichiometry of 0.199 was obtained at  $1600^\circ\text{C}$  and a pressure of  $10^{-7}$  bar. On the other hand, at lower vacuum pressure, the reduction reaction becomes extremely limited, even at very high pressures, whereby only around 0.025 of  $\delta$  was obtained at around  $1475^\circ\text{C}$ . The corresponding  $\delta$  becomes around 0.06 and 0.124 at pressures of  $10^{-5}$  and  $10^{-7}$  bar respectively. Alternately, this also implies that to operate the reduction reactor at a lower vacuum condition, a higher temperature range needs to be maintained to have acceptable reduction yields. Therefore, the claim of the necessity to operate the reduction at high vacuum conditions, or, in other words, at very low partial pressures of oxygen is reinstated. This, however, provides an energy penalty from vacuum creation even though the corresponding yield increases.

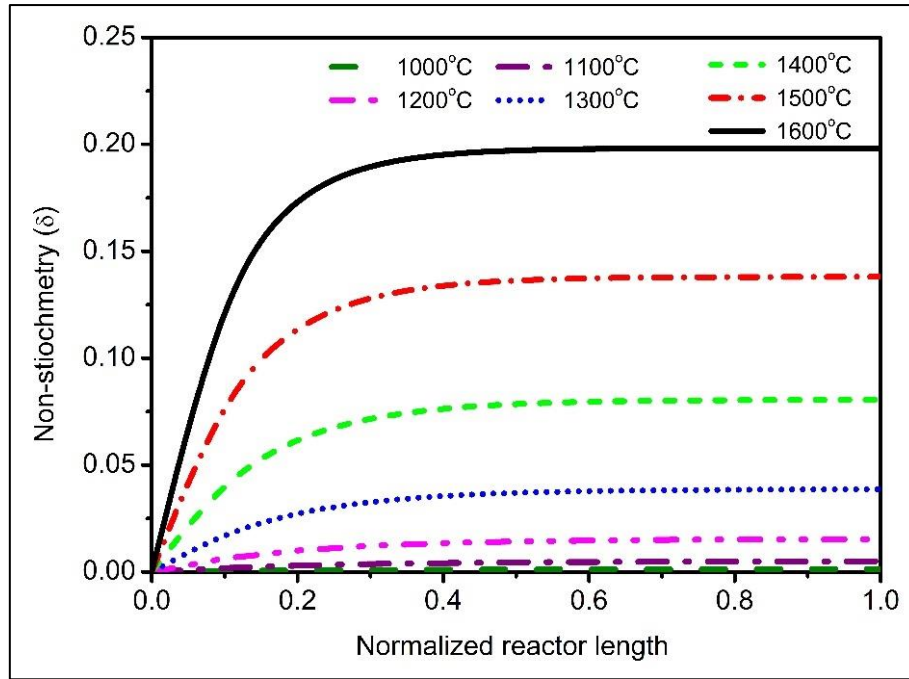


Figure 3-9 Variation of Non-Stoichiometry ( $\delta$ ) along the length of the reactor at a constant reduction reactor volume of  $1 \text{ m}^3$ , a constant  $\text{CeO}_2$  flow of  $285.71 \text{ mol/s}$  and a constant reactor temperature and a vacuum pressure of  $1600^\circ\text{C}$  and  $10^{-7} \text{ bar}$  respectively.

The variation of the non-stoichiometry along the length of the reactor is shown in Figure 3-9. For lower temperatures, below  $1200^\circ\text{C}$ , the evolution of  $\delta$  along the length of the isothermal reactor is mostly linear. However, for temperatures of  $1300^\circ\text{C}$  and higher, most of the reaction occurs before half the reactor length. This can directly be followed from the discussed reactor kinetics, whereby the rates of the backward and the forward reaction becomes almost equal after an initial reduction of the ceria. Therefore, this implies that the reactor can either be made smaller in size, or the focus volume of the solar concentrator can be more concentrated to ensure the desired reaction while minimizing the solar energy input to perform the same.

In the end, the variation of the heat of reaction at a constant reduction temperature of  $1600^\circ\text{C}$  and pressure of  $10^{-7} \text{ bar}$  (plotted as the negative logarithm of the vacuum pressure) with a variable oxygen carrier inlet temperature is shown in Figure 3-10. Since the reactor has been modelled as an isothermal reactor, no change in the non-stoichiometry of the reduced metal oxide would occur with respect to the variable oxygen carrier inlet temperature to the reactor. As can be followed from previous arguments, at higher oxygen carrier inlet temperatures with a corresponding lower operating temperature of the reduction reactor, the net heat requirement for the reaction to occur increases. Indeed, for a metal oxide inlet temperature of  $900^\circ\text{C}$ , the heat requirement increases by almost 20 MW to around 39.3 MW in relation to the base case oxygen carrier inlet temperature of  $1300^\circ\text{C}$ . Therefore, the importance of the metal oxide inlet temperature to the reduction reactor, which in other terms is the metal oxide outlet temperature from the oxidation reactor, on the overall system performance is crucial, with a higher the metal oxide inlet temperature resulting in a lower heat requirement in the reduction reactor.

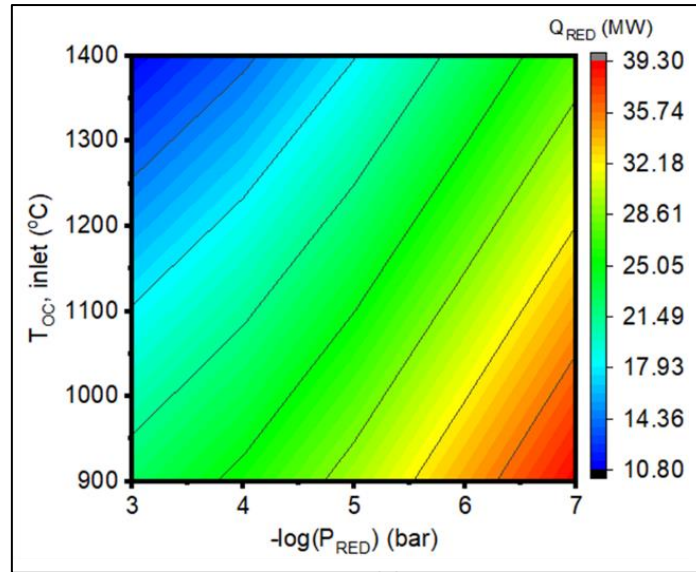


Figure 3-10 Variation of the heat of reaction ( $Q_{red}$ ) with metal oxide inlet temperature to the reduction reactor ( $T_{oc, inlet}$ ) and reactor pressure for a constant reduction temperature of 1600°C for a constant reactor volume of 0.5 m<sup>3</sup> and CeO<sub>2</sub> molar flow 285.71 mol/s

### 3.4.1.3 Oxidation Reaction

After the sensitivity of the reduction reactor, a complete set of sensitivity studies were performed on the moving bed oxidation reactor, as modelled in ASPEN plus. As for the inlet to the reactor, a constant non-stoichiometry factor of 0.35 was assumed to be generated in the reduction reactor. For a CeO<sub>2</sub> flow of 285.71 mol/s, as assumed previously for the reduction reactor, this leads to the production of an equivalent of 100 mol/s of Ce<sub>2</sub>O<sub>3</sub>, as per discussed in equations (3.6) and (3.7). Besides, a constant metal oxide and gas feed temperature to the oxidation reactor (OXI) of 800°C was also assumed. A 5% excess of CO<sub>2</sub> or H<sub>2</sub>O or CO<sub>2</sub>/H<sub>2</sub>O mixture was sent for CO or H<sub>2</sub> production respectively. The composition of the mixture was varied between five mixture compositions, more specifically 100% CO<sub>2</sub>, 75% CO<sub>2</sub> and 25% H<sub>2</sub>O, 50% each of CO<sub>2</sub> and H<sub>2</sub>O, 25% CO<sub>2</sub> and 75% H<sub>2</sub>O, only H<sub>2</sub>O.

The solid conversion (from a non-stoichiometry factor of 0.35 of the reduced metal oxide state to fully oxidized state) – X, was evaluated with a variation to the reactor volume and the composition of the inlet gas. As can be followed from the oxidation kinetics discussion in the reaction kinetics section, due to the relatively faster kinetics of water splitting, a higher conversion is achieved at a similar reactor volume as opposed to CO<sub>2</sub> splitting. As can be seen from the following Figure 3-11, with 5% excess flow with relation to the stoichiometry and at lower reactor volumes below 4 m<sup>3</sup> for water splitting, a lower solid conversion is noticed (around 95%) due to insufficient reactor volume. However, after an X of 95%, the reaction rate drops significantly, making the complete conversion of the reduced ceria much difficult within acceptable reactor volumes for the given scale of application. The maximum conversion achieved for a 5m<sup>3</sup> reactor volume was 98%, while for a reactor volume of 4 m<sup>3</sup>, the corresponding solid conversion was 97.5%. The selectivity of the splitting product would follow the same profile as the metal oxide conversion and hence not plotted separately.

Nevertheless, the selectivity of hydrogen for water splitting for a 4 and 5 m<sup>3</sup> reactor volume was obtained as 93.2% and 93.6% respectively, indicating the necessity of trade-off for selecting the moving bed reactor volume.

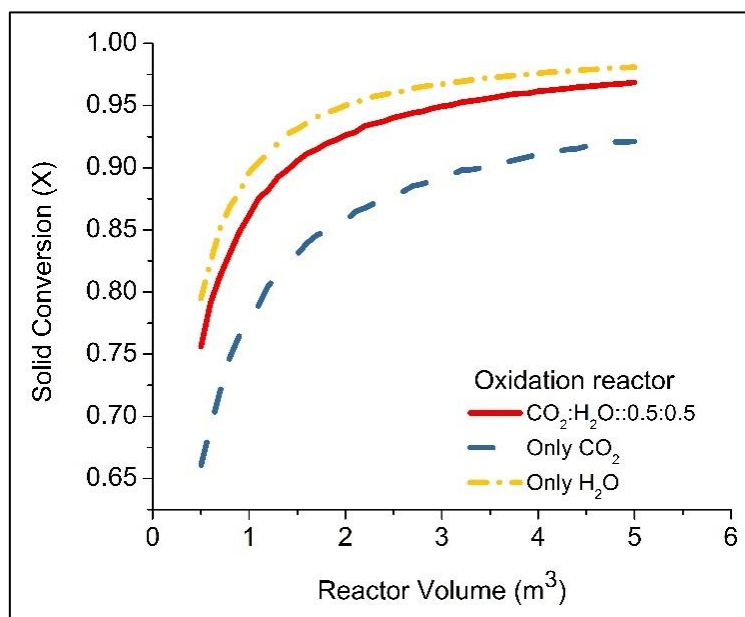


Figure 3-11 Impact of variation of the reactor volume on the Solid Conversion (X) in the oxidation reactor (OXI) with a variation of the inlet gas mixture composition, all other parameters and molar flow being constant.

On the contrary, CO<sub>2</sub> splitting kinetics being slower than water splitting kinetics results in the solid conversion to be lower than that for water splitting, even though the variation of X with reactor volume follows a similar profile to that of water splitting. Corresponding to the 4 and 5 m<sup>3</sup> reactor, the solid conversion with CO<sub>2</sub> splitting was found to be 91% and 92% respectively, showing a higher relative increase in the yield with the same change in reactor volume as compared to water splitting. The corresponding CO selectivity is respectively 86.3% and 87.7%. All the mixtures of CO<sub>2</sub> and H<sub>2</sub>O for co-splitting lie within the two limits whereby CO<sub>2</sub> provides the lower bound and H<sub>2</sub>O the upper bound of the conversion. Nonetheless, the presence of water (steam) in the mixture enhances the reaction rate significantly, being not only more exothermic but also due to faster kinetics. Therefore, as can be followed from Figure 3-11, the co-splitting of an equimolar mixture of CO<sub>2</sub> and H<sub>2</sub>O yields almost 96.2% metal conversion at a reactor volume of 4 m<sup>3</sup>, a significant increase from stand-alone CO<sub>2</sub> splitting. The H<sub>2</sub>/CO molar ratio was calculated as 1.06, showing similar selectivity of H<sub>2</sub> and CO, a major benefit of a moving bed reactor.

Indeed, a sensitivity to evaluate the solid conversion (X) with an increased flow of steam, together with an increased reactor volume was performed and the results are shown in Figure 3-12. The flow of steam was varied between 100 mol/s (stoichiometric) to 200 mol/s (stoichiometric excess 100%). As can be followed from Figure 3-12a, a moderate increase in the solid conversion of 0.4% can be seen up to 20% excess of flow for a reactor volume of 4 m<sup>3</sup>, while the corresponding increase in yield is 0.6% and 0.2% for reactor volumes of 3 and 5 m<sup>3</sup> respectively. Nevertheless, beyond 20% of excess flow to the reactor, the relative increase

in the metal conversion decreases, while the selectivity of the  $H_2$  would drop proportionally. Another disadvantage of sending much excess flow to the reactor, together with having a higher reactor operating volume can be concluded from Figure 3-12b. A linear drop in the oxidized metal oxide outlet temperature is observed, with a drop of over  $100^\circ C$  being observed for a 100% excess flow in relation to the stoichiometric flow of steam for water splitting to the oxidation reactor. Also, for more than 50% excess flow of steam and for higher reactor volume, the outlet temperature is lower signifying a relative cooling of the oxidized metal oxide inside the reactor. Being a counter-current reactor, a higher reaction extent is seen for a larger reactor, which in turn lowers the oxidation reaction rate further. This results in minimal reaction and hence a lower exothermicity of the reaction and a net cooling effect of the outlet solid product is observed even though the conversion is higher. A higher temperature of the outlet metal oxide being always desired for decreasing the heat requirement for reduction as described in an earlier section and this would require a reactor design optimization while performing the entire system in a redox cycle of thermal reduction of ceria with  $CO_2$  and water splitting.

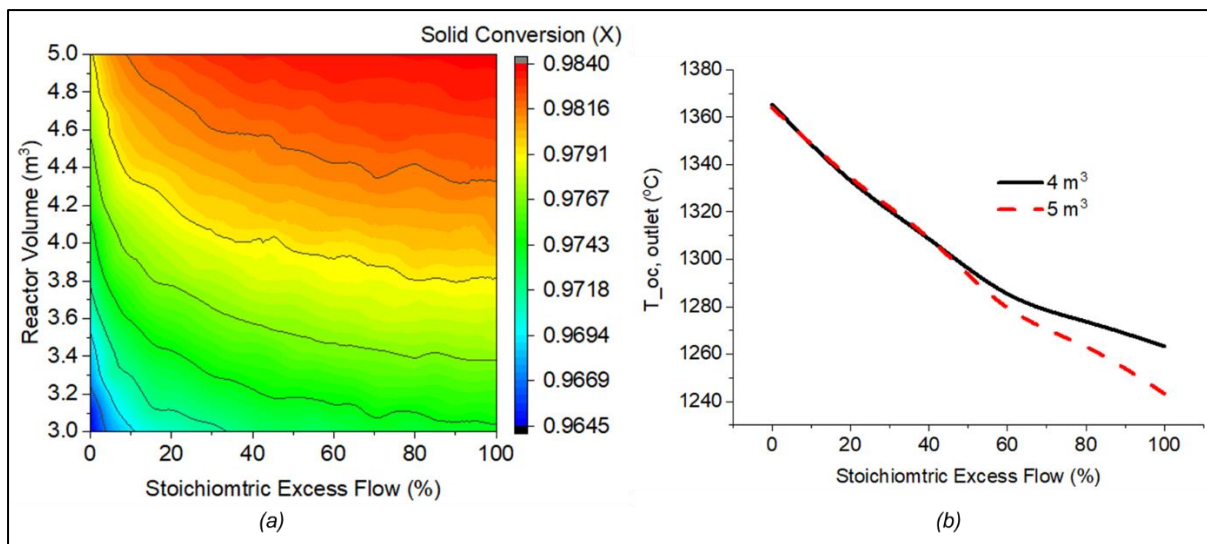


Figure 3-12 (a) Impact of variation of the reactor volume and the flow of steam (Stoichiometric excess) on the Solid Conversion (X) and (b) the variation of the metal oxide outlet temperature ( $T_{oc, outlet}$ ) with the flow of steam (Stoichiometric excess) on the Solid Conversion (X) in the oxidation reactor (OXI) for water splitting for an inlet non-stoichiometry of 0.35, completely oxidized  $CeO_2$  flow rate of  $285.71 \text{ mol/s}$  and pressure of 2 bar.

Based on the above discussion, a reactor volume of  $4 \text{ m}^3$  was fixed to evaluate the variation of the solid conversion (X), and the metal oxide temperature ( $T_{oc}$ ) along the length of the reactor for the five different gas compositions. As can be seen from Figure 3-13a, a similar reaction extent is noticed until around midway through the reactor length irrespective of the gas mixture composition. However, beyond that, with 50% or more fraction of water in the gas mixture, a considerable increase in the reaction extent occurs which results in the final solid conversion to be 97.6%, similar to that of only water splitting. However, below 50% water content in the inlet gas flow, the reaction rate drops, resulting in a slower reaction along the length of the reactor after midway through the reactor. The corresponding impact on the metal oxide temperature variation along the length of the reactor is evident as well. A higher exothermicity

of water splitting results in proportionality to higher metal temperatures attained within the reactor with an increased content of steam in the inlet gas mixture to the oxidation reactor. Indeed, both the reaction extent along the length of the reactor and the relative proportion of  $\text{CO}_2$  and  $\text{H}_2\text{O}$  plays a crucial role in the metal oxide temperature within the reactor. For a faster water-splitting reaction, a maximum metal oxide temperature within the oxidation reactor of about  $1460^\circ\text{C}$  is reached at about 80% of the reactor length, while a maximum reactor temperature of  $1275^\circ\text{C}$  was achieved at similar stages along the reactor length for only  $\text{CO}_2$  splitting. The drop in the metal outlet temperature is due to a counterflow reactor configuration, whereby a cooler reactant gas being supplied results in cooling down of the metal oxide temperature by  $\sim 100^\circ\text{C}$  shown in Figure 3-13b. Also, at such later stages, due to the advanced condition of the oxidation, the reaction rate is much slower, resulting in lower exothermicity of the reaction. This lowering of the metal temperature would result in the requirement of higher energy in the reduction reactor as discussed earlier following Figure 3-8. One feasible alternative can be a multi-entry reactor design whereby the gases can be fed in stages along the length of the reactor. This alternative was studied in brief and not reported in detail in the present work since the net outcome was found to decrease the metal oxide conversion in the OXI, even though the outlet metal oxide temperature from the OXI increased. Nevertheless, the benefit of working with water in splitting, even to lower extents over pure  $\text{CO}_2$  can be emphasized through the following Figure 3-13. Even a presence of 50% of water in the  $\text{CO}_2/\text{H}_2\text{O}$  mixture ensures similar solid conversion to that of water splitting together with increasing the metal oxide outlet temperature from the OXI by almost a  $100^\circ\text{C}$  from around  $1150^\circ\text{C}$  to around  $1300^\circ\text{C}$  for the same fixed reactor volume and fixed molar reactant gas flow.

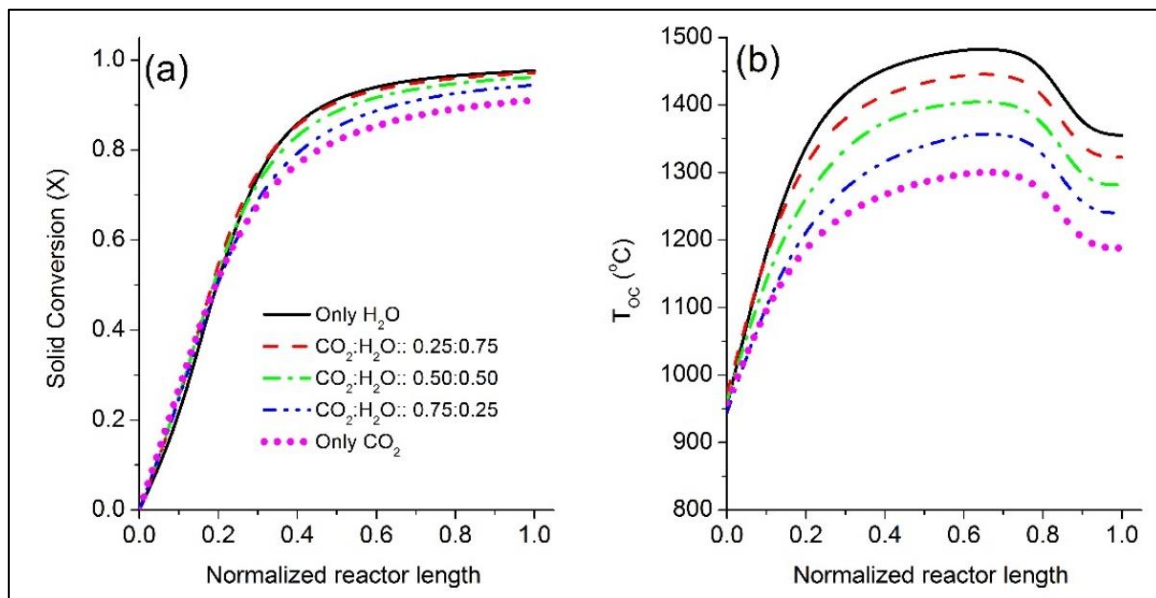


Figure 3-13 Variation of the Solid Conversion (X) (left) and metal temperature (right) in the oxidation reactor with variable inlet gas mixture composition, at a constant oxidation reactor volume of  $2\text{ m}^3$ , a constant non-stoichiometry factor of 0.35 and a constant molar flow of  $110\text{ mol/s}$  of gas in the oxidation reactor, with a fixed metal and gas inlet temperature of  $800^\circ\text{C}$

Even a presence of 50% of water in the  $\text{CO}_2/\text{H}_2\text{O}$  mixture ensures similar solid conversion to that of water splitting together with increasing the metal oxide outlet temperature from the OXI

by almost a 100°C from around 1150°C to around 1300°C for the same fixed reactor volume and fixed molar reactant gas flow. Figure 3-14a represent the impact of the gas inlet temperature on the outlet temperature of the oxidized metal and the solid conversion respectively. Irrespective of the variation of the metal oxide or gas inlet temperature, the impact of the relatively slower kinetics of the CO<sub>2</sub> with respect to the water-splitting reaction is evident. A linear increase in the outlet metal oxide temperature of about 100°C is noticed with an increase in the gas inlet temperature of 500°C (from 500 to 1000°C), which can be argued from the perspective of a counter-current flow in the reactor. No notable change in the relative solid conversion is however obtained, as can be followed from the previous discussions. A linear relation exists between the temperatures and the percentage of water in the inlet gas mixture. While a maximum  $T_{OC, outlet}$  of 1398°C was obtained for water splitting at a steam inlet temperature of 1000°C, the lowest temperature of 1114°C was found to occur for only CO<sub>2</sub> splitting at a CO<sub>2</sub> inlet temperature of 500°C.

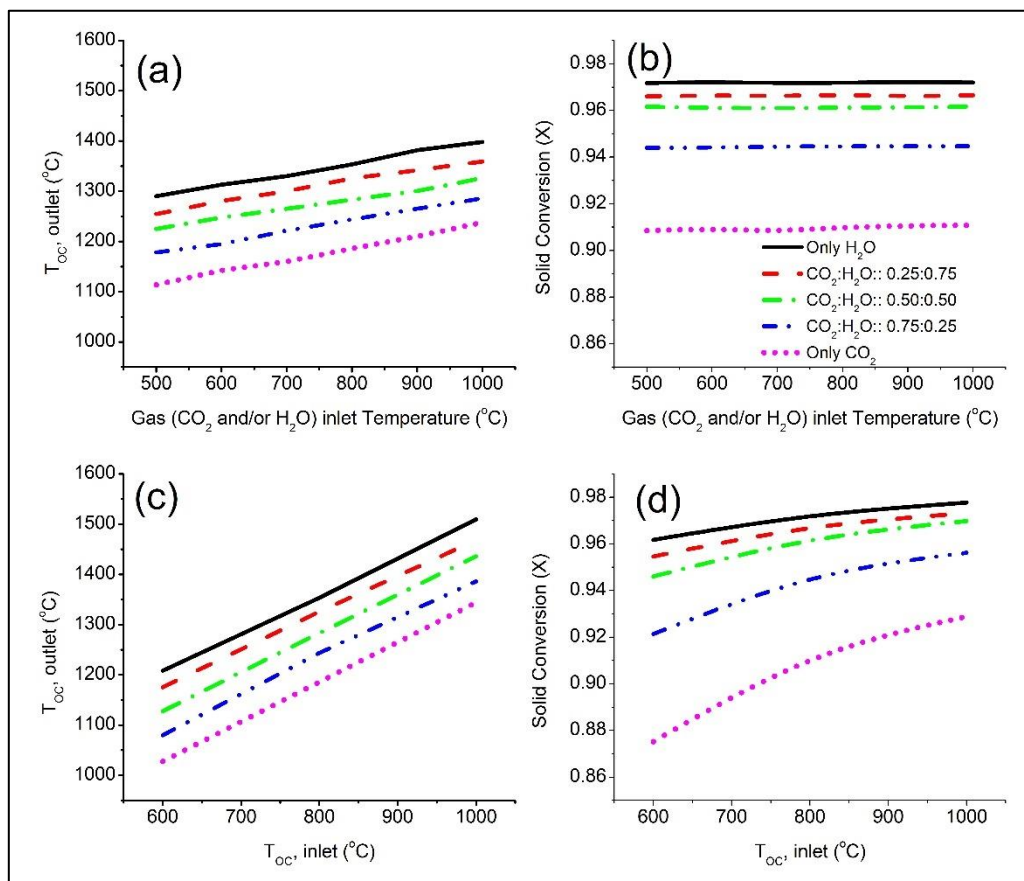


Figure 3-14 Variation of (a) metal outlet temperature from the oxidation reactor and (b) solid conversion (X) in the oxidation reactor with variable gas inlet temperature; Variation of (c) metal outlet temperature from the oxidation reactor and (d) solid conversion (X) with variable metal oxide inlet temperature ( $T_{OC, inlet}$ ) in the oxidation reactor for a variable gas mixture composition at a constant oxidation reactor volume of 4 m<sup>3</sup>, a constant inlet metal non-stoichiometry factor of 0.35 and a constant molar flow of 105 mol/s of gas in the oxidation reactor.

Indeed, an alternative to varying the gas inlet temperature, the metal inlet temperature can also be varied. This was studied at a constant gas inlet temperature of 800°C, all other parameters

being constant. Figure 3-14c and d represent the respective results. In fact, the results indicate this to be a better choice, since a significant increase in the metal oxide outlet temperature, as well as the overall solid conversion is noticed. For a variation of 400°C of the reduced metal oxide inlet temperature a corresponding variation of 300°C in the outlet temperature of the metal oxide is noticed, irrespective of the composition of the inlet gas. It is noticed that for a metal oxide inlet temperature 1000°C, the outlet temperature of the oxidized metal oxide increases to almost 1350°C, significantly improving the slower CO<sub>2</sub> splitting kinetics and hence the net metal oxide conversion (from 87% at 600°C to 92% at 1000°C of metal oxide inlet temperature). The relative impact of solid conversion decreases with the increase in the water content in the inlet gas mixture due to inherently faster water splitting kinetics and a more advanced oxidation condition (with the solid conversion of 97% for water splitting). Nonetheless, a high metal oxide outlet temperature of around 1500°C from the oxidation reactor can be seen, which would significantly reduce the heat requirement for reduction of ceria in the reduction reactor. However, one challenge would be faced, whereby due to counter-current configuration, a very high metal oxide temperature within the reactor might occur. Thus, adequate reactor design optimization, from multiple aspects is necessary to develop a moving bed oxidation reactor for CO<sub>2</sub> and H<sub>2</sub>O splitting for a two-step chemical looping cycle with ceria. The results presented further motivate in developing a closed loop reduction and oxidation moving bed reactor cycle and integrate into an oxyfuel power plant to investigate the efficiency of the solar thermochemical power generation.

### **3.5 Solar Thermochemical Power Generation**

The oxy-fuel combustion is currently one of the most promising alternatives among the portfolio of all the low-emission technologies (LETs) [133,134]. In this technology, the fuel (coal or natural gas or bio-methane) is burnt in an oxygen (O<sub>2</sub>) rich environment (near stoichiometric O<sub>2</sub> flows), instead of air, thereby improving combustion efficiency [135] and eliminating NO<sub>x</sub> emissions and only CO<sub>2</sub> and H<sub>2</sub>O as the product of combustion unit. The oxygen is supplied via an air separation unit (ASU). Burning fuels under these conditions generate combustion gases, which after condensation yields a very high purity of CO<sub>2</sub> exhaust. Oxy-combustion can also be applied to natural gas combined cycle (NGCC), however, subject to the redesign of gas turbines, because alternation in the physical properties of the metal occurs due to the increased CO<sub>2</sub> concentrations in the flue gas [10,135]. Nevertheless, ease and ability to retrofit existing systems at low cost are the primary attractions towards such systems [134], together with the high efficiency of 96-99% carbon capture [136].

Similar to other LETs, technical challenges exist for the oxy-fuel combustion process. The most critical limitations lie in the higher energy penalties associated with air separation unit (ASU) for O<sub>2</sub> production and CO<sub>2</sub> processing unit (CPU) for CO<sub>2</sub> purification and compression [2,137,138] after the combustor unit. The existing commercialized technology for air separation for utility-scale application is the cryogenic air separation process (CASU). It works on the principle of the cryogenic distillation via compression of air to its liquefaction stage, followed by the fractional distillation of its constituent components, such as N<sub>2</sub>, O<sub>2</sub>, Ar and other rare gases. The primary advantage is that this process can produce liquid or gaseous

streams of  $N_2$  and  $O_2$  as per the specification of the end user and for large-scale requirements also. Indeed,  $O_2$  production, via such a process of cryogenic distillation of air, demanding 160 to 250 kWh per tonne of  $O_2$  produced [139,140] is acknowledged as the bottleneck [2,134]. The efficiency loss after integrating the ASU unit to make the oxy-fuel combustion power unit would be 13% compared to the conventional NGCC unit without carbon capture [141]. The penalties incurred using ASU could easily offset any advantages gained by oxyfuel combustion prompting many researchers to investigate the use of alternative air separation systems. However, to date, none of the alternative technologies for air separation have been able to produce high purity oxygen at large utility scale, either due to high costs, such as for adsorption processes, or the technology is still under development or in demonstration stage, as for membrane technologies such as oxygen transport membranes [142,143]. State of the art of ASU can consume between 10 and 40% of the gross power output after retrofitting a conventional coal-fired power, resulting in a net energy penalty as high as 8-13 percentage points [6,144]. True, with a lower purity of  $O_2$  of about 95%, if acceptable for such oxy-fuel applications, the energy requirement for oxygen production with ASU can be further reduced, together with the energy penalty [134].

Several studies of different schemes have been proposed to increase the efficiency for carbon capture. Improving the efficiency through a novel chemical looping air separation technology has been proposed by Moghtaderi [140]. From a system perspective, chemical looping combustion has been shown to have considerable potential for a relatively high efficiency of power production together with carbon capture. For a pulverized coal power plant, around 39% efficiency was calculated while ensuring a  $CO_2$  capture efficiency of almost a 100% [145]. Chemical looping for thermo-chemical dissociation of the captured  $CO_2$ , by producing fuel from  $H_2O$ /recycled $CO_2$ , has exciting potential to improve the system efficiency by providing additional fuel.

In this regard, considering chemical looping syngas production still a developing technology, the reactor design and operation feasibility were considered to utilized while retrofitted to a scale of 100 MW Power Plant with CCS. A simple Oxyfuel NGCC with CCS was modelled to evaluate the net  $CO_2$  and water generated.

The end use of the  $CO/H_2$  produced varies based on local needs, plant design and configuration ranging from power production to the production of chemicals like methane or fuels or advanced Fischer Tropsch liquids. However, for such polygeneration systems, no direct definition of efficiency exists [146]. Hence to evaluate the primary benefits of the excess fuel generation by chemical looping splitting, a solar thermochemical cycle dedicated to power generation from the excess fuel produced was conceived. A conceptual layout development, with a performance assessment, has been subsequently studied as a technology feasibility assessment of such integrations and possibilities of scaling up to utility scales.

### **3.5.1 Plant Layout and Configuration**

Natural gas combined cycle (NGCC) power plants are among the most efficient fossil fuel-fired power plants, able to reach net efficiencies of up to 57% at the commercial scale based

on the Lower Heating Value (LHV) of the fuel [147]. Correspondingly, the specific CO<sub>2</sub> emissions are low as well, compared to other fossil fuel power generation units, at around 350 gCO<sub>2</sub>/kWh, besides having much less SO<sub>x</sub> and NO<sub>x</sub> emissions due to the lower Sulphur and Nitrogen content of the fuel [147]. Addition of CCS units to considerably decrease the specific CO<sub>2</sub> emissions to much below 100 gCO<sub>2</sub>/kWh have therefore been studied and presented in multiple literatures via diverse technologies [147–149]. Like solid fuel power units, the primary motivation of many studies included the decrease in the energy penalty of the capture process, thereby increasing the efficiency of the power plant alongside keeping the capture efficiency to its maximum potential. Oxyfuel combustion using Air separation unit provides one of the highest clean-up efficiencies resulting almost 100% CO<sub>2</sub> capture, however, subject to a large energy penalty. Hence, an add-on unit, utilizing the thermal reduction of ceria by a concentrated solar power with the corresponding splitting of a part of the gaseous exhausts (CO<sub>2</sub> and/ or H<sub>2</sub>O) has been proposed for syngas (fuel) and subsequently power generation to improve on the suffered energy penalty from carbon capture. A part of the stream of pure CO<sub>2</sub> and wastewater generated in the CCS unit has been proposed to be utilized within the add-on unit. Figure 3-15 below shows the plant layouts and configuration of the proposed solar thermochemical power system to be set as an add-on unit to an oxyfuel power unit with CCS. It needs to be clarified that the add-on unit is not limited to integration with only NGCC. The availability of pure CO<sub>2</sub> and H<sub>2</sub>O from other oxyfuel power plants with different feedstock (coal and oil) would allow the proposed add-on unit to be integrated different oxyfuel power plants.

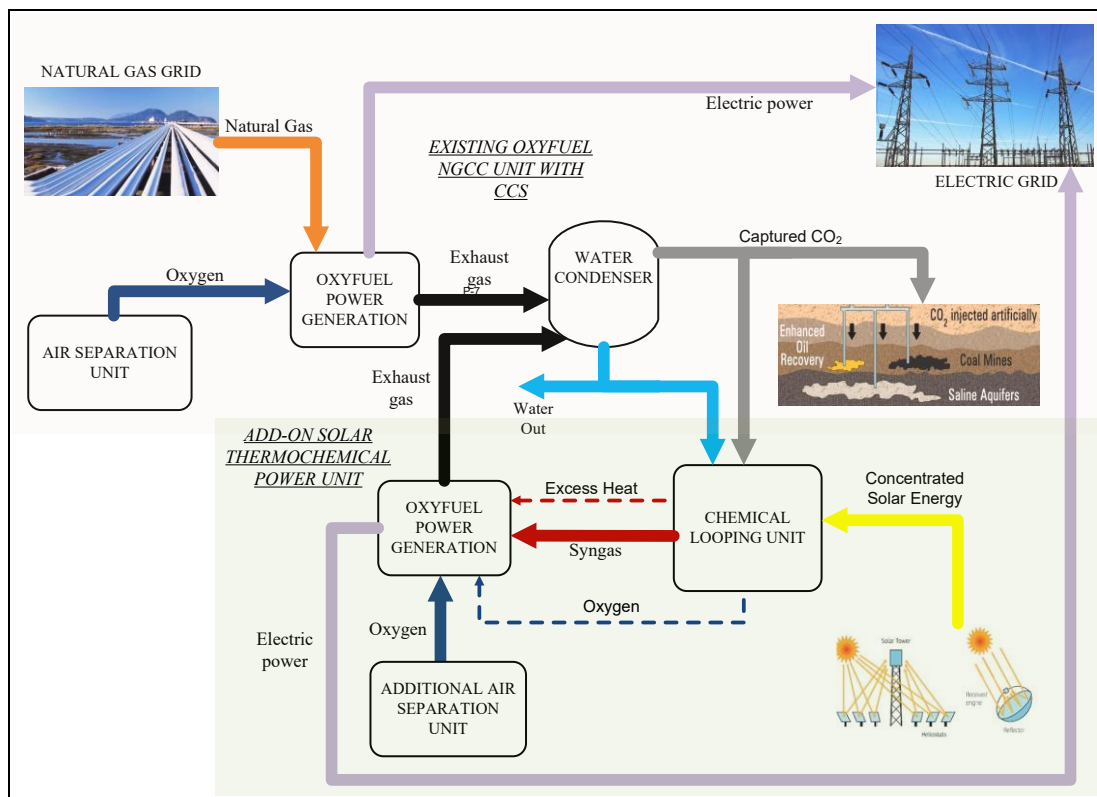


Figure 3-15 Solar Thermochemical plant Conceptual layout with CO<sub>2</sub> and/ or H<sub>2</sub>O recycling for power generation, integrated as add-on unit to an existing Oxyfuel NGCC with CCS

The add-on plant primarily comprises the chemical looping unit, for the generation of syngas from the splitting of recycled CO<sub>2</sub> and /or H<sub>2</sub>O. The reduction reactor would be operated under vacuum, as per the discussions carried out in the previous sections. Several heat exchangers need to be employed for heat integration within the system for CO<sub>2</sub> heating or steam generation for splitting, as well as steam generation from the excess heat for expansion in the steam turbine. Indeed, all the excess heat in the present layout has been integrated to heat recovery steam generation (HRSG) for subsequent steam generation and use in a single bottoming steam cycle. Irrespective of the gas composition an oxyfuel combustion configuration of the produced syngas has been considered. The exhaust gases would then be and sent back for CCS, either by employing a separate clean-up unit or through minor modifications to the existing condenser of the CCS unit. Since the reduction reactor is operated under vacuum conditions, pure oxygen is produced, which has been proposed to be utilized in the combustor for power generation. This would decrease the need for oxygen from an additional air separation unit. The oxidation reactor would be operated at 2 bar pressures instead of at atmospheric conditions to decrease the compression work of the produced CO and/or H<sub>2</sub> needed for the corresponding operation of the combined cycle.

The solar field can either be a central tower configuration, or a beam down configuration. Indeed, the reactor design concept presented by Muhich et al [70] utilizes a beam-up reactor concept via a central tower, where the oxidation reactor is a fluidized bed reactor. However, since in the present layout, a moving bed reactor has been considered for the oxidation, the beam down reactor configuration might seem to be easier to operate, especially with regards to solids handling between the reduction and the oxidation reactor. Nevertheless, solar field design considerations have not been included in the present study, except for the necessary performance evaluation of the proposed add-on unit, though the assumption of solar field efficiency.

### **3.5.2 System Modelling in ASPEN Plus**

In this section, the detailed schematics of the Solar Chemical Looping Power Generation add-on unit with oxyfuel combustion involving CO<sub>2</sub> and/or H<sub>2</sub>O and carbon capture (SCLP-OXY-CC) has been presented and discussed. Subsequent evaluation of the proposed add-on unit was carried out in ASPEN Plus<sup>®</sup> (v 8.8) and its corresponding existing functions and built-in modules. Following from the previous discussion, the PR-BM method was selected for the simulations.

#### **3.5.2.1 Assumptions**

The generic assumptions as discussed while modelling the individual reduction and oxidation reactors were included in the present simulation as well. Besides such, additional considerations were necessary simulations as follows:

- Steady-state simulations were performed, and the results hence obtained are not applicable to start-up or transient operations.

- The maximum Turbine Inlet Temperature (TIT) of 1377°C (1650K) was considered, within the range of maximum TIT of commercially available gas turbines [150].
- The maximum pressure ratio for a single stage expansion in a stationary gas turbine is 18:1 as of commercial gas turbines [151]. This limit was respected within the present layout as well.
- No heat loss and inefficiencies in the lines were accounted for.
- The ambient condition was assumed as 25°C and 1.01325 bar. Also, the composition of air was assumed to comprise 79% N<sub>2</sub> and 21% O<sub>2</sub> on a volume basis.
- Minimum approach temperature in heat exchangers was taken as 10°C [131].
- The isentropic efficiency and mechanical efficiency for compressors and turbines were considered as 0.9 and 0.98, respectively. The pump efficiency was assumed to be 0.85 and 0.9, for isentropic and mechanical efficiency respectively.
- The primary objective of the present study is to recognize the potential efficiency gain from the addition of the chemical looping and a downstream power generation unit in a conventional oxyfuel plant. Hence the turbines and the HSRG were modelled as simple units, without reheating or multi-pressure systems. Indeed, by increasing the model complexity, together by performing design optimization, the net efficiency can be improved considerably by process optimization studies.

Moreover, design assumptions with respect to individual units of the respective layouts are listed in the following Table 3-3.

A simplistic model of a 100MW power NGCC and a corresponding oxyfuel NGCC power plant of the same capacity with CCS was developed in ASPEN Plus, incorporating all the necessary assumptions stated above. This was necessary to evaluate the performance of the base case power plants, together with the availability of CO<sub>2</sub> and H<sub>2</sub>O necessary for added fuel generation via splitting. Since the primary aim of the present study is to develop the feasibility investigation of integration of the splitting cycle in an add-on unit and to evaluate the net benefit from the generation of additional electricity, the need for detailed modelling of the base case was not considered crucial. The net molar flow of CO<sub>2</sub> to the CCS unit from the base case of 100 MW oxyfuel NGCC with CCS was obtained around 330 mol/s. The corresponding water released from the condenser of the exhaust gas was 550 mol/s. For the layouts of the base case power plants with and without CCS integration as modelled in ASPEN Plus refer to Chapter 6.2.

From the limitation of the present technology development of not only the CL unit but also on the perspectives of Concentrated Solar technology and the possibility of providing high-temperature heat over a large control volume, the use of 20% of CO<sub>2</sub> from the CCS unit was considered for splitting in the base case scenario. The molar flow of gas for splitting would thus be 66 mol/s. Corresponding water utilization for the base case scenario is 12%. The ceria flow was calculated accordingly and has been discussed in subsequent sections.

### 3.5.2.2 Simulation Description

A common configuration of the add-on, applicable irrespective of the gas mixture into the oxidation reactor was then modelled and simulated in ASPEN Plus. Figure 3-16 shows the system configuration developed thus.

Table 3-3 Design assumptions used for developing the process flowsheet models in ASPEN plus

Unit	Parameters
ASU	<ul style="list-style-type: none"> <li>• O<sub>2</sub> purity: 99.9% (by volume)</li> <li>• ASU O<sub>2</sub> and N<sub>2</sub> delivery pressure: 1.2 bars</li> <li>• O<sub>2</sub> compression pressure: 18 bars</li> <li>• A small fraction of the N<sub>2</sub> was used as sweep gas in CL unit</li> </ul>
Solar Field	<ul style="list-style-type: none"> <li>• A generic solar field efficiency of 75% was assumed based in the consideration of a central receiver configuration [152].</li> <li>• Thermal Receiver efficiency was assumed as 89% [153].</li> </ul>
Reduction Reactor (RED) and Thermal Receiver	<ul style="list-style-type: none"> <li>• An isothermal reactor at 1600°C and a vacuum pressure of 10<sup>-7</sup> bar was considered for the base case scenario.</li> <li>• Continuous metal transportation between the oxidation reactor (OXI) and reduction reactor (RED) reactors was assumed, neglecting work expended in metal handling.</li> </ul>
Oxidation reactor (OXI)	<ul style="list-style-type: none"> <li>• An adiabatic reactor with adequate insulation to ensure no heat loss was considered.</li> <li>• The oxygen carrier outlet temperature from OXI was considered as the oxygen carrier inlet temperature to RED</li> </ul>
Vacuum Pump (VACPMP)	<ul style="list-style-type: none"> <li>• Modelled as a four-stage compressor with inter-cooling</li> <li>• Isentropic efficiency: 90%</li> <li>• Mechanical Efficiency: 98%</li> <li>• Discharge pressure: 1 atm</li> </ul>
Compressors	<ul style="list-style-type: none"> <li>• Isentropic efficiency: 90%</li> <li>• Mechanical Efficiency: 98%</li> </ul>
Combustor (COMB)	<ul style="list-style-type: none"> <li>• Excess oxygen factor of 1.05 for CO and/or CO and H<sub>2</sub> mixture combustion was considered. For H<sub>2</sub> combustion, no additional supply of O<sub>2</sub> was considered besides the O<sub>2</sub> from the reduction reactor (around 1% excess with respect to the H<sub>2</sub> produced).</li> <li>• Pressure drop within combustor: -0.2 bar</li> <li>• Heat loss from combustor: 0.2 MW</li> </ul>
Gas Turbine	<ul style="list-style-type: none"> <li>• Isentropic efficiency: 90%</li> <li>• Mechanical Efficiency: 98%</li> </ul>
Steam Turbine and HRSG	<ul style="list-style-type: none"> <li>• Single stage expansion in the steam turbine was considered.</li> <li>• Turbine Isentropic efficiency: 90%</li> <li>• Mechanical Efficiency: 98%</li> <li>• Steam Pressure: 150 bars</li> <li>• Live Steam Temperature for Steam Turbine Inlet: 600°C</li> <li>• Condenser pressure: 0.04 bar</li> <li>• Pump Isentropic Efficiency: 0.8</li> </ul>

The heart of the proposed SCLP-OXY-CC add-on unit is the chemical looping (CL) unit, modelled as moving bed reactors, as per the reactor model developed in ASPEN Plus and discussed in the previous Section 3.2. For the reduction reactor (RED), a vacuum pump (VACPMP) is necessary to maintain the vacuum pressure and has been modelled as a four-stage compressor with inter-cooling. The oxygen from the RED (Stream 14) is first cooled and then released at atmospheric pressure by the vacuum pump. The heated and reduced metal from the RED (Stream 25) is then cooled in steps, modelled as two heat exchangers (METHX-1 and MET HX-2) for simplicity. The first heat exchanger would conceptually be used to heat up the inlet gas mixture to the oxidation reactor (OXI) in the form of steam generation in STEAMGEN or CO<sub>2</sub> heating. METHX-2 would then ensure the necessary metal oxide inlet temperature to the OXI via steam generation. This would, however, limit the plant operation at lower temperatures of the reduction reactor due to the chances of temperature cross-over for a constant feed temperature to the OXI.

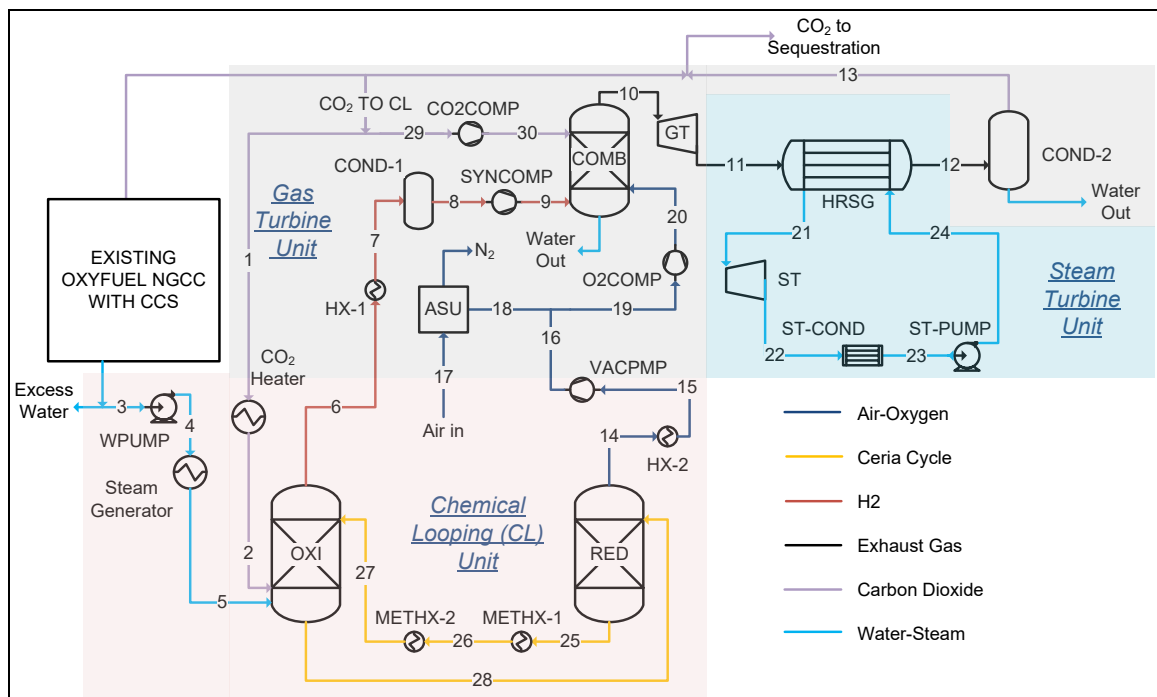


Figure 3-16 Conceptual layout of the SCLP-OXY-CC add-on unit utilizing CO<sub>2</sub> and/or H<sub>2</sub>O splitting with thermal reduction of ceria recycling for power generation via fuel-air combustion

The product gas from the OXI (Stream 6) is first cooled against steam generation till ambient temperature and subsequently passed through a condenser to remove the moisture (COND-1). However, this becomes a redundant unit while working with only CO<sub>2</sub>, wherein no water is present in the product gas. Subsequently, the syngas (Stream 19) is compressed in SYNCOMP to a pressure of 18.2 bar and fed into the combustor. Since the exhaust gas needs to be fed back to the CCS stream, an oxyfuel combustion is necessary. Excess O<sub>2</sub>, as required for the combustion (Stream 18) is sourced from an additional air separation unit and compressed together with the oxygen from the RED for the combustor. Since near stoichiometric oxygen necessary for the combustion of syngas is produced from the reduction reactor, the size of the ASU required is significantly small in comparison to the scale of the add-on unit. Thus, a

significant energetic benefit from the internal use of the generated oxygen can be obtained, countering the energy penalty of vacuum generation for reduction.

In the combustion chamber (COMB), a pressure drop of 0.2 bar results in the inlet pressure to the gas turbine (GT) of 18 bars. The temperature at the combustor outlet, or in other words, the turbine inlet temperature (TIT) is maintained at 1377°C by recycling CO<sub>2</sub> from the CCS stream (Stream 29) via a CO<sub>2</sub> compressor (CO2COMP). The exhaust gas from the combustion chamber (COMB) is expanded in a gas turbine (GT) up to a pressure of about 1.04 bar and further subsequently fed to an HRSG for steam generation to be used in the bottoming steam cycle. Due to the absence of SO<sub>x</sub>, the gas can be expanded to temperatures as low as 50°C. The exhaust gas, after water condensation, comprises almost pure CO<sub>2</sub> (Stream 13). Therefore, it would be sent back to the CCS stream from where it was originally sourced from. Thus, the zero-emission system of the original plant is maintained, as can be visualized in the plant layout detailed in the above Figure 3-16.

A major advantage of the proposed cycle working with or without CO<sub>2</sub> is the fact that the entire cycle continues at the same molar flow of the sourced CO<sub>2</sub> from the CCS stream, with no additional product being generated to that of the recycled CO<sub>2</sub>. This simplifies the integration of the add-on unit to the original power plant significantly, by requiring minimum additions or changes for the necessary retrofit. Indeed, a direct utilization of the exhaust of the original Oxyfuel power plant, which essentially is a mixture of approximately 86% of CO<sub>2</sub> and about 14% of H<sub>2</sub>O would be of significant interest. Hence, analyses with three possible gas mixtures, only CO<sub>2</sub>, only H<sub>2</sub>O and a CO<sub>2</sub>/H<sub>2</sub>O mixture replicating the typical exhaust of an oxyfuel power plant were performed to evaluate the performance of the SCLP-OXY-CC add-on unit with respect to the gas composition to the OXI.

### 3.5.3 Energy Performance Evaluation

To obtain the comparative thermodynamic system performance of the add-on solar thermochemical power plant with respect to individual efficiency and with respect to the combined efficiency with the oxyfuel power plant, an energy analysis is necessary to be evaluated.

The energy analysis is based on the First Law of Thermodynamics and considers the principle of conservation of energy applied to a prescribed system. The thermal efficiency of the proposed power plant, directly concluded based on the First Law of thermodynamics is therefore evaluated in terms of the rate at which solar power ( $\dot{Q}_{sol}$ ) is converted to the net

electric power output ( $\dot{W}_{el,net}$ ) [154], as defined by the following equation (3.23):

$$\eta_{th} = \frac{\dot{W}_{el,net}}{\dot{Q}_F} = 1 - \frac{\dot{Q}_L}{\dot{Q}_F} \quad (3.23)$$

Where,  $\dot{Q}_L$  is the system energy loss. However, for components such as pumps or compressors, where the thermal efficiency is not possible to be evaluated in terms of useful energy output, the thermodynamic performance is assessed via the concept of ‘isentropic efficiency’. By this, a comparative analysis is developed between the actual and ideal performance of a device. The ideal conditions are related to no entropy generation, together with negligible heat transfer between the device and the surrounding [155]. Nevertheless, beyond the thermal efficiency of the power plant, the efficiency of the receiver and the solar field play a crucial role in the overall solar to electricity of the proposed add-on unit. Indeed, this limits the overall performance of the proposed SCLP-OXY-CC unit. For a solar field efficiency of  $\eta_{\text{solar-field}}$  and a receiver efficiency denoted by  $\eta_{\text{receiver}}$ , the solar to electricity efficiency of the proposed add-on unit ( $\eta_{\text{solar-e}}$ ) can be written as per the following equation (3.24). In the following analysis, the solar-to-electricity efficiency has usually been referred to describe the SCLP-OXY-CC plant efficiency, unless otherwise mentioned.

$$\eta_{\text{solar-e}} = \eta_{\text{th}} \times \eta_{\text{solar-field}} \times \eta_{\text{receiver}} \quad (3.24)$$

However, in addition to the net plant efficiency of the add-on unit, interest lies in the study of the CL unit efficiency in itself. The efficiency is derived based on the similar principle described above, however, the output being the net chemical potential in the split gas in terms of its Lower Calorific Value (LHV). The definition of efficiency for the CL unit has been defined as follows by equation (3.25).

$$\eta_{\text{SCL}} = \frac{(\dot{m}_{H_2} LHV_{H_2} + \dot{m}_{CO} LHV_{CO})_{\text{oxy}}}{(\dot{Q}_{\text{red}} - \dot{Q}_{\text{oxd}}) + \dot{Q}_{\text{CO}_2/\text{H}_2\text{O}} + (\dot{Q}_{\text{sphtr}} - \dot{Q}_{\text{sld}}) + W_{\text{VAC}}} \quad (3.25)$$

Where,  $\dot{Q}_{\text{red}}$  is the heat requirement at the reduction reactor,  $\dot{Q}_{\text{oxd}}$  is the heat released from the oxidation reactor. Since the OXI is an adiabatic reactor,  $\dot{Q}_{\text{oxd}}$  would be zero.  $\dot{Q}_{\text{CO}_2/\text{H}_2\text{O}}$  is the net heat needed for the system operations, including the heat needed for heating up the sweep gas and the inlet  $\text{CO}_2$  and/or  $\text{H}_2\text{O}$  for splitting.  $\dot{Q}_{\text{sld}}$  represents the heat recovered from the solids from the reduction reactor before it enters oxidation, while  $\dot{Q}_{\text{sphtr}}$  is the heat delivered to the solids for preheating. However, in the present layout, no pre-heating was employed and hence would be equal to zero as well. Heat losses from system components were neglected in the efficiency assessment. Finally,  $W_{\text{VAC}}$  represents the pumping work resulting from vacuum generation and removal of generated oxygen from the reduction reactor.

### 3.5.4 System Evaluation

To perform the necessary system evaluation of the proposed SCLP-OXY-CC unit, the metal flow rate was first fixed. As explained before, for the base case add-on unit, 66 mol/s of gas

(CO<sub>2</sub> and/or H<sub>2</sub>O) was utilized. This would ideally require 66 mol/s of equivalent Ce<sub>2</sub>O<sub>3</sub> flow into the oxidation reactor. However, considering a 20% excess gas flow in the oxidation reactor based on the sensitivity studies, and the corresponding maximum non-stoichiometry of 0.1982 at a reduction temperature and pressure of 1600°C and 10<sup>-7</sup> bar, a CeO<sub>2</sub> recirculation rate of 275 mol/s in the CL unit was fixed.

Indeed, the value closely follows the mole flow of CeO<sub>2</sub> used for the previous sensitivity analysis. Additionally, the temperature range within which the proposed add-on unit was analysed was 1300 and 1600°C, to obtain a considerable reduction extent. Hence, as per the previous discussion of Section 3.4, a reduction reactor volume of 0.5 m<sup>3</sup> was selected to minimize the heat requirement for the reduction by avoiding unnecessary heating of a large volume of the reactor without significant reaction. Also, this would ensure predicting well the heat requirement for the reduction since ASPEN Plus reports the heat of reaction and not the heat supplied to the reactor. However, the oxidation reactor volume needs to be decided separately due to a maximum reduction extent of 0.2 as opposed to 0.35 considered for the sensitivity studies. Additionally, the impact on the system performance is crucial to be analysed. In this regard, a sensitivity analysis to decide upon the reactor volume was performed by comparing two extreme cases of water splitting and CO<sub>2</sub> splitting. The results are shown in Figure 3-17.

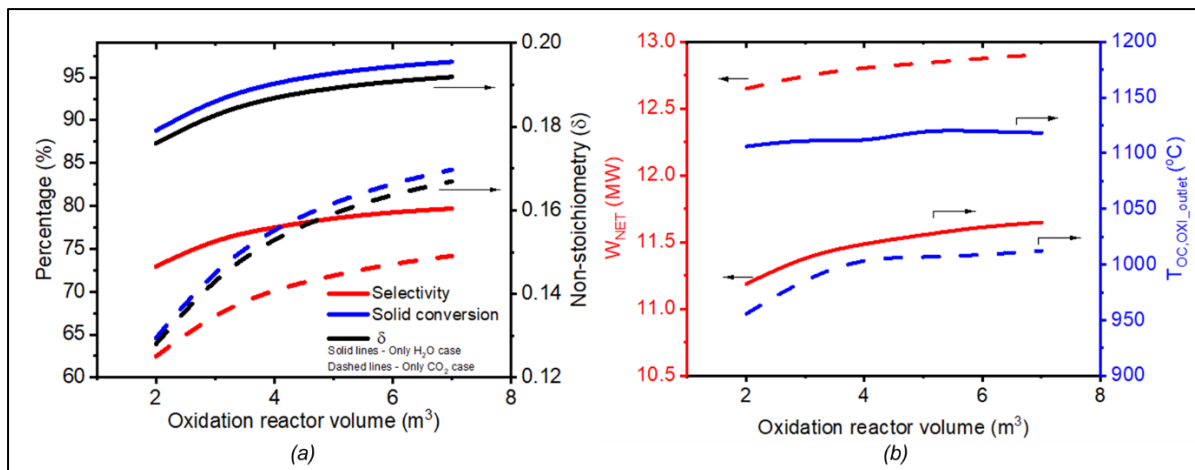


Figure 3-17 Impact of the variation of the oxidation reactor volume with water splitting (Solid Lines) and CO<sub>2</sub> splitting (Dashed Lines) on the specific system performance of the proposed SCLP-OXY-CC add-on at a constant RED temperature and pressure of 1600°C and 10<sup>-7</sup> bar respectively, a constant molar flow rate of CeO<sub>2</sub> and CO<sub>2</sub>/H<sub>2</sub>O of 275 mol/s and 66 mol/s respectively, and a constant metal oxide and gas inlet temperature of 800°C to the OXI.

As can be followed from the above Figure 3-17, the oxidation reactor volume was varied between 2 and 7 m<sup>3</sup>. Due to the faster kinetics of water splitting, a reactor volume of 4 m<sup>3</sup> results in a minimum enhancement to the system performance. However, for a slower CO<sub>2</sub> splitting reaction, a larger reactor volume is required. Indeed, the highest impact of the variation of the reactor volume is seen on the solid conversion, whereby for CO<sub>2</sub> splitting it increases from 65% for a 2 m<sup>3</sup> reactor to 80.4% for a 5 m<sup>3</sup> reactor and 84.2% for a 7 m<sup>3</sup> reactor. This also results in the net reduction extent in the RED to increase, due to a higher number of oxygen

vacancies in the oxidized metal. Nevertheless, besides the CL unit itself, a reactor volume of more than 5 m<sup>3</sup> is seen to have a lower impact on the overall system performance. While a rise of 0.2 MW of the net power production is noticed irrespective of the gas composition, the relative variation in the oxidized metal outlet temperature from the oxidation reactor (OXI) is minimal beyond a reactor volume of 5 m<sup>3</sup>. A combined effect of such variation of the system operating parameters results in a stable solar-to-electricity efficiency of the system of about 24.2% for working with the only H<sub>2</sub>O while the corresponding efficiency is 25.4% for only CO<sub>2</sub> splitting. Accordingly, 5 m<sup>3</sup> was selected as the reactor volume of the OXI. In the end, it can be claimed with confidence that such a conservative design would also ensure an operational flexibility with respect to available feedstocks.

#### 3.5.4.1 Sensitivity Analysis

To decide on the operating parameters and hence evaluate the achievable system efficiency, a comprehensive set of sensitivity was performed. The first set of sensitivity was performed to determine the impact of the inlet temperature of the gas and metal oxide into the OXI, all other parameters remaining constant. Following the discussions of the individual reactor sensitivity presented in Section 3.4.1.3, a minimal variation of the system performance was noted with varying the gas inlet temperature to the OXI, irrespective of the gas composition. Irrespective of the gas composition, a net increase in the net power output of 0.5 MW is obtained at for decreasing the gas inlet temperature from 1000°C to 500°C due to a decrease in the steam available for expansion in the steam turbine. However, with the rise in the gas inlet temperature, a rise in the metal oxide temperature at the OXI outlet is also observed, which would decrease the heat requirement for the same extent of reduction. Thus, no significant impact on system efficiency is obtained by varying the gas inlet temperature to the OXI, with an average efficiency of 24.2% and 25.4% being achieved for the only CO<sub>2</sub> and the only H<sub>2</sub>O cases respectively. Furthermore, for lower reduction temperatures, a gas inlet temperature beyond 800°C would result in temperature cross-over between STEAMGEN and METHX-1 for water splitting, due to a higher heat requirement to evaporate water in comparison to sensible heat requirement for CO<sub>2</sub> heating. Hence, to ensure a flexible system operation irrespective of gas composition to the OXI, a gas inlet temperature of 800°C was set.

Thereafter, by fixing the gas inlet temperature to the OXI at 800°C, the reduced metal oxide temperature ( $T_{OC,OXI\_inlet}$ ) to the OXI as varied between 600 and 1000°C. A discussion on the variation in the individual power generation from the GT and ST, as well as the auxiliary power requirement, while working with either CO<sub>2</sub> or H<sub>2</sub>O is necessary. This can be followed from the results plotted in Figure 3-18 b and c with varying the metal oxide inlet temperature to the OXI. A solid conversion (X) between 93% and 96.7% is noted between 600 and 1000°C of  $T_{OC,OXI\_inlet}$  for water splitting, while the corresponding values for CO<sub>2</sub> splitting yields and X between 74.3% and 86%. This higher impact of  $T_{OC,OXI\_inlet}$  on the CO<sub>2</sub> splitting reaction results in significant improvement to the reduction reaction as well for the only CO<sub>2</sub> case, whereby the non-stoichiometry ( $\delta$ ) generated from reduction increases from 0.147 to 0.171. However, with a higher and a more constant solid conversion for water splitting, more oxygen is available to be removed via reduction, resulting in the net  $\delta$  generated to be improved from 0.184 at

600°C to 0.191 at 1000°C of  $T_{OC,OXI\_inlet}$  (Figure 3-18c). For the same molar flow of gas to the OXI, a higher reduction extent in the RED results in a higher selectivity of  $H_2$  (79.9% at  $T_{OC,OXI\_inlet}$  1000°C) in comparison to the selectivity of CO (51.17% at  $T_{OC,OXI\_inlet}$  1000°C), as can be seen from Figure 3-18b.

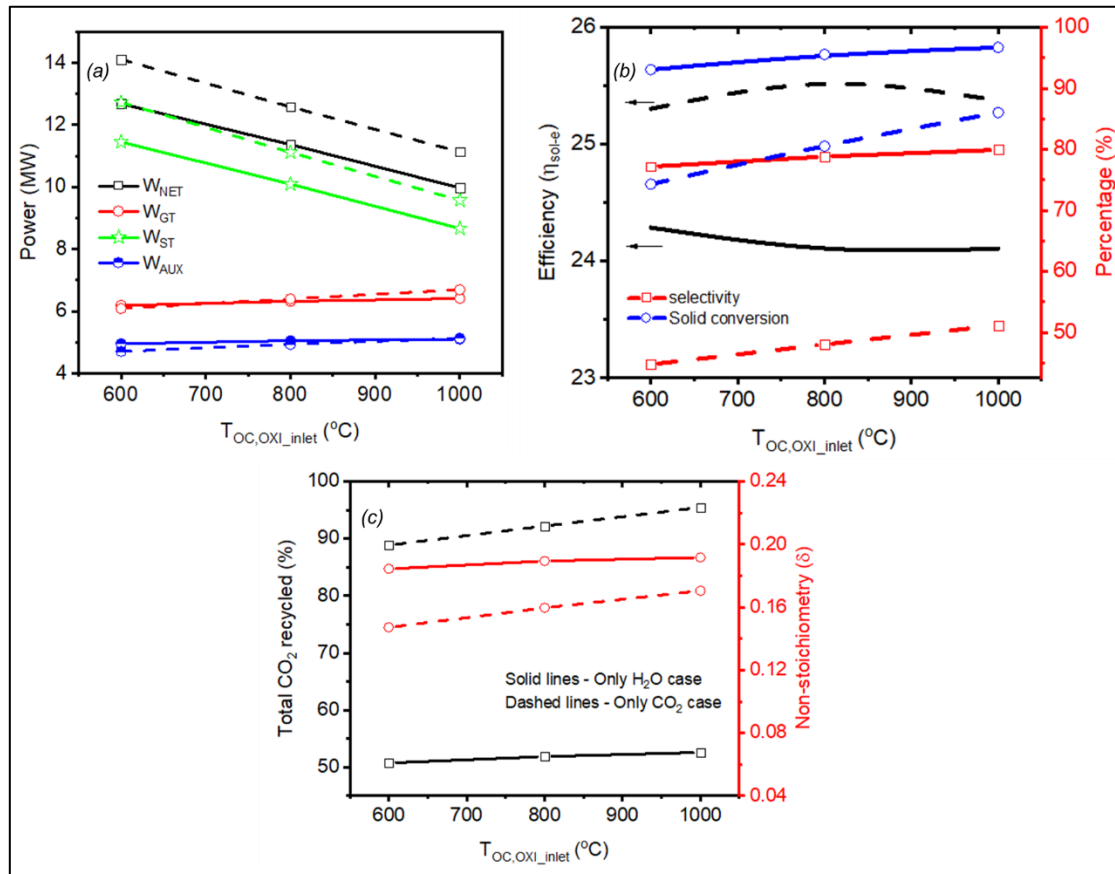


Figure 3-18 . Impact of the variation of the reduced metal inlet temperature to the OXI on the operating parameters of the SCLP-OXY-CC at a constant RED temperature and pressure of 1600°C and  $10^{-7}$  bar respectively, a constant molar flow rate of  $CeO_2$  and gas to the OXI of 275 mol/s and 66 mol/s respectively and a constant gas inlet temperature to the OXI of 800°C

Based on the selectivity, excess  $CO_2$  is circulated to the combustion chamber to maintain the TIT at 1377°C (1650K). For water splitting, the excess water is removed in the condenser before compression and combustion with recycled  $CO_2$ . For a lower variation in the selectivity of  $H_2$ , this results in similar molar flow to be expanded in the GT irrespective of  $T_{OC,OXI\_inlet}$ . On the other hand, for  $CO_2$  splitting the final  $CO_2$  expanded is balanced by the recirculated carbon dioxide into the combustor. Hence, the GT output remains constant at 6.3 MW irrespective of the gas composition used for splitting. However, a higher heat is required to heat water from 25°C to 800°C than  $CO_2$  due to the requirement of latent heat for the former. This would result in a lower heat availability in METHX-2 for steam generation causing a lower steam to be expanded in the steam turbine for the water only scenario. A drop of almost 1 MW drop in the power output from the ST is observed hence. As for the auxiliary power demand, no significant effect is noticed from the variation of the  $T_{OC,OXI\_inlet}$ . Therefore, a drop in the net electricity output from 14.1 MW to 11.1 MW is observed with increase in  $T_{OC,OXI\_inlet}$

from 600°C to 1000°C for working with only CO<sub>2</sub> with the corresponding output with only H<sub>2</sub>O being always about 1.2 MW lower.

A combined impact of the individual variations is obtained in the plant efficiency ( $\eta_{\text{sol-e}}$ ). Indeed, to comment on the plant efficiency, the impact of the metal oxide and split gas temperature from the oxidation reactor is crucial to be considered as well. As can be followed from the previous sensitivity results, an increase in the  $T_{\text{OC,OXI\_inlet}}$  significantly increases both the  $T_{\text{OC,OXI\_outlet}}$  and the gas outlet temperature from the OXI. While the former decreases the thermal requirement in the RED, the cooling of the gas from higher temperature results in a larger steam generation. Indeed, the exothermicity of water splitting is higher, a higher temperature of both metal oxide and the product gas from the OXI is obtained for water splitting than with CO<sub>2</sub> splitting. Thus, a constant lower heat (around 1.5 MW) would be required in the RED to maintain the temperature while working with only water as opposed to that while working with the only CO<sub>2</sub>. Notwithstanding this fact, due to a relatively higher net electricity output, the overall efficiency for a pure CO<sub>2</sub> operated SCLP-OXY-CC unit is higher by one percentage point than for a pure water operating cycle. Based on the relative impact of all the parametric variations resulting from the variation of the  $T_{\text{OC,OXI\_inlet}}$ , an optimum efficiency is reached (25.5%) at 800°C of  $T_{\text{OC,OXI\_inlet}}$  for CO<sub>2</sub> only operation (Figure 3-18b).

A variation in the reduction temperature between 1300 and 1600°C was performed and its impact on the system performance was evaluated. Similar logical reasoning can be followed from the discussions of the previous sections. A lower reduction temperature results in a lower non-stoichiometry ( $\delta$ ), which significantly increases with temperature (Figure 3-19a). A constant molar flow in the OXI would therefore significantly decrease the selectivity of the product gas in the OXI. So much so, that for CO<sub>2</sub> splitting with no separation of the product and reactant gas, the TIT would not be possible to be maintained for a constant molar feed rate of gas to the OXI from around a RED temperature of 1400°C. This is shown in Figure 3-19b, whereby the molar flow sent to the OXI corresponds to only 15% and 2.5% of the total CO<sub>2</sub> molar flow sent for CCS from the original Oxyfuel power plant. This, however, results in the selectivity of CO to increase at 1300°C from that of 1400°C of reduction temperature. On the other hand, even though the H<sub>2</sub> selectivity drops to almost around 2%, the presence of the condenser ensures a stable TIT to be maintained by varying the flow of the recycled CO<sub>2</sub> in the combustor accordingly. Nevertheless, with the decrease in the production of H<sub>2</sub> with reduction temperature, the overall CO<sub>2</sub> recycled would drop as well from around 52% at  $T_{\text{RED}}$  of 1600°C to lower than 2% for a  $T_{\text{RED}}$  of 1300°C, as shown in Figure 3-19c. A maximum CO<sub>2</sub> recycling rate of about 65% is obtained for working with the only CO<sub>2</sub> at a reduction temperature of 1600°C.

As can be followed from the kinetic discussions, a lower non-stoichiometry in the reduction reactor would also significantly decrease the reaction rate of the oxidation reaction. Due to slower kinetics resulting from a smaller number of vacancies in the reduced metal oxide, the solid conversion drops as well with a decrease in the reduction temperature. This effect can be seen in Figure 3-19b as blue coloured lines. The solid conversion with water splitting is inherently higher than that with CO<sub>2</sub> splitting, yielding a conversion of over 96% at  $T_{\text{RED}}$  of

1600°C, while the corresponding value with CO<sub>2</sub> splitting is 80%. Indeed, it needs to be clarified that a higher solid conversion fraction does not imply a higher H<sub>2</sub> or CO generation since the conversion fraction essentially indicates the relative change in the oxidation state of the ceria between the inlet and outlet of the reduction reactor, irrespective of the absolute value of  $\delta$  generated.

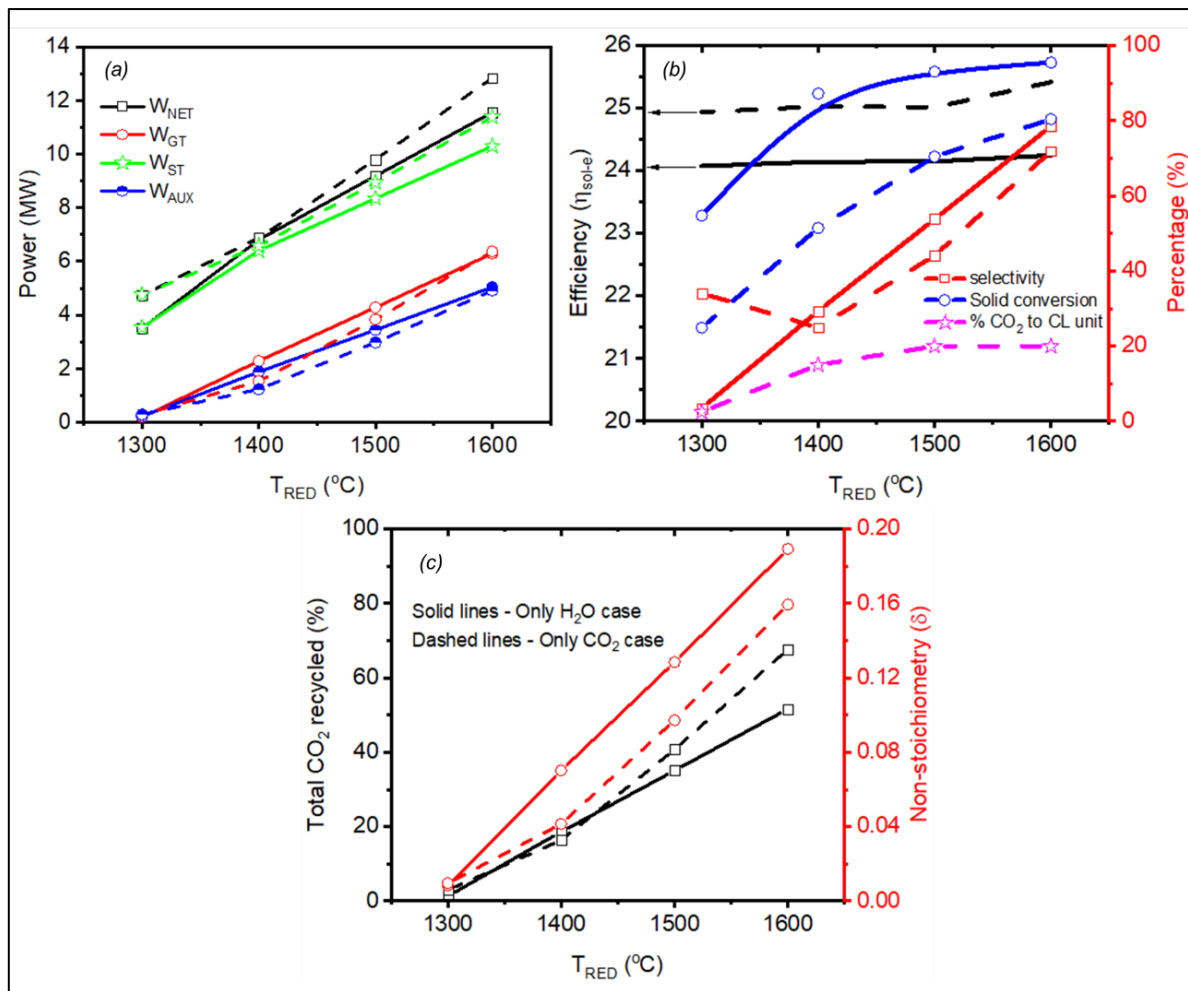


Figure 3-19 . Impact of the variation of the reduction temperature on the operating parameters of the SCLP-OXY-CC at a constant RED temperature and pressure of 1600°C and 10<sup>-7</sup> bar respectively, a constant molar flow rate of CeO<sub>2</sub> and gas to the OXI of 275 mol/s and 66 mol/s respectively and a constant gas inlet temperature to the OXI of 800°C

The impact of the absolute amount of H<sub>2</sub> or CO generated in the OXI, directly proportional to the net non-stoichiometry generated in the RED can be visualized through the relative power outputs from the GT and ST and the auxiliary consumptions within the proposed unit. A higher  $\delta$  at a higher  $T_{RED}$ , results in higher H<sub>2</sub> and CO yield, leading to a higher power output from the GT, the maximum being around 6.3 MW. On the other hand, a higher  $T_{RED}$  leads to greater heat availability and steam generation from MET-HX2, increasing the output from the ST as well. The power of the ST in only water cycle is lower due to reasons already discussed previously. The auxiliary power requirement is primarily due to the CO<sub>2</sub> recycle compressor and product gas compressors necessary prior to the combustor. Additional power needs for

ASU operation and pump work are, however, much smaller in the proposed plant design. Therefore, with the drop in the overall CO<sub>2</sub> recycled in the add-on unit, as well as for less product gas generated with a drop in the temperature of reduction, the auxiliary power requirement drops as well for a lower T<sub>RED</sub>. A combined effect is seen on the net power output from the system, whereby only around 4.5 MW of electric power output is achieved at a T<sub>RED</sub> of 1300°C irrespective of gas composition for the OXI. However, for a higher T<sub>RED</sub> resulting in greater solid conversion, together with a higher power requirement for hydrogen compression than CO compression, and a corresponding lower output from the ST, the net power output from the H<sub>2</sub>O only cycle is lower. At a T<sub>RED</sub> of 1600°C, thus, around 11.6 MW of electric power is obtained, compared to 12.8 MW from the CO<sub>2</sub> only cycle (Figure 3-19a).

Indeed, like the discussions and conclusion of the previous sensitivity analysis, the impact of T<sub>RED</sub> on the efficiency of the power plant is shown in Figure 3-19b. No notable change in the efficiency is seen for a cycle operating with only H<sub>2</sub>O, whereby the efficiency remains constant at around 24.2%. On the other hand, a maximum efficiency of 25.4% is obtained with only CO<sub>2</sub> and T<sub>RED</sub> of 1600°C, which becomes constant at 25% below a T<sub>RED</sub> of 1500°C.

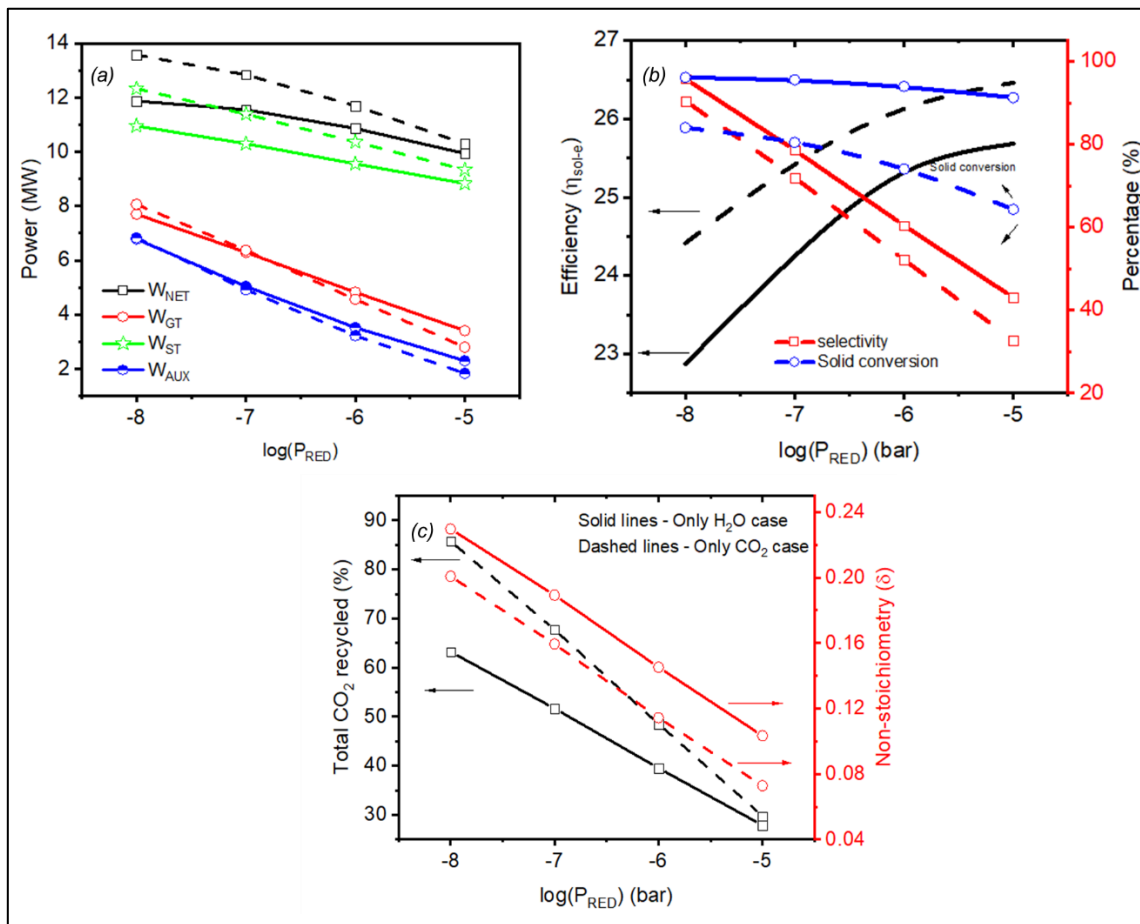


Figure 3-20 . Impact of the variation of the reduction vacuum pressure on the operating parameters of the proposed SCLP-OXY-CC add-on unit at a constant RED temperature of 1600°C, a constant molar flow rate of CeO<sub>2</sub> and gas of 275 mol/s and 66 mol/s respectively and a constant gas and metal oxide inlet temperature to the OXI of 800°C.

The impact of the variation of the reduction vacuum pressure is shown in the following Figure 3-20. Like the variation of the  $T_{RED}$ , a higher vacuum pressure increases the system yield significantly, in terms of the generated non-stoichiometry, as well as the selectivity for a constant molar flow of the gas to the OXI. As discussed before, due to a lower solid conversion in the OXI from  $CO_2$  splitting, the resulting  $\delta$  in the RED for the  $CO_2$  only cycle is lower by about an average of 0.03. The corresponding selectivity of CO is also lower by 5 to 10% compared to that of  $H_2$ , which varies between 95.8% to 43% at reduction vacuum pressure of  $10^{-8}$  and  $10^{-5}$  bar respectively.

A higher selectivity would hence imply a higher net  $CO_2$  recirculation within the add-on unit, which is indeed the case, as shown in Figure 3-20c. For lower vacuum conditions of the  $10^{-5}$  bar, the selectivity of the CO generated is lower, requiring around 10% of the total flow of  $CO_2$  to be recirculated in the combustor while maintaining the desired TIT. The net  $CO_2$  recycled was then 30% (20%  $CO_2$  being sent previously directly to the OXI). As for operating with  $H_2O$ , around 30% of  $CO_2$  is necessary to ensure the desired TIT with  $H_2$  combustion. Nonetheless, for higher vacuum pressures and with an increase in the selectivity, the overall  $CO_2$  circulated in the add-on unit increases, whereby a maximum recirculation of 85.7% is seen at a pressure of  $10^{-8}$  bar. The corresponding value at  $10^{-7}$  bar was 51.7% and 67.7% for working with only water and  $CO_2$  respectively.

Similar trends in the power generation from the GT and the ST, together with the auxiliary power requirement and the net power produced in the add-on unit as was previously seen by varying  $T_{RED}$ , is shown in Figure 3-20a. Besides all previous discussions, it is important to mention that a higher vacuum pressure, even though would ensure a higher reduction extent of ceria, and hence a higher selectivity, for a constant reactant gas molar flow, would also result in an increased auxiliary consumption from vacuum pumping. Also, the heat of reaction increases with reduction extent, requiring more heat to be supplied. These factors, therefore, offset the net gains of the productivity of OXI and hence an increased power output from the proposed layout at increased vacuum conditions of reduction. Thus, even though a decrease in the operating pressure of the RED from  $10^{-7}$  bar to  $10^{-8}$  bar operation would increase the  $W_{NET}$  by 0.3 to 0.7 MW (for  $H_2O$  and  $CO_2$  respectively), the net system efficiency drops by over 1% in both the cases (Figure 3-20b). Hence a trade-off in the reduction pressure with respect to system optimization is necessary for the proposed add-on unit.

The impact of the quantity of water and  $CO_2$  into the OXI for a constant ceria recirculation rate was performed subsequently. A reduction temperature of  $1600^\circ C$  with a metal and gas inlet temperature of  $800^\circ C$  was fixed. Indeed, interesting to note is the maximum flow of water that can be utilized within the plant without temperature cross-over. Though not shown explicitly in Figure 3-21, it can be understood that a maximum of around 42% of the available water (230 mol/s) could be utilized at the set temperature configuration of the system. This would allow scale-up of the system further.

Nevertheless, as can be seen from the Figure 3-21a, around 10% of the flow (55 mol/sec) corresponds to the stoichiometric amount of water necessary to oxidize the non-stoichiometry of Ceria. Below this, a sub-stoichiometric flow would cause an incomplete reaction in the

oxidation reactor, and hence significantly diminish the system effectiveness, as well as the efficiency. Beyond the stoichiometric flow (10% of H<sub>2</sub>O from the CCS unit), the selectivity of hydrogen drops due to stoichiometrically excess flow, however, without any significant benefit to the solid conversion, and hence subsequently, the reduction extent,  $\delta$ , of the oxidized metal (Figure 3-21a). By increasing the fraction of H<sub>2</sub>O to CL, a peak oxidized metal outlet temperature from the OXI ( $T_{OC\_OUT,OXI}$ ) of 1120°C at around stoichiometric flow rates. Indeed, it needs to be mentioned that unlike the sensitivity study, where a  $\delta$  of 0.35 was assumed at the OXI inlet, in the present layout, the  $\delta$  is 0.198. Hence, a much lower temperature of both the gas and the metal oxide from the outlet of the OXI is obtained. This considerably limits the overall performance of the CL unit while operating in a closed cycle. Nevertheless, at lower flow fraction of H<sub>2</sub>O, the product outlet temperature (both gas and metal) is lower due to unreacted metal, while at higher flow, the cooling from the excess gas flow, lowers the metal oxide outlet temperature. However, with a higher flow rate, due to be a counterflow reactor, a paradigm difference in the temperature of the gas outlet at the OXI is noticed, a rise in almost 150°C between before and after the stoichiometry flow respectively (Figure 3-21c).

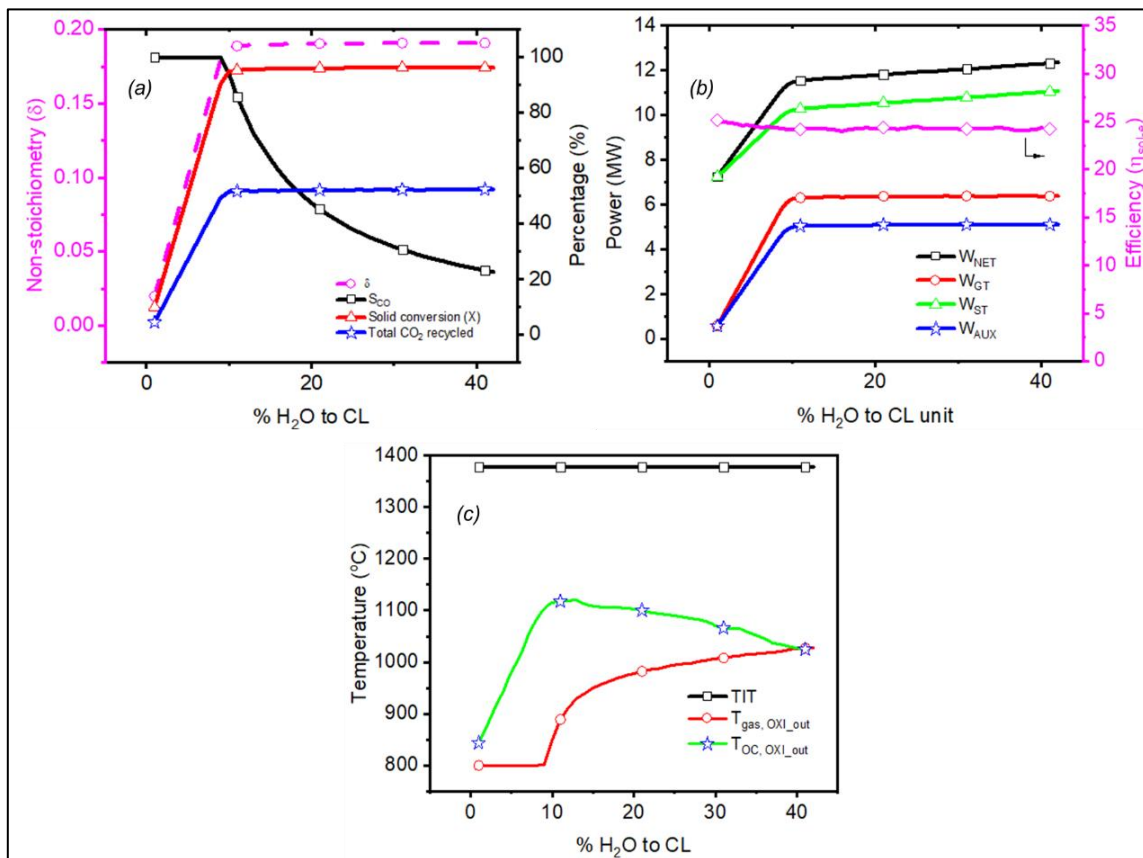


Figure 3-21 . Impact of the variation of the water flow rate (% H<sub>2</sub>O to CL) on the parameters of the proposed SCLP-OXY-CC unit working with only water at a constant molar flow rate of CeO<sub>2</sub> and water of 120 mol/s, a constant gas and metal inlet temperature of 800°C to the OXI and a constant reduction temperature and pressure of 1600°C and 10<sup>-7</sup> bar

Being limited by the molar flow of metal in the OXI for a constant molar flow of CeO<sub>2</sub>, the molar flow of hydrogen generated beyond 10% of H<sub>2</sub>O from CCS exhaust to the CL unit

becomes constant. The moisture being separated, this results in a constant molar flow of hydrogen and hence a constant GT power of 6.3 MW beyond 10% of H<sub>2</sub>O to CL in the proposed add-on SCLP-OXY-CC power plant. The TIT could also be maintained constantly at 1377°C, as can be followed from Figure 3-21c.

However, since a higher amount of steam is sent for splitting, a larger heat content in the gas from the OXI results in the generation of more steam from cooling a higher volume of gas, which subsequently increases the power output from the steam turbine. The auxiliary power need being almost constant (Notwithstanding the minimal power increase from pumping additional water), the net power output from the system increases up to 12.35 MW for an H<sub>2</sub>O to CL fraction of 0.42. Nevertheless, an increase in the heat requirement in RED from lowering the metal inlet temperature to the RED by passing excess steam in the OXI results in no net benefit to the system efficiency beyond 10% of H<sub>2</sub>O to CL. A maximum average system efficiency with water at the proposed operating conditions can hence be said to be 24.2% as seen in Figure 3-21b. Interesting to note, however, that such excess flows would often be limited to operating power cycles only, which do not require a high purity product gas from the OXI. For chemical processes like Fischer-Trops synthesis, the need for high purity product gas from the OXI. For chemical processes like Fischer-Trops synthesis, the need for high purity product gas would limit the excess of steam into the OXI reactor to around 5% excess to the stoichiometry and hence, a limit of the attainable system performance.

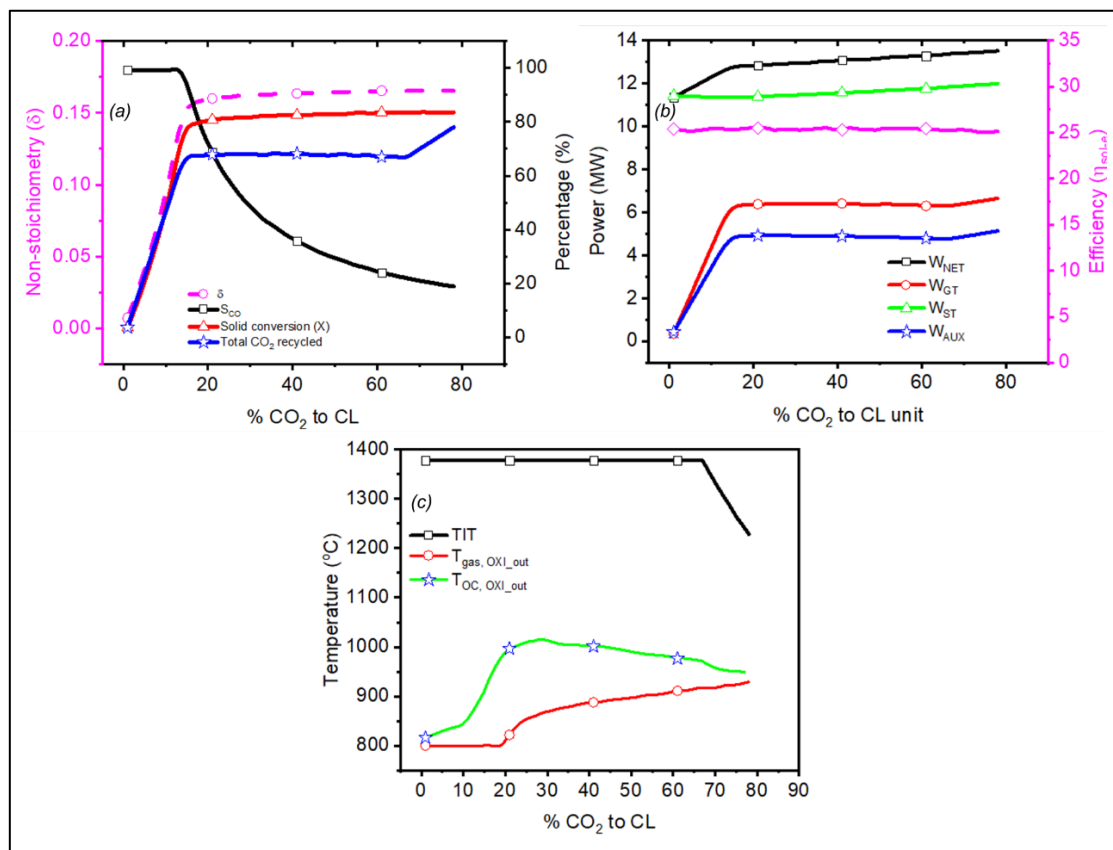


Figure 3-22 . Impact of the variation of the CO<sub>2</sub> flow rate (% CO<sub>2</sub> to CL) on the parameters of the proposed SCLP-OXY-CC unit working with only water at a constant molar flow rate of CeO<sub>2</sub> and water of 120 mol/s, a constant gas and metal inlet temperature of 800°C to the OXI and a constant reduction temperature and pressure of 1600°C and 10<sup>-7</sup> bar

On the other end, the impact of the variation of the CO<sub>2</sub> flow into the CL unit on the different system operating parameters, together with the individual outputs of the turbine, as well as the auxiliary power input to the system and the net system efficiency is plotted in Figure 3-22. The reduction temperature was fixed at 1600°C, together with the gas and reduced metal oxide inlet temperature to the OXI at 800°C. No temperature cross-over was noticed until a 78% recycling fraction of the CO<sub>2</sub> to the CL unit. This is since, unlike water, no phase change of CO<sub>2</sub> takes place, and hence the sensible heat required to heat up the CO<sub>2</sub> is much lower.

Similar profiles to that of only water splitting are observed in all the cases. At around 16.7% of the CO<sub>2</sub> fraction to the CL unit, which corresponds to the stoichiometric flow, a complete conversion of the gas (Figure 3-22a), together with a stable solid conversion of 83% is obtained. Being an exothermic reaction, this also results in the highest output temperature to the metal oxide from the OXI, around 1020°C, about 100°C lower than the maximum temperature achieved in water splitting. All the related arguments of obtaining a lower temperature are valid for CO<sub>2</sub> as well and hence not discussed separately. However, the gas outlet temperature rises gradually, being a counterflow reactor. However, no significant benefit is gained, since the metal oxide outlet temperature drops, signalling a higher thermal requirement in the reduction reactor. Due to a high conversion rate in the OXI for the gas at stoichiometry, the corresponding requirement of the CO<sub>2</sub> in the combustor for maintaining the TIT also peaks at 15% of CO<sub>2</sub> to CL unit, (not shown). With a further rise in the CO<sub>2</sub> fraction to CL, the selectivity starts to drop lower, and beyond 65%, the excess CO<sub>2</sub> in the product gas results in a drop in TIT without additional need of CO<sub>2</sub> to be recycled, as can be seen in Figure 3-22c.

Figure 3-22b shows the net power output, together with the outputs from the GT and the ST and auxiliary power requirements with the variation of the CO<sub>2</sub> flow to the splitting unit. As can be seen, after the 16% CO<sub>2</sub> from the CCS stream to CL, the GT power remains constant, since the total gas expanded is constant following previous arguments. However, with a higher flow of the CO<sub>2</sub> to the CL unit, and with a rise in temperature of the outlet gas from the OXI, as seen in Figure 3-22a, the net steam generation increases, resulting in the increase of the net power output from the system. Beyond the 65% of CO<sub>2</sub> to CL, the net gas compressed for the COMB increases to a limit that decreases the TIT. This results in a steady rise in the auxiliary power demand. Even though the TIT decreases, the gas turbine sees a slight increase in power output due to the expansion of a larger volume of gas. The ST power increases, however, at a lower rate, since the temperature of the GT exhaust decreases, even though the net volume of the gas flow increase. Combining all these factors, a linear increase in the net power output from the system is noticed beyond 65% fraction of the CO<sub>2</sub> to CL unit. However, due to the lowering in the metal oxide outlet temperature from the OXI, leading to an increased heat load in the RED, the net system efficiency remains unaffected throughout at around 25.4%, as can be seen in Figure 3-22b.

#### **3.5.4.2 Comparative Evaluation**

A comparative evaluation of the performance of the proposed SCLP-OXY-CC add-on unit by utilizing three different gas mixtures (only CO<sub>2</sub>, only H<sub>2</sub>O and 86% CO<sub>2</sub> and 14% H<sub>2</sub>O as

replication of the composition of an Oxyfuel NGCC exhaust) was performed, fixing the operating conditions, based on the above sensitivity analyses. The reduction reactor temperature and operating pressure were chosen as a 1600°C and  $10^{-7}$  bar, together with the metal oxide and gas inlet temperature to the OXI at 800°C. Since the primary aim of the proposed layout was power generation, the net molar flow of the gas was kept constant at 66 mol/s (equivalent to the utilization of 20% of CO<sub>2</sub>). With regards to the product gas, no limit to the purity of the gas produced in the OXI is necessary as it will be fed to the combustor for power generation.

Table 3-4 Comparative performance evaluation of the proposed SCLP-OXY-CC, add-on unit with varying gas compositions to the OXI at equivalent operating conditions of 1600°C and  $10^{-7}$  bar reduction temperature and pressure respectively, metal and gas inlet temperature to the OXI of 800°C, 275 mol/s flow of CeO<sub>2</sub> and gas flow to the OXI of 66 mol/s

Plant data	Units	Only CO <sub>2</sub>	86% CO <sub>2</sub> , 14% H <sub>2</sub> O	Only H <sub>2</sub> O
Solar Energy Input (A)	MWth	33.72	31.76	31.81
Net GT Output	MWe	6.30	6.30	6.30
ST Output	MWe	11.380	10.512	10.30
Gross Electric Power Output (B)	MWe	17.68	16.812	16.596
ASU Consumption + O <sub>2</sub> compression	MWe	0.024	0.024	0.024
Recycled CO <sub>2</sub> Compression	MWe	1.754	1.659	1.877
Compressor/ Pump Work for OXI Feed	MWe	0.324	0.319	0.353
Power Cycle Pumps	MWe	0.130	0.119	0.117
Syngas Compressors	MWe	0.562	0.552	0.455
Vacuum Pump	MWe	2.033	1.997	2.216
Total Auxiliary Power Consumption (C)	MWe	4.827	4.67	5.041
Net Electrical Power Output (D=B-C)	MWe	12.853	12.142	11.555
Gross Electrical Efficiency (B/A*100)	%	52.43%	52.93%	52.17%
Net Electrical Efficiency (excluding solar field and receiver efficiency) (D/A*100)	%	38.12%	38.23%	36.32%
Net System Efficiency (Solar to Electricity)	%	25.44%	25.52%	24.25%
Non-Stoichiometry yield		0.1652	0.1706	0.1893
Metal oxide Inlet Temperature to RED	°C	1006.17	1032.26	1121.36
Gas Selectivity	%	0.719	NA	0.786
Metal oxide Conversion in the OXI	%	80.43	86.09	95.53

The above Table 3-4 lists the comparative plant performance of the proposed SCLP-OXY-CC add-on unit with the three different gas mixtures discussed above. As can be observed, working with only water forms the lower bound to the system performance, while that with CO<sub>2</sub> provides the upper bound to the system performance in terms of the solar to electricity efficiency of the proposed add-on unit.

Indeed, following previous discussions, even though the power generated in the gas turbine is almost constant irrespective of the gas composition, the steam turbine output decreases significantly with increased water content in the gas mixture to the OXI. Additionally, a higher vacuum pumping power is necessary due to a higher yield of non-stoichiometry for H<sub>2</sub>O splitting, which significantly increases the overall auxiliary power requirement as well. Even though this results in a higher yield of product from the system, indicated by a higher non-stoichiometry obtained by working with only water, as compared to working with CO<sub>2</sub>/ CO<sub>2</sub>-H<sub>2</sub>O mixture. Furthermore, a higher temperature solid outlet temperature from water splitting would result in the net heat required for reduction to decrease, which is a significant benefit of increasing the amount of water in the gas mixture to the OXI. Also, the solid conversion increases significantly with the increase in water content of the mixture, whereby, even with 14% water content, a 5.5% increase in the solid conversion is noticed, while the corresponding increase is 15% between working with only CO<sub>2</sub> and only H<sub>2</sub>O.

Indeed, a maximum thermal efficiency of 38.12% of the proposed layout is obtained while working with only CO<sub>2</sub> splitting. This also provides simplest of configurations, without the need of HRSG for steam generation for splitting and additional condensers for water removal from different streams of the power plant. Nevertheless, the overall solar-to-electricity efficiency drops to 25.4% due to the efficiency penalties arising from the solar field losses and losses in the receiver, which, in fact, is the heat inlet to the reduction reactor. The maximum net electricity yield of 12.9 MW is obtained correspondingly.

Table 3-5 Comparative performance evaluation of the proposed CL unit of the proposed SCLP-OXY-CC with varying gas composition to the OXI at equivalent operating conditions of 1600°C and 10<sup>-7</sup> bar reduction temperature and pressure respectively, metal and gas inlet temperature to the OXI of 800°C, 275 mol/s flow of CeO<sub>2</sub> and gas flow to the OXI of 66 mol/s

Description	Only CO <sub>2</sub>	86% CO <sub>2</sub> , 14% H <sub>2</sub> O	Only H <sub>2</sub> O
Solar Energy Input (A)	33.72	31.76	31.81
H <sub>2</sub> Flow (mol/s)	0	8.946	51.812
CO Flow (mol/s)	47.469	37.955	0
Energy yield rate (MW)	13.481	12.855	12.02
Vacuum pump work in RED (MW)	2.033	1.997	2.216
Heat Need for CO <sub>2</sub> /H <sub>2</sub> O Heating (MW)	2.329	2.7	4.947
Efficiency of CL Unit ( $\eta_{SCL}$ )	35.41%	35.26%	30.84%

In addition to evaluation of the solar to electricity efficiency of the entire layout, the efficiency of the CL unit alone is also of interest. The corresponding evaluation results are shown in the

following Table 3-5. As can be seen, at similar operating conditions, due to a higher metal oxide inlet temperature to the RED, the solar energy input for operating with only water is the minimum. However, due to latent heat requirement in heating water, the heat need for the water heating is significantly higher than the corresponding for CO<sub>2</sub>, by more than 2.5 MW. In addition, a higher  $\delta$  with water results in an increased requirement of vacuum pump work to maintain the necessary vacuum pressure in the reduction reactor. Thus, like the trend of results obtained for the overall plant efficiency, the efficiency of the CL unit decreases proportionally with increased water content in the gas mixture to the OXI as well. A maximum CL unit efficiency without considering heat recuperation is therefore obtained as 35.4% while working with only CO<sub>2</sub>.

### **3.5.5 Comments and Discussions**

In this section a comprehensive evaluation of the proposed SCLP-OXY-CC add-on unit as performed with not only varying multiple operating conditions but also the gas composition to the OXI. Based on such analyses, operation strategies and concerns with two extreme mixture compositions (only CO<sub>2</sub> and only H<sub>2</sub>O) have been described and evaluated. The net efficiency obtained was found to vary between 24.5% and 25.7%. This can however, be sought to be increased via further system optimization. The net power generated was correspondingly found to be between 11.5 and 12.9 MW with the add-on unit. Considering the solar energy to be free, the power generation from the combined 100MW CCS and the SCLP-OXY-CC add-on unit would result in a maximum net system efficiency of about 49.72%, a 5.7% rise to the original efficiency of 44% of the Oxyfuel with CCS unit, as described above. Besides, the variability in the power output, without a significant drop in the system efficiency would aid flexible operations with the necessary control system. However, a significant drop in the power output at low reduction reactor temperature would often limit the operation of the cycle throughout the day without integrating adequate storage. This becomes increasingly more a significant, since at start-up conditions, occurring every day, a temperature of 1600°C could seldom be reached. This would, therefore, limit the system performance to achieve its maximum potential only during a few hours around mid-day. Thus, a further complex system design with the integration of storage would be necessary for the resilient operation of the proposed layout and would form part of future work.

### **3.6 Conclusions**

In this chapter, a comprehensive model was developed in ASPEN Plus to simulate the chemical looping syngas fuel generation from water and carbon dioxide splitting in a dual moving bed reactor with redox cycling through metal oxides. An extensive FORTRAN subroutine was developed and hooked into ASPEN Plus to appropriately model the complexities of the reaction kinetics and the two-phase flow within the reactors. The entire set-up was evaluated considering industrial scale applications and hence generation of 100 mol/s of syngas fuel. An isothermal reduction reactor and an adiabatic oxidation reactor model was developed and evaluated. The sensitivity of the reduction reactor was performed by varying the temperature

and pressure between 1200-1600°C and  $10^{-3}$  and  $10^{-7}$  bar respectively. Close agreement with experimental data in literature was obtained. A maximum reduction non-stoichiometry of 0.1982 was obtained in the reduction reactor at 1600°C and  $10^{-7}$  bar pressure. The residence time was around 1.5 minutes, an increase in residence time will not yield any further benefit due to a faster backward reaction rate of recombination of the released oxygen in redactor reactor. For the oxidation reactor, system parametric sensitivity was studied considering maximum non-stoichiometry extent achievable for ceria of 0.35, as reported in the literature. The volume of the oxidation reactor to achieve an over 90% conversion of the reduced metal oxide was 8 times higher to the volume of the reduction reactor. The impact of the variation of the gas inlet temperature was found to be minimal, while an increase in the metal oxide inlet temperature would significantly increase the solid conversion and selectivity of the generated syngas fuel. A faster water splitting kinetics would result in not only a higher solid conversion and selectivity but also result in a higher product outlet temperature due to higher exothermicity. Indeed, a relatively substantial increase in the yields from the oxidation reactor with 25% water in the gas mixture is noticed than while working with pure CO<sub>2</sub>. Nevertheless, similar selectivity from co-splitting of CO<sub>2</sub> and H<sub>2</sub>O would allow generating the H<sub>2</sub>/CO ratio similar to the input H<sub>2</sub>O/CO<sub>2</sub> ratio, a major benefit of the moving bed reactor system. A large temperature variation long the length of the adiabatic oxidation reactor is also noticed, which would thus require further reaction design optimization of the moving bed oxidation reactor for CO<sub>2</sub> and/or H<sub>2</sub>O splitting. This gives the motivation to further investigate the reactor model as a chemical looping syngas production unit as an add-on unit to the power plant and investigate the efficiency of the system.

The CL unit model was then integrated to a proposed power plant layout to be implemented as an add-on unit to an existing Oxyfuel power plant with CCS. Retrofitting a 100 MW Oxyfuel NGCC was thus evaluated with multiple sensitivity studies varying different operating parameters and composition of the gas to the oxidation reactor of the CL unit. Utilizing 20% of the CO<sub>2</sub> generated for CCS, a maximum of 12.85 MW of electricity can be generated, which can be improved subject to system optimization. A maximum solar to electricity efficiency of 25.4% was obtained while working with CO<sub>2</sub> only and operating the reduction reactor at 1600°C and  $10^{-7}$  bar vacuum pressure. The oxidation reactor was operated at 2 bar pressure. Considerable variation in the output of the system is noticed with the variation of the reduction temperature, which would often limit the steady operation of the system to only a few hours of the day without storage.

## 4 Thermodynamic Analysis of the Chemical Looping Cycle with Methane reduction of Ceria

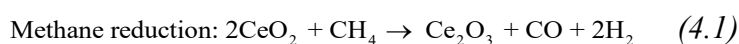
As obtained from the previous analyses, even though technologically attractive, multiple practical limitations exist for the solar thermochemical cycle for CO<sub>2</sub>/H<sub>2</sub>O splitting. Especially restrictive are the need for a high temperature of reduction and a very high vacuum conditions, indicating a high temperature and pressure swing between the two reactors. This is considerably limiting to the flexible operation of the system, as well as increasing its complexity by requiring additional components like the vacuum pump, heat recuperators, etc. Additionally, the variation of output with the available solar flux throughout the day is of considerable concern to the stable output from the system. In this regard, the use of methane as the reducing agent can be considered as an interesting alternative.

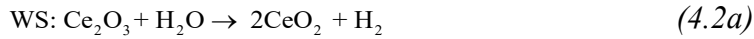
This chapter therefore has been focused to study the thermodynamic performance of methane reduction of ceria with subsequent oxidation of the reduced metal. Since a thermodynamic study has been considered, this would provide the maximum yield from an idealistic performance from the proposed metal oxide, in the present case, Ceria.

### 4.1 Introduction

Unlike iron oxide, which has received wide attention for thermodynamic analysis for redox chemical looping cycles [41,156,157], that for ceria is limited in literature, especially for methane reduction. Bader et. al [158] reported a thermodynamic analysis of isothermal redox cycling of ceria at 1773K, achieving efficiencies of up to 10% and 18% for hydrogen and carbon monoxide production, respectively. The efficiencies were considerably improved to over 30% for hydrogen production by introducing a temperature swing of 150 K between the reduction and the oxidation reactors. Practical investigation for non-stoichiometric ceria cycle by Furler et al. [159] in a thermally driven cycle reported much lower solar-to-fuel energy conversion efficiency using sweep inert gas as 1.73% with peak achieved as 3.53%. In order to improve the system with respect to the scale and efficiency, a moving packed bed of reactive particle reactors have been employed to investigate and analyse the efficiency [129]. Indeed, the scope for increasing the energy efficiency through multiple processes including heat recovery was suggested, enabling the conversion efficiency of solar energy into H<sub>2</sub> and CO at the design point to exceed 30%.

In the present study, thermodynamic analysis for stoichiometric reduction of ceria for maximum redox pair utilization was performed. Accordingly, the redox pair considered was CeO<sub>2</sub>/Ce<sub>2</sub>O<sub>3</sub> with a reduction in the presence of methane, as described by the equations (4.1-4.2).





In the reduction reactor, the methane reduces the metal oxide at a higher oxidation state ( $\text{CeO}_2$ ) to a lower completely oxidation state ( $\text{Ce}_2\text{O}_3$ ), while itself getting oxidized to  $\text{CO}$  and  $\text{H}_2$  via reaction (4.2). The reduced ceria oxide is then recycled back to the higher oxidation state through reactions (4.2a) and (4.2b). In both the reactors, syngas can be generated, however, with varying  $\text{H}_2/\text{CO}$  fractions. While, from thermodynamic and mass conservation conditions, the  $\text{H}_2$  to  $\text{CO}$  ratio of the syngas from the reduction reactor is mostly 2:1, the ratio in the oxidation reactor can be varied based on the inlet gas feed mixture, and other thermodynamic parameters.

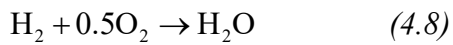
Multiple studies, mostly based on iron oxide-based redox metal pairs have reported the conversion efficiencies and operating conditions for conversion of methane into syngas over metal oxides [160–162]. Such studies also include the limiting operation range based on the need to prevent carbon deposition reactions as crucial for the system operation. Thermodynamics of Ceria reduction with hydrogen have been investigated to explore the maximum extent of reaction and reported in the literature [163]. Solar-driven thermal reduction for ceria coupled with either  $\text{CO}_2$  or  $\text{H}_2\text{O}$  splitting has been studied extensively by Welte [89,164] and other researchers [19,158]. However, limited literature on the thermodynamic assessment regarding methane reduction of ceria followed by splitting of waste gas (a mixture of  $\text{CO}_2$  and  $\text{H}_2\text{O}$ ) is available [27]. Additionally, the need to identify the regimes for carbon formation is crucial to identify the suitable operation regimes of the reaction system further.

Within the reduction reactor, carbon deposition, through Boudouard reaction (4.3) and methane dissociation mechanisms (4.4) is important. This carbon is subsequently transported into the oxidation reactor along with the reduced ceria. Within the oxidation reactor, even though the carbon does not directly inhibit any reaction, it forms its own set of reaction towards syngas production with  $\text{H}_2\text{O}$  (Water Gas Reaction) and  $\text{CO}_2$  (Reverse Boudouard Reaction) as given by reactions (4.5) and (4.6) respectively. Therefore, the presence of carbon results in competitive reactions against the reduced metal oxide for the subsequent oxidation, which would cause the metal oxide to remain at a reduced state, while the solid carbon takes preference in oxidation. This would become more critical under a stoichiometric quantity of reactants, lowering the utilization of the metal oxide.

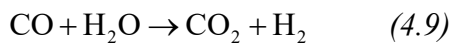


Besides carbon formation, the oxygen released from the reduced metal in the reduction reactor has the potential to react with the produced  $\text{CO}$  and  $\text{H}_2$  to form  $\text{CO}_2$  and water and respectively at suitable thermodynamic conditions, as per the equations (4.7) and (4.8). This would

considerably reduce the effectiveness of the entire system by lowering the calorific value of the syngas produced in the reduction reactor, thereby decreasing the system efficiency.



Based on the present chemical components, the water gas shift reaction (4.9) and the methane reformation reaction (4.10) can also occur. However, the thermodynamic and chemical conditions would render such reactions unfavourable from being primary contributors to system thermodynamics.



Therefore, the aim of the present study is to perform thermodynamic and process simulation studies to obtain the ideal operating conditions, close to equilibrium, avoiding carbon deposition, of the  $\text{CeO}_2/\text{Ce}_2\text{O}_3$  redox pair chemical looping syngas production via methane reduction. The analysis has been performed by evaluating the thermodynamic equilibrium composition of the reaction system, the impact of the reactant feed molar ratios and temperature on the product compositions for the reduction and oxidation reactors, respectively. Furthermore, the system efficiency regarding the redox cycle performance was assessed

## 4.2 Thermodynamics method

The thermodynamic simulation of methane reduction and water and  $\text{CO}_2$  splitting was performed in ASPEN Plus®.

Gibbs free energy minimization principle (GFEM) was used to perform the thermodynamic calculations. For a reaction system, where multiple simultaneous reactions take place, equilibrium calculations are often performed through the GFEM approach, details of which can be found in the literature [165,166]. For the complete set of reactors and components modelled, the gaseous species included were:  $\text{CH}_4$ ,  $\text{CO}$ ,  $\text{CO}_2$ ,  $\text{H}_2$ , and  $\text{H}_2\text{O}$ ; while the solid species were:  $\text{C}$ ,  $\text{Ce}_2\text{O}_3$ , and  $\text{CeO}_2$ .

The process layout of the simulation system is shown in Figure 4-1. The ASPEN Plus® RGIBBS reactor model was used to simulate both the reduction and oxidation reactors, using the Peng Robinson equation of state. Within the RGIBBS reactor, the equilibrium composition of all feasible combination of reactions within the thermodynamic domain was considered. The RGIBBS reactor calculates the most stable phase combination obtained through chemical reactions where the Gibbs free energy of the reaction system reaches its minimum at a fixed mass balance, constant pressure, and temperature. Besides the RGIBBS module, the other components simulated were cyclone units to separate solid and gas streams, and heat exchangers, in which streams are preheated to reach the temperatures of reaction and heat is removed from the reaction products.

For the reduction reactor, the temperature was varied in the range of 500-1000°C, at a constant pressure of 1 atm. The CH<sub>4</sub>/CeO<sub>2</sub> feed molar ratio was varied from 0.4 (sub-stoichiometric value according to reaction (4.1)) to 4. The solid product of the reduction reactor was fed to the oxidation reactor after cyclone separator. The oxidation reactor was modelled by a series of two RGIBBS reactor. The oxidation of CO<sub>2</sub> and H<sub>2</sub>O over Ce<sub>2</sub>O<sub>3</sub> is a highly exothermic reaction. Therefore, two reactors with an intercooler were modelled to simulate an ideal isothermal reactor. The first reactor was modelled as an adiabatic reactor, while the second reactor was an isothermal reactor, set at the temperature of the reaction. In the oxidation reactor, the Ce<sub>2</sub>O<sub>3</sub> was reacted with a mixture of steam and carbon dioxide according to reactions (4.2a) and (4.2b). Similar to the reduction reactor, the oxidation reactor temperature was varied between 500-1000°C at a constant pressure of 1 atm. The feed flow of the mixture was varied between the range of 0.5 to 2 kmol/h (stoichiometric to excess flow). The study corresponding to the oxidation reactor was performed to obtain the quantitative H<sub>2</sub> and CO produced at multiple regimes and hence identify the conditions of operations for different H<sub>2</sub>/CO ratio requirements for subsequent downstream processes. Additionally, determination of the minimum amount of gas flow and the corresponding composition to regenerate completely the reduced ceria was also aimed for within the regime of favourable reaction thermodynamics. However, it should be noted that, in the present study, all the simulation calculations performed were based on theoretical thermodynamic considerations, since no heat and mass diffusional limitations along with kinetics effects were considered for the conformation to the present thermodynamic analysis. This corresponds to the theoretical limits that must be considered during further experimental evaluations of the reaction systems.

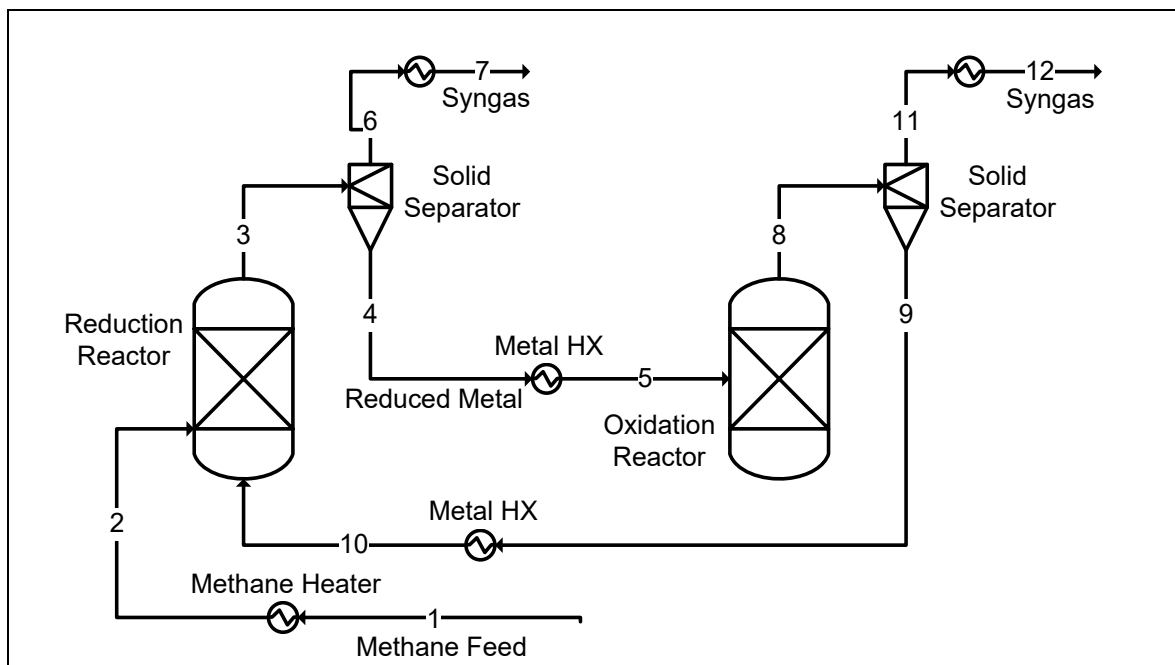


Figure 4-1 Process simulation flowsheet of interconnected reduction and oxidation reactors.

## 4.3 Results and discussion

### 4.3.1 Reduction reactor

The equilibrium composition of  $\text{H}_2$ ,  $\text{CO}$ ,  $\text{CO}_2$ ,  $\text{H}_2\text{O}$ ,  $\text{O}_2$  and  $\text{CH}_4$  and  $\text{C}$ ,  $\text{CeO}_2$  and,  $\text{Ce}_2\text{O}_3$  obtained from the reduction of methane over  $\text{CeO}_2$  in a temperature range of 500 to 1000°C and  $\text{CH}_4/\text{CeO}_2$  feed molar ratios from 0.4 to 4 are discussed in the following section.

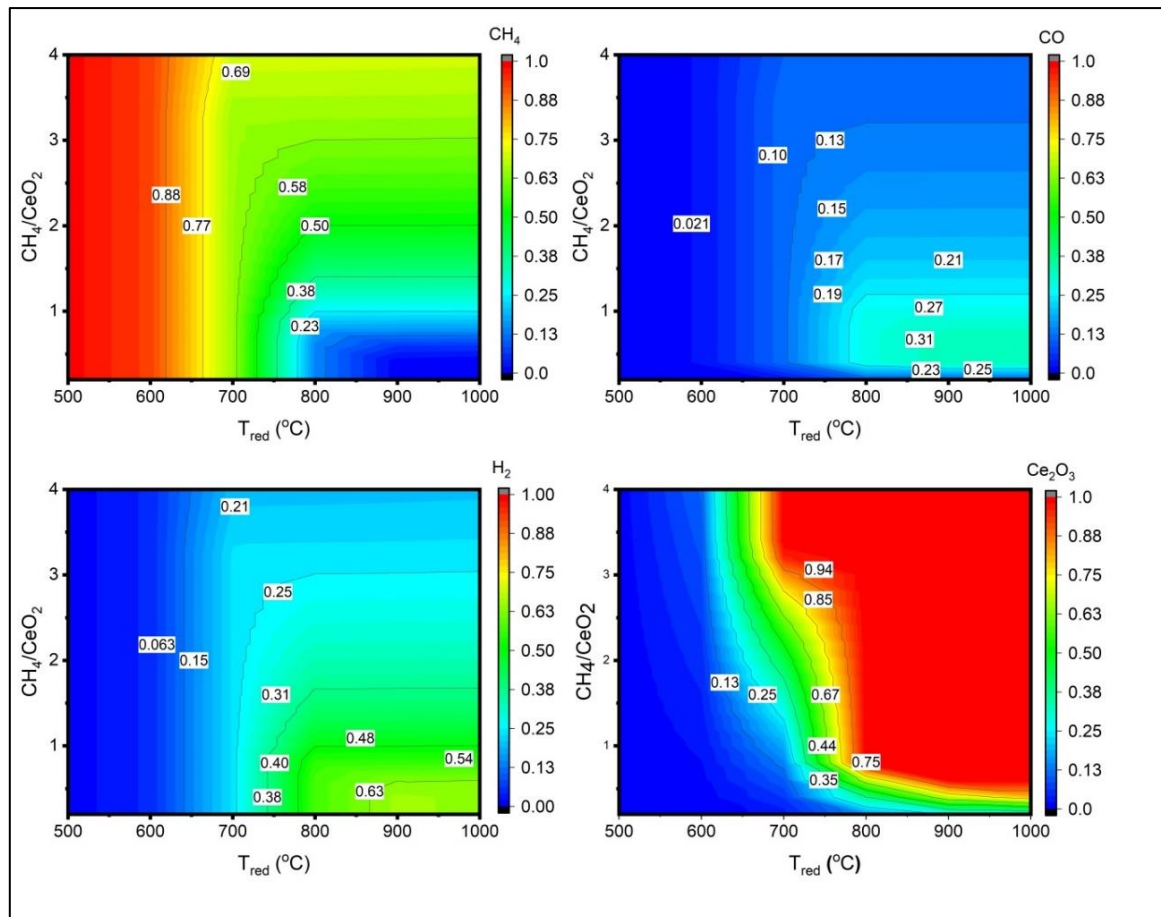


Figure 4-2 Impact of the variation of the  $\text{CH}_4/\text{CeO}_2$  ratio and temperature on the yield of the following chemical species as molar fractions of outlet streams within the reduction reactor: a) unreacted methane; b)  $\text{CO}$ ; c)  $\text{H}_2$ ; d)  $\text{Ce}_2\text{O}_3$  (solids)

Figure 4-2 shows the equilibrium production of  $\text{H}_2$  and  $\text{CO}$  within the reduction reactor (dry basis) as the molar fraction of the outlet product gas stream with respect to temperature and  $\text{CH}_4/\text{CeO}_2$  feed molar ratio, together with the methane molar fraction at the outlet of the reactor. Oxygen, being always present as trace gases were not depicted separately. Additionally, the reduced  $\text{CeO}_2$  as a solid fraction is also plotted with respect to the mentioned conditions, as shown in Figure 4-2(d). Within the conditions investigated, the methane reduction reaction initiates over 600°C. Lower methane to ceria ratios yielded lower products than higher feed ratios at same temperatures. At stoichiometric conditions, that is with 0.5 mole  $\text{CH}_4$  per mole of  $\text{CeO}_2$ , 50% of  $\text{CeO}_2$  conversion occurs around 800°C, while the reaction yielded 99.9%

conversion at temperatures over 900°C. This can be attributed to the intrinsic reactivity of solid CeO<sub>2</sub> with respect to the gaseous fuel, methane, and availability of the metal oxide lattice oxygen into the gas phase for partial oxidation reactions. At lower temperatures (500 to 600°C) and for a lower CH<sub>4</sub>/CeO<sub>2</sub> feed ratio (below 0.5), the availability of oxygen and temperature is limited to drive the reaction towards the production of syngas (CO + H<sub>2</sub>), resulting in the metal oxide to be poorly active for reaction (4.1). In any case, even with higher CH<sub>4</sub>/CeO<sub>2</sub> feed ratio, the complete reaction occurs at temperatures over 700°C, providing a thermodynamic limit to the reduction temperature of pure CeO<sub>2</sub> over methane.

Nevertheless, as can be visualized from Figure 4-2, an operation with 0.7 to 0.8 mole of CH<sub>4</sub> per mole of CeO<sub>2</sub> at around 900-950°C would provide the ideal operating conditions with respect to methane utilization, without the need to feed a high fraction of methane. A syngas stream of 31% CO and 63% H<sub>2</sub> can be obtained (balance 1% H<sub>2</sub>O, 0.4% CO<sub>2</sub> and 4.6% CH<sub>4</sub>) at around 950°C and a CH<sub>4</sub>/CeO<sub>2</sub> feed ratio of 0.7 to 0.8. Indeed, for higher methane flows, the excess methane at the outlet of the reduction reactor would decrease the effectiveness of the chemical looping system.

Figure 4-3 shows the molar fraction of unwanted chemical species in the outlet gas of the reduction reactor, produced within the studied conditions, namely elementary carbon, CO<sub>2</sub> and H<sub>2</sub>O resulting from the reactions (4.3-4.4) and (4.7-4.8), occurring alongside the primary reaction, namely (4.1). It can be observed that, at a higher temperature, and especially at the content of methane, there is a considerable increase in CO<sub>2</sub> formation. A similar trend is observed for H<sub>2</sub>O formation, even though the yield of H<sub>2</sub>O is considerably higher than CO<sub>2</sub>, at corresponding temperature and pressure. Together, they make up about 4% of the product gas flow for near stoichiometric operations. The primary reason for the initiation of reactions (4.7) and (4.8) can be attributed to the lower availability of methane for reaction at higher temperatures. The oxygen released from the metal lattice reacts instead with the produced CO and H<sub>2</sub> to oxidize them further into CO<sub>2</sub> and H<sub>2</sub>O.

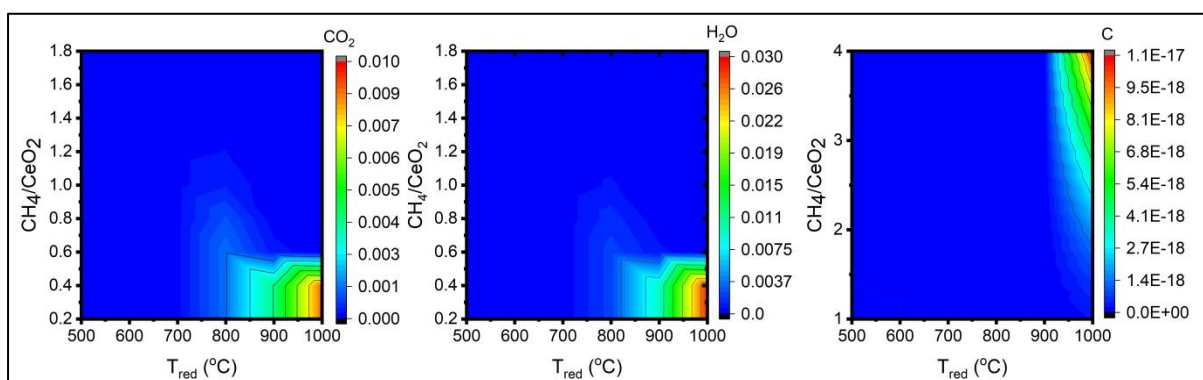


Figure 4-3 Impact of the variation of the CH<sub>4</sub>/CeO<sub>2</sub> ratio and temperature on the yield of the following unwanted chemical species as molar fraction of the outlet product streams within the reduction reactor: a) CO<sub>2</sub>; b) H<sub>2</sub>O; c) elementary carbon (solids)

It can be observed from that the carbon formation starts at temperatures over 900°C and higher feed ratios. As indicated in Figure 4-3 (c), the carbon deposition initiates at methane to ceria feed ratios above 1.0, and subsequently increases with higher molar flows of methane and temperature. This is because the thermodynamics for either the Boudouard and/or the methane decomposition reactions (4.3 and 4.4) are not favourable at other conditions. As discussed before, the production of carbon in the reduction reactor has considerable influence on the system efficiency due to competitive reactions with Ce<sub>2</sub>O<sub>3</sub> in the oxidation reactor. Even though the fraction of carbon content is exceedingly low, this would restrict the working conditions with methane reduction to around 900°C, and the molar feed ratio, to around 1.0. These results agree well with experimental results reported by Welte et al. [28].

Combining all factors, as discussed above, it can be concluded that favourable operating zone of the reduction reactor must be limited to around 900-950°C with 0.7-0.8 mole of CH<sub>4</sub> per mole of CeO<sub>2</sub> to ensure complete reduction of CeO<sub>2</sub>, without the need of high methane content and avoiding unwanted reactions from taking place. Moreover, in this operating range the syngas obtained has the desired ratio of H<sub>2</sub>/CO equal to 2, as shown in Figure 4-4. Hence, in the subsequent analysis of system efficiency and sensitivity studies, the regime of over 900-950°C was used for the reduction reactor to evaluate the system performance.

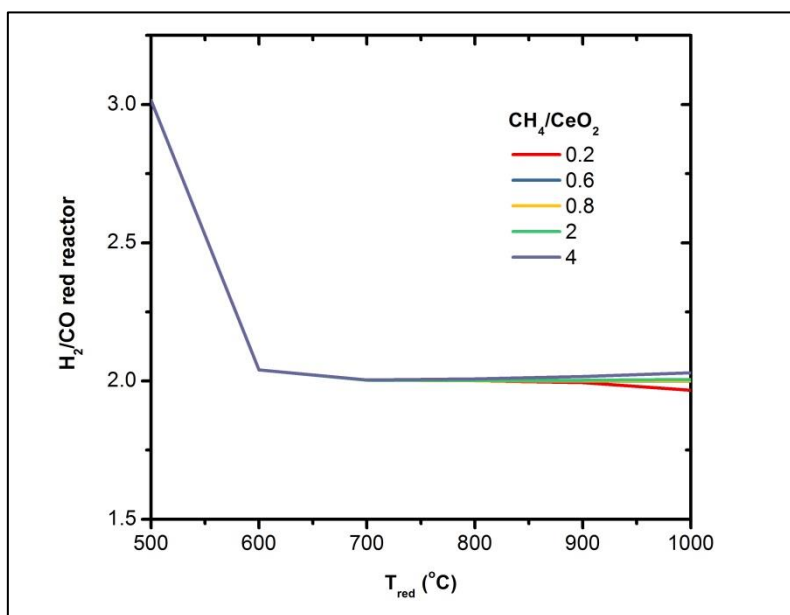


Figure 4-4 H<sub>2</sub>/CO ratio at the exit of the reduction reactor for different reduction temperatures for various CH<sub>4</sub>/CeO<sub>2</sub>

#### 4.3.2 Oxidation reactor

The equilibrium amounts of H<sub>2</sub> and CO obtained by splitting CO<sub>2</sub> and H<sub>2</sub>O over reduced Ce<sub>2</sub>O<sub>3</sub> within the oxidation reactor is presented in the following section. The parametric study was carried out within a temperature range of 500 to 1000°C, considering completely reduced Ceria (Ce<sub>2</sub>O<sub>3</sub>) being fed into the oxidation reactor. A variation of H<sub>2</sub>O/CO<sub>2</sub> mixture composition (from 5% to 95% CO<sub>2</sub>) and the molar flow rate of the mixture from 0.5 to 2 kmol/hr was also

performed. In all the cases the flow of  $\text{Ce}_2\text{O}_3$  was kept constant at 0.5 kmol/hr, is considered to be completely reduced from 1 kmol/hr of  $\text{CeO}_2$  in the reduction reactor as per reaction (3).

For the base case study, an equimolar mixture between  $\text{H}_2\text{O}$  and  $\text{CO}_2$  was fed into the oxidation reactor at varying feed rates and temperatures. Figure 4-5 (a) and (b) presents results from the oxidation reactor at the described conditions as the mole fraction of the products in the outlet gas stream from the reactor. It is observed that the hydrogen production was obtained as a function of temperature and the feed molar flow to the reactor. Therefore, the region of maximum hydrogen production can be identified, varying between 600 to 700°C, depending on the molar feed flow rate. With higher feed flow rate, the peak of hydrogen shifts towards a lower temperature. More specifically, for a waste gas flow rate of 1 kmol/hr, for an equimolar mixture between  $\text{CO}_2$  and  $\text{H}_2\text{O}$ , with each 0.5 kmol/hr, the peak hydrogen production occurs around 650°C, which shifts to 600°C with an increase of the molar feed rate of 2 kmol/hr.

On the other hand, the CO yield increases at a higher rate till around 650 °C, after which the rate of increase of CO yield drops considerably. Higher the flow of the waste gas, lower is the difference in the rate of yield increase between the two temperature ranges (below and above 650 °C). For molar flows higher than stoichiometry (0.5 kmol/hr), the yield becomes stable at about 0.28 kmol/hr with a further rise in temperature irrespective of the increase in molar feed flow.

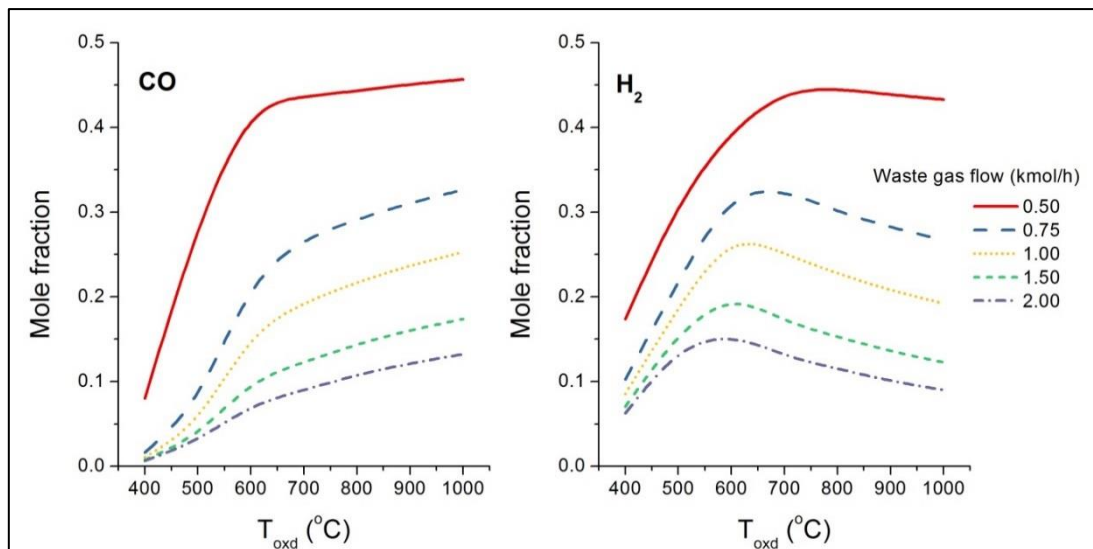


Figure 4-5 Impact of the variation of the waste gas (equimolar mixture of  $\text{CO}_2$  and  $\text{H}_2\text{O}$ ) flow rate and temperature on the yield of the a) CO and b)  $\text{H}_2$  as the mole fraction of the product gas of the oxidation reactor

The yield variations based on the thermodynamic conditions play a critical role in varying  $\text{H}_2/\text{CO}$  ratio obtained at the outlet of the oxidation reactor, which therefore can be controlled to obtain the  $\text{H}_2/\text{CO}$  ratios required for specific processes. Combining the yields of the two gases, for the stoichiometric flow of waste gas (1 kmol/hr and equimolar mixture), a syngas stream of 45%  $\text{H}_2$  and above 40% CO could be obtained. The remaining fraction of the gas is composed of un-reacted species. However, sending above-stoichiometric flows, even though

would result in complete oxidation of  $Ce_2O_3$  and providing maximum yield, would result in syngas fraction to drop considerably. This would decrease the effectiveness of the process by requiring additional downstream processes to separate  $CO_2$  and water for obtaining pure syngas.

The  $H_2$  and  $CO$  results can be combined to obtain the  $H_2/CO$  ratios at the outlet of the oxidation reactor with varying molar feed flows of the equimolar mixture of  $H_2O$  and  $CO_2$  as presented in Figure 4-6 (a). At lower temperatures, the formation of  $H_2$  is thermodynamically favourable over that of  $CO$ . Additionally, with an increase in molar feed rate, the preferential splitting of water over carbon dioxide increases the  $H_2/CO$  ratio further at lower temperatures. The  $H_2/CO$  ratio decreases considerably with an increase of temperature to around a constant 0.6 at  $1000^\circ C$ , irrespective of the waste gas feed flow, as  $H_2$  formation peaks around  $600-650^\circ C$ , while there is no specific peak for  $CO$  formation that constantly increases with the temperature. Also, interestingly, at a lower flow of  $0.5$  kmol/hr of the waste gas, when neither of the chemical species can completely oxidize the reduced metal, the  $H_2/CO$  ratio remains constant at around 0.6 irrespective of the temperature variation. This can be concluded from the fact that the  $H_2O$  and  $CO_2$  split can then occur simultaneously since the individual gases are lower than the stoichiometric quantity necessary to oxidize the reduced metal by themselves as per reaction (4.2). However, it needs to be kept in mind that the complete oxidation of the  $Ce_2O_3$  to  $CeO_2$  was ensured within the defined conditions, and the produced  $CeO_2$  was recirculated back to the reduction reactor.

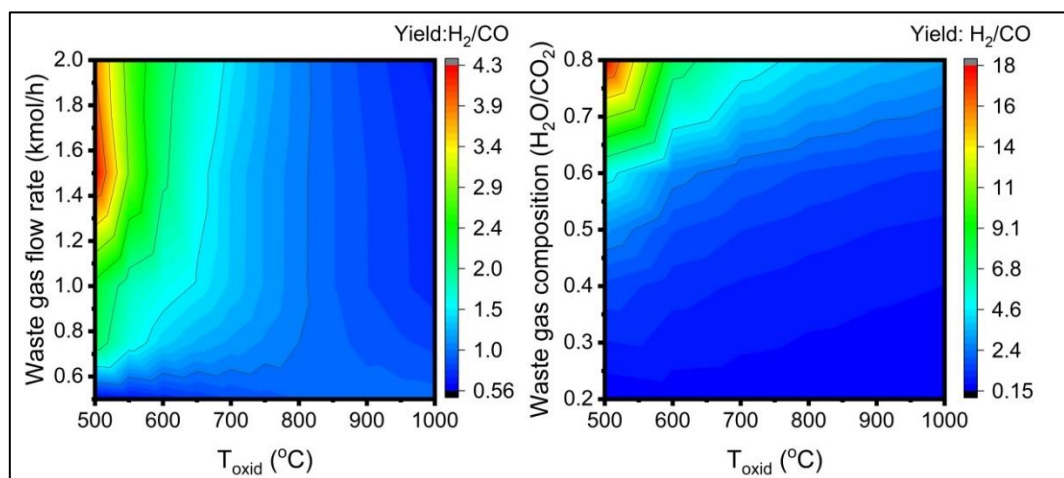


Figure 4-6 Impact of the variation of the waste gas flow parameters and temperature on the  $H_2/CO$  yield ratio in the oxidation reactor: a) variation of flow of waste gas with an equimolar mixture of  $CO_2$  and  $H_2O$ ; b) variation of the composition of the waste gas at a constant waste gas feed rate of 1 kmol/hr

The variation of the ratios  $H_2/CO$  from the oxidation reactor, based on varying compositions of  $H_2O$  and  $CO_2$  at a constant waste gas feed flow of 1 kmol/hr of the mixture is presented in Figure 4-6 (b). The formation of  $H_2$  is 18 times more than that of  $CO$  for a waste gas containing 80% of water vapour and 20% of  $CO_2$  at a temperature of  $500^\circ C$ . However, at the same temperature, for a gas containing 80%  $CO_2$ , the  $H_2/CO$  ratio is about the same ratio as  $H_2O/CO_2$ . Indeed, as can be followed from the previous discussions, with the formation of  $H_2$

peaking at around 600°C, with the corresponding increase in the CO yield, the ratio of H<sub>2</sub>/CO decreases to about 2.5 even with 80% H<sub>2</sub>O at the feed stream. This would result in the outlet gas to contain a significant fraction of unreacted H<sub>2</sub>O, while all the CO<sub>2</sub> would have been converted to CO. At higher fractions of CO<sub>2</sub>, higher temperatures would yield better result from the conversion perspective of the waste gas feed. It needs to be mentioned, that higher flow rates were also studied for variation of composition with similar trends and hence not shown separately. By such consideration, therefore, the need for determining the operating temperature of the oxidation reactor, depending on the composition of the waste gas, would play a crucial role in determining the most effective conversion, besides ensuring complete oxidation of the reduced metal. Also, the importance of the requirement of the H<sub>2</sub>/CO ratio for subsequent downstream processes is to be given importance. Nonetheless, it can be concluded that for waste gases, with large fractions of water content, it is preferable to maintain the oxidation reactor at a temperature about 600 to 700°C to ensure maximum reactivity of H<sub>2</sub>O. However, for higher CO<sub>2</sub> content, typically occurring for exhaust of power plants, the temperature of the oxidation reactor can be set at higher temperatures of around or above 900°C, thereby ensuring high conversion of CO<sub>2</sub>, and also presenting the possibility to operate the redox cycle at isothermal conditions.

### 4.3.3 Heat balance

The heat necessary for the reactions to occur in the reduction reactor and the heat that must be removed from the oxidation reactor to ensure the isothermal operation is plotted in Figure 4-7 (a) and (b) respectively. The methane reduction reaction is endothermic over the entire thermodynamic conditions studied in the paper. Interesting, however, is to note the similarity of the heat demand curve with the reaction extent plot, as in Figure 4-7. The lower heat rates at lower temperatures and molar feed ratio can be attributed to the lower reactivity between ceria and methane. However, with complete reactivity, the heat requirement stabilizes to 50kW per mole of CeO<sub>2</sub> reduced. Indeed, for complete conversion of methane, with a molar feed rate ratio of over 0.7 to 0.8, and above 900°C, the heat required for the reaction to occur stabilizes.

On the other hand, the oxidation reaction is exothermic over the entire thermodynamic conditions considered in the paper. As follows from thermodynamic laws, an exothermic reaction is favoured at lower temperatures. This is indeed represented in Figure 4-7 (b), where, at lower temperatures, the heat released from the reaction is much more pronounced, than the heat released at higher temperatures. Additionally, at lower temperatures, the heat released is primarily from the splitting of water, which is much more exothermic than the corresponding CO<sub>2</sub> splitting reaction, which gains predominance at higher temperatures. However, the overall reaction continues to be exothermic. Indeed, the drop of exothermicity at higher temperatures impact on the overall system efficiency and thermodynamics and has been subsequently discussed in the following sections.

As discussed, the advantage of ceria reduction by methane is the lowering of the reduction temperature. Therefore, as can be deduced from the present analysis, an isothermal system with complete reduction and oxidation of ceria in the respective reactors can be obtained via the

present layout. This, however, would limit the isothermal operation zone to between 850-950°C, since this would ensure the complete reduction and corresponding oxidation of CeO<sub>2</sub> with the selected flow of methane as discussed earlier. In fact, it is interesting to note, that even though the oxidation reactor is exothermic, the exothermicity is lower than the endothermicity of the reduction reactor within the defined range of isothermal operations. Hence, external heat would be required for driving the system. Often, due to elevated temperatures of 900°C or 1000°C, concentrated solar is implemented to provide the necessary heat, more specifically required for the reduction reaction.

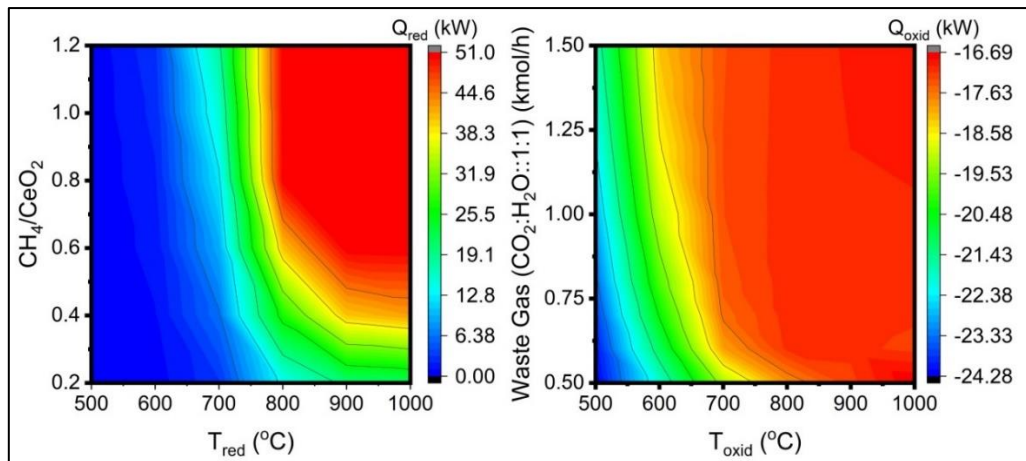


Figure 4-7 Heat need/release from the reduction and oxidation reactions as per: a) with a variation of  $CH_4/CeO_2$  feed ratio and temperature in the reduction reactor; b) with a variation of the waste gas flow at an equimolar mixture composition and temperature in the oxidation reactor.

## 4.4 Efficiency Assessment

### 4.4.1 Definition

To evaluate the system performance and identify the scope of improvement, the efficiency of the system is to be evaluated. As the case, two parallel streams of syngas are produced, of which, however, the syngas from the oxidation reactor is the main aim of such thermo-chemical cycles, as the goal of the system is to produce a syngas from waste streams of CO<sub>2</sub> and H<sub>2</sub>O. In the reduction reactor, methane is converted to syngas to drive the redox cycle with the methane content in the syngas varying significantly depending on the operating conditions of the reactor (i.e., temperature and  $CH_4/CeO_2$  fraction), as discussed previously in the paper. Even with high fractions of unreacted CH<sub>4</sub>, this syngas can be utilized for multiple purposes as well. Besides being further upgraded to syngas by chemical conversions via steam reforming reactions, it can be utilized directly for combustion. However, efficiencies of such conversions are directly dependant on the downstream conversion process required and hence was left out of scope within the present definitions. In the case that the methane is fully converted, and the reduction syngas composition matches with the one of the syngas obtained in the oxidation reactor, the two syngas flows can be mixed for a subsequent use in the same process.

Therefore, considering the diverse opportunities, two efficiencies were defined for the proposed system considering the performance of both the reactors, the preheating requirements of the solids and gas reactants in both the reactors, as well as the heat recuperated from solid. The first efficiency considers the syngas produced in both the reactors, while the second efficiency is defined considering only the syngas from the splitting of CO<sub>2</sub> and H<sub>2</sub>O in the oxidation reactor.

Based on the above-described conditions, Equation (4.11) depicts the system efficiency for the two-step chemical looping syngas production via methane reduction and subsequent CO<sub>2</sub> and H<sub>2</sub>O splitting considering syngas produced in both the reactors, while Equation (4.12) depicts the system efficiency considering only the syngas produced in the oxidation reactor.

$$\eta_1 = \frac{(\dot{m}_{H_2} LHV_{H_2} + \dot{m}_{CO} LHV_{CO})_{red} + (\dot{m}_{H_2} LHV_{H_2} + \dot{m}_{CO} LHV_{CO})_{oxy}}{(\dot{m}_{CH_4} LHV_{CH_4} + (\dot{Q}_{red} - \dot{Q}_{oxd}) + \dot{Q}_{need, net}) + (\dot{Q}_{spht} - \dot{Q}_{sld})} \quad (4.11)$$

$$\eta_2 = \frac{(\dot{m}_{H_2} LHV_{H_2} + \dot{m}_{CO} LHV_{CO})_{oxy}}{(\dot{m}_{CH_4} LHV_{CH_4} + (\dot{Q}_{red} - \dot{Q}_{oxd}) + \dot{Q}_{need, net}) + (\dot{Q}_{spht} - \dot{Q}_{sld})} \quad (4.12)$$

Where,  $\dot{Q}_{need, net} = (\dot{Q}_{need, CH_4} + \dot{Q}_{need, waste\ gas}) - (\dot{Q}_{syngas, red} + \dot{Q}_{syngas, oxd})$  is the net heat needed for the system operations, including the heat needed for methane and waste gas heat-up and the heat recovered from the syngas product streams, that are directly used to pre-heat the inlet gases, and hence included in the defined manner. Heat losses from system components were neglected in the efficiency assessment.

#### 4.4.2 Efficiency Evaluation

To illustrate the benefits of the proposed cycle as per the definition of efficiency, the results of the effect of the operating parameters on the efficiency of the system are presented in the following section.

The impact of the variation of the feed flow rate of the oxidation reactor, as well as the variation of the gas composition on the overall system efficiency, for constant methane to ceria feed ratio of 0.8 to the reduction reactor is shown in Figure 4-8. The impact on the combined efficiency definition, considering both the reactors have been discussed since a constant CH<sub>4</sub>/CeO<sub>2</sub> ratio of 0.8 would yield a fixed output from the reduction reactor above 900°C. The optimal temperature of operation of the reduction reactor being identified as 900°C, the efficiency study showed has been carried out at temperatures of 900°C and 950°C. It is seen that neither the variation of the flow of the waste gas nor the composition of the gas has a significant impact on the net system efficiency. A slight decrease of the efficiency is however noticed for an increased water content for the waste gas flow. Acknowledging the fact that the minimum flow, that is 0.5 kmol/hr of waste gas, corresponds to the stoichiometric conditions, and that the present thermodynamic conditions are feasible for the splitting reactions, (4.2a) and (4.2b), the results indicate the complete oxidation of the reduced metal. Indeed, with an increase in the

flow of waste gas, stoichiometric fraction of the CO<sub>2</sub> and H<sub>2</sub>O takes part in the reaction, with the excess gases remaining unreacted.

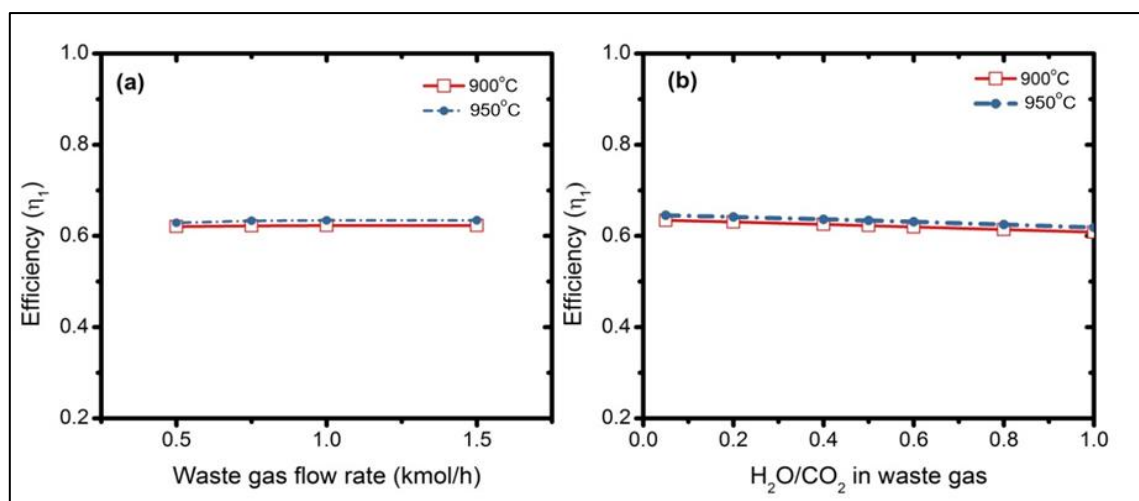


Figure 4-8 Variation of system efficiency considering syngas from both the reactors ( $\eta_1$ ) based on the parametric variations within the oxidation reactor, at a constant CH<sub>4</sub>/CeO<sub>2</sub> flow ratio of 0.8 in the reduction reactor based on: *a*) variation of waste gas flow rate at a constant equimolar mixture of CO<sub>2</sub> and H<sub>2</sub>O and temperature; *b*) variation of waste gas composition and temperature.

The impact of the variation of the methane to ceria feed flow in the reduction reactor on the system efficiency considering syngas from both the reactors, is shown in Figure 4-9, together with the corresponding total CO and H<sub>2</sub> yield as obtained from both the reactors. The feed flow in the oxidation reactor was kept constant at 1 kmol/hr, and an equimolar flow of CO<sub>2</sub> and H<sub>2</sub>O was considered, with an isothermal redox cycle operation between 800 °C and 950 °C. At 800°C and with a CH<sub>4</sub>/CeO<sub>2</sub> flow ratio of up to 0.8, the metal oxide remains largely unreacted, leading to system efficiencies of about 60%, always lower than that of the system working at higher temperatures of 900°C and 950°C. At temperatures over 850°C, the methane conversion becomes 99%, even at lower than stoichiometric flow rates. However, with lower than stoichiometric flow rates of methane to the reduction reactor, even though methane conversion is maximum, a part of the ceria remains unreacted. By definition of efficiency, this leads to a high system efficiency of around 90%, even though the total yield of CO and H<sub>2</sub> is considerably less than the maximum potential. At a methane to ceria flow ratio of 0.5 and below, the yield corresponds to only around 50% of the maximum potential yield of the redox system, which starts occurring at CH<sub>4</sub>/CeO<sub>2</sub> flow ratios of 0.7 at temperatures over 850°C and 0.8 for a temperature of 800°C. Indeed, once the yield of the system becomes comparable irrespective of temperature at CH<sub>4</sub>/CeO<sub>2</sub> flow ratio over 0.8, the system efficiency starts becoming comparable irrespective of working temperature of the system.

Based on the defined efficiency  $\eta_1$  the excess methane plays no significant role in increasing the H<sub>2</sub> and CO yield of the system, however, it decreases the system efficiency. Following the discussion, to ensure high system efficiency together with maximum possible system yield, the system should operate with a CH<sub>4</sub>/CeO<sub>2</sub> molar feed ratio between 0.7 and 0.8 at a temperature

of 900 °C or higher. In these conditions the efficiency is around 70%, yielding 1.2 kmol/hr of H<sub>2</sub> and 0.8 kmol/hr of CO from a stream of 1 kmol/hr (CO<sub>2</sub>/H<sub>2</sub>O ratio equal to 1).

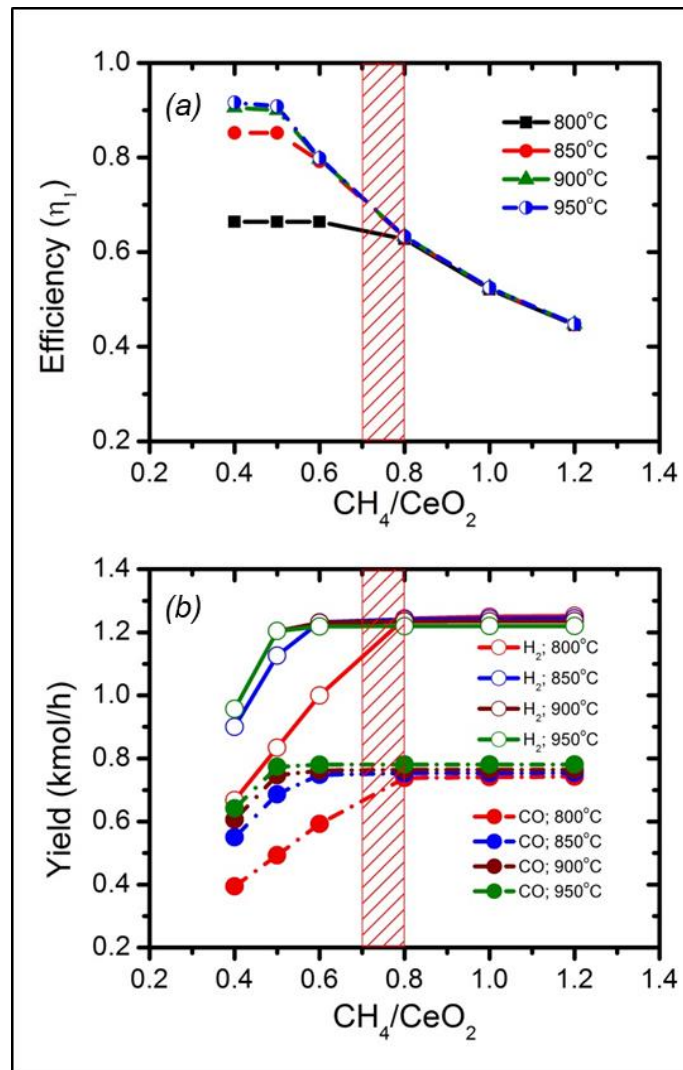


Figure 4-9 Impact of the CH<sub>4</sub>/CeO<sub>2</sub> molar feed ratio and temperature, based on an isothermal system operation and a constant flow of 2 kmol/hr of waste gas at equimolar composition within the oxidation reactor on *a*) the system efficiency,  $\eta_1$  *b*) net H<sub>2</sub> and CO yield from the redox cycle, considering both the oxidation and reduction reactors.

Corresponding to the definition of the system efficiency with only the yield from the splitting reaction, an overall system efficiency of 16%, corresponding to the maximum system yield is obtained, as can be visualized from Figure 4-10. This result, indeed, is comparable to solar thermochemical cycles, showing similar efficiency trends where only syngas from splitting reaction is prevalent. The trend of both the efficiencies is, however, similar, further justifying the need to operate within the specific region as already discussed in the previous sections for maximum system effectiveness and resource utilization.

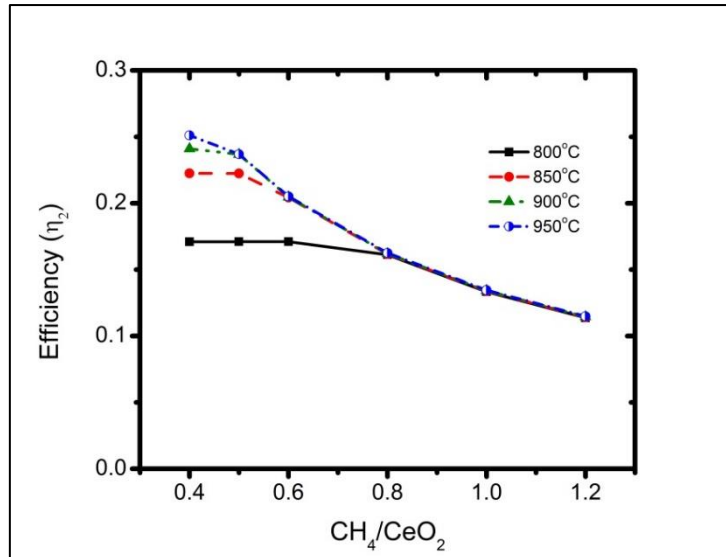


Figure 4-10 Impact of the CH<sub>4</sub>/CeO<sub>2</sub> molar feed ratio and temperature, on the system efficiency considering only the yield from CO<sub>2</sub> and H<sub>2</sub>O splitting ( $\eta_2$ ), based on an isothermal system operation and a constant flow of 1 kmol/hr of waste gas at equimolar composition within the oxidation reactor.

## 4.5 Pinch Analysis

The pinch analysis has been also performed to evaluate the thermal integration within the thermochemical cycle for an isothermal operation at 950 °C. Results are shown in Figure 4-11.

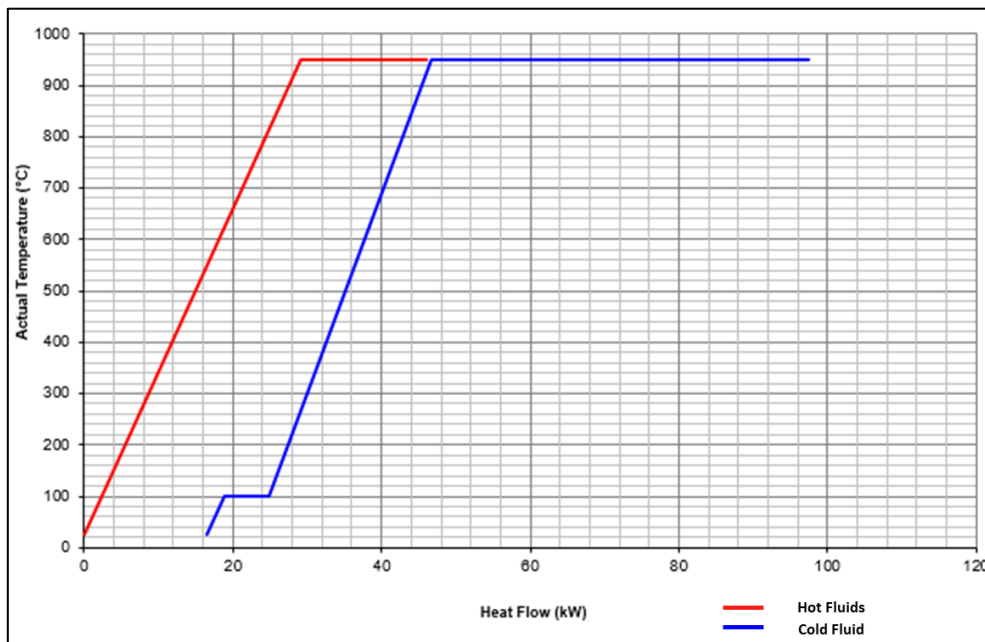


Figure 4-11 Pinch Analysis of the Methane driven chemical looping cycle at an isothermal temperature of 950°C

As can be seen, the amount of high-temperature heat needed is significant due to the highly endothermic reduction reaction. Such heat, however, can be provided either through

concentrated solar energy – even if this option could not allow the continuous operation of the system – or by burning a fuel, for example, additional methane or renewable fuels, thereby enabling the system to run continuously. Even combined solutions can be proposed, by providing heat from burning fuels only to integrate the solar heat flux when it is not sufficient. The analysis of these solutions has not been included in the paper, as it is outside of the scope.

Indeed, as can be seen, due to the considerable amount of heat content from the exiting product gas streams from both the reactors, a considerable amount of heat is available at lower temperatures, increasing the system efficiencies as per the defined efficiencies. Integration with larger systems, therefore, would yield benefits through the availability of significant amounts of low-temperature waste heat.

## 4.6 Conclusion

In the present chapter, the performance of the  $\text{CeO}_2/\text{Ce}_2\text{O}_3$  redox pair was evaluated for chemical looping syngas production through methane reduction and carbon dioxide and water splitting using thermodynamic analysis. Process simulation was performed to identify the most favourable working conditions with corresponding efficiency evaluation. In the fuel reactor, syngas production was studied via reduction of the metal oxide by methane. For the primary aim of the reduction reactor to produce syngas, methane to  $\text{CeO}_2$  feeding ratio of 0.7 to 0.8 at a temperature of  $900^\circ\text{C}$  was obtained as the most suitable condition, resulting in a complete reduction of  $\text{CeO}_2$  to  $\text{Ce}_2\text{O}_3$  while avoiding the formation of  $\text{CO}_2$  and carbon deposition. The high yield at atmospheric pressure and lower temperature levels are therefore of much benefit as compared to thermal reduction of ceria. The temperature and composition of waste gas (a mixture of  $\text{CO}_2$  and  $\text{H}_2\text{O}$ ), coupled with the end use of produced syngas would govern the operating conditions of the oxidation reactor. However, water splitting reaction peaks at temperatures between  $600\text{--}650^\circ\text{C}$ , while a monotonic increase of  $\text{CO}$  production with the temperature was obtained for  $\text{CO}_2$  splitting reaction. A minimum molar flow of  $0.75\text{ kmol/hr}$  of waste gas at the equimolar composition of  $\text{CO}_2$  and  $\text{H}_2\text{O}$  would be required to oxidize a flow of  $0.5\text{ kmol/h}$   $\text{Ce}_2\text{O}_3$  completely to  $\text{CeO}_2$  to close the redox cycle. This corresponds to a flow of 50% excess than the stoichiometric quantity. Further, the system efficiency was evaluated based on two defined efficiency terms for the chemical looping configuration. It is observed that the variations of the flow of waste gas (a mixture of  $\text{CO}_2$  and  $\text{H}_2\text{O}$ ), as well as the composition, had little or no impact on the overall system efficiency. Nevertheless, for lower flows of methane, high system efficiency was obtained, however with lower yields of  $\text{H}_2$  and  $\text{CO}$ . A system efficiency of around 70%, considering syngas from both the reactors, with a production of syngas composed by 60%  $\text{H}_2$  and 40%  $\text{CO}_2$  was obtained for an isothermal operation at  $900^\circ\text{C}$  or higher, as the optimum for the entire chemical looping cycle. However, the value drops to 16% while considering only the syngas from the splitting of  $\text{CO}_2$  and  $\text{H}_2\text{O}$ . The corresponding isothermal system temperature needs to be  $900^\circ\text{C}$  between the reduction and oxidation reactor. In the end, it can be concluded that these results can be taken as a limiting basis for future experimental and theoretical studies in determining the extent of reactions with ceria-based chemical looping  $\text{CO}_2$  and  $\text{H}_2\text{O}$  splitting with methane reduction to evaluate the proposed technology.

## 5 Kinetic Modelling of POM with Commercial Ceria followed by CDS

To elaborate on the encouraging results obtained through thermodynamic evaluation, the kinetics study is essential. Literature study on the reduction of ceria through partial oxidation of methane (POM) has largely focused on the characterization of the material performance including the study of the effects of doping through transition metal promoters and/or by addition of inert supports or the investigation of the different sample morphologies [28,60,167]. Otsuka et al [168] studied the reaction mechanism between both doped and undoped ceria for POM, where, the recombination or desorption of the produced  $H_2$  was identified as the rate determining step for the reduction reaction. In a further study, the same author reported activation energy of POM over pure Ceria to a value around 160 kJ/mol [169]. Nair and Abanades [170] carried out experiments in a solar assisted reactor between the temperature range of 900-1100°C in a solar assisted thermogravimetric system and reported an activation energy of 109 kJ/mol and a reaction order of 0.62. The maximum non-stoichiometry ( $\delta$ ) obtained for commercial ceria was reported as 0.378 [170]. Warren et al [29], in a recent work published in 2018 have explored further kinetic behaviours related to POM over pure Ceria including studying the impact of different factors like the limitation of gas/solid diffusion, gas composition ratio between the reactant and the product, etc. Through experiments conducted at the range between 750°C and 1100°C and atmospheric conditions, and carrying out measurements through a thermogravimetric analyser, activation energy for the reaction was obtained using Arrhenius-type plots [29]. The activation energy reported was much lower, between 20 kJ/mol and 80 kJ/mol, with the higher value being obtained at a  $\delta > 0.15$ . Furthermore, a complete reduction of ceria was reported beyond 900°C [29]. Also, none of the studies, to the best knowledge of the authors have considered model based kinetic approach to report the overall reaction kinetics of POM with ceria reduction. This model specifically benefits in the identification of the rate controlling mechanism, while at the same time assign parameters to the kinetic model, so as to successfully predict the outcomes of the reactions over the entire envelope of the fuel curve [128].

For the oxidation reaction, multiple studies of kinetics of catalytic oxidation of  $Ce_2O_3$  at low temperatures (below 800°C) with water or  $CO_2$  have been studied and reported in multiple literature, especially due to its applications in catalytic convertors, fuel cells and other applications [128]. Nevertheless, such low temperature studies for catalytic reactions are typically not applicable for higher temperature non-catalytic oxidation reactions. Ishida et al [125] studied the kinetic models for water splitting while Le Gal and Abanades [55] studied and reported the kinetics of both water and  $CO_2$  splitting in the context of solar fuel chemistry. For undoped Ceria, Le Gal et al obtained the second-order power law model to best describe the CDS kinetics, through a surface-limited reaction mechanism, even though no kinetic parameters were reported. “Master Plot” approach [171,172] was used in this regard to analyse the mass gain measured by the thermogravimetric analyser (TGA) during oxidation. As mentioned previously in Section 3.1.2, Arifin et al [128], using a similar, but a modified

approach, by separating the experimental effects from material specific H<sub>2</sub> and CO curve rates, reported the WS kinetics to be best described by a first-order kinetic model. All model parameters were also reported, whereby, a low apparent activation energy of 29 kJ/mol was obtained in the range of 750-900°C. On the other hand, CDS kinetics was found to be surface-mediated phenomena with a much higher complexity than the WS reaction, leading to no one solid state kinetic model (SS) to accurately predict the product yield over the entire range of experimental conditions, 600-875°C and 10–40 vol% CO<sub>2</sub>. This is due to the fact, that the SS models, essentially lumped parameter models with a minimal level of detail about the reaction mechanisms, does not account for the transient phenomena occurring during the CDS reactions. Farooqui et al [173] in another recent study, tried to further this limitation for identification of the proper kinetic model for the CDS reaction. The authors compared the different reaction models to experimental data (CO<sub>2</sub> oxidation of reduced Ceria in an atmosphere of H<sub>2</sub> at a temperature range of 700-1100°C) by curve fitting, followed by statistically comparison using the Residual sum of squares (RSS), Akaike information criterion (AICc) and the F-test methods. The Sestak-Berggren (SB) model was found to fit best to the experimental data of the CDS reaction together with an activation energy of  $79.1 \pm 6.5$  kJ/mol being obtained [173].

Nevertheless, the different experimental conditions, including experimental artifacts significantly affect the overall outcomes and hence the results of the experiments. A detailed discussion in this regard has been reported by Scheffe et al [118]. This not only results in a wide discrepancy in the reported results, but also in developing a comprehensive model to best describe a reaction over a wide range of temperature and operating conditions. Unlike the model developed by Bulfin et al [51] which comprehensively describes the solar thermal reduction of Ceria, over a wide range of operating conditions, no one model exists that can accurately predict the reduction of ceria by methane. In addition, all the oxidation kinetics have been studied after thermal reduction of ceria. CO<sub>2</sub> kinetics, being so heavily dependent on the surface phenomena, thus needs to be re-evaluated for oxidizing methane-reduced ceria.

Therefore, in this section, the kinetics of methane reduction of commercial ceria with subsequent oxidation with CO<sub>2</sub> was investigated with SS kinetic model development. In the following section, a detailed methodology, experimental set-up and results of the kinetics of methane reduction of commercial ceria and oxidation of the reduced methane at isothermal conditions are presented and discussed.

## 5.1 Reaction Mechanism

The complete chemical reaction, leading to conversion to the desired product and the corresponding kinetics involves a series of individual chemical steps. However, to define the exact mechanism followed during the reaction is often a challenging task, especially for gas-solid, solid-solid kinetics. Hence, for such reactions, the determination of the reaction kinetic involves application and verification of a derived mechanistic model following literature, based on the process with the experimental data. Figure 5-1 shows the schematic description of the general kinetic models, most often used in literature for non-catalytic gas-solid heterogeneous reactions.

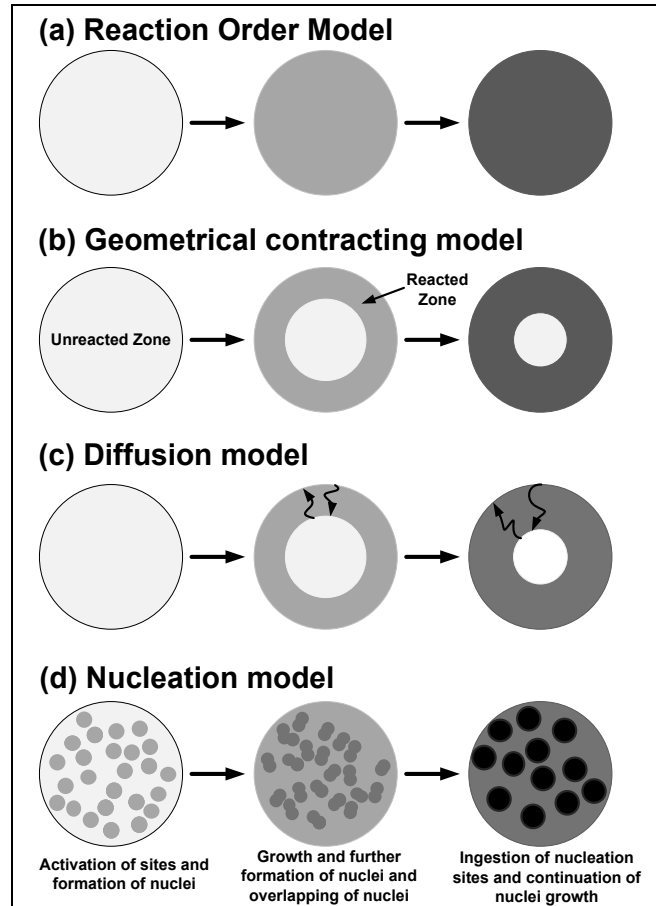


Figure 5-1. Kinetic models with corresponding reaction mechanisms (a) Reaction order model (b) Geometrical contracting model (c) Diffusion model (d) Avrami-Erofeev (Nucleation) model applicable for Ceria-based oxygen carrier.

The kinetic models can be grouped into several well-defined categories and are represented in Table 5-1. The most simplistic models, based on reaction order (F in Table 5-1) assume a homogenous reaction process. On the other hand, geometrical contracting models (R) assume phase boundary reaction control with different geometries with a shrinking core mechanism (SCM). Of the SCMs, R2 represents two-dimensional shrinking or growth whereas R3 represents three-dimensional shrinkage or growth [173]. The Diffusion models (D1-D4) represent rate-controlled reaction mechanisms. The reaction-transport of reactants and products to and from the active interfaces [174] control the reaction kinetics. Another set of models of reaction kinetics are the nucleation and nuclei growth models, also called Avrami-Erofeev models (AE) involve the formation and growth of nuclei at the reaction site [173]. Bhatia and Perimutter [175] have proposed a new model called the Random Pore Model (RPM) following the pore growth during the reaction and based on the population balance concept. Modifications to this model depending on the material and the operating conditions have been reported in the literature [173]. Finally, the Sestak-Breggen (SB) model is used for more complex crystallization processes involving partial nuclei overlapping and growth steps [176]. Yet another model, the Prout-Tompkins (PT) model, based on autocatalysis, proposes that the nuclei growth formation rate and chain breaking rate constants are equal [177].

Table 5-1 Rate and integral expressions for different solid-state kinetic models [172] based on  $\alpha$ , which indicates the conversion,  $f(X)$  represents the differential form of the kinetic model, and  $g(X)$  is the integral form of the model.

No	Reaction Model	$f(X)=(1/k) dX/dt$	$g(X)=kt$	$n_{AE}$
F1.5	Three – halves order	$(1-X)^{3/2}$	$2[(1-X)^{-1/2}-1]$	0.91
F2	Second – order	$(1-X)^2$	$1/(1-X)-1$	0.83
F3	Third – order	$(1-X)^3$	$(1/2)[(1-X)^{-2}-1]$	0.70
R1	Zero – order (Polanyi – Winger equation)	1	X	1.24
R2	Phase boundary controlled reaction (contacting area, i.e, bi – dimensional shape)	$2(1-X)^{(1/2)}$	$1-(1-X)^{(1/2)}$	1.11
R3	Phase – boundary controlled reaction (contracting volume, i.e, tridimensional shape)	$3(1-X)^{(2/3)}$	$1-(1-X)^{(1/3)}$	1.07
D1	One – dimensional diffusion	$1/(2X)$	$X^2$	0.62
D2	Two – dimensional diffusion Valensi equation	$1/[-\ln(1-X)]$	$(1-X)\ln(1-X)+X$	0.57
D3	Three dimensional diffusion Jander equation	$3(1-X)^{(1/3)}[2(1-X)^{(-1/3)}-1]$	$[1-(1-X)^{(1/3)}]^2$	0.54
D4	Three dimensional diffusion Ginstling – Brounshtein	$3/[2(1-X)^{(-1/3)}-1]$	$(1-2X/3)-(1-X)^{(2/3)}$	0.57
AE1	First – order (Mampel) (F1) or Avrami – Erofe'ev ( $n=1$ )	$(1-X)$	$-\ln(1-X)$	1
AE0.5	Avrami – Erofe'ev ( $n=0.5$ )	$(1/2)(1-X)[-\ln(1-X)]^{-1}$	$(-\ln(1-X))^2$	0.5
AE1.5	Avrami – Erofe'ev ( $n=1.5$ )	$(3/2)(1-X)[-\ln(1-X)]^{1/3}$	$(-\ln(1-X))^{2/3}$	1.5
AE2	Avrami – Erofe'ev ( $n=2$ )	$2(1-X)[-\ln(1-X)]^{1/2}$	$(-\ln(1-X))^{1/2}$	2
AE3	Avrami – Erofe'ev ( $n=3$ )	$3(1-X)[-\ln(1-X)]^{2/3}$	$(-\ln(1-X))^{1/3}$	3
AE4	Avrami – Erofe'ev ( $n=4$ )	$4(1-X)[-\ln(1-X)]^{3/4}$	$(-\ln(1-X))^{1/4}$	4
AEn	Avrami – Erofe'ev	$n(1-X)[-\ln(1-X)]^{(n-1)/n}$	$(-\ln(1-X))^{1/n}$	n
SB	Sestak – Berggren Function	$X^{y_1} (1-X)^{y_2}$	-	-
PT	Prout – Tompkins	$X(1-X)$	$\ln(\alpha/(1-X))$	-

Generally, most of the models listed in Table 5-1 contain one fitting parameter - rate constant,  $k$ . However, with an increase in complexity, some models allow a better fit for the kinetic data. These models are grouped into three groups based on the number of independent variables i.e., one parameter, two-parameter and three-parameter models. The SB model is a three fitting parameters model, while the AE model with the exponent  $n$ , ( $AE_n$ ) and Random pore model (RPM) are a two-parameter models. All the remaining models listed in Table 5-1 are one-parameter models.

### 5.1.1 Model-Free Method

The Model Free method, alternatively called the Hancock and Sharp method, is a simple method to identify the mechanism of isothermal solid-state reaction kinetics [178]. It is often considered as model-free method based on the nucleation model and can be expressed by the following equation (5-1):

$$\ln(-\ln(1-X)) = \ln \alpha + n_{AE} \ln t \quad (5-1)$$

where  $X$  is the solid conversion (extent of reaction),  $t$  is the reaction time,  $a$  is the constant based on the frequency of the nuclei formation and rate of crystallite growth and  $n_{AE}$  is called Avrami-Erofeev exponent [179]. To implement this method, it is necessary to plot  $\ln(-\ln(1-X))$  vs.  $\ln(t)$ , which has been shown to give approximately linear plots with or without nucleation [178] up to a conversion limit of 0.15 to 0.5. The authors also reported that this conversion range is independent of experimental uncertainty and error at  $t=0$  or by geometrical factors. The corresponding values of  $n$  for models other than AE models are also listed in Table 5-1.

The Hancock and Sharp slope is primarily utilized as a diagnostic tool to preliminary choose between the reaction mechanisms, as has been listed in Table 5-1. However, the disadvantage of this method is that the complete distinguishing of models become difficult sometimes like for the four diffusion models that exhibit different slopes of 0.5 to 0.6 for different order kinetics. Also, for  $n_{AE}=1$  a non-conclusive behaviour is obtained, that indicates the suitability of F1.5, R3 and AE1 models. This limits the sole use of the Hancock and Sharp method to select between the group of standard reaction models with linear plots of similar  $n_{AE}$  values (slopes). Therefore, in addition, it is recommended also to find the best fit model by plotting  $dX/dt$  vs.  $X$  and  $X$  over time and wide conversion range.

## 5.2 Experimental Section

Isothermal redox cycles of  $CeO_2$  commercial powders were performed in a horizontal tubular reactor in the temperature range of 900–1100°C. Methane ( $CH_4$ ) was used for the ceria reduction to evaluate the reaction kinetics for methane reduction of commercial ceria and explore the maximum non-stoichiometric capacity ( $\delta$ ) achieved at a set-point temperature. Corresponding oxidation with different concentration of carbon dioxide in the oxidation step was performed with the aim to develop the reaction kinetics of reduction and subsequent oxidation of a methane-driven two-step chemical looping cycle with commercial ceria. The temperature swing is thus replaced by isothermal operation for developing the kinetics.

During the reduction, an online mass spectrometer was used to measure the  $H_2$  and CO production during reduction and CO production during the oxidation reaction. Upon analysis of the reactivity data obtained from the experiments, different kinetic models based on alternative reaction mechanisms (i.e., reaction order, geometrical contracting, diffusion, and nucleation models) were compared using statistical criteria – the Residual sum of squares (RSS), – and the best-fitting model was selected. Hence, the corresponding ceria reduction and oxidation mechanism were identified.

The experimental setup comprised a horizontal alumina tubular reactor, a control unit, a gas delivery system and a real-time gas analysis system with an online mass spectrometer. The system layout and the details of the reactor are shown in Figure 5-2. Three Bronkhorst EL-FLOW mass flow controllers (MFCs) were used to control the gas flow into the reactor set-up. The reactor is an alumina tube positioned inside a tubular furnace (Lenton UK) able to maintain an isothermal environment up to 1600°C. As can be seen from, Figure 5-2, the reactor comprises an outer alumina tube of 90 cm in length, an inner diameter ( $i_d$ ) of 50 mm, an inner concentric alumina tube with 12 mm outer diameter ( $o_d$ ) and 10 mm  $i_d$  and 1m of length.

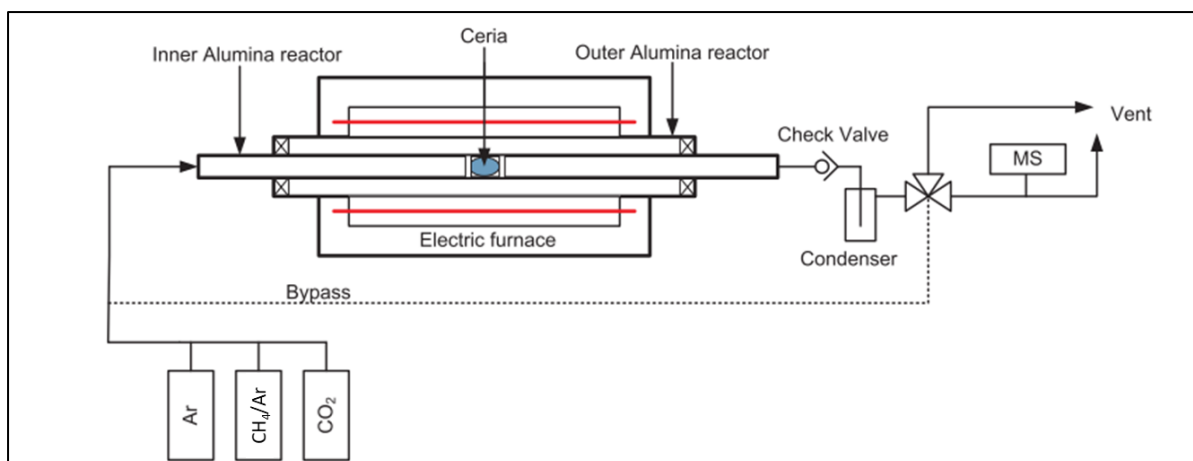


Figure 5-2 Experimental set-ups for developing reaction kinetics in micro-reactor configuration

The sample supported with quartz wool is placed within the inner tube and the gas flows over it. A Quadrupole Mass Spectrometer (QMS) (Hiden Analytical Inc.) was used to analyse the gas composition. Commercial ceria powder from Alfa Aesar (99.95% purity) was chosen for the reaction study. The sample was crushed and sieved to  $32\mu\text{m}$  before the tests. A 250mg amount of ceria powder ( $m_{\text{CeO}_2}$ ) was embedded in quartz wool and placed at the centre of the inner alumina tube. The total flow rate of gases into the reactor during both the reduction and the oxidation steps were maintained constant at  $120\text{Nml/min}$  ( $\dot{V}_{\text{gas}}$ ). During both the reduction and the oxidation, the mole fraction of the reactant gases ( $\text{CH}_4$  and  $\text{CO}_2$  respectively), were varied between 20% and 50%, balance argon. During the reduction, since one mole of methane leads to the formation of 2 moles of  $\text{H}_2$  and one mole of  $\text{CO}$ , the molar flow at the outlet is higher than the inlet. However, as the production of 1 mol of  $\text{CO}$  leads to the consumption of 1 mol of  $\text{CO}_2$ , the total molar flow rate throughout the control volume remains constant during the oxidation cycle.

Each experiment was performed in a cycle of four steps. The first step included the ceria reduction step where the mixture of argon and methane was passed over the sample. Different concentrations of  $\text{CH}_4$  (20%, 30% and 40% and 50%) was passed to evaluate the reduction mechanism. The readings of the QMS were observed to analyse for complete reduction of ceria. However, in the case of lower reaction rates at lower temperatures, the reactant gases were passes for 75 minutes to ensure enough reduction to study the corresponding oxidation. After completion of the reduction cycle, a purging stream of pure Ar was fed for 10 min, to remove the reactants and products present in the fixed bed from the previous cycle. The following step was the oxidation reaction where a mixture of Ar and different concentrations (20%, 30% and 40% and 50%) of  $\text{CO}_2$  was sent for 15 min. The last step was the purging with pure Argon for approximately 10 min or until the QGA reading was stable enough to begin the next cycle, whichever is earlier. Isothermal redox cycles were performed at 900, 950, 1000, 1050 and  $1100^\circ\text{C}$ . The measure of  $\text{H}_2$  and  $\text{CO}$  concentrations for the reduction cycle and the  $\text{CO}$  for the oxidation cycle at the outlet flow of the reactor allowed to extrapolate the reaction rate of the reduction and oxidation reactions respectively. However, for the reduction step, the methane

splitting reaction (equation 4.4) can occur, which would give erroneous results from the reading of the hydrogen measurements due to the formation of H<sub>2</sub> and elementary solid carbon, which would be deposited inside the reactor. Indeed, this would be reflected by the corresponding oxidation, whereby the reaction kinetics would depend not only on the ceria oxidation but also on the Boudard reaction (equation 4.3).

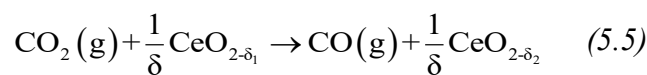
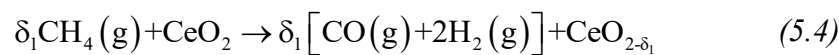
Nevertheless, for most parts of the experimental regime, no significant carbon formation was noticed. In any case, the measurements of CO both during the reduction and the oxidation cycle were considered for developing the necessary kinetics as follows:

$$\dot{\omega}_{\text{CO,red}} = \frac{X_{\text{CO,out}} \dot{n}_{\text{red,out}}}{m_{\text{CeO}_2}} = \frac{X_{\text{CO,out,red}}}{m_{\text{CeO}_2}} \frac{P^0 \dot{V}_{\text{red,in}}^0}{RT^0} \quad (5.2)$$

$$\dot{\omega}_{\text{CO}} = \frac{X_{\text{CO,out}} \dot{n}_{\text{ox,out}}}{m_{\text{CeO}_2}} = \frac{X_{\text{CO,out}}}{m_{\text{CeO}_2}} \frac{P^0 \dot{V}_{\text{ox,in}}^0}{RT^0} \quad (5.3)$$

where  $X_{\text{CO,out}}$  is the measured mole fraction of CO at the exit of the reactor,  $\dot{n}_{\text{out}}$  is the total molar outflow rate of the gas mixture for the reduction and oxidation respectively, as per the designation in equations (5.2) and (5.3), which are equal to the inlet molar flow, while  $P^0$ ,  $T^0$  and  $\dot{V}_{\text{in}}^0$  are the pressure, temperature and the total volumetric inflow rate at standard temperature and pressure (STP) with respect to the two alternate reduction and oxidation cycles. The reaction rates for both the reduction and oxidation cycles have been normalized by the total ceria sample  $m_{\text{CeO}_2}$  – i.e. 250 mg – used in the measurement. During the entire experiments, a quasi-steady-state was assumed. Hence, the accumulation or depletion effect in the control volume was neglected. This can be attributed to the fact that the residence time of the gases is negligible in relation to the characteristic time of the redox conversion.

The bulk-phase non-stoichiometry change of ceria would be first evaluated through the extrapolated reduction rate, as per the reaction is written in the following equation (Eq. 5.4). Correspondingly, the bulk-phase non-stoichiometry change of ceria can also be evaluated by extrapolating the oxidation reaction rate based on oxidation with carbon dioxide. The oxidation reaction can be rewritten as per the equation (Eq. 5.5):



where the non-stoichiometry reached after the reduction step is represented by  $\delta_1$  and  $\delta_2$  correspond to the non-stoichiometry at the end of the ceria oxidation step and  $\delta = \delta_1 - \delta_2$  is the bulk-phase non-stoichiometry change, calculated as per the following equation [173] (Eq. 5.6):

$$\delta(t) = \frac{n_{\text{O}}(t)}{n_{\text{CeO}_2}} \quad (5.6)$$

where  $n_{\text{O}}(t) = \int_0^t \dot{\omega}_{\text{CO}_{\text{red}}} dt = \int_0^t \dot{\omega}_{\text{CO}_{\text{oxy}}} dt$  represents the accumulated release and intake of oxygen ions during the reduction and the oxidation reactions respectively,  $n_{\text{CeO}_2} = m_{\text{CeO}_2} / M_{\text{CeO}_2}$  is the moles of ceria used in the experiment, with  $M_{\text{CeO}_2}$  is its molar mass.

The non-stoichiometry is calculated by the amount of oxygen that the solid can release and accept when reduced by methane and oxidized with  $\text{CO}_2$ , starting from a neutral state. Therefore, at the end of oxidation, which also represents the completion of one cycle, oxygen vacancies are depleted, and no more oxygen is incorporated in the material. The maximum non-stoichiometry is affected by the temperature, where, an increase in temperature results in an increased rate of oxygen release and hence, an increased availability of vacancies.

### 5.3 Reactivity results

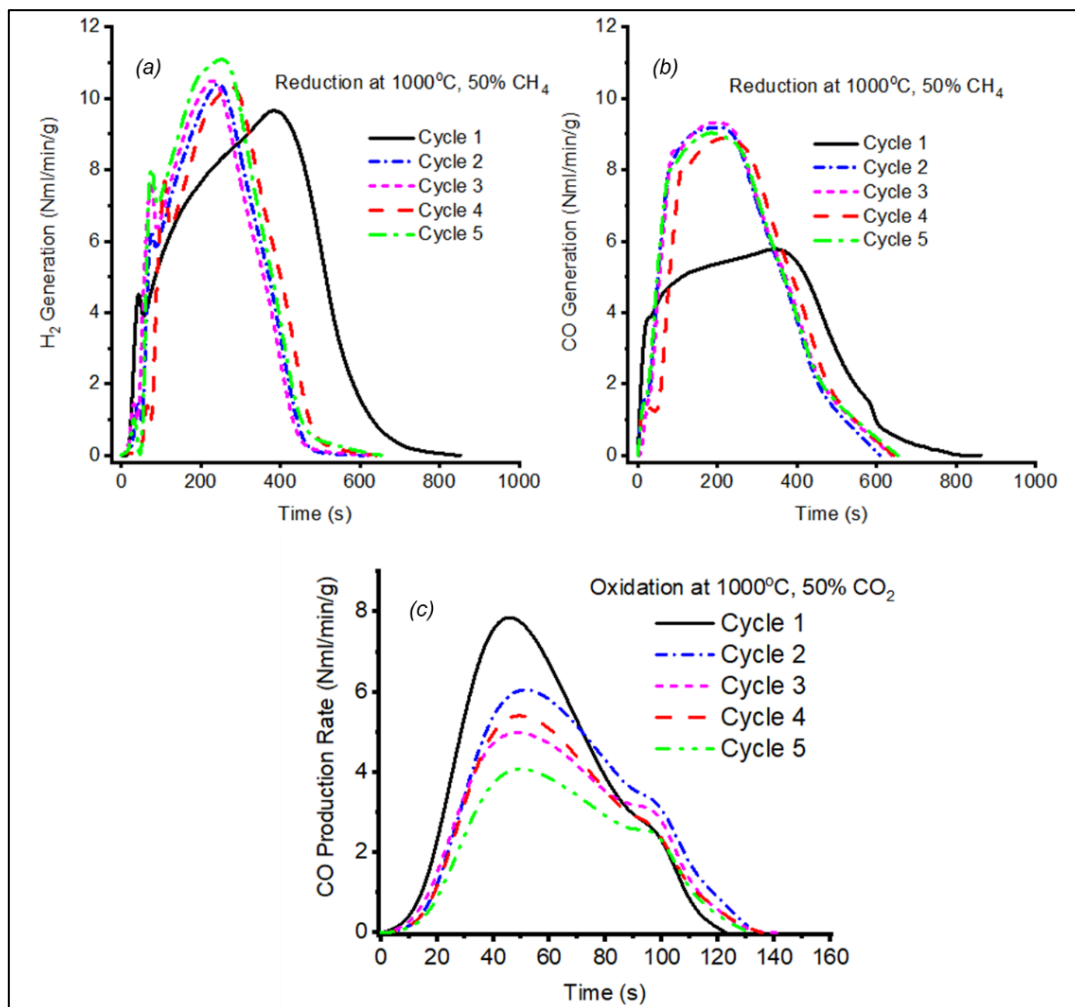


Figure 5-3. a) H<sub>2</sub> and b) CO production rate from the reduction of CeO<sub>2</sub> over 50% CH<sub>4</sub> and c) oxidation of the reduced metal oxide with 50% CO<sub>2</sub> over five cycles each. Operating conditions:  $m_{\text{CeO}_2}$  : 250 mg;  $\dot{V}_{\text{gas}}$  : 120 Nml/min (balance Argon); Isothermal redox cycling temperature: at 1000°C (1273 K); for all cases, the baseline reactor pressure: 1 atm.

The results of the tests for methane reduction and the CO<sub>2</sub> splitting performance in terms of the CO production rate (Nml/min/g) and the total CO yield (Nml/g) were investigated. The below Figure 5-3 represents the result of the reduction and the oxidation for a representative cycle to show the cyclability of the reactions conducted. The yield of both H<sub>2</sub> and CO have been measured and plotted for the reduction reaction. As can be seen, besides the first cycle, all the other cycles show a consistent repeatability for both the oxidation and the reduction reactions. The ceria in the first cycle of the reduction suffers from lower activation, and hence the deviation from the other cycles. Other cycles were also obtained to have similar behaviour and hence not further plotted in the present work.

The primary motive behind the set of experiments was to evaluate the performance and the dependence of commercial CeO<sub>2</sub> as oxygen carrier on temperature and reactant gas concentration. Hence a series of tests were performed in different experimental conditions and are described in the following sections.

### 5.3.1 Effect of temperature

Figure 5-4 shows the CO production rate as a function of temperature for both the oxidation and reduction reactions. For both the reactions, the temperature was varied from 900 to 1100°C. In each plot, the reaction rate is characterized by a slow initial stage, a fast-middle stage, also resulting in a peak reaction rate, and subsequently a decrease.

During reduction, the slow increase in the CO release results from the release of oxygen from the crystal lattice of the metal oxide. Both temperature and reactant concentration play a role in determining the maximum rate. Indeed, the relative length of each of the three phases depends much on the reaction temperature, which is especially significant for the reduction reaction. This, in turn, would lead to a much longer time for completion of the reduction with a subsequent lower yield. As can also be seen for both the reduction and oxidation reactions, the peak rate varies non-linearly with temperature, and for temperatures lower than 900°C, the reaction becomes slow enough to limit the overall non-stoichiometric ceria yield.

For the reduction reaction, the impact of temperature is much more pronounced on the peak product yield, as can be seen from Figure 5-4a. From increase in temperature from 950°C to 1100°C, the peak yield of CO was observed to increase almost six times, with the most marked rise in the yield rate occurring between 1000°C and 1050°C, when the production rate almost triples (from around 15 Nml/min/g to around 47 Nml/min/g of CO). Also, with temperature, the peak rate becomes faster and quicker to occur (around 600 secs for 950/1000°C and around 400 secs for 1050°C. At 900°C, no significant peak is even noticed, with a flatter trajectory occurring over a larger time due to the lower amount of available oxygen sites. After the peak yield, the production rate drops rapidly, with a complete reaction taking place in around 1000s for all temperatures beyond 900°C. Thus, a strong temperature dependence of the reduction yield rate profile of methane reduction of ceria, which becomes higher and narrower at a higher temperature.

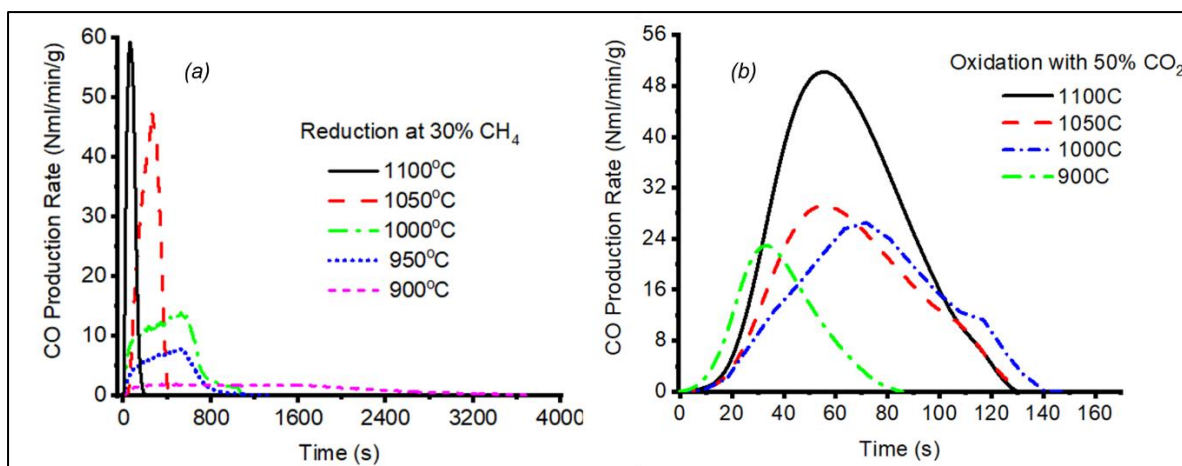


Figure 5-4. Variation of yield rates of CO in a) reduction and b) oxidation of CeO<sub>2</sub> in redox cycle of methane reduction followed by oxidation with CO<sub>2</sub> with the variation of temperature in the range 900°C and 1100°C at the following conditions:  $m_{\text{CeO}_2}$  : 250 mg;  $\dot{V}_{\text{gas}}$  : 120 Nml/min (balance Argon); Methane concentration during reduction: 30%; CO<sub>2</sub> concentration during oxidation: 50%, baseline reactor pressure: 1 atm.

On the other hand, for the oxidation reaction, a rapid rise in the CO yield is observed due to the rapid oxygen vacancies ion incorporation. Similar to the reduction reaction, after peak CO yield, the yield drops sharply for all temperatures approaching zero in 80-150 secs. It needs to be mentioned here that the oxidation cycles have experimented directly with the reduction cycles. Therefore, the performance of the oxidation reaction is directly influenced by the net non-stoichiometry generated in the reduction step. In this regard, since a lower non-stoichiometry was generated in the reduction reaction ( $\delta = 0.1015$ ) for reduction at 900°C, the net reaction time was lower. However, with an increase in temperature, the peak CO yield becomes higher and wider, indicating a high activation barrier associated with the CO<sub>2</sub> splitting process [180]. Figure 5-4.b emphasizes the observed behaviour of the peak rates at varying temperature for a fixed CO<sub>2</sub> molar fraction. The strong temperature dependence of CO<sub>2</sub> splitting observed in the present study is evident from the earlier studies as well [49,86,181].

Figure 5-5 shows the total yield of CO from the reduction of ceria by methane and the also the maximum non-stoichiometric factor ( $\delta_{\text{max}}$ ) of ceria reached in each reduction cycle with respect to temperature. The methane flow was kept constant at 30% and the total gas flow was maintained at 120 Nml/min.

The concentration of oxygen vacancies in the ceria slightly increases with an increase of CO<sub>2</sub> concentration in the feed, mainly at the higher temperatures. Figure 5-5 compares the difference in profiles of the non-stoichiometry ( $\delta$ ) as calculated in Eq. (5.6) during reduction. The initial stage of oxidation ends within the 20s, but accounts for more than 70% of the overall  $\delta$  change, while the remaining oxidation leads to a lower change of non-stoichiometry. It is evident that the oxygen carrying capacity increases due to a higher extent of non-stoichiometry achieved at higher temperatures. It can be noted that the non-stoichiometry increases from 0.07 to 0.21 in the 700–1000°C temperature range for 20% CO<sub>2</sub> mole fraction, and a maximum of 0.25 is

reached at 1000°C for 30% CO<sub>2</sub> mole fraction. Similar non-stoichiometry results for oxidation are reported elsewhere [49,72,173,182].

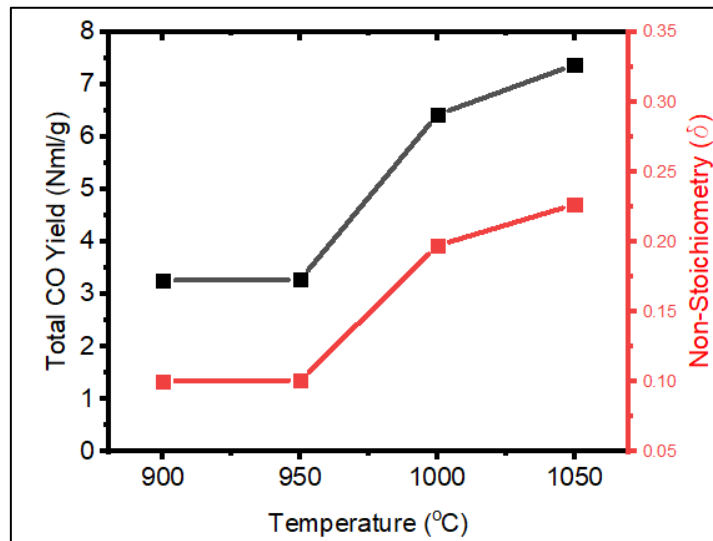


Figure 5-5. CO production and the maximum non-stoichiometry ( $\delta_{\max}$ ) during reduction as a function of temperature at the following conditions:  $m_{\text{CeO}_2}$  : 250 mg;  $\dot{V}_{\text{gas}}$  : 120 Nml/min (30% CH<sub>4</sub>, balance Argon); baseline reactor pressure: 1 atm.

### 5.3.2 Effect of concentration

The effect of the concentration of the reactants on the reduction and the oxidation kinetics of ceria with methane and CO<sub>2</sub> respectively was also investigated. Figure 5-6 clearly indicates that for both the reduction and the oxidation reaction, the reaction time decreases with an increase in the partial pressure of CH<sub>4</sub> and CO<sub>2</sub> in the feed, together with a higher peak rate of product yield. Similar effects from lower activation energies at higher CH<sub>4</sub> concentration during CH<sub>4</sub> reduction was reported by Warren et al [29] and Zhao et al [123], while for oxidation, Farooqui et al [173] reported similar reaction profiles. An increase in the conversion rate is counter-balanced by a decrease in the conversion time, and hence the net yield remains fairly constant for the point of interest.

For an instant, for the reduction at 1000°C, the maximum non-stoichiometry generated at lower concentrations (30% CH<sub>4</sub>, balance Argon) was slightly higher, 0.20, than for higher methane concentrations (50% CH<sub>4</sub>, balance Argon), around 0.184. On the other hand, the overall net yield of the oxidation with CO<sub>2</sub> remains constant always, due to a fixed reduction extent of ceria, the result is always completely oxidized ceria.

Also, as can be seen from Figure 5-6a, the peak shifts considerably to a lower time with higher methane concentrations, with a peak yield being noticed at around 200 secs for 50% concentration of methane, while for 20% methane in feed, a peak was obtained only after 1750 secs. In contrary, the oxidation reaction, even though occurring at a higher temperature, does not show such a significant impact of the variation of concentration, as can be noticed from Figure 5-6b. The peak remains constant between 60-70 secs range. In relation to the peak rate

variation with temperature, the variation was non-linear for the reduction reaction (Figure 5-6a). However, for the oxidation, the peak rate increases linearly with the concentration of CO<sub>2</sub> in the feed. The lower dependence of CO<sub>2</sub> splitting on the concentration of the CO<sub>2</sub> in the feed in comparison to methane for reduction has been reported elsewhere as well [49,173,182,183].

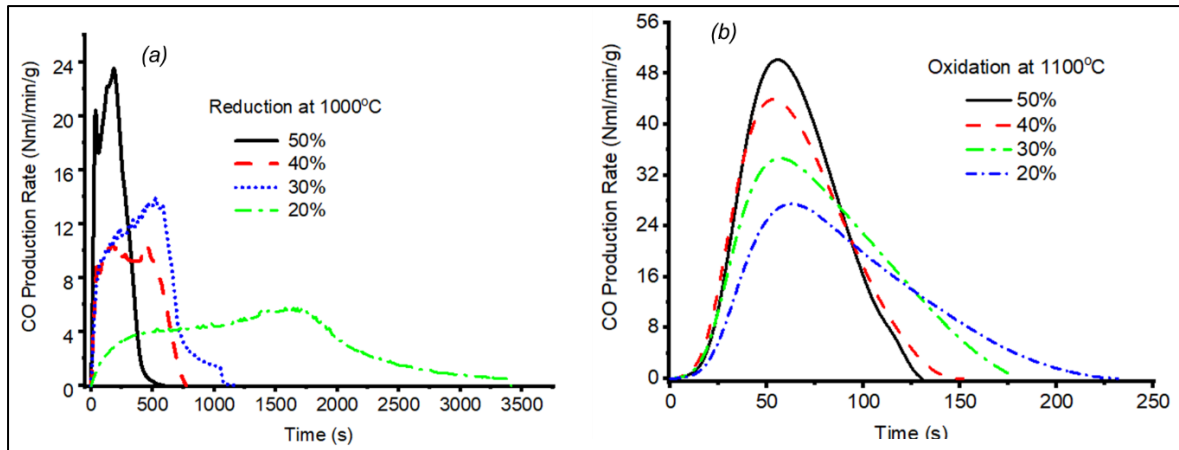


Figure 5-6. Variation of yield rates of CO in a) methane reduction of ceria at 1000°C and b) oxidation of reduced ceria at 1100°C with the variation of concentration of the gaseous reactants at the following conditions:  $m_{\text{CeO}_2}$  : 250 mg;  $\dot{V}_{\text{gas}}$  : 120 Nml/min (balance Argon); reactor pressure: 1 atm

## 5.4 Kinetic study

The evaluation of kinetic model parameters includes iso-conversion and isothermal reaction analysis [184]. For the present set of reactions, within the working envelope of the chemical looping process for narrow temperature range, the isothermal method was chosen. As reported by Han et al [185] the intra-particle heat gradients can be assumed negligible and thus the particle can be approximated to be isothermal.

In this work, the reaction kinetics study was evaluated by fitting different models to the experimental data shown in Section 5.3 to identify the solid-state reaction kinetic mechanistic model for both the reduction and oxidation of ceria. The most common metric adopted for the comparison of reaction models with experimental evidence is the reaction rate, measured in terms of the time profile of reactant conversion or product yield [186]. Three methods were used to compare several solid-state reaction kinetic models against isothermal experimental data. In particular, the methods are: (a) the fit quality of the transient conversion, ( $X$  vs.  $t$ ); (b) the fit quality of the transient time derivative of conversion ( $dX/dt$  vs.  $X$ ), and (c) the Hancock and Sharp Method or model-free method [178].

### 5.4.1 Model fitting method

The extent of reaction during the time is an important parameter involved in the kinetic study, which can be derived from the cumulative of the CO produced as equation (5.7). As CO was chosen the common parameter for both the reduction and oxidation reactions, hence, the following equation remains valid irrespective of the type of experiment performed.

$$cum(\dot{\omega}_{CO,i}) = \sum_{p=1}^{i-1} (\dot{\omega}_{CO,p}) + \dot{\omega}_{CO,i} \quad (5.7)$$

The extent of reaction (X) for each time instant is given by equation (5.8).

$$X(t_i) = \frac{cum(\dot{\omega}_{CO,i})}{cum(\dot{\omega}_{CO,N})} \quad (5.8)$$

Alternately, the extent of reaction at time  $t_i$  can be defined as the ratio between the  $i^{\text{th}}$  value of the cumulative and the final value of the cumulative. Essentially, this fixes the X to vary between 0 and 1. This results in the obtaining of the experimental  $\alpha$  that could be compared against the X derived from the models.

To obtain the kinetic model, a mathematical equation was being developed and the kinetic expression for the gas-solid reaction was expressed as per the following equation (5.9) [187]:

$$\frac{dX}{dt} = k_1 \cdot f(X) \cdot [P]^m \quad (5.9)$$

Where X is the conversion,  $k_1 = A \exp(-E_a / RT)$  and P is the partial pressure of the gas phase reactants (CH<sub>4</sub> or CO<sub>2</sub>), m is the reaction order and f(X) is a function of  $\alpha$  following the reaction mechanism. The coefficients A and E<sub>a</sub> are the Arrhenius parameters; E<sub>a</sub> being the activation energy. R is the universal gas constant equal to 8.314 kJ/mol/K.

The first step of calculations involves the fitting of the model to the raw data. This requires Eq. (5.8) to be transformed to the following equation (5.10):

$$\frac{dX}{f(X)} = K \cdot dt \quad (5.10)$$

Where  $K = k_1 \cdot P^m$  is expressed in terms of partial pressure of the gas phase reactants. The integral of the reaction model is expressed by integrating equation (5.11), which can also be expressed in a simplified manner as per equation (5.12).

$$g(X) = \int_0^X \frac{dX}{f(X)} \quad (5.11)$$

$$g(X) = K \cdot t \quad (5.12)$$

The slope of the curve  $g(X)$  vs  $t$  gives the parameter  $K$ . The slope between natural log of  $K$  vs  $1/T$  (Eq. 5.13) provides the activation energy, obtained as a negative slope. The intercept is the value of  $\ln(AP^m)$  where  $P$  is the partial pressure of the gas phase reactants. The reaction order was thereby evaluated by plotting  $\ln(AP^m)$  vs.  $\ln P$  (Eq. 5.14) with the slope being the reaction order and the intercept yielding the 'A' value.

$$\ln K = -\frac{E_a}{RT} + \ln A \cdot P^m \quad (5.13)$$

$$\ln[A \cdot P^m] = \ln A + m \ln P \quad (5.14)$$

The basic procedure needs to utilize the kinetic expressions of the models reported in Table 5-1 to match the experimental data obtained by evaluating  $dX/dt$  vs  $X$  and  $X$  vs  $t$  profiles. This is performed by fitting the value of the  $K$  parameter, and hence selecting the models with the smallest residual sum of squares (RSS) among candidate models with the same number of parameters [188].

## 5.5 Kinetic Parameter Evaluation

Based on the models listed in Table 5-1, a comprehensive evaluation with all the models was performed, together with finding the least RSS by fitting each model to the experimental results. Nevertheless, the AE3 model was found to fit best with the experimental results for both the reduction and oxidation reactions. The following section summarizes the kinetic results of the two sections of the redox cycle starting from the reduction of ceria with methane.

### 5.5.1 Reduction of $CeO_2$ by $CH_4$

As mentioned, based on the calculation of the least errors of all the models fitted to the experimental results, an average  $R^2$  value of 0.97 was obtained for the AE3 model, showing a good match. After the selection of the kinetic model, the evaluation of the kinetic parameters was carried out.

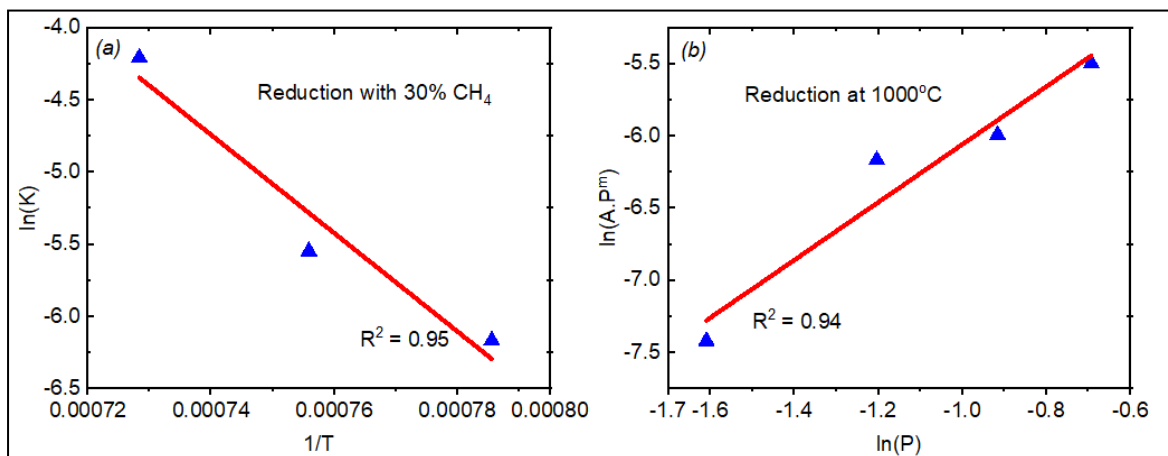


Figure 5-7. (a)  $\ln(K)$  vs  $(1/T)$  Arrhenius plot of the reduction reaction for AE3 model; (b)  $\ln(AP^m)$  vs  $\ln(P)$  plot for reduction reaction order determination.

The  $\ln(A \cdot P^m)$ , as obtained directly from the slope of the curve  $g(X)$  vs  $t$  was plotted first versus log of concentration in terms of partial pressure ( $\ln(P)$ ) to obtain the reaction order, as described in equation (5.14), as shown in Figure 5-7b. The reaction order obtained is  $2.0 \pm 0.36$ . Correspondingly,  $\ln(K)$  was plotted versus inverse of the temperature ( $1/T$ ) as described through equation (5.13). Figure 5-7a represents the  $\ln(K)$  vs ( $1/T$ ) plot reduction of ceria with 30% methane, the average activation energy was calculated as  $283.65 \pm 0.66$  kJ/mol within a 95% confidence level. The pre-exponential factor,  $A$  was calculated as  $8.67E9 \pm 433$  s<sup>-1</sup>.

Nonetheless, the concentration effect in terms of reactor order was further evaluated through curve fitting and was obtained to vary both with temperature and concentration. In this regard, a regression analysis between  $m$ ,  $T$  and  $P$  in terms of concentration was carried out for temperatures below 1050°C using statistical methods. The relation obtained is described by the following equation (5.14) and the corresponding RSS value obtained was 0.983. Beyond 1050°C, the reaction order was found to remain constant at 2.2.

$$m = 19.897 - 0.013 \times [T] - 1.28 \times [P] \quad (5.15)$$

Where  $T$  is in Kelvin and  $P$  is the concentration or partial pressure of the gaseous reactant, considering ideal gas laws.

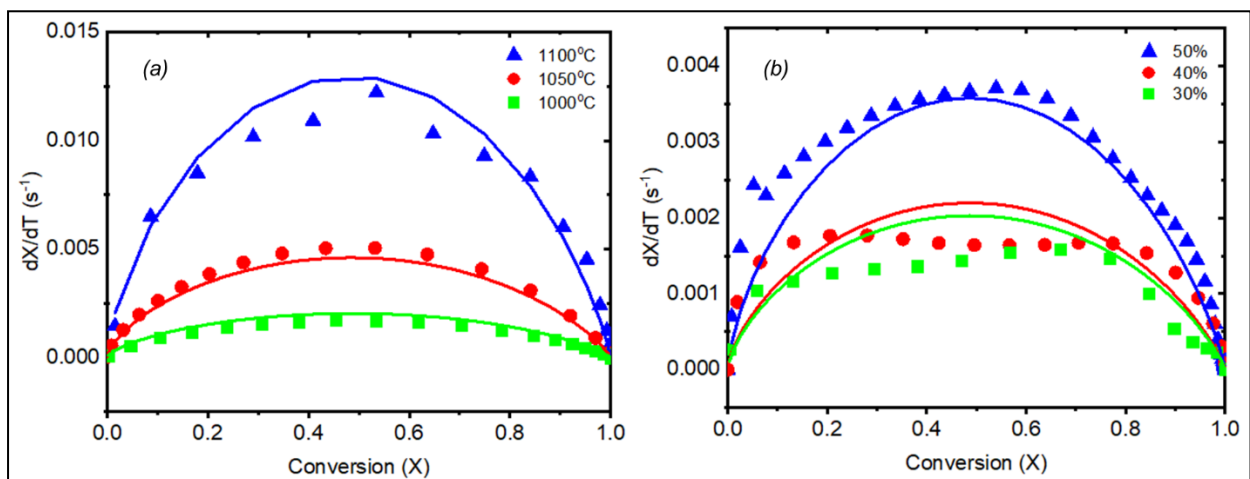


Figure 5-8. Comparison of the kinetic model and the experimental data for methane reduction of ceria (a) with the variation in temperature, 1000°C, 1050°C, 1100°C and (b) with the concentration of CH<sub>4</sub> of 30%, 40% and 50% for reactor pressure of 1 atm. The symbol represents experimental data and lines represent the kinetic model

The value of activation energy and the other constants obtained in the model fit well to the experimental results, as obtained through curve fitting using the proposed model, shown in the following Figure 5-8. A good agreement of the results, both with respect to concentration and temperature variation can be seen. Nevertheless, as opposed to the report by Warren et al [29], the present results show considerable divergence towards a higher value of activation energy, as available in literature. Even so, no study has reported the complete SS model development for the said reaction. Therefore, no comprehensive comparison with literature data can be done. Nonetheless, A slight over-estimation for lower concentrations are obtained, while for higher concentration, the model slightly underpredicts the yield of the products. Nevertheless, all the

results lie within the 95% confidence level and agree well with values obtained in literature, as described earlier.

### 5.5.2 Oxidation of $CeO_{2-\delta}$ by $CO_2$

Like the reduction reaction, a similar curve fitting was performed using least square of errors on all the models listed in Table 5.1. As like the reduction reaction, the AE3 model fits best with the experimental results and the average  $R^2$  value obtained was 0.98, showing a good match.

A similar procedure, as discussed for the reduction reaction, to obtain the reaction order and the activation energy was carried out. The  $\ln(A \cdot P^m)$ , as obtained directly from the slope of the curve  $g(X)$  vs  $t$  was plotted first versus log of concentration ( $\ln(P)$ ) to obtain the reaction order, as described in equation (5.14) (Figure 5-9b). The reaction order obtained is  $0.732 \pm 0.186$ . Correspondingly,  $\ln(K)$ , was plotted versus inverse of temperature ( $1/T$ ) as described through equation (5.13). Figure 5-9a represents the  $\ln(K)$  vs ( $1/T$ ) plot oxidation with 50%  $CO_2$ , the average activation energy was calculated as  $59.68 \pm 16.09$  kJ/mol. The pre-exponential factor, A was calculated as  $59.68 \pm 1.45$  s<sup>-1</sup>.

Nonetheless, the concentration effect in terms of reactor order was further evaluated through curve fitting similarly as before and was obtained to vary both with temperature and concentration. In this regard, a regression analysis between  $m$ ,  $T$  and  $P$  in terms of concentration was carried out for all temperatures and concentrations using statistical methods. The relation obtained is described by the following equation (5.16) and the corresponding RSS value obtained was 0.985.

$$m = 0.002 \times [T] - 7.5 \times [P] - 1.996 \quad (5.16)$$

Where  $T$  is in Kelvin and  $P$  is the concentration or partial pressure of the gaseous reactant, considering ideal gas laws.

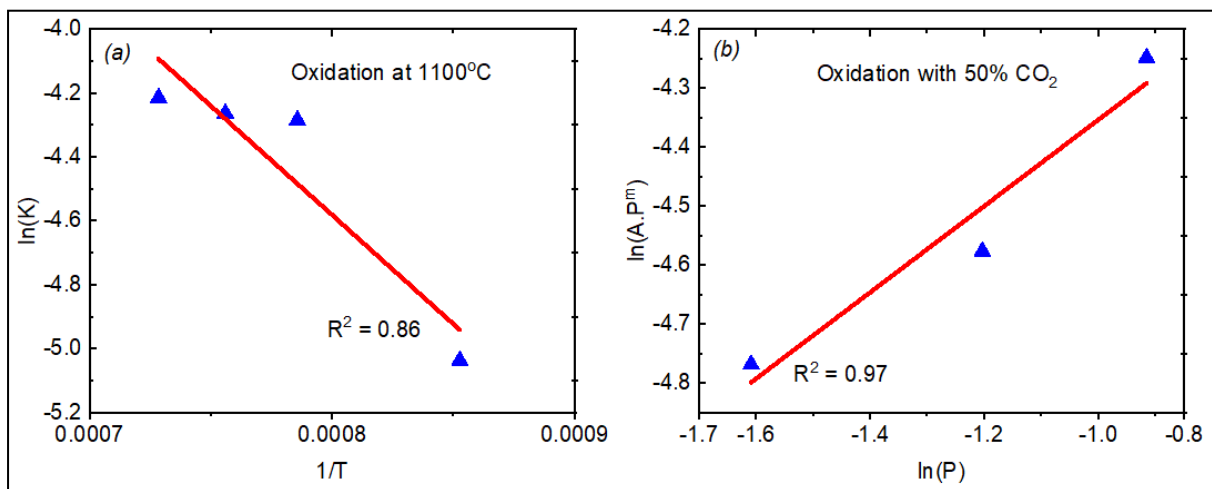


Figure 5-9. (a)  $\ln(K)$  vs ( $1/T$ ) Arrhenius plot of the reduction reaction for AE3 model; (b)  $\ln(AP^m)$  vs  $\ln(P)$  plot for reduction reaction order determination

Similar validation studies were performed with the model fit and the experimental results. The values obtained match closely with the results presented by Farooqui et al [173] for oxidation of ceria following hydrogen reduction, where the activation energy obtained was 79 kJ/mol [173]. Nonetheless, curve fitting using the obtained value was performed and presented in the following Figure 5-10. A good agreement of the results, both with respect to concentration and temperature variation can be seen. A slight over-estimation for lower concentrations are obtained like reduction, however, for higher concentrations a very good fit with is seen. An overall confidence level of the model with respect to experimental results of more than 95% is reached while agreeing well to the values obtained in similar studies performed reported in the literature.

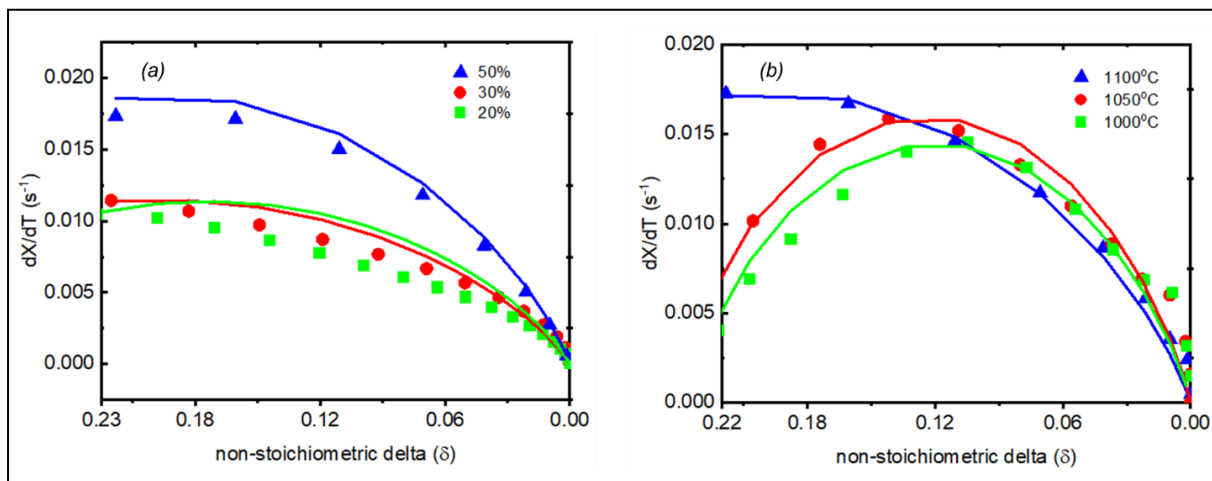


Figure 5-10. Comparison of the kinetic model and the experimental data for oxidation of reduced ceria with  $CO_2$  (a) with the variation in concentration of  $CO_2$  of 50%, 30% and 20% (b) with temperature of 1000°C, 1050°C, 1100°C for reactor pressure of 1 atm and a constant non-stoichiometric extent of reduced ceria of 0.22. The symbol represents experimental data and lines represent the kinetic model

## 5.6 Discussions and Conclusions

Carbon deposition was noticed to small extents at 1050°C, which increased subsequently at 1100°C. However, this can be followed from numerous discussions presented in literature regarding the same. Carbon deposition for methane reduction of ceria at over 1100°C and for a  $\delta$  of over 0.2 has been reported by Otsuka et al [168,169]. Furthermore, methane cracking has also been reported to be enhanced at temperatures above 1100°C in the presence of alumina ( $Al_2O_3$ ) [189], which is also the material of the crucible used in the present reactor. In addition, passing of excess amount of methane or excessive residence times could also lead to significant carbon deposition, even though not considered as conditions in the present set of experiments [190]. However, Warren et al reported decreased Carbon deposition from using Platinum crucible as a replacement of alumina or quartz crucible for experimental purpose [29].

Nevertheless, in this chapter the comprehensive Kinetic model was developed to describe the reaction of POM with commercial ceria and corresponding oxidation with  $CO_2$  over a wide

range of temperature, 900-1100°C and concentration of the reactants. The entire reaction set-up was carried out in atmospheric conditions, indicating the high kinetic potential of the reduction reaction even at such conditions, as opposed to thermal reduction of ceria, requiring deep vacuum conditions. The AE3 model was found to fit best to the experimental data for both the reduction and oxidation reactions. A varying reaction order with varying reaction conditions was noticed and a relation was obtained for both the cases. Carbon deposition would limit the operation of the reduction at temperatures over 1100°C, even though a very fast reaction would result.

## **6 System Evaluation of Novel Oxy-fuel NGCC Integrated with Chemical Looping Cycle and CCS**

As discussed previously, the energy penalty from CCS is of considerable concern, even though it ensures lower emissions of power production from fossil fuels. Plant scale configurations integrating chemical looping for power production has been carried out, however, utilizing thermal reduction utilizing concentrated solar. Even though Gencer et al proposed a system for solar hydrogen generation with subsequent round the clock power production at an average efficiency of 35% with ceria as the oxygen carrier [116], till date, no complete system analysis of the NGCC power production with the CL CO<sub>2</sub>/H<sub>2</sub>O splitting unit with methane reduction of ceria has been studied for utility-scale applications. Furthermore, existing literature, comparative evaluation of individual capture technologies is difficult due to variations in modelling assumptions regarding the type of fuel used, the scale of power output and efficiencies of individual process units. In the previous section an add-on unit with solar reduction of ceria has been proposed and evaluated, however, with limitations of optimal operation round the clock, variation of yield with availability of solar energy and need for operation under very high vacuum conditions. Indeed, unlike the previous plant layout design, the present design focuses on a new NGCC power plant integrated with the CL unit, rather than a retrofit power plant. This is because the methane reduction of ceria would necessitate considerable system design changes to the original plant.

In the present section, an Oxy-fuel combustion power plant integrated with a chemical looping CO<sub>2</sub>/H<sub>2</sub>O dissociation with methane reduction of ceria (MCLP-OXY-CC) unit has been proposed and evaluated. The results have been compared with a conventional NGCC without carbon capture and an Oxyfuel-combustion power plant (OXY-CC) with carbon capture technology through simulation studies via common modelling assumptions and considerations. The two capture technologies were analysed against a conventional NGCC process without capture to estimate and compare, besides the energy penalty associated with CO<sub>2</sub> capture, economic and other environmental impacts as well. An overall exergetic performance comparison was also performed for the NGCC, OXY-CC and MCLP-OXY-CC processes to compare the plant performance. A detailed exergetic study was carried out for the proposed system separately to identify the sources of irreversibility in each process, and hence, the scope for improvement and optimization. Power production, power consumption, electrical efficiency, CO<sub>2</sub> capture efficiency, exergy, economic performance, land and water footprint are the key parameters investigated and their variation is reported in the present work.

### **6.1 Process Description and Plant Configuration**

As described in the previous section, methane reduction of ceria presents multiple advantages over solar driven chemical looping cycles, including continuity of operation and lower operating temperatures of the chemical looping unit. To develop the system layout and evaluate

the highest possible performance of the integrated system, a thermodynamic redox pair of  $\text{CeO}_2/\text{Ce}_2\text{O}_3$  for stoichiometric reduction of ceria for maximum redox pair utilization was considered. Accordingly, the  $\text{CeO}_2/\text{Ce}_2\text{O}_3$  redox pair with reduction of  $\text{CeO}_2$  in the presence of methane, and subsequent oxidation with  $\text{CO}_2/\text{H}_2\text{O}$  was utilized, as described by the equations (Chapter 4). Details of the reactions in the respective reactors can be found in Chapter 4.1

Figure 6-1 presents the block diagrams of the conventional NGCC, OXY-CC and the novel CL coupled Oxyfuel (MCLP-OXY-CC) process. The process description of the traditional NGCC and OXY-CC are outside the scope of this text and can be found in multiple kinds of literature [148,191]. A complete CL integrated novel Oxyfuel NGCC power plant (MCLP-OXY-CC), comprising several operating units including the reduction reactor (RED) and the oxidation reactor (OXI), as integral parts of the CL unit, together with traditional units of an oxyfuel power plant including cryogenic ASU has been proposed and described in the following section.

The heart of the proposed MCLP-OXY-CC plant is the chemical looping  $\text{CO}_2/\text{H}_2\text{O}$  splitting unit (CL). The CL unit works at a considerably lower pressure than that of the natural gas supply of around 70 bars from the gas networks from the outside battery limit (OSBL). Therefore, the gas needs to be expanded to the working pressure of the CL unit. Pre-heating of the inlet natural gas by the process heat of the power plant can considerably improve the net work obtained by such expansion. The expanded methane is further pre-heated and supplied to the reduction reactor (RED) where it is partially oxidized into CO and  $\text{H}_2$ , producing syngas, while reducing the cerium (IV) oxide to cerium (III) oxide as per equation (3). The selection of the operating temperatures is crucial to prevent the complete oxidation of the methane to  $\text{CO}_2$  and water, simultaneously preventing carbon deposition through methane cracking.

The reduction reaction is highly endothermic, requiring a large amount of supplemental heat to maintain the reforming temperature and drive the reaction forward. The metal oxide reduction by methane is preferably operated at elevated temperatures of above  $900^\circ\text{C}$  to ensure more than 99% conversion of the methane to CO and  $\text{H}_2$ . However, it has been observed from thermodynamic studies that around 40% to 60% excess flow of methane is necessary to ensure complete reduction of metal at temperatures below  $950^\circ\text{C}$ . As also deduced in the previous Chapter4, the most suitable methane to ceria ( $\text{CH}_4/\text{CeO}_2$ ) flow ratio was 0.7, higher than the stoichiometric ratio of 0.5, and was hence selected for the present system deployment. As for the pressure, multiple advantages and disadvantages exist for systems working at higher pressures. While solids handling is a major challenge for higher pressure, the previous study by Harrison [192] revealed the economic advantage of methane conversions at a higher pressure between 5-25 atm. Nevertheless, commercial relatively low-cost technologies were found to increase the metal oxide pressure to 6 bars [193], together with the thermodynamic constraints limiting the very high operating pressures for reduction step of thermochemical redox cycle.

In the present power plant, instead of combusting the natural gas, combustion of syngas in the form of partially oxidized methane has been proposed. Being an oxyfuel power plant, the combustion is done by near stoichiometric oxygen (5% excess) generated via a cryogenic ASU,

that adds to considerable power penalty to the conventional NGCC. A part of the captured CO<sub>2</sub> is re-circulated back to the combustor to maintain the temperature of the outlet combustion gases into the turbine of the Gas turbine cycle.

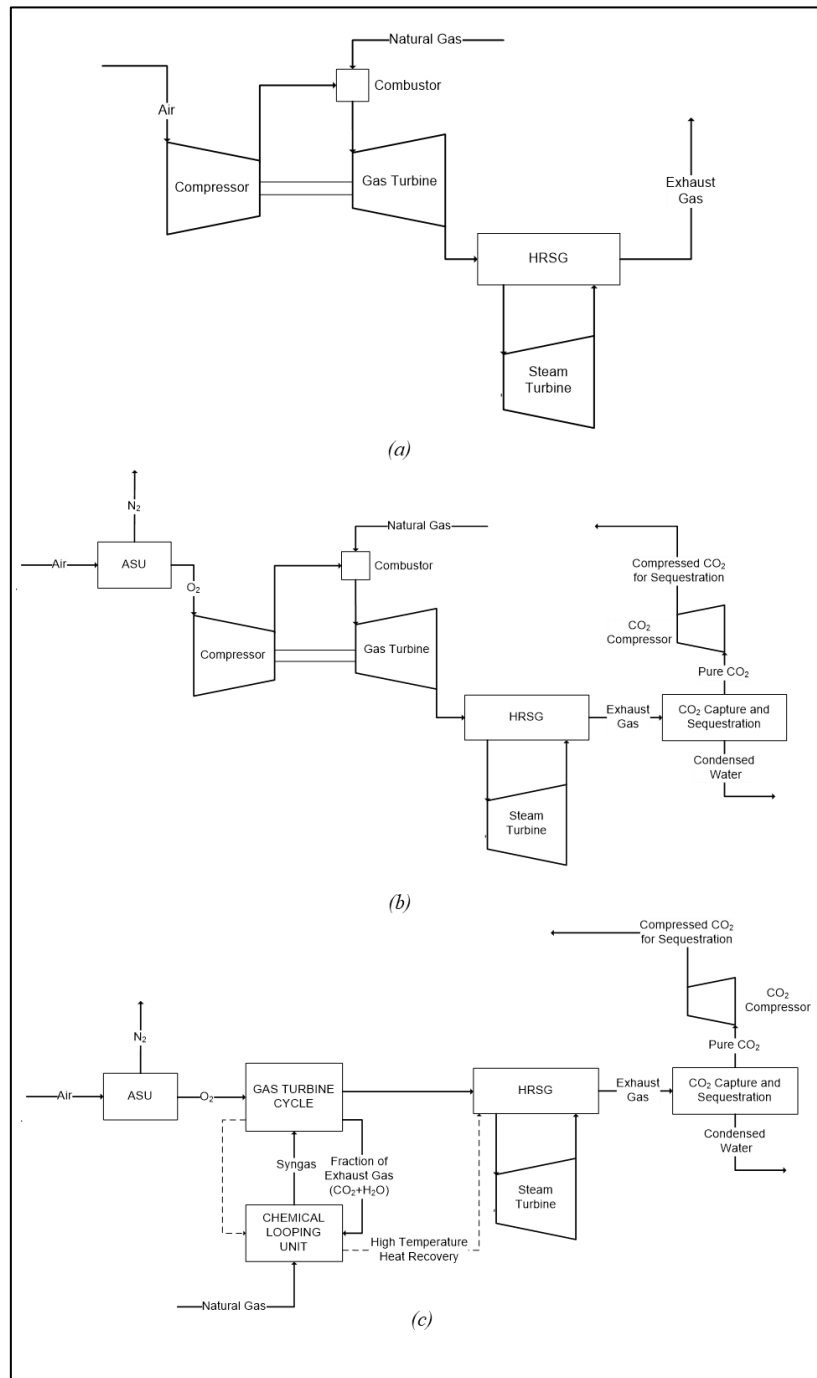


Figure 6-1 Block Diagram of NGCC, OXY-CC and the novel MCLP-OXY-CC process

The partial oxidation of methane in reduction reactor (RED) is highly endothermic, requiring around 50kW of heat per mol of Ce<sub>2</sub>O<sub>3</sub> reduced. A large amount of heat has been proposed to be supplied by heat integration with the combustor of the gas turbine cycle as shown in Figure 6-1. An annular reactor design is hence necessary whereby, the inner reactor would be the

reduction reactor of the chemical looping unit, while the outer reactor would perform the work of the combustor. Such a reactor design, however, exist in literature, whereby detailed information on such reactor design concept can be obtained [194]. Modulating the quantity of CO<sub>2</sub> for recirculation within the reduction reactor, the net duty of the reduction reactor can be controlled, to provide the necessary heat required to drive the reduction reaction.

A part of the exhaust from the gas turbine has been proposed to be utilized for CO<sub>2</sub>/H<sub>2</sub>O splitting within the oxidation reactor (OXI) of the CL unit. A complete reaction would not only generate additional fuel in the form of syngas, that will then be utilized to produce additional power, adding to the system capacity further, but also oxidize the metal oxide back to the higher valence state (CeO<sub>2</sub>), that can then be recirculated back to the reduction reactor (RED) to continue the chemical looping cycle. However, auxiliary consumptions from compression for syngas and CO<sub>2</sub> for recycling would necessitate system optimization and identify suitable operating conditions. The oxidation reactions, as presented in equation (4) are essentially exothermic, which provides benefits of system control and improvement of efficiency by allowing generation of additional steam, as shown in Figure 6-1 (c). This would also simplify the recycling of the metal oxide between and RED and OXI reactors by eliminating the need of an additional heat exchanger for heating the oxidized metal oxide, and hence requiring lower heat duty for the reduction step. Higher the metal oxide temperature lower would be needed for supplementary heating. Therefore, an outlet temperature of around 1300-1400°C from the oxidation reactor (OXI) would provide a significant advantage, requiring no intermediate heating needs for the oxidized metal oxide and increasing the mass flow of the exhaust gas due to higher recirculation of CO<sub>2</sub>.

The exhaust gases from the gas turbines at elevated temperatures of over 800°C would then be utilized for steam generation within the heat recovery steam generator (HRSG). Being an oxyfuel power plant and having natural gas as fuel, the impurities in the exhaust gas, especially SO<sub>x</sub>, NO<sub>x</sub> and particulates are negligible, allowing the gas to be cooled down to near ambient temperatures of around 50°C, providing considerable advantages to the system efficiency, unlike traditional NGCC, where it is limited to about 140°C to prevent acid condensation. Carbon capture methodologies are followed from traditional oxyfuel units, where, due to the high purity of the flue gas, simple water condensation leads to more than 99% pure CO<sub>2</sub>. Besides the recirculated fraction of CO<sub>2</sub>, the rest was sent for storage after compressing to a pressure of 110 bars.

In general, due to the addition of the CL unit, that recycles and utilizes a part of the exhaust gases within and for the system, a net improvement of the system efficiency has been envisaged. The novelty of this layout is, therefore, to improve the efficiency penalty through the addition of the CL unit to the conventional oxyfuel combined cycle with carbon capture while maintaining the same effectiveness of carbon capture by a typical oxyfuel unit of close to 100%.

## 6.2 Process Simulation and Assumptions

In this section, the detailed schematic of the conventional NGCC, OXY-CC and the proposed novel MCLP-OXY-CC are simulated using ASPEN Plus<sup>®</sup> (v8.8) and its corresponding existing functions and built-in modules. As per discussed in Chapter 3.5, in all the three processes, the PR-BM method was selected for the simulations. Similar nomenclature to the corresponding units as taken for the SCLP-OXY-CC add-on unit (Section 3.5) have also been used in the present section and hence not explain in detail again.

The assumptions considered in the three processes based on ASPEN Plus are summarized below:

- The heat losses in the RED and combustion process were neglected, while a pressure drop of 0.1 bar was considered in the combustion chambers (COMB1 and COMB2).
- A loss of 1% in the high-temperature gas lines were considered, especially for gases being transferred between components.
- The excess air number was considered as 1.05 for the oxy-combustion process.
- Equilibrium reactions have been considered in the RED and OXI, as well as the combustion chambers (COMB1 and COMB2), where the reaction residence time was long enough to achieve chemical and phase equilibrium.
- Steady-state simulations were performed, and the results hence obtained are not applicable to start-up or transient operations.
- Ambient temperature was assumed as 25°C. Air was assumed to comprise 79% N<sub>2</sub> and 21%O<sub>2</sub> on a volume basis.
- Minimum approach temperature in heat exchangers was taken as 10°C [131].
- The isentropic efficiency and mechanical efficiency for compressors and turbines were considered as 0.9 and 0.98, respectively. The pump efficiency was assumed to be 0.85 and 0.9, for isentropic and mechanical efficiency respectively.
- In actual scenario, natural gas instead of pure methane would be fed to RED. Even though the purity of natural gas with respect to the sulphur content is considerably high, typical clean-up processes would be required. However, the removal of sulphur from the specific application was not considered within the specific layout. Nevertheless, since no catalyst exists within the entire process, the purity on natural gas would not be a major concern, especially with respect to the operation of the CL unit.
- The primary objective of the present study is to recognize the potential efficiency gain from the combination of the chemical looping unit in a conventional oxyfuel plant, then the turbines and the HSRG were modelled as simple units, without reheating or multi-pressure systems. Indeed, by increasing the model complexity, the net efficiency can be gained considerably by process optimization for all the three cycles.

In addition to the general assumptions, specific design assumptions with respect to individual units of the NGCC, OXY-CC and MCLP-OXY-CC units, that were considered, have been shown in Table 6-1. Indeed, it has to be mentioned that the new system is not a retrofit, as it

has been designed considering a separate entity, not being limited by parameters of a conventional NGCC.

Table 6-1 Design assumptions used for developing the process flowsheet models in ASPEN plus

Unit	Applicable to	Parameters
ASU	OXY-CC and MCLP-OXY- CC	<ul style="list-style-type: none"> <li>• O<sub>2</sub> purity: 99.9% (by volume)</li> <li>• ASU O<sub>2</sub> and N<sub>2</sub> delivery pressure: 1.2 bars</li> <li>• O<sub>2</sub> compression pressure: 26 bars for COMB-1 and 18 bars for COMB-2</li> <li>• No use of N<sub>2</sub> was considered</li> </ul>
Turbo Expander	MCLP-OXY- CC	<ul style="list-style-type: none"> <li>• Feed Pressure of Natural Gas from OSBL: 70 bars</li> <li>• Expansion Ratio: 35</li> <li>• Inlet Temperature of NG: 25° C</li> </ul>
Combustion Chamber	All	<ul style="list-style-type: none"> <li>• Excess Air factor: 182%</li> <li>• Excess Oxygen factor: 5%</li> <li>• Combustor Pressure Drop: 0.1 bar</li> </ul>
Reduction Reactor (RED) and Combustion Chamber, COMB-1	MCLP-OXY- CC	<ul style="list-style-type: none"> <li>• Reactors were modelled separately with complete heat integration</li> <li>• Working pressure: 26 bars in Combustor Side and 2 bars in Reducer Side</li> <li>• Methane Conversion: 99%</li> </ul>
Oxidation reactor (OXI)	MCLP-OXY- CC	<ul style="list-style-type: none"> <li>• Reactor Type: Adiabatic, jacketed for high-temperature steam generation</li> <li>• Outlet Product Temperature: 1380°C</li> <li>• Working Pressure: 2 bars</li> </ul>
CO <sub>2</sub> Drying and Compression	OXY-CC and MCLP-OXY- CC	<ul style="list-style-type: none"> <li>• Delivery pressure: 110 bars</li> <li>• Delivery temperature: 40°C</li> <li>• Compressor isentropic efficiency: 90%</li> <li>• Compressor mechanical efficiency: 98%</li> </ul>
Gas Turbine/ Expander	All	<ul style="list-style-type: none"> <li>• Isentropic efficiency: 90%</li> <li>• Maximum pressure ratio: 18:1</li> <li>• Discharge pressure: 1.04 bar</li> <li>• Turbine inlet temperature (TIT): 1277°C (1550K) for NGCC and Oxy-CL and 1377°C (1650K) for MCLP-OXY-CC</li> </ul>
Steam Turbine and HRSG	All	<ul style="list-style-type: none"> <li>• Turbine Isentropic efficiency: 90%</li> <li>• Steam Pressure: 120 bars for NGCC and OXY-CC and 150 bars for MCLP-OXY-CC</li> <li>• Condenser pressure: 0.04 bar</li> <li>• Pump Isentropic Efficiency: 0.8</li> <li>• Minimum Approach Temperature: 10°C with no pressure drop</li> </ul>

A detailed description of the MCLP-OXY-CC cycle as simulated within the ASPEN Plus environment is described as per depicted in Figure 6-2. Natural Gas (as per composition shown in Table 6-2) is fed into the system at 20°C and 70 bar pressure from outside battery limit (OSBL) [195].

Table 6-2 NG Composition Assumed

Component	Value (% Mole Fraction)
Methane	94.00%
Ethane	4.20%
Propane	0.30%
CO <sub>2</sub>	0.50%
N <sub>2</sub>	1.00%
Total	100.00%

This natural gas is preheated with the syngas from the reduction reactor (Stream 4) before being expanded through a turbo-expander (TURBO-EXP) to the operating pressure of the chemical looping (CL) unit of 2 bars. The natural gas is then further pre-heated, where it is then fed to the reduction reactor (RED) at a temperature of approximately 890°C. The oxidized Ceria, in the form of Ceria (IV) Oxide, Ce<sub>2</sub>O<sub>3</sub>, (Stream 44), is fed at a temperature of 1375°C to the reduction reactor. Based on the thermodynamic results, the natural gas to ceria (CH<sub>4</sub>/CeO<sub>2</sub>) feed flow ratio of 0.7 is maintained for complete reduction of metallic ceria, to increase its effectiveness as an oxygen carrier. The heat of the reaction in the RED is provided directly by the heat of oxy-combustion of the syngas. The syngas, after exiting the reduction reactor at around 906°C, is used for methane heating, as well as, preheating of oxygen to around 140°C before entering the combustion chamber (COMB-1). The cooled syngas, compressed to 26 bars by COMP-1 is fed to the combustion chamber, COMB-1. The Combustion outlet temperature and hence the TIT is directly regulated by the flow of recycled CO<sub>2</sub>, which, however, is also dependant on the heat needed to carry the reduction reactor forward in RED. The oxygen supplied for combustion is produced via a cryogenic air separation unit (ASU). A cryogenic pump was employed (O-PUMP) to increase the pressure of liquid oxygen, removing the need for an oxygen compression, thereby significantly reducing the plant auxiliary consumption.

To take advantage of the fact that the CL unit operates at a pressure of 2 bars, the turbine inlet pressure to the primary gas turbine was set at 26 bars to maximize the system outputs. The expanded gas (Stream-10) from the first gas turbine (GT1-1), around 1115°C is split into two streams. One stream is fed to the oxidation reactor (OXI) for CO<sub>2</sub> and H<sub>2</sub>O splitting to produce syngas as a fuel, while the remaining flue gas (Stream-12) is fed into the second gas turbine (GT1-2), where it is expanded to a near atmospheric pressure of 1.04 bar.

The CO<sub>2</sub>/H<sub>2</sub>O splitting reactions are highly exothermic, and the metal oxide exit temperature is controlled via jacketed cooling. The product exit temperature of OXI is set as being equal to the feed temperature of the reduction reactor RED, which is around 1380°C. The hot raw syngas at around 1380°C from OXI (Stream-16) is cooled to around 50°C in a heat recovery steam generation unit (HRSG-2). The cooled raw syngas is compressed to 18 bars (COMP-2) before

being fed into the second combustion chamber (COMB-2) and subsequently into the Gas turbine at 1650K, 18 bars (Stream 19). The exhaust gases from the two combustion chambers (Streams 13 and 20) are then mixed and fed into the HRSG (HRSG-1) for heat recovery steam generation by the downstream steam cycle. Being high purity gas, composed primarily of CO<sub>2</sub> and water, the gas was cooled down to near ambient temperatures of 50°C. A live steam of 150 bars and 596°C was generated for power production via the steam cycle from both the HRSGs (Stream-38 and 39). The flow of steam was calculated accordingly. As mentioned, a simple single turbine Rankine cycle was modelled. The expanded steam at 0.4 bars is passed through a condenser (ST-COND) and pump (ST-PUMP) to subsequently complete the steam cycle.

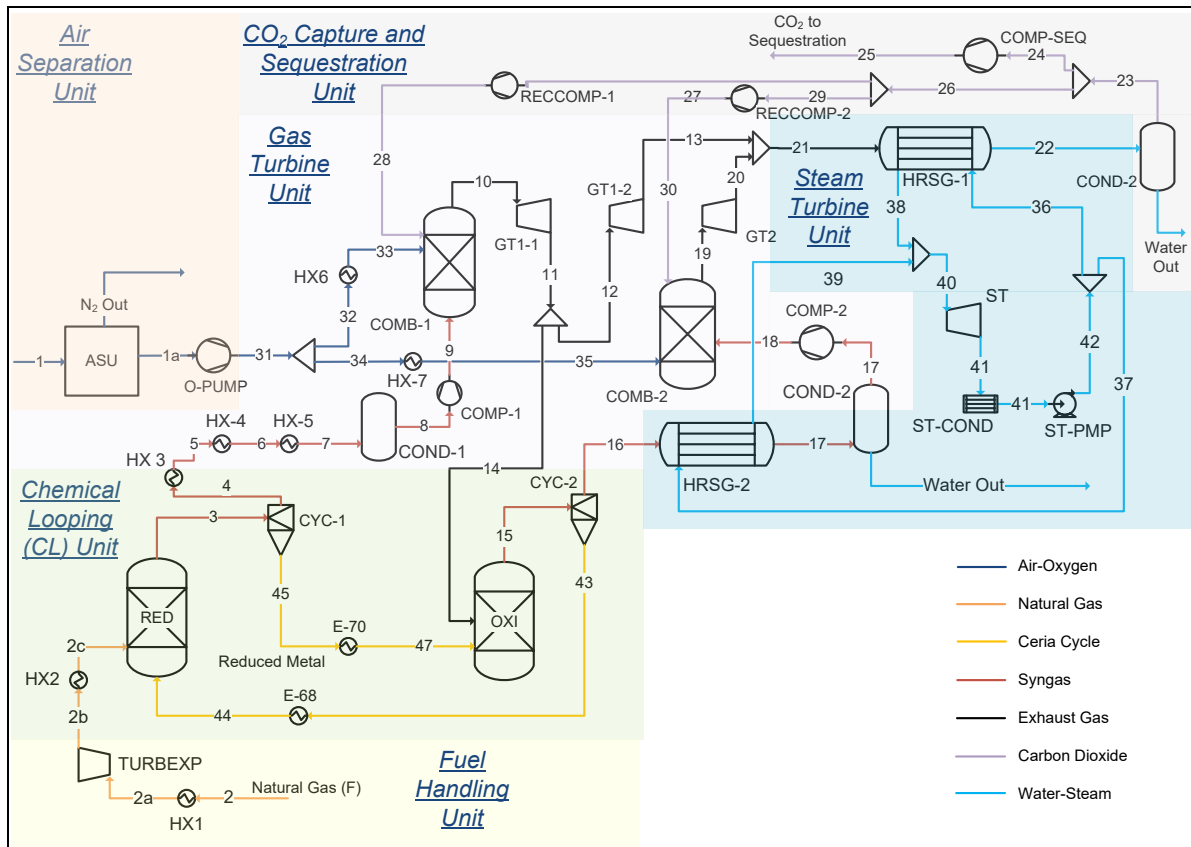


Figure 6-2 Process simulation flowsheet of MCLP-OXY-CC unit

The clean and cool exhaust gas from HRSG-1 (Stream-21), at 50°C and 1.04 bar is fed into a flash chamber (COND-3), where the water is separated and almost 99% pure CO<sub>2</sub> is obtained. This CO<sub>2</sub> is therefore split into two streams. One stream (Stream-26) is further compressed and recycled back into the combustion chambers for temperature control as mentioned before. However, the other stream (Stream-24) is compressed to 110 bars by COMP-SEQ and sent for sequestration outside the battery limit of the designed power plant. Besides the discussed heat exchangers, no additional heat integration was considered. Indeed, a pinch analysis would be necessary thus to understand the heat availability in the unit and subsequently an improved design with better and improved location of heat exchangers can be developed in future.

The syngas composition exiting the two reactors of the chemical looping unit is shown in Table 6-3. The noticeable differences lie in the relative fraction of the H<sub>2</sub> and CO compositions of the two streams. While the H<sub>2</sub>/CO ratio in the RED is 1.9, the corresponding value for the OXI is 0.16. Due to the supply of excess methane to the RED, the methane content in the outlet stream of the Reduction reactor is considerable. However, no methane is produced during the splitting reaction in the OXI. The content of water and CO<sub>2</sub> forms about 1.2% in the reduction reactor, while the corresponding value is higher in the OXI since excess reactants were passed to ensure complete reaction.

Table 6-3 Syngas composition from the Reduction Reactor (RED) and the Oxidation Reactor (OXI) of the Chemical Looping Unit

Mole Fraction (%)	From RED	FROM OXI
CO	28.43	61.4
H <sub>2</sub>	54.23	9.84
CO <sub>2</sub>	0.85	18.87
H <sub>2</sub> O	0.35	9.63
CH <sub>4</sub>	15.71	Trace
N <sub>2</sub>	0.43	0.26
Total	100	100

Chemical looping, for the simultaneous splitting of CO<sub>2</sub> and H<sub>2</sub>O, resulting in the formation syngas has great potential to improve the system efficiency by providing additional fuel with high calorific value leading to CO<sub>2</sub> recycling. The cycle can either be driven by concentrated solar energy or through the chemical energy of methane, the later having multiple benefits, as already discussed in the previous sections.

### 6.3 Thermodynamic Assessment Methodology

Based on the above selections, the system performance and techno-economic assessments of the MCLP-OXY-CC power plant were carried out as per the methodology, depicted in Figure 6-3. It should be stressed that several alternative plant configurations, differing in strategies for integration of the CL unit to the traditional system and subsequent mode of utilization of the syngas generated from the oxidation reactor were conceptualized and examined. However, all possible combinations of interest could not be presented within the scope of the present work. The assessments presented herein were performed using a combined ASPEN Plus model and an in-house spread-sheet developed specifically for the current study.

The process evaluation, techno-economic study and sustainability assessments summarized in the subsequent chapter does not include considerations of retrofitting existing state of the art NGCC or oxyfuel NGCC power plants. This is due to considerable complexity identified for such integrations, which can be found within the explanations of the subsequent sections. The key technical performance indicators evaluated are (i) plant thermal efficiency, (ii) plant

thermal efficiency penalty, and (iii) relative efficiency gain, (iv) plant exergetic efficiency and (v) plant-specific emission savings.

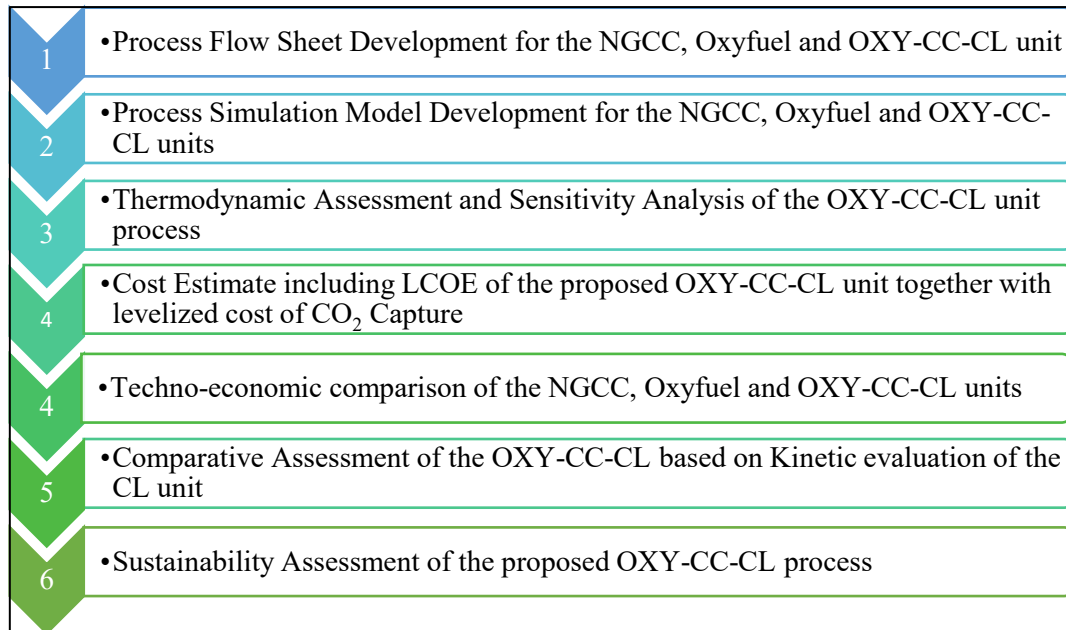


Figure 6-3 Methodology for Techno-economic and Sustainability Assessment

The economic assessment of the proposed MCLP-OXY-CC unit with the corresponding comparison with NGCC and OXY-CC with Carbon capture was performed based on the different cost data available in the literature. The key economic performance indicators being evaluated are (i) power plant capital cost, (ii) operating costs, (iii) Levelized Cost of Electricity (LCOE) and (iv) cost of CO<sub>2</sub> avoided as Levelized Cost of CO<sub>2</sub> Savings. Besides techno-economic assessment, sustainability assessment through water and land footprint assessment was performed based on existing methodologies available in the literature.

### 6.3.1 Energy Analysis

Similar to energy assessment performed in previous chapters, the energetic efficiency based on the first law of thermodynamics has been defined and used depending on the fuel energy input in natural gas to the system ( $\eta_I$ ). However, this simplified approach fails to provide a detailed system evaluation, especially concerning the correct evaluation of heat flows (in heat exchangers and other components where significant heat transfer is designed to occur).

### 6.3.2 Exergy Analysis

Exergy analysis or availability analysis, based on the second law of thermodynamics, is used to measure the maximum theoretical work. The exergy value, unlike the energy value of a stream, is based on its temperature, pressure and compositions as the stream passes from a given state to a state in equilibrium with the environment. Therefore, exergetic evaluation of

each material or energy stream is directly related to the assumed environmental state, which, in the present study was considered as  $T_0 = 25^\circ\text{C}$  and  $P_0 = 1\text{atm}$ .

For steady state operations of an entire process, the total exergy destruction ( $\dot{E}x_{\text{destr}}$ ) can be calculated via exergy balance as written by the following equation (6.1):

$$\dot{E}x_{\text{destr}} = \dot{E}x_{\text{in}} - \dot{E}x_{\text{out}} \quad (6.1)$$

where  $\dot{E}x$  represents exergy, the subscripts 'in' and 'out' representing the inlet and outlet, respectively. The overall inlet exergy of an NGCC or an oxyfuel NGCC cycle is derived directly from the exergy contained within the fuel ( $\dot{E}x_F$ ). For the MCLP-OXY-CC plant, individual components like compressors, pumps, the energy required are derived directly from the energy generated within the system. As for heat needed for the reduction reactor of the CL unit, the system is designed to be self-sufficient due to the integration of the reduction reactor (RED) and the combustion chamber (COMB). Therefore, no additional external input is necessary for the proposed system in terms of exergy besides the fuel. The outlet exergy including the desired output in the form of electricity ( $W$ ), material streams in the form of exhausted gas ( $\dot{E}x_{\text{exhaust}}$ ) and available heat ( $\dot{E}x_{Q,\text{av}}$ ), can be represented as per equation (6.2).

$$\dot{E}x_{\text{out}} = W + \dot{E}x_{\text{exhaust}} + \dot{E}x_{Q,\text{av}} \quad (6.2)$$

The un-used exergy of the system ( $\dot{E}x_{\text{loss}}$ ) is defined as the sum of the amount of exergy destroyed ( $\dot{E}x_{\text{destr}}$ ) and the amount of exergy wasted in the exhaust stream ( $\dot{E}x_{\text{exhaust}}$ ) as shown in the following equation (6.3).

$$\dot{E}x_{\text{loss}} = \dot{E}x_{\text{exhaust}} + \dot{E}x_{\text{destr}} \quad (6.3)$$

A considerable amount of heat might also be available (based on system optimization and pinch analysis) from the proposed system, which adds benefits over the traditional NGCC or the oxyfuel unit ( $\dot{E}x_{Q,\text{ph}}$ ). Hence, the net system output from the proposed MCLP-OXY-CC unit can be written as per the following equation (6.4).

$$\dot{E}x_{\text{destr}} = \dot{E}x_{\text{in}} - \dot{E}x_{\text{out}} \quad (6.4)$$

In general, the heat exergy is obtained as per the temperature of the available heat, given by the following equation (6.5).

$$\dot{E}x_Q = Q(1 - (T/T_0)) \quad (6.5)$$

where  $Q$  is the amount of heat and  $T$  represents the temperature at which the heat is available.

For a multicomponent material stream, the exergy ( $Ex_m$ ) is often divided into three components of exergy, namely, the physical exergy ( $Ex_{ph}$ ), chemical exergy ( $Ex_{ch}$ ) and mixing exergy ( $Ex_{mix}$ ) and written as per the following equation (6.6)

$$Ex_m = Ex_{ph} + Ex_{ch} + Ex_{mix} \quad (6.6)$$

The physical exergy is defined as the maximum work that can be extracted from a stream when it is made to pass from its current working conditions to the state of equilibrium with the environmental atmosphere [196,197]. The physical exergy is, therefore, dependent on the physical parameters, primarily temperature and pressure and can be calculated by Eq. (6.7), as obtained through the simulation results.

$$Ex_{ph} = (H - H_0) - T_0(S - S_0) \quad (6.7)$$

where  $H$  and  $H_0$  are the enthalpy flow and  $S$  and  $S_0$  are the entropy flow of a material stream at working and environmental state respectively.

Chemical exergy is defined as the maximum work which can be obtained when a substance is brought from the environmental state (physical equilibrium) in a state of further chemical equilibrium with the so named “dead state” by a reversible process which involves only heat transfer and exchange of substances with the environment [198]. The chemical exergy of pure components can be obtained from Bejan’s reference environmental model [155], where the chemical exergy of a material stream is given by equation (6.8) as follows.

$$Ex_{ch} = F \left( y_{0,L} \sum_{i=1}^n y_{0,i} Ex_{ch,i}^{0L} + y_{0,V} \sum_{i=1}^n y_{0,i} Ex_{ch,i}^{0V} \right) \quad (6.8)$$

where  $F$  is the molar flow rate of a material stream,  $y_{0,L}$  and  $y_{0,V}$  denote the liquid and vapour mole fractions, respectively,  $y_{0,i,L}$  and  $y_{0,i,V}$  denote the mole fraction of component  $i$  in the liquid and vapour phases, respectively and denote the standard chemical exergy of component  $i$  in liquid and vapour phases, respectively.

The standard chemical exergies of pure solids, on the other hand, are mostly covered by the values provided by Kotas [199] and Szargut [196] in their respective works. Even though the standard chemical exergy of elementary Cerium (Ce) and  $CeO_2$ , as the most abundant form of ceria available in nature is available, the standard chemical exergy of Cerium (III) oxide ( $Ce_2O_3$ ) is not a reference subject in any readily available literature. However, it can be formed through the reaction of two moles of Ce and 1.5 moles of  $O_2$  with known chemical exergies according to the reaction between Ce and  $O_2$  as per the following equation (6.9)



Subsequently, the chemical exergy of  $Ce_2O_3$  can be calculated as per the following equation (6.10).

$$Ex_{ch,Ce_2O_3}^0 = 2Ex_{ch,Ce}^0 + 1.5Ex_{ch,O_2}^0 + \Delta G_{Ce_2O_3}^0 \quad (6.10)$$

where  $Ex_{ch,Ce_2O_3}^0$ ,  $Ex_{ch,Ce}^0$  and  $Ex_{ch,O_2}^0$  are the standard chemical exergy of  $Ce_2O_3$ ,  $Ce$  and  $O_2$ , respectively;  $\Delta G_{Ce_2O_3}^0$  represents the Gibbs free energy for the formation of  $Ce_2O_3$  as per  $Ce/O_2$  reaction shown in equation (15).

Finally, the mixing exergy, which always has a negative value, and can be estimated as per the following equation (6.11) [131]

$$Ex_{mix} = \Delta H_{mix} - T_0 \Delta S_{mix} \quad (6.11)$$

where  $\Delta H_{mix}$  and  $\Delta S_{mix}$  are the enthalpy and entropy change due to mixing, respectively.

Hence, the common exergetic efficiency ( $\eta_{II}$ ) of the power plants is given as the ratio of the useful exergy output from the system and the necessary exergy input to the process as follows from equation (6.12). On the other hand, the total exergy destruction from the individual components of the overall system is given as the summation of all the individual component exergy destruction as per equation (6.13).

$$\eta_{II} = \frac{W + Ex_{Q,av}}{Ex_F} \quad (6.12)$$

$$Ex_{destr} = \sum_i Ex_{destr,i} \quad (6.13)$$

where  $Ex_{destr,i}$  refers to the exergy destruction of  $i^{th}$  component.

## 6.4 Economic Performance

To evaluate the economic performance of the proposed MCLP-OXY-CC unit, the most important economic parameters such as the capital cost (including specific investment costs), Operational and Maintenance (O&M) costs, levelized cost of electricity (LCOE) and levelized cost of  $CO_2$  savings/avoided have been focused. In addition, not all the costs of all component were available up to date. In this regard, the costs would need to be updated for present day calculation. Chemical plant cost indexes were employed to transfer the literature values as per the present day values [200]. Also, a currency conversion factor of 1.23 USD/EUR was employed besides such considerations.

To determine the total Capital cost of the plant (CAPEX), the capital cost of each module or equipment is first estimated by utilization of the component scaling factor exponent, which is shown as the following equation (6.14)

$$C_E = C_B \times (G / G_{ref})^{SF} \quad (6.14)$$

where  $C_E$  and  $C_B$  represent the equipment cost with a capacity of  $G$  and  $G_{ref}$ , respectively;  $SF$  being the equipment scaling factor exponent, varying between the range of  $0.6 - 1$ , depending on the type of component [195,201]. The summary of the scale factors for the different components of the plant is presented in the following Table 6-4.

Table 6-4 Summary of the Different Plant Component Scale Factors [115,195,202,203]

Plant Component	Scale factor SF
Gas turbine, generator and auxiliaries	1
HRSG, ducting and stack	0.67
Steam turbine, generator and auxiliaries,	0.67
Cooling Water System and Balance of Plant	0.67
CO <sub>2</sub> Compressor and Condenser - Compressor 1	0.67
Chemical Looping, Combustor and Oxy Reactor	1
Turbo Expander	0.67
Other Heat Exchangers	1

To assess further costs related to setting up of the power plant including installation and other direct and indirect costs related to the project development, a bottom-up approach following the work of the CAESER project [195] was selected and is briefly described as follows and is shown in Table 6-4.

The *Total Equipment Cost (TEC)* is the sum of all module costs in the plant. Besides this, additional *installation costs* are incurred due to additional expenses required while integrating the individual modules into the entire plant, including costs for piping or valves, civil works, instrumentations, electrical installations, insulations, paintings, steel structures, erections and other outside battery limit (OSBL) activities.

*Total Direct Plant Cost (TDPC)* is then obtained as the sum of the Module/Equipment Costs and the Installation Costs. *Indirect Costs* have been fixed to 14% of the TDPC for all the three technologies [195], which include the costs for the yard improvement, service facilities and engineering costs as well as the building and sundries.

*Engineering, Procurement and Construction Costs (EPC)* was calculated as the sum of the Total Direct Plant Cost and Indirect Costs. Finally, the *Owner's Costs and Contingencies (OCC)* were included as the owner's costs for planning, designing and commissioning the plant and for working capital, together with contingencies, and were fixed to 15% of the total EPC cost for all the technology options as per literature [195]. In addition, the cost of initial metal oxide loading also adds an important consideration to the overall system CAPEX. Therefore, the overall CAPEX or *Total Plant Cost (TPC)* of the project could be obtained as per the following equation (6.15) based on the explanation above.

$$TPC = EC + \text{Installation Costs} + \text{Indirect Costs} + \text{OCC} + \text{Metal Loading Costs} \quad (6.15)$$

In parallel, the O&M costs mainly comprise two aspects, namely fixed O&M costs and variable O&M costs. Fixed O&M costs comprise five components, i.e. general annual maintenance cost including overhead cost, property taxes and insurance and direct labour cost. On the other

hand, variable costs are connected with the costs associated with power generation, include the cost of water (including both process water and make-up water), cost of a metal oxide for make-up, and fuel costs [195]. Table 6-5 presents the basic parameters used for calculating economic indicators of the proposed power plant including those discussed in the previous sections.

Table 6-5 Basic economic assumptions [195,204,205]

Item	Assumption
Natural gas price	0.04 \$/kWh
Ceria oxide price	49 \$/kg
Process Water	7.43 \$/m <sup>3</sup>
Make-up Water	0.43 \$/m <sup>3</sup>
Erection, Steel structures and Painting	49% of Equipment Cost
Instrumentation and Controls	9% of Equipment Cost
Piping	20% of Equipment Cost
Electrical Equipment and Materials	12% of Equipment Cost
Indirect Costs, including Yard Development, Building, etc.	14% of TDPC
Owner's Costs	5% of EPC
Contingencies	10% of EPC
Annual operational time	7450 hours
Property Taxes and Insurance	2% of TPC
Maintenance Cost	2.5% of TPC
Labour Cost (Million Euro)	\$100 per kW
Operational Life of Plant	30 years
Discount Factor	10%
Carbon Credits	None
Electricity Price	58.3 \$/MWh

The levelized cost of electricity (LCOE) provides the “break-even” value for producing a unit of electricity, often employed as a parameter to compare different electricity production technologies from the economic point of view. The LCOE is expressed as the following expression (equation 6.16), based on the investment cost at time  $t$  ( $I_t$ ), O&M Costs at time  $t$  ( $M_t$ ), Fuel Cost at time  $t$  ( $F_t$ ), the electricity generated at time  $t$  ( $E_t$ ) and the interest rate  $r$ .

$$LCOE = \frac{\sum \frac{I_t + M_t + F_t}{(1+r)^t}}{\sum \frac{E_t}{(1+r)^t}} \quad (6.16)$$

The levelized cost of CO<sub>2</sub> capture (LCOA), on the other hand, is calculated based on the corresponding formula as presented by the equation (6.17). The calculation is based on the discounted expenses of operating the power plant including the investment costs with respect to the emissions saved in comparison to a conventional NGCC.

$$\text{LCOA} = \frac{\sum \frac{I_t + M_t + F_t}{(1+r)^t}}{(\text{CO}_2\text{abated} / \text{yr}) \times t} \quad (6.17)$$

## 6.5 Environmental Performance

The environmental performance of the MCLP-OXY-CC in comparison with the conventional NGCC and the oxyfuel combustion units was evaluated based on multiple criteria. The fundamental criteria selected were the CO<sub>2</sub> savings. Indeed, this forms the single most interesting criterion for such assessments. However, other criteria were studied to observe the broader picture with respect to the sustainability of a technology.

Water availability will become a critical issue in future and especially for plants with carbon capture [206]. In this regard, an analysis of the water requirement with respect to conventional technologies was evaluated after the method proposed by Martin, 2012 [207]. The specific water needs (I) for the present system in terms of litre/kWh was calculated based on the following equation (6.18) accounting for the water needed for both cooling and process applications [207]. An assumption of employing wet cooling tower was considered and corresponding values were selected from the literature.

$$I = A \times (\text{HR} - B) + C \quad (6.18)$$

Where A is a constant depending on the type of cooling =  $5.03 \times 10^{-4}$  litre/kJ based on wet cooling [207]; HR represents the heating rate and B represents the net output of the system, both with respect to useful energy in electricity or heat and system losses. Hence, (HR-B) represents the amount of cooling load necessary. C represents the process water needed by the system other than the cooling system. It is to be noted that the Chemical looping unit demands no additional water beside cooling. Therefore, the water need for a conventional NGCC with CCS remains constant also in this case = 0.2 Litre/kWh [207].

Land footprint assessment is another additional sustainability criterion, important to analyse the system viability. Indeed, additional systems with increased system complexity would increase the need for space required to accommodate additional units. Florin and Fennel [208] proposed an alternative to the linear model of spatial footprint assessment due to its oversimplistic approach leading to inaccurate evaluations. A suggestion was made to take a modular approach and scale footprint with respect to the number of capture trains. Berghout et al [203] proposed to evaluate the capacity increase of process equipment as the third power of the size (determined by volume) while the capital costs would increase in a quadratic way (based on the surface area). Therefore, the spatial footprint of the capture components for plant scale k (m<sup>2</sup>) was assessed as follows from the following equation (6.19).

$$A_k = \sum_i [A_{i,\text{ref}} \times (\frac{S_i}{S_{i,\text{ref}}})^{SF_i}] \quad (6.19)$$

where  $A_{i,ref}$  represents the space requirement for component  $i$  for the reference capacity ( $m^2$ ),  $S_i$  refers to the capacity of component  $i$  for plant scale  $k$  (unit as per the component),  $S_{i,ref}$  being the reference capacity of component  $i$  for plant scale  $k$  (unit as per the component), and  $SF_i$  refers the scaling factor for component  $i$ . As per Berghout et al [203], a scaling factor of 0.67 (or 2/3) was used. An additional 20% margin was added to the computed physical footprints considering space requirements for installation and maintenance.

## 6.6 Thermodynamic Evaluation of the MCLP-OXY-CC Unit

### 6.6.1 Energy Analysis of MCLP-OXY-CC

Table 6-6 lists the detailed technical assessment results for the proposed MCLP-OXY-CC power plant. The results are expressed in terms of power generation from gas and steam turbines, overall plant thermal efficiency, total energy penalty, net CO<sub>2</sub> emission savings and relative efficiency gain.

Table 6-6. Global Energy Flow and Energetic Efficiency of the Proposed MCLP-OXY-CC Unit

Plant data	Units	MCLP-OXY-CC
Fuel Energy Input, LHV (A)	MWth	990.708
Net GT Output	MWe	484.233
GT Output from CO <sub>2</sub> recycling	MWe	110.039
ST Output	MWe	255.937
Gross Electric Power Output (B)	MWe	750.206
ASU Consumption + O <sub>2</sub> compression	MWe	63.383
CO <sub>2</sub> Capture and Compression	MWe	19.222
Power Cycle Pumps	MWe	3.287
Air/ Recycled CO <sub>2</sub> Compression	MWe	142.8797
Syngas Compressors	MWe	17.1881
Total Parasitic Power Consumption (C)	MWe	245.959
Net Electrical Power Output (D=B-C)	MWe	504.247
Gross Electrical Efficiency (B/A*100)	%	75.72%
Net Electrical Efficiency (D/A *100)	%	50.7%
CO <sub>2</sub> Capture Efficiency	%	100%
CO <sub>2</sub> captured	t/h	178.658
Energy Output per tonne of CO <sub>2</sub> Captured	MWh/t	2.822

As can be observed from Table 6-6 a considerable share of the generated electrical energy is used up for oxygen separation in the ASU and for recycling the carbon dioxide for being fed into the combustion chamber for temperature control. Some fraction, around 3.8% is also used for compressing the captured CO<sub>2</sub>. The extra energy needed for carbon capture and storage is known as the energy penalty with respect to the conventional base case NGCC without carbon capture. These, in addition to the auxiliary power requirement, become the two major penalties for the conversion of energy from the chemical energy of natural gas to electricity. However, generation of around 110 MW of electricity from the recycling of the waste gas through splitting of CO<sub>2</sub> and H<sub>2</sub>O in the oxidation reactor (OXI) to produce syngas results in considerable improvement of the net power output, even with almost 100% Carbon Capture. An impressive energy efficiency of 50.7% with carbon capture is obtained. This correspondingly aids the lowering of the net energy penalty due to CCS in a conventional oxyfuel NGCC. Additionally, generation of heat by integration of the power plant units might result in energy savings and decrease the overall penalty by working the power plant on a combined heat and power mode.

### 6.6.2 Exergy Analysis of MCLP-OXY-CC

The exergy flow of the proposed MCLP-OXY-CC unit is depicted in Table 6-7. As can be clearly observed, due to both electricity and heat self-sufficiency of the system, the input fuel, namely natural gas contributes entirely (100% of the total exergy input) to the net exergy input to the system. The work consumed for compressors and pumps comprise a relatively small contribution to the entire input exergy (4.83%). However, the ASU alone would consume around 3.04% of the net input exergy of the entire system.

Table 6-7. Global Exergy Flow and Efficiency of the MCLP-OXY-CC unit

	Exergy (kJ/mol CH <sub>4</sub> )	% of total Ex <sub>in</sub>
Net Exergy into the Plant	835.34	100
Exergy in Methane	835.34	100
W <sub>compressors</sub>	40.31	4.83
W <sub>pump</sub>	0.23	0.03
W <sub>ASU</sub>	25.43	3.04
CO <sub>2</sub> Capture including CO <sub>2</sub> compression	60.73	7.27
Exergy Out	597.66	71.55
Exhausted gas	203.92	24.41
Exergy destroyed	237.68	28.45
Exergy un-used	441.59	52.86
Exergy efficiency (4)	393.75	47.14

The exergy consumed for capturing CO<sub>2</sub> represents a large fraction of the total exergy input (7.27%), which includes the net exergy destruction related to water condensation and compressing the CO<sub>2</sub> to 110 bars for the sequestration.

On the other hand, most of the system output is electricity (393.75 kJ/mol of CH<sub>4</sub>). The exergy exhausted in gas contributes 24.4% of the process inlet exergy. Approximately 28.5% of the exergy was destroyed due to irreversibility within the system. Indeed, the system optimization would considerably improve upon the net exergy destroyed by decreasing the unused fraction of exergy amounting to 52.9% of the net input exergy.

Table 6-8. Exergy balance in MCLP-OXY-CC break-down by component

Type	Component	Ex <sub>in,i</sub> (MW)	Ex <sub>out,i</sub> (MW)	Ex <sub>dest,</sub> (MW)	Component η <sub>II</sub> (%)	Ex <sub>destr</sub> % of Total
Physical process	<b>FPH-1</b>	2043.98	2031.8	22.47	99.404	1.33
	<b>TURBEXP</b>	1082.35	1078.34	12.18	99.629	0.438
	<b>FPH-2</b>	2138.06	2089.36	4.01	97.722	5.314
	<b>CMP-1</b>	976.05	975.76	48.7	99.97	0.031
	<b>RECCOMP-1</b>	323.83	303.55	0.29	93.735	2.214
	<b>GT1-1</b>	1007.57	932.69	63.05	92.569	8.17
	<b>GT1-2</b>	859.54	848.36	74.87	98.699	1.221
	<b>HRSG-2</b>	292.64	254.88	36.59	87.098	4.12
	<b>COMP-2</b>	222.67	221.8	37.76	99.612	0.094
	<b>RECCOMP-2</b>	125.54	95.38	0.86	75.971	3.292
	<b>GT2</b>	319.38	287.27	3.17	89.945	3.504
	<b>HRSG-1</b>	628.37	547.73	343.82	87.166	8.801
	<b>ST-COND</b>	25.78	9.63	80.65	37.373	1.762
	<b>ST-PUMP</b>	12.9	12.6	16.14	97.698	0.032
	<b>COND-3</b>	351.95	301.19	0.3	85.579	5.539
<b>COMPSEQ</b>	73.87	46.87	50.76	63.447	2.947	
Physical and Chemical Processes	<b>ASU</b>	63.19	40.73		64.447	2.452
	<b>RED &amp; COMB-1</b>	2653.46	2590.42	20.29	97.624	6.88
	<b>OXI</b>	561.58	524.99	11.18	93.484	3.993
	<b>COMB-2</b>	322.55	319.38	30.17	99.018	0.346
	<b>Mixture</b>	960.75	616.93	32.11	64.213	37.52
	<b>Total</b>	1069.55	501.65	27	7	100

To evaluate the primary reasons of exergy destruction caused in the simulated MCLP-OXY-CC process, an exergy analysis of each component was performed, as listed in Table 6-8. The methane preheating, occurring between HX-1 and HX-3 before the turbo-expander and HX-2 and HX-4 (hot side and cold side respectively) after the turboexpander is referred to as FPH-1 and FPH-2 respectively as two separate heat exchangers. Also, for physical processes occurring in heat exchangers, pumps, compressors, etc., the chemical exergy is not involved in the energy transformation process, and the component exergy efficiency  $\eta_{II,comp}$  can be predicted by equation (6.12). The final column depicts the relative irreversibility of each component with respect to the net irreversibility of the entire process, that is, reports the component exergy destruction percentage ( $Ex_{destr,i}$ ) with respect to the total exergy destruction ( $Ex_{destr}$ ).

Clearly, compressors (COMP-1, COMP-2 and RECCOMP 1 and 2) and pump work represent a minor fraction of total  $Ex_{destr}$ . Turbines, heat exchangers and the reactors contribute a higher percentage of exergy destruction. The heat exchangers contribute 21.27% of  $Ex_{destr}$ , which are inherently destroyed exergy due to the heat transfer across a finite temperature difference [209]. However, the mixture, from the mixing of the two gases from turbine outlets plays the most significant role in the net exergy destruction of the proposed power plant, contributing to over 37% of the same.

A significantly high exergetic efficiency can be observed in the combustion chamber due to oxyfuel combustion and the assumptions of no heat losses. The CO<sub>2</sub> separation unit in the form of the water separator and corresponding CO<sub>2</sub> compression contributes to a significant fraction of the total exergy losses, accounting for over 8% of the total  $Ex_{destr}$ .

Therefore, as can be observed from the exergy analysis of each of the component of the MCLP-OXY-CC a better integration of the entire power plant through design optimization would lead to a considerable decrease in exergy losses.

### 6.6.3 Effect of key operating parameters

The impact of key process variables, viz., temperature, pressure, system size, etc. on the process performance characteristics of the MCLP-OXY-CC process was systematically examined through a comprehensive series of simulations using the proposed power plant integration scheme. The variation of the outputs from the gas turbines, the steam turbine, the net power output and the system efficiency have primarily been analysed. Results of these analyses are presented in this section from Figure 6-4 through Figure 6-7.

Figure 6-4 (a) represents the effect of operating pressure of the CL unit on the defined parameters. A minimal rise in the net power output from the entire plant is observed with increase of pressure in the CL unit. While there is a proportional increase and decrease of the power output from GT1-1 and GT1-2 respectively, due to varying pressure ratios, the power outputs from the steam turbine and that of WGT2 remains constant. However, at a pressure of 1 bar, the compression ratio of the produced syngas from the CL unit for power generation is

the highest, 26, leading to the efficiency recorded as lower than 50%. Indeed, with a rise in the operating pressure of the CL unit, the compressor work for syngas compression decreases considerably. However, beyond 5 bars, the conversion of methane in the reduction reactor drops, together with a slight decrease in compression ratio of syngas and a low power output from the turbo-expander. These factors combined lead to a drop in the efficiency of the power plant beyond 5 bars to around 50.5% at 15 bars operation pressure of the CL unit.

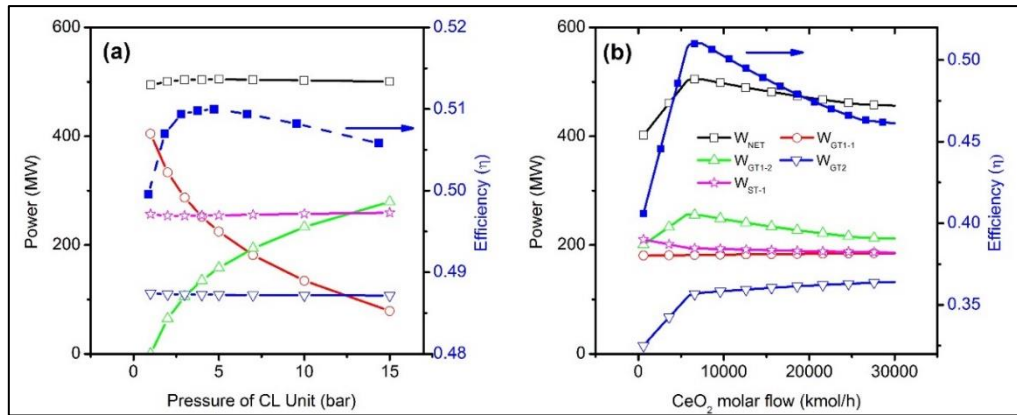


Figure 6-4. Impact of the variation of a) pressure of the CL unit and b) molar flow rate of Cerium Oxide ( $CeO_2$ ) at a constant natural gas flow and on the power generating components, the net power produced and the efficiency of the MCLP-OXY-CC power plant.

The performance study of the system with respect to the variation of the circulating metal oxide indicated similar trends in efficiency of the plant. At lower  $CeO_2$  flowrates in the CL unit, the combustion in the COMB-1 is with natural gas, since no partial oxidation takes place in the reduction reactor (RED). All other parameters remaining constant, this results in a power output like traditional OXY-CC, and hence a corresponding low efficiency. However, with higher  $CeO_2$  flow in the CL unit, the production of syngas in the OXI and subsequent power production through exhaust gas recycling increases not only the efficiency, but also the net power output of the system. However, with higher  $CeO_2$  flow rates, and therefore, with correspondingly higher fraction of exhaust being sent to the OXI, the net yield from WGT1-2 decreases, with no net increase in the efficiency. This leads to a drop-in efficiency at very high  $CeO_2$  flow rates (5 times the  $CH_4/CeO_2$  stoichiometry for metal oxide reduction) to as low as 46%. Interestingly, the highest efficiency, around 51% occurs at a  $CH_4/CeO_2$  stoichiometric ratio of around 0.8.

The variation of fraction of exhaust gas (mixture of  $CO_2$  and  $H_2O$ ) from the WGT1-1 to the oxidation reactor (OXI) for syngas production through splitting was investigated. It was observed that a peak system efficiency of 50.7% occurs at a split fraction of 0.1. At lower split fractions, the net utilization of the circulating  $CeO_2$  is low, thereby producing low syngas for power production in WGT2. However, a higher split fraction, even though increases the power generated from WGT2, lowers the power output from WGT1-2 nonetheless, while simultaneously increasing the auxiliary power consumption of COMP-2. This results in the net efficiency to be lowered to around 48.5% with 25% recycling of exhaust gas to the oxidation reactor as seen in Figure 6-5(a).

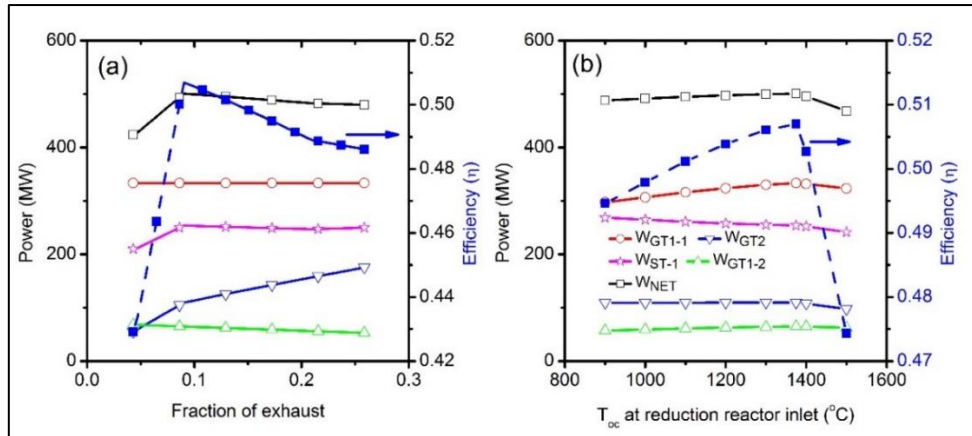


Figure 6-5. Impact of the variation of a) fraction of the exhaust gas from GT1-1 recirculated into the oxidation reactor (OXI) of the CL unit for production of syngas and b) temperature of the  $CeO_2$  at the inlet of the reduction reactor (RED) of the CL unit at constant natural gas flow on the power generating components, the net power produced and the efficiency of the MCLP-OXY-CC power plant.

The temperature of the  $CeO_2$  (oxygen carrier) inlet to the reduction reactor ( $T_{oc}$ ) has a significant impact on the system efficiency as shown in Figure 6-5 (b). An optimal value of about 50.7% is reached at a temperature of around  $1375^{\circ}C$ . This is directly related to the fact that the endothermicity of the reaction needs to be maintained through variation of the recycled  $CO_2$  in the combustor (COMB-1). This is due to the fact, that with higher oxygen carrier temperature, the endothermicity of the reaction (equation (3)) drops, requiring more carbon dioxide to be recycled to the combustor to maintain the TIT to its desired level. Consequently, an increase in the GT1-1 output power is noticed, however, beyond  $1375^{\circ}C$ , a steep drop in the system efficiency is observed. Due to an increased reaction endothermicity, the system performance is adversely affected, both with respect to the power produced and auxiliary consumptions. Therefore, an efficiency, as low as around 47.5% is obtained at a  $T_{oc}$  of  $1500^{\circ}C$ .

The variation of the Turbine inlet pressure of the Gas turbines was also studied. Commercial scale stationary gas turbines are usually limited to a working pressure ratio of 18:1 [151]. Considering an operation pressure of the CL unit of 2 bars, the inlet pressure of GT1-1 was varied between 15 bars and 30 bars. As can be seen from Figure 6-6(a), the inlet pressure primarily increases the power output from GT1-1, and therefore, the net system power output, and the efficiency. However, it correspondingly also increases the compression ratio of COMP-1, lowering the net benefit of increased power output to some extent. At a turbine inlet pressure of GT1-1 of 30 bars (pressure ratio 15) an efficiency of 51.2% was obtained.

Turbine Inlet Temperature (TIT) of the gas turbines critically impacts the system efficiency. All the gas turbines have been assumed to be kept at the same TIT. A lower TIT results in a lower efficiency, more specifically, around 48.5% at 1250K, which is subsequently improved to around 51% for a TIT of 1750K as shown in Figure 6-6(b). Hence, the efficiency of the MCLP-OXY-CC unit, proposed for operation at 1650K TIT, can be increased further. Interesting to note, that even if the absolute power output from the individual turbines, besides the steam turbine, decreases, the net power output and the efficiency increases. This can be

explained by the fact, with a higher TIT the CO<sub>2</sub> recycled into the combustion chambers (COMB-1 and COMB-2) decreases, thereby considerably improving the overall power output from the system. However, at temperatures beyond 1750K, the power output from the all the gas turbines (GT1-1, GT1-2 and GT2) decreases, with subsequently lower gain from decreased CO<sub>2</sub> compression. This results in a drop of efficiency to about 50.75% at a TIT of 1850K.

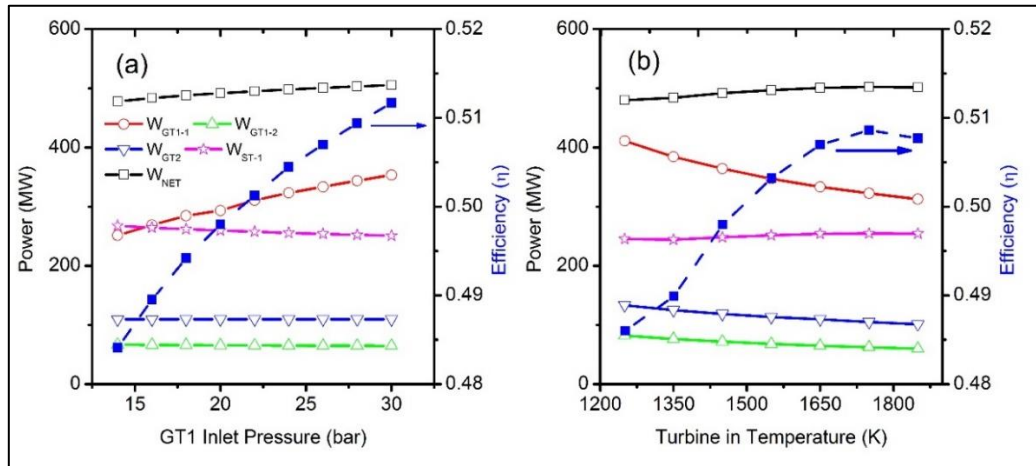


Figure 6-6. Impact of the variation of a) GT1-1 inlet pressure and b) Turbine Inlet Temperature (TIT) for both the turbines (GT1-1 and GT2) at constant natural gas flow on the power generating components, the net power produced and the efficiency of the MCLP-OXY-CC power plant.

Finally, the impact of scale on the system efficiency is depicted in Figure 6-7. For a 500MW power plant, the efficiency obtained was 50.7% corresponding to a natural gas flow rate of 73.75 tonnes per hour. Indeed, the impact of the scale was obtained to be limited towards the net system efficiency till around 10 MW. As can be seen, the efficiency of the system above 10 MW is constant around 50.7%. However, below such size, the efficiency drops significantly to about 46% for a size of 1MW, limiting downsizing of such systems beyond certain limits as shown in Figure 6-7.

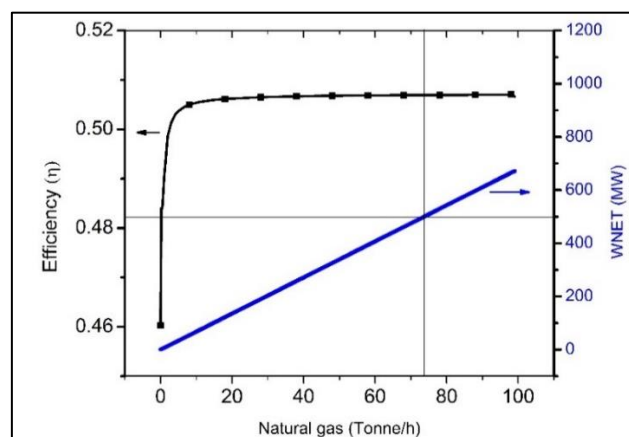


Figure 6-7. Impact of the variation of the natural gas flow rate on the system capacity (net power produced) and the efficiency of the MCLP-OXY-CC power plant

## 6.7 Comparative Performance Evaluation of State of the Art NGCC, Oxyfuel NGCC with Carbon Capture and MCLP-OXY-CC unit.

### 6.7.1 Thermodynamic Performance

The performance of the NGCC, OXY-CC and MCLP-OXY-CC plants are compared based on net electrical efficiency and CO<sub>2</sub> emissions for thermodynamic evaluation. Detailed simulation results for both cases are summarised in Table 6-9. The base case, without any CO<sub>2</sub> capture, emits 178.65 t/h of CO<sub>2</sub>. In contrast, both the OXY-CC and the MCLP-OXY-CC with CO<sub>2</sub> capture does not emit any significant quantity of CO<sub>2</sub>, leading to near 100% capture of CO<sub>2</sub>.

Table 6-9. Plant performance indicators for State of the Art NGCC, oxy-fuel NGCC, and the oxyfuel NGCC with CL unit (MCLP-OXY-CC) processes obtained by ASPEN plus simulations

Plant data	Units	NGCC	OXY-CC	MCLP-OXY-CC
Fuel Energy Input, LHV (A)	MWth	910.764	1155.267	990.708
Net GT Output	MWe	693.332	570.372	484.233
ST Output	MWe	160.400	259.042	255.937
Gross Electric Power Output (B)	MWe	853.732	829.414	750.206
ASU Consumption + O <sub>2</sub> compression	MWe		113.507	63.383
CO <sub>2</sub> Capture and Compression	MWe		26.523	19.222
Power Cycle Pumps	MWe	1.880	3.067	3.287
Air/ Recycled CO <sub>2</sub> Compression	MWe	351.759	186.664	142.8797
Syngas Compressors	MWe			17.1881
Total Parasitic Power Consumption (C)	MWe	353.639	329.762	245.959
Net Electrical Power Output (D=B-C)	MWe	500.093	499.652	504.247
Gross Electrical Efficiency (B/A*100)	%	93.74%	71.79%	75.72%
Net Electrical Efficiency (D/A*100)	%	54.91%	43.25%	50.70%
CO <sub>2</sub> Capture Efficiency	%		100%	100%
CO <sub>2</sub> Emissions	t/h	178.658		
CO <sub>2</sub> specific Emissions	t/MWh	0.505		

As per the developed ASPEN plus model, the non-optimized base case NGCC has an efficiency of 54.65%, agreeable to efficiencies of state of the art NGCC, as available in the literature [148,210]. However, this considerably drops due to the addition of the ASU and CO<sub>2</sub> sequestration compressor for the OXY-CC power plant, which has a much lower efficiency of 43.25%. Therefore, an efficiency penalty of more than 11 percentage points can be seen. Indeed, as predicted with the above analysis, the novel MCLP-OXY-CC unit, with an efficiency of 50.7% was able to improve the efficiency of the power plant by around 7.5 per cent points due to internal recycling of a part of the exhaust gases that can be termed as CO<sub>2</sub>

recycling. This also decreases the corresponding total parasitic load of the power plant due to a relative increase in the net work output from the proposed unit.

Figure 6-8 shows the relation between power produced and consumed in different units for three cases studied. The net power output from the three cases was kept constant to develop a comparative evaluation. The net thermal energy input from the natural gas, is, however, different in the three different cases resulting in the variation of the net energy efficiency from the three units. In the base case NGCC, the overall heat is completely produced in a single combustion chamber, whereby, the natural gas is combusted with an excess of air in the combustion chamber, the exhaust gases of which being first fed into the gas turbine for electricity generation and then in HRSG for heat recovery. Like this, OXY-CC also combusts the natural gas in a single step, however, with 5% excess of oxygen and recycled CO<sub>2</sub>, reducing the power output by 77 MW. Unlike to the previous two cases, a mixture of CO, H<sub>2</sub> and CH<sub>4</sub> is burned in 5% excess oxygen and over 90% recycled CO<sub>2</sub>, lowering further the net power output from the gas turbine. Indeed, for the MCLP-OXY-CC, the net power output from the gas turbines include two-step expansion, one from 26 bars to 2 bars and subsequently up to 1.04 bar after exhaust gas separation for splitting, together with the gas turbine output from the split exhaust gas containing syngas. This lowers the contribution from the gas turbine, however, increasing the contribution from the steam cycle, comparable to that of OXY-CC unit. Nevertheless, the gross power of the MCLP-OXY-CC unit is significantly lower by around 100 MW from the base NGCC and 80 MW from the OXY-CC power plant. However, interestingly, the parasitic load of the proposed MCLP-OXY-CC unit decreases by more than 105 MW and 85 MW respectively than base NGCC and OXY-CC unit, thereby showing better energy performance than the traditional OXY-CC system.

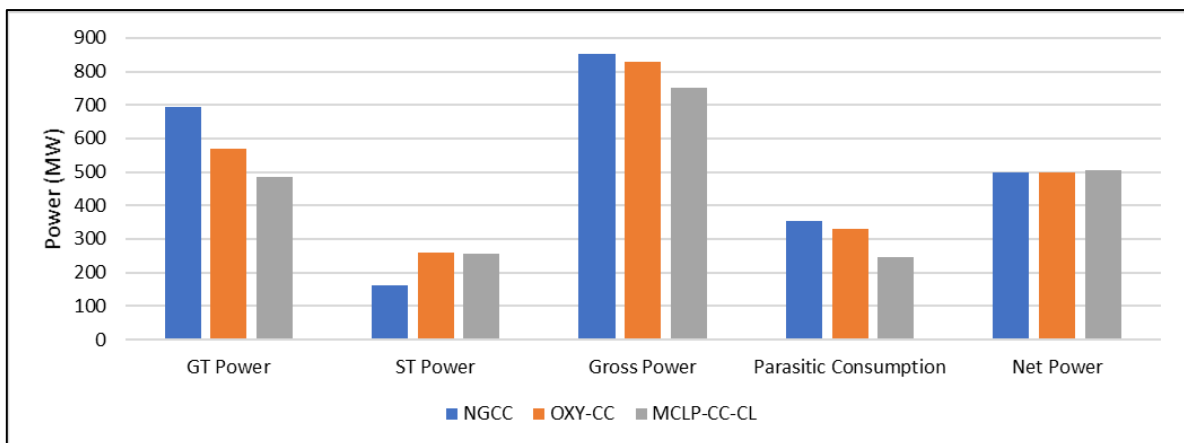


Figure 6-8. Comparison between GT, ST, gross, parasitic and net power output for base NGCC, OXY-CC and MCLP-OXY-CC

Table 6-10 depicts the comparative energy and efficiency penalty associated with CO<sub>2</sub> capture between the reference base case NGCC, OXY-CC and the proposed novel MCLP-OXY-CC unit. As can be seen from Table 6-10, the relative decrease in net electrical efficiency from the NGCC to the OXY-CC and the MCLP-OXY-CC units is around 11.4% and 4% respectively. Therefore the proposed new system performs better than Oxyfuel-CC with carbon capture as

reported in the CAESER project [195]. The CO<sub>2</sub> captured per MWh of energy expended in the MCLP-CC-CL (11.34 t/MWh) is therefore significantly higher than the corresponding energy expended for CO<sub>2</sub> capture in the OXY-CC process (4.35 t/MWh). These results suggest that MCLP-OXY-CC unit is a more favourable option from the energetic point of view (without economic considerations) to capture CO<sub>2</sub> from NGCC power plants compared to simple Oxyfuel unit. Indeed, a much lower relative decrease, by about 14 percentage points, with respect to the base case NGCC makes the proposed technology highly interesting for future NGCC power plants with CCS, especially while striving for higher efficiencies. However, the OXY-CC power plant is a practically proven and commercially available technology, while the MCLP-OXY-CC unit requires considerable further research and optimization to be available for commercial use.

Table 6-10. CO<sub>2</sub> Captured per unit energy and efficiency penalty with reference to conventional Oxyfuel NG Power Plant

Plant data	Units	NGCC	Oxyfuel-CC with CCS	MCLP-OXY-CC with CCS
Energy Penalty (A)	MW		57.635	18.453
CO <sub>2</sub> Captured (B)	t/h		251.014	209.3
CO <sub>2</sub> captured per MW decrease in energy Production than Base Case NGCC (C=B/A)	t		4.355	11.342
Net Electrical Efficiency (D)	%	54.91%	43.25%	50.7%
Net Electrical Efficiency Penalty Compared to Base Case NGCC, E=(54.65-D)	%		11.52%	3.69%
Relative Decrease in Net Electrical Efficiency Compared to Base NGCC F=E*100/54.65	%		21.089%	6.752%
CO <sub>2</sub> Captured per unit decrease in net electrical efficiency from Base Case NGCC (B/E)	t		21.780	56.721

## 6.8 Economic Analysis

### 6.8.1 Capital Cost and Operational Expenses

As developed from the process simulations, it can be easily concluded that the MCLP-OXY-CC unit has a clear technical edge over conventional and advanced NGCC system with and without carbon capture. However, for integration purposes, the MCLP-OXY-CC unit needs considerable new system additions including solid handling units, reactors for reduction and

oxidation, an additional combustion chamber among others. This would incur additional capital investments. Therefore, an economic analysis was performed to find the economic feasibility of the proposed MCLP-OXY-CC systems and is presented in detail in this section.

Table 6-11. Capital Cost Breakdown of the proposed MCLP-OXY-CC unit

Plant Component	Values (million \$)	% Contribution
Primary Gas turbine, generator and auxiliaries	76.09	6.20%
Primary Low-Pressure Gas turbine, generator and auxiliaries	14.79	1.20%
Secondary Gas turbine, generator and auxiliaries	25.1	2.05%
HRSG, ducting and stack	21.39	1.74%
Steam turbine, generator and auxiliaries,	49.76	4.05%
Cooling Water System and Balance of Plant	63.26	5.15%
CO2 Compressor and Condenser - Compressor 1	16.27	1.33%
Chemical Looping, Combustor and Oxy Reactor	48.72	3.97%
Turbo Expander	2.93	0.24%
Other Heat Exchangers	1.73	0.14%
<b>Total Equipment Costs (TEC)</b>	<b>320.04</b>	<b>26.07%</b>
Cost of Metal Loading	0.01	0.00%
Total Installation Costs	309.1	25.18%
<b>Total Direct Plant Cost (TDPC)</b>	<b>624.48</b>	<b>50.87%</b>
Indirect Costs	87.43	7.12%
Engineering Procurement and Construction Costs (EPC)	711.91	57.99%
Owner's Costs	8.74	0.71%
Contingencies	71.19	5.80%
ASU (Complete CAPEX as an add-on unit)	435.7	35.49%
<b>Total Project Costs (TPC)</b>	<b>1,227.55</b>	<b>100.00%</b>

Table 6-11 represents the cost breakdown of the proposed MCLP-OXY-CC unit. The ASU was assumed as an add-on unit, with a CAPEX of \$435.70 million, contributing to about 35.5% of the entire plant cost. The net project CAPEX was obtained at around \$1227 million, which amounts to around 2455 \$/kW, a relatively high cost than the present day NGCC power plants

without carbon capture, with overnight capital costs reported as 978 \$/kW [211]. On the other hand, the capital costs become comparable to advanced NGCC with carbon capture, quoted around 2050 \$/kW as per the 2016 study by the US Department of Energy [211].

In addition, the operational expenses were calculated based on the assumptions mentioned in the earlier section. The net fixed OPEX was obtained as \$62.58 million, while the variable cost was calculated as 50.15 \$/MWh of gross power generation. Hence a net annual operating cost of \$347.1 million was calculated to run the proposed 500 MW MCLP-OXY-CC unit.

### 6.8.2 LCOE and LCOA Calculations

LCOE calculations were hence developed based on equation (6.16) with assumptions listed in Table 6-5 to perform a comparative evaluation of the system economic performance. As mentioned, no carbon tax was assumed. Correspondingly an LCOE of 128.01 \$/MWh was obtained. However, as depicted in Figure 6-9, with a carbon credit of 6 \$/tonne CO<sub>2</sub>, the LCOE would drop to comparable prices of the average wholesale electricity market prices [212]. Therefore, the importance of Carbon Credits for such systems to be economically competitive is most crucial.

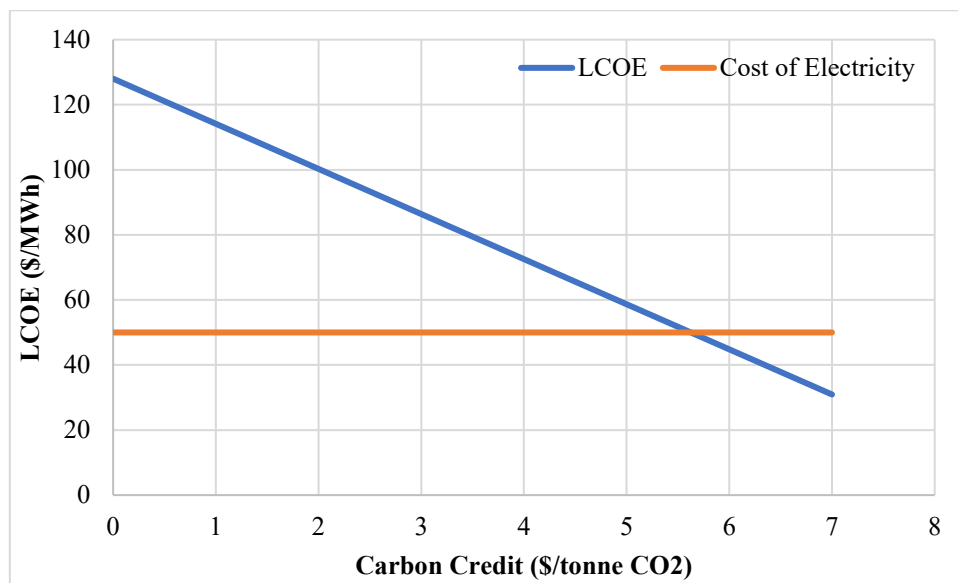


Figure 6-9. Impact of Carbon Tax on the Levelized Cost of Electricity of the proposed MCLP-OXY-CC unit

Additionally, the levelized cost of CO<sub>2</sub> savings (LCOA) was calculated to obtain the economic performance of carbon capture. Indeed, as can be seen in Figure 6-10, the levelized cost of carbon capture for the proposed OXY-CC compares well to those of already available technologies. Indeed, with an LCOA of 96.25 \$/tonne of CO<sub>2</sub>, the cost is lower than that of the oxyfuel power plant with carbon capture, reported as 104 \$/tonne of CO<sub>2</sub> by Khorshidi et al., 2012 [213]. A higher efficiency, lowering the need for fuel consumption for similar power production is a considerable benefit. As for post-combustion capture, the value is on the higher side, is needed to be integrated for a new and much-complicated power plant, increasing the

costs. Also for the OXY-CC power plant, a LCOA of 104 \$/tonne CO<sub>2</sub> captured was reported by the study by Rubin et al 2015 [214], higher than that of the MCLP-OXY-CC unit proposed.

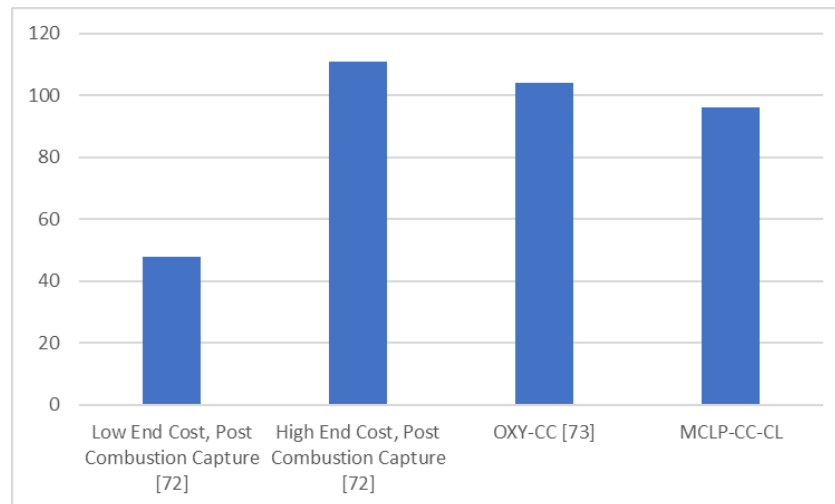


Figure 6-10. Comparative Evaluation of the Levelized Cost of Carbon Capture between MCLP-OXY-CC and post-combustion capture at new NGCC power plants

## 6.9 Pinch Analysis

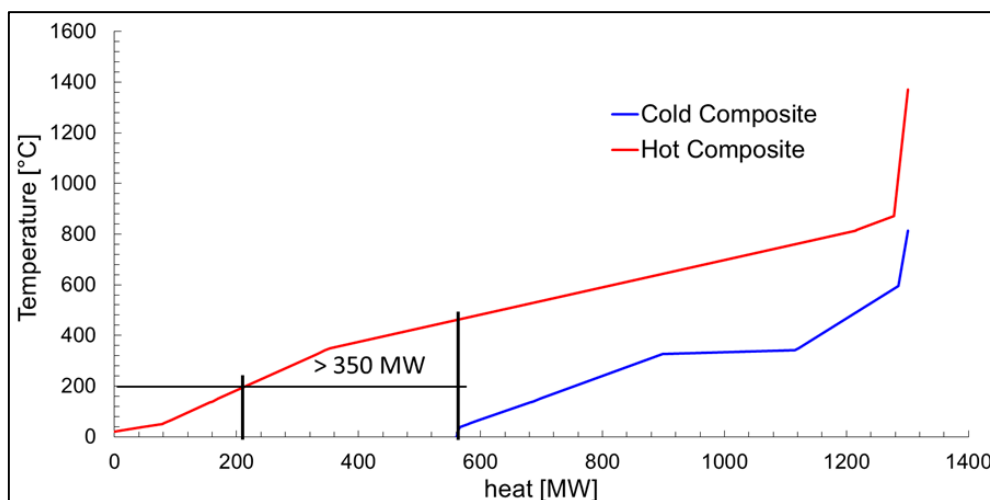


Figure 6-11. Pinch Analysis of the proposed MCLP-OXY-CC unit

The optimization for the proposed MCLP-OXY-CC plant concept with CCS was performed through heat and power integration analysis (via pinch technique), often used for maximization of power generation [215,216]. A conservative value of 10°C was assumed for the minimum approach temperature, necessary for the pinch assessment [216]. As assumed in the methodology, a simple steam cycle was modelled with the primary aim to obtain the relative efficiency gain from integrating the CL unit to a conventional oxyfuel power plant with CCS. A self-sustained system with regards to thermal integration was obtained. Furthermore, as illustrated from the Hot and Cold Composite curve in Figure 6-11, a strong potential for system

optimization to improve the efficiency further was identified through the production of steam for power generation.

About 350 MW thermal of high-temperature heat can be seen to be available for optimized use. Assuming a conservative system efficiency of 30% for electricity generation via steam an additional 105 MW of electricity can be generated by the proposed layout. This would increase the system efficiency to 61.5%, higher than the state of the art base case NGCC without CCS.

## 6.10 Thermodynamic and Kinetic Evaluation of MCLP-OXY-CC

To improve on the thermodynamic evaluations, the GIBBS reactors for the RED and OXI were replaced by moving bed reactors. A similar model, as developed in the previous Section 3.2. for moving bed reactors was integrated into the described MCLP-OXY-CC unit and the energetic performance of the proposed plant layout was evaluated. As for the oxidation reaction, since the primary component of the exhaust comprises over 86% CO<sub>2</sub>, the available water splitting kinetics were used alongside the newly developed CO<sub>2</sub> splitting kinetics by in-house experiments described in the previous chapter. A few important deviations to the original assumptions have been taken to adapt the moving bed layout into the existing system. Based on the experimental results, an isothermal reduction reactor at 1000°C was considered in the kinetic model. The heat integration and the annular combustion chamber concept was kept unchanged, whereby, the heat needed in the reduction reactor would be supplied from the heat generated in the combustion chamber. Additionally, the oxidation reactor was also considered a well-insulated adiabatic as opposed to a jacketed isothermal reactor at 1380°C considered during the thermodynamic analysis.

To explain the comparative results of the overall plant performance, the need to understand separately, the efficiency of the CL unit as a separate entity and the efficiency of the entire layout is crucial. In this regard, the efficiency of the CL unit, calculated as per equation (4.20) defined in chapter 4.4 was modified as follows into the following form (equation 6.20).

$$\eta_1 = \frac{(\dot{m}_{H_2} LHV_{H_2} + \dot{m}_{CO} LHV_{CO})_{red} + (\dot{m}_{H_2} LHV_{H_2} + \dot{m}_{CO} LHV_{CO})_{oxy}}{(\dot{m}_{CH_4} LHV_{CH_4} + (\dot{Q}_{red} - \dot{Q}_{oxd}) + \dot{Q}_{NG}) + (\dot{Q}_{sphtr} - \dot{Q}_{sld})} \quad (4.20)$$

where,  $\dot{Q}_{NG}$  is the heat necessary for heating the natural gas from after the turbo-expander to the condition necessary for the inlet to the reduction reactor. Since the exhaust of the turbine is directly sent to the oxidation unit, no heat-up of the same is necessary. Like before, the heat needed for heating of the solids and the heat required for cooling of the solids was not considered since an isothermal reactor system between the RED and the OXI was considered. However, it was ensured that no temperature cross-over takes place.

The results of the comparative evaluation of the performance of the CL unit from the thermodynamic to the kinetic evaluation is shown in Table 6-12. As can be seen, all other parameters being constant, the net energy rate content in the syngas formation in both the reactors is much less for the kinetic study. Indeed, for a lower non-stoichiometry, more

specifically 0.295 obtained in the reduction reactor of 10 m<sup>3</sup> volume, results in the production of a lower volume of syngas in both the reduction and oxidation reactors, unlike in thermodynamics, where a complete reduction of CeO<sub>2</sub> to Ce<sub>2</sub>O<sub>3</sub> was assumed with an equivalent non-stoichiometry of 0.5. However, a lower non-stoichiometry also ensures the heating load of the reduction reactor to diminish, as compared to the thermodynamics levels. Nevertheless, the overall efficiency of the CL unit drops from 64.07% for ideal conditions to 42.88% for the evaluated operating conditions using developed reaction kinetic models. Also, it should be noted that the outlet temperature of the oxidized metal from the OXI drops to 1350°C as opposed to 1380°C obtained in the thermodynamic evaluation, requiring an additional heat removal of 4 MW. Nevertheless, such a high temperature of metal oxide in the RED, even though will considerably decrease the heat requirement of the reaction, might result in carbon deposition to occur as seen through experimental evaluations and discussed in Section 5.6. Therefore, a detailed design optimization from multiple design perspectives needs to be assessed in further detail, which is beyond the scope of the present study.

Table 6-12 Comparison between the Thermodynamic and Kinetic Evaluation of the CL unit of the MCLP-OXY-CC unit

Parameter	Unit	Thermodynamic Evaluation	Kinetic Evaluation
Rate of Energy Content of Syngas from RED	MW	589.186	375.961
Rate of Energy Content of Syngas from OXI	MW	227.101	134.541
Rate of Net Energy in the Syngas Generated (H <sub>2</sub> +CO)	MW	816.287	510.502
Q <sub>RED-IN</sub>	MW	231.433	149.65
Q <sub>OXY-OUT</sub>	MW	-4.44	0
Q <sub>NG</sub>	MW	57.38	51.19
Rate of Energy Content in the Inlet Fuel (NG)	MW	989.667	989.667
The efficiency of the CL Unit		64.07%	42.88%

However, unlike the efficiency of the CL unit, the plant efficiency depends not only on the net syngas generated in the CL unit but also on the total heat balance within the plant. Table 6-13 lists the comparison of the plant data for the thermodynamic assessment of the CL unit and the kinetic assessment of the same, all other parameters being kept constant. Since the combustion is a very highly exothermic and spontaneous reaction, no kinetic study is necessary to evaluate the reactions occurring in the combustion chamber, and no other chemical reactions occur in the entire plant. Indeed, interesting to note the net efficiency of the plant increases slightly from 50.7% for the thermodynamic model to 50.96% utilizing a kinetic model of the CL unit. Multiple points of comparison between the two analyses of the same layout can be observed. They can be discussed as follows.

The heat requirement in the reduction reactor decreases due to a lower reaction extent, resulting in a lower non-stoichiometry of the reduced ceria. In addition, based on the concept developed

for the oxidation reactor for the solar reduction-based cycle, an excess of exhaust gas was sent to the reduction reactor increase the net power produced from syngas generation via splitting in the OXI. Additionally, being directly from the gas turbine outlet at a pressure of 2 bars, a high gas temperature of 921°C at the inlet of the OXI was achieved. This results in the oxidized metal oxide temperature from the OXI to be at 1350°C as opposed to 1380°C for the thermodynamic layout.

Table 6-13 Plant Data Comparison of the MCLP-OXY-CC unit based on Thermodynamic and Kinetic Evaluation of the CL unit

Plant data	Unit	MCLP-OXY-CC	MCLP-OXY-CC with Kinetics
Fuel Energy Input, LHV (A)	MW <sub>th</sub>	990.708	990.708
Net GT Output	MW	484.233	523.488
ST Output	MW	255.937	251.003
Gross Electric Power Output (B)	MW	750.206	774.491
ASU Consumption + O <sub>2</sub> compression	MW	63.383	63.021
CO <sub>2</sub> Capture and Compression	MW	19.222	18.021
Power Cycle Pumps	MW	3.287	3.10
Air/ Recycled CO <sub>2</sub> Compression	MW	142.8797	153.61
Syngas Compressors	MW	17.1881	31.833
Total Parasitic Power Consumption (C)	MW	245.959	269.585
Net Electrical Power Output (D=B-C)	MW	504.247	504.906
Gross Electrical Efficiency (B/A*100)	MW	75.72%	78.18%
Net Electrical Efficiency (D/A*100)	%	50.70%	50.96%
CO <sub>2</sub> Capture Efficiency	%	100%	100%
CO <sub>2</sub> captured	t/h	178.658	178.658
Energy Output per tonne of CO <sub>2</sub> Captured	MWh/t	2.822	2.826

On the other hand, the gas outlet temperature from the OXI drops considerably. Due to a countercurrent reactor configuration, as well as from a lower reduction extent, the net exothermicity dropped considerably in the kinetic analysis than in the thermodynamic model. Hence, the gas outlet temperature noted was 1120°C, as opposed 1380°C for the thermodynamic layout assessment. This lowers the heat availability within the system. However, the outlet temperature from the RED increases as well from 905°C to 1000°C from the thermodynamic to the kinetic model. Besides, the composition of the syngas produced being varying significantly between the two models, the heat transfer characteristics are different as well.

The heat requirement in the RED being significantly lower for the kinetic model (by 80 MW), while the TIT remains constant, the net CO<sub>2</sub> recycled for temperature control in the COMB increases. Thus, the power produced in the GT increases. However, this also increases accordingly the auxiliary consumption the CO<sub>2</sub> recycling compressor for COMB1. Nonetheless, both the energy production and consumption from auxiliary for the COMB2 cycle decreases due to a lower non-stoichiometry generated from reduction, as can be seen from the results in Table 6-13. Furthermore, a lower temperature of the syngas from the OXI results in

a lower steam generation in HRSG-2. Therefore, even though the gas expanded in GT1 and GT1-2 increases, the gas expanded in GT2 falls. The combined effect leads to a net drop in the power generated in the ST.

In summary, as can be followed from Table 6-13, the net efficiency of the power plant is governed by the output from the GT, by far the single largest energy generating unit of the power plant. Even though the auxiliary consumption increases, the net efficiency of the power plant increases slightly for a lower non-stoichiometry resulting from integrating kinetics of methane reduction and corresponding oxidation of the reduced metal oxide by  $\text{CO}_2$  and  $\text{H}_2\text{O}$ . Nevertheless, it needs to be highlighted that similar to the thermodynamic system, the kinetic layout is also a non-optimized one. Therefore, to develop a more even comparison between the maximum achievable efficiency by complete heat integration between the two layouts, a pinch analysis for the latter is required as well.

The pinch analysis of the layout using kinetic assessment of the CL unit is shown in Figure 6-12. A clear comparison to the pinch analysis of the layout using the thermodynamic assessment, as presented in Figure 6-11 of the CL unit can be drawn. Unlike the available 350 MW of high-temperature heat above  $200^\circ\text{C}$  for the thermodynamic layout, the system with kinetics of the CL unit seems to be completely optimized without any heat available for further improvement of system performance. Therefore, the maximum achievable electrical efficiency is also limited to the present obtained value of 50.96%, as opposed to 61.5% achievable by system optimization of the thermodynamic layout. Nevertheless, even with kinetic limitations of the reduction and oxidation reactions, a reduction in the energy penalty, from 11.6 to only 3.8 percentage points is obtained, which would show the significant benefit of the proposed layout.

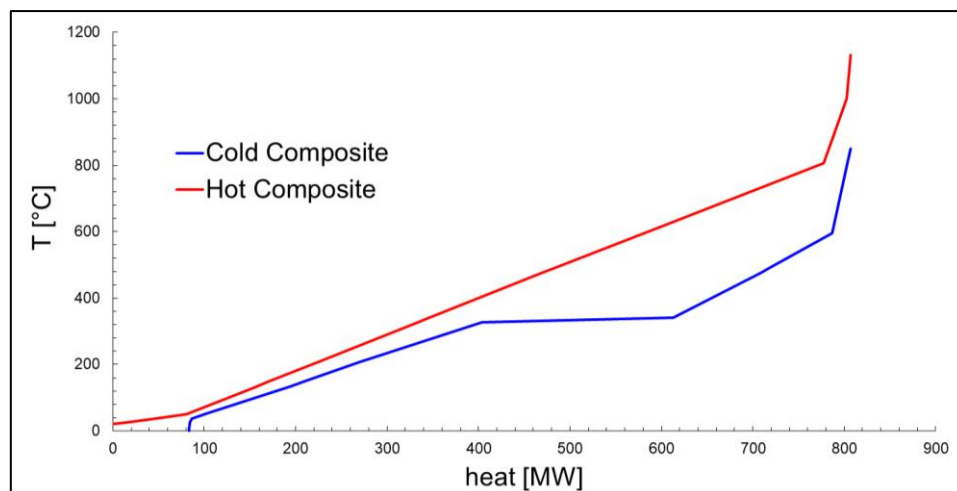


Figure 6-12. Pinch Analysis of the proposed MCLP-OXY-CC unit based on a Kinetic assessment of the CL unit

In fact, a net economic comparison with the thermodynamic layout was also performed, which are of interest due to the relative change in the sizes of the turbine and the compressors, resulting from a lower non-stoichiometry of ceria reduction. The total TOC of the plant was

calculated as 1224 million\$, around 3 million\$ lower than the corresponding CAPEX calculated using thermodynamic evaluation of the layout. This change is however insignificant with respect to the other operating costs of the power plant and hence no further detailed techno-economic calculation was performed.

## 6.11 Environmental Evaluations

### 6.11.1 Water Footprint Analysis

Table 6-14. Summary of Water footprint analysis of the MCLP-OXY-CC unit.

Description	Unit	Values
LHV of NG	MJ/kg	48.3
Flow of NG	tonne/hr	73.75
Plant Capacity	MW	500.69
Heat Rate (HR)	kJ/kWh	7114.432
Electricity produced	kJ/kWh	3600
Other Heat Losses	kJ/kWh	355.722
Net Energy Out (B)	kJ/kWh	3955.722
Water needed for cooling using tower cooling (A)	litre/kJ	0.001
Specific Cooling Water Requirement	litre/kWh	1.589
Plant Capacity Factor		85%
Net Energy Generated	MWh	3,728,137.74
Total Cooling Water Requirement	m <sup>3</sup>	5,923,382.20
Process Water (gross)	litre/kWh	0.2
Gross Plant Capacity	MW	761.74
Gross Energy Generated	MWh	5,671,916.04
Excess Water need for Chemical Looping	litre	0
Total Process Water Requirement	m <sup>3</sup>	1,134,383.21
Total Water Footprint	m <sup>3</sup>	7,057,765.41
Net Specific Water Footprint	litre/kWh	1.893

Following the methodology presented in the earlier section, a detailed water demand was calculated for the proposed MCLP-OXY-CC system, based on the thermodynamic evaluation. The net specific water footprint was calculated to be 1.893 litres/kWh and more detailed results for water need analysis is summarized in Table 6-14. As can be seen from Figure 6-13, the net specific water need of the proposed MCLP-OXY-CC system is comparable to existing commercial power plant technologies [217]. However, compared to NGCC, the increase of water need is almost 2.5 times. Considering water sustainability, hence the proposed system

lags and system optimization focusing on lowering the specific water requirement hence are necessary.

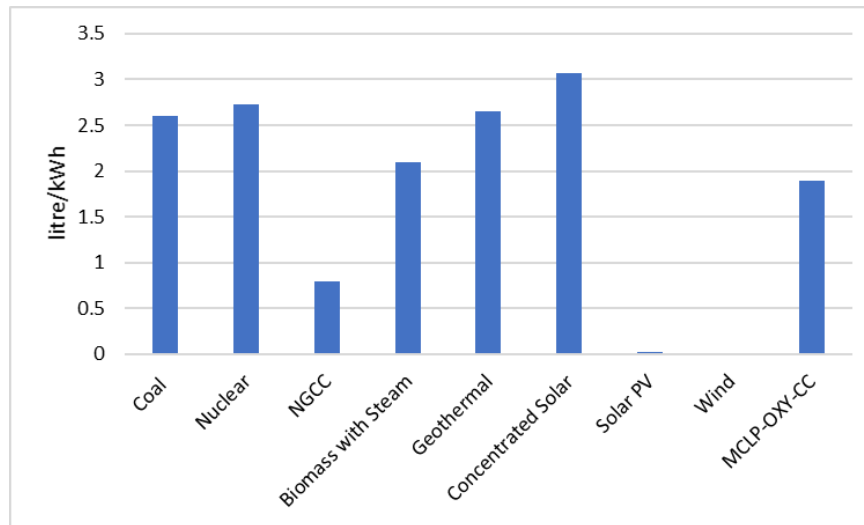


Figure 6-13. Comparison of specific water need of power production of the proposed MCLP-OXY-CC and commercial technologies with cooling tower-based cooling

### 6.11.2 Land Footprint Analysis

Table 6-15. Comparative Land Area Requirement in m<sup>2</sup> for NGCC, Oxy-CC and MCLP-OXY-CC unit for a net power output of 500MW

Component	NGCC	Oxy-CC	MCLP-OXY-CC
NGCC (Combustion Turbine)	1,689.078	1,689.078	1,689.078
ASU		323.13	286.087
CO <sub>2</sub> Drying and Compression		1,288.038	1,288.038
Chemical Looping Unit - Included as Boiler Units			582.254
Solids Handling Units - Included as equivalent to Coal Handling Plants			210.854
Net Spatial Footprint	1,689.078	3,300.246	4,056.311

Comparative Land Footprint Analysis, as presented in Table 6-15, clearly indicates the larger area needed for similar power production from the three units. The proposed MCLP-OXY-CC unit, comprising of ASU, CL units and additional metal handling units, with a higher number of turbines, would require a much higher land area. Indeed, it would need as much as 2.5 times the land area than a simple NGCC power plant without carbon capture. The CO<sub>2</sub> drying and compression unit accounts for largest share of the increased area, followed by the chemical looping unit, accounting for about 15% of the total land area needed for the proposed power

plant. The ASU, on the other hand, takes up around 7% of the total land area, is considered as a separate unit to the NGCC, connected through pipelines supplying oxygen for combustion.

## 6.12 Conclusions

Thermochemical looping of ceria for splitting  $\text{CO}_2/\text{H}_2\text{O}$  in a methane-driven redox cycle producing syngas is integrated with oxyfuel-combustion natural gas combined cycle (MCLP-OXY-CC). Except for the chemical looping  $\text{CO}_2/\text{H}_2\text{O}$  dissociation unit (consisting of two interconnected reactors), which is still under technological development, the remaining process design comprises already existing industrial components. The resulting improvement in the system efficiency, even with carbon capture and storage is observed. A system design and simulation were performed in ASPEN Plus to evaluate the thermodynamic performance of the proposed system. An energetic efficiency of 50.7% and an exergetic efficiency of 47.4% was obtained. Sensitivity analysis with different operating parameters of the system showed scopes for improvement, however, subject to the development of corresponding technologies. Comparison with natural gas oxyfuel power plant with carbon capture (OXY-CC) revealed a net efficiency gain of around 7.5 percentage points even with 100% CCS, making this technology promising for subsequent applications in future. An economic analysis was further performed and compared with the existing technologies for power production. Even though the specific overnight capital cost was high, at 2455\$/kW, the levelized cost of  $\text{CO}_2$  savings was obtained at 96.25 \$/tonne $\text{CO}_2$ , well within limits of commercial technologies. An LCOE of 128.01 \$/MWh was calculated without carbon credits, which, however, would drop to the rates of existing wholesale electricity prices with carbon credits of around 6 \$/tonne $\text{CO}_2$ . However, as per the pinch analysis performed, with better heat integration, the system efficiency can be improved to almost 61.5%, resulting in the much-improved performance of the proposed system. Nevertheless, a kinetic study of the CL unit to predict a more accurate system performance was performed. A similar efficiency of 50.9% was obtained for the entire power plant, even though the efficiency of the CL unit in itself was found to be almost 20% lower while compared to thermodynamic considerations. However, the heat balance of the system plays a significant role, whereby, considering the kinetic assessment of the CL unit, no additional heat was obtained to improve the system efficiency further, beyond a value of 50.9%. However still, the improvement in the net efficiency penalty from CCS is much reduced and hence the present system design proves to be an interesting alternative for future CCS plants with NGCC. Besides techno-economic assessments, however, in comparison to NGCC without carbon capture, both the water and land footprints for the proposed technology was obtained to be more than 2.5 times higher for the same scale. This would need to be further optimized by improved system design and integration of the different units of the proposed power plant.

## 7 Conclusions

In this work the Solar Chemical-looping (CL) syngas production as an innovative fuel production technology based on splitting CO<sub>2</sub> and H<sub>2</sub>O, for production of syngas (CO and/or H<sub>2</sub>) has been studied in detail. The primary focus was given to the development of a kinetic model in the commercial software ASPEN Plus, whereby a moving bed model was developed to replicate the reduction and oxidation reactions. Results indicated good agreement to literature data. Thereafter, the CL unit was integrated into a power generation layout via an oxyfuel combined cycle power plant to be retrofitted to a 100 MW Oxyfuel NGCC with CCS (SCLP-OXY-CC). A maximum power output of 12.9 MW at a solar to electricity efficiency was obtained while working with CO<sub>2</sub> recycling. This would reduce the efficiency penalty suffered by NGCC from CCS from 11.3 to 6 percentage points. Nevertheless, the reduction reactor would be needed to operate at 1600°C and 10<sup>-7</sup> bar vacuum pressure to obtain the maximum output, which would limit the applicability of the cycle to only a few hours during the day without storage integration.

Subsequently, methane reduction of ceria as an alternative to thermal reduction was considered and studied in detail. At first, a thermodynamic analysis was performed to obtain the optimum operating condition of the methane driven redox cycle from a thermodynamic point of view. Operation between 900 and 950°C with 50% excess of methane than stoichiometry would result in the optimal system performance, resulting in a system efficiency of 62%, while ensuring avoidance of complete oxidation of methane and carbon deposition. The oxidation reactor yielded a highly exothermic complete oxidation of ceria, whereby a high outlet temperature would considerably benefit the energetic efficiency of the complete redox cycle. The variation of H<sub>2</sub>/CO ratio at the output with respect to varying input parameters including the composition of the gas to the oxidation reactor was studied to specify the necessary operating conditions, while combined to subsequent chemical production from the generated syngas.

No comprehensive solid state kinetic model exists in literature to describe the methane partial oxidation with ceria reduction over a wide range of operating conditions. Especially since ceria reduction most often follows a non-stoichiometric reduction pathway, kinetic models would result in a more accurate prediction of results. Experiments were performed in a packed bed reactor within a temperature range of 900-1100°C of methane reduction followed by CO<sub>2</sub> splitting. CO<sub>2</sub> splitting, being a more complex reaction than water splitting was chosen to be studied for kinetic development, while water splitting kinetics was obtained from literature. The Avrami-Erofeev 3 (AE 3) model was found to fit best to both the cases, with respective activation energies being obtained as 283 kJ/mol and 59.687 kJ/mol respectively. The order of the reaction was found to vary with both temperature and concentration of the reactants, the relation of which was also obtained.

Acknowledging the drawbacks of the SCLP-OXY-CC add-on unit, a new power plant layout using NGCC and oxyfuel combustion, with subsequent CCS was developed by integrating the CL unit with methane reduction (MCLP-OXY-CC). A 500 MW scale plant was designed and

comparative system performance with state of the art NGCC and Oxyfuel NGCC with carbon capture was performed using idealistic (thermodynamic) approach as a proof of concept. A system efficiency of 50.7% was obtained, which could be improved to 61.5%, subject to system optimization with pinch analysis. A detailed exergy analysis was also performed with regards to individual components. An exergetic efficiency of 47.4% was obtained. A comprehensive sensitivity analysis was also performed to evaluate the impact of operating conditions on the overall system output. A detailed techno-economic assessment revealed a specific overnight capital cost of 2455\$/kW, the levelized cost of CO<sub>2</sub> savings of 96.25 \$/tonneCO<sub>2</sub>, and an LCOE of 128.01 \$/MWh. However, with carbon credits of 6 \$/tonneCO<sub>2</sub>, the LCOE would drop below 50 \$/MWh.

To improve upon the proof of concept, the kinetic model of the obtained methane kinetics and CO<sub>2</sub> splitting was incorporated to evaluate the proposed MCLP-OXY-CC layout. A drop of 20% in the efficiency of the CL unit was observed. However, due to thermal balance within the system, the similar thermal efficiency of the overall plant was achieved as 50.9%, showing an energy penalty of only 3.8% with CCS as opposed to state of the art Oxyfuel NGCC with CCS. However, unlike the thermodynamic layout, no excess heat was available to improve the system efficiency was further. Besides CO<sub>2</sub> savings, the land and water footprint as sustainability assessment criteria were analysed for the proposed layout. Both the land and water requirements increase by 2.5 times with respect to a state of the art NGCC.

Even though a considerable amount of work was performed within the present research, significant future work can also be identified. System optimization of both the SCLP-OXY-CC add-on unit and the MCLP-OXY-CC power plant needs to be performed. Since both the plants were designed to obtain essentially proof of concepts, with positive results, a more detailed design and optimization is necessary. Development of the kinetic model of water splitting subject to methane reduction of ceria would also be an important continuation of the present work to develop a complete set of reaction kinetic models, homogenous with assumptions and reaction set-up. Innovative layout combining the CL unit and chemical looping combustion was envisaged during the thesis work to substitute the need of ASU but was not evaluated. Also, the impact of other metal oxide redox pairs on the proposed SCLP-OXY-CC and MCLP-OXY-CC units, especially perovskites with higher oxygen storage capacities at lower temperatures could be evaluated to increase the significance and benefit of the proposed power cycles.

## 8 References

- [1] J.G.J. (PBL) Olivier, G. (EC-J. Janssens-Maenhout, M. (EC-J. Muntean, J.A.H.W. (PBL) Peters, Trends in Global CO<sub>2</sub> Emissions: 2016 Report, PBL Netherlands Environ. Assess. Agency Eur. Comm. Jt. Res. Cent. (2016) 86. [http://edgar.jrc.ec.europa.eu/news\\_docs/jrc-2016-trends-in-global-co2-emissions-2016-report-103425.pdf](http://edgar.jrc.ec.europa.eu/news_docs/jrc-2016-trends-in-global-co2-emissions-2016-report-103425.pdf).
- [2] R.P. Cabral, N. Mac Dowell, A novel methodological approach for achieving £/MWh cost reduction of CO<sub>2</sub> capture and storage (CCS) processes, *Appl. Energy*. 205 (2017) 529–539. doi:10.1016/j.apenergy.2017.08.003.
- [3] IPCC, Foreword, Preface, Dedication and In Memoriam, *Clim. Chang.* 2014 Mitig. Clim. Chang. Contrib. Work. Gr. III to Fifth Assess. Rep. Intergov. Panel Clim. Chang. (2014) 1454. doi:10.1017/CBO9781107415416.
- [4] EIA, International Energy Outlook 2017 Overview, U.S. Energy Inf. Adm. IEO2017 (2017) 143. doi:www.eia.gov/forecasts/ieo/pdf/0484(2016).pdf.
- [5] P. Viebahn, D. Vallentin, S. Höller, Prospects of carbon capture and storage (CCS) in China's power sector - An integrated assessment, *Appl. Energy*. 157 (2015) 229–244. doi:10.1016/j.apenergy.2015.07.023.
- [6] M.E. Boot-Handford, J.C. Abanades, E.J. Anthony, M.J. Blunt, S. Brandani, N. Mac Dowell, J.R. Fernández, M.-C. Ferrari, R. Gross, J.P. Hallett, R.S. Haszeldine, P. Heptonstall, A. Lyngfelt, Z. Makuch, E. Mangano, R.T.J. Porter, M. Pourkashanian, G.T. Rochelle, N. Shah, J.G. Yao, P.S. Fennell, Carbon capture and storage update, *Energy Environ. Sci.* 7 (2014) 130–189. doi:10.1039/C3EE42350F.
- [7] N. MacDowell, N. Florin, A. Buchard, J. Hallett, A. Galindo, G. Jackson, C.S. Adjiman, C.K. Williams, N. Shah, P. Fennell, An overview of CO<sub>2</sub> capture technologies, *Energy Environ. Sci.* 3 (2010) 1645. doi:10.1039/c004106h.
- [8] C.M. Quintella, S.A. Hatimondi, A.P.S. Musse, S.F. Miyazaki, G.S. Cerqueira, A. De Araujo Moreira, CO<sub>2</sub> capture technologies: An overview with technology assessment based on patents and articles, *Energy Procedia*. 4 (2011) 2050–2057. doi:10.1016/j.egypro.2011.02.087.
- [9] J. Gibbins, H. Chalmers, Carbon capture and storage, *Energy Policy*. 36 (2008) 4317–4322. doi:10.1016/j.enpol.2008.09.058.
- [10] D.J. Dillon, V. White, R.J. Allam, R.A. Wall, J. Gibbins, *Oxy Combustion Processes for CO<sub>2</sub> Capture from Power Plant*, (2005).
- [11] A. Bose, K. Jana, D. Mitra, S. De, Co-production of power and urea from coal with CO<sub>2</sub> capture: Performance assessment, *Clean Technol. Environ. Policy*. 17 (2015). doi:10.1007/s10098-015-0960-7.
- [12] Q. Zhang, Nurhayati, C.L. Cheng, D. Nagarajan, J.S. Chang, J. Hu, D.J. Lee, Carbon capture and utilization of fermentation CO<sub>2</sub>: Integrated ethanol fermentation and

- succinic acid production as an efficient platform, *Appl. Energy*. 206 (2017) 364–371. doi:10.1016/j.apenergy.2017.08.193.
- [13] C. Graves, S.D. Ebbesen, M. Mogensen, K.S. Lackner, Sustainable hydrocarbon fuels by recycling CO<sub>2</sub> and H<sub>2</sub>O with renewable or nuclear energy, *Renew. Sustain. Energy Rev.* 15 (2011) 1–23. doi:10.1016/j.rser.2010.07.014.
- [14] D.Y.C. Leung, G. Caramanna, M.M. Maroto-Valer, An overview of current status of carbon dioxide capture and storage technologies, *Renew. Sustain. Energy Rev.* 39 (2014) 426–443. doi:10.1016/j.rser.2014.07.093.
- [15] C.Y. Cheng, G.H. Kelsall, L. Kleiminger, Reduction of CO<sub>2</sub> to CO at Cu-ceria-gadolinia (CGO) cathode in solid oxide electrolyser, *J. Appl. Electrochem.* 43 (2013) 1131–1144. doi:10.1007/s10800-013-0566-x.
- [16] Y.A. Daza, R.A. Kent, M.M. Yung, J.N. Kuhn, Carbon dioxide conversion by reverse water-gas shift chemical looping on perovskite-type oxides, *Ind. Eng. Chem. Res.* 53 (2014) 5828–5837. doi:10.1021/ie5002185.
- [17] C. Agrafiotis, M. Roeb, C. Sattler, A review on solar thermal syngas production via redox pair-based water/carbon dioxide splitting thermochemical cycles, *Renew. Sustain. Energy Rev.* 42 (2015) 254–285. doi:10.1016/j.rser.2014.09.039.
- [18] A. Stamatiou, P.G. Loutzenhiser, A. Steinfeld, Solar Syngas Production via H<sub>2</sub>O/CO<sub>2</sub>-Splitting Thermochemical Cycles with Zn/ZnO and FeO/Fe<sub>3</sub>O<sub>4</sub> Redox Reactions †, *Chem. Mater.* 22 (2010) 851–859. doi:10.1021/cm9016529.
- [19] G.P. Smestad, A. Steinfeld, Review: Photochemical and thermochemical production of solar fuels from H<sub>2</sub>O and CO<sub>2</sub> using metal oxide catalysts, *Ind. Eng. Chem. Res.* 51 (2012) 11828–11840. doi:10.1021/ie3007962.
- [20] A.J. Traynor, R.J. Jensen, Direct Solar Reduction of CO<sub>2</sub> to Fuel: First Prototype Results, *Ind. Eng. Chem. Res.* 41 (2002) 1935–1939. doi:10.1021/ie010871x.
- [21] Y. Nigara, B. Cales, Production of carbon monoxide by direct thermal splitting of carbon dioxide at high temperature, *Bull. Chem. Soc. Jpn.* 59 (1986) 1997–2002. doi:10.1246/bcsj.59.1997.
- [22] J.L. Lyman, R.J. Jensen, Chemical reactions occurring during direct solar reduction of CO<sub>2</sub>, *Sci. Total Environ.* 277 (2001) 7–14. doi:10.1016/S0048-9697(01)00829-4.
- [23] R. Sadeghbeigi, *Fluid catalytic cracking handbook*, (1995). doi:10.1016/B978-0-12-386965-4.X0001-8.
- [24] M. Tang, L. Xu, M. Fan, Progress in oxygen carrier development of methane-based chemical-looping reforming: A review, *Appl. Energy*. 151 (2015) 143–156. doi:10.1016/j.apenergy.2015.04.017.
- [25] N. Dilmaç, Ö.F. Dilmaç, E. Yardımcı, Utilization of Menteş iron ore as oxygen carrier in Chemical-Looping Combustion, *Energy*. 138 (2017) 785–798. doi:10.1016/j.energy.2017.07.126.

- [26] P. Chiesa, G. Lozza, A. Malandrino, M. Romano, V. Piccolo, Three-reactors chemical looping process for hydrogen production, *Int. J. Hydrogen Energy*. 33 (2008) 2233–2245. doi:10.1016/j.ijhydene.2008.02.032.
- [27] P.T. Krenzke, J.H. Davidson, Thermodynamic analysis of syngas production via the solar thermochemical cerium oxide redox cycle with methane-driven reduction, *Energy and Fuels*. 28 (2014) 4088–4095. doi:10.1021/ef500610n.
- [28] M. Welte, K. Warren, J.R. Scheffe, A. Steinfeld, Combined Ceria Reduction and Methane Reforming in a Solar-Driven Particle-Transport Reactor, *Ind. Eng. Chem. Res.* 56 (2017) 10300–10308. doi:10.1021/acs.iecr.7b02738.
- [29] K.J. Warren, J.R. Scheffe, Kinetic insights into the reduction of ceria facilitated via the partial oxidation of methane, *Mater. Today Energy*. 9 (2018) 39–48. doi:10.1016/j.mtener.2018.05.001.
- [30] S. Bhavsar, G. Vesper, Chemical looping beyond combustion : production of synthesis gas via chemical looping partial oxidation of methane, *RSC Adv.* 4 (2014) 47254–47267. doi:10.1039/c4ra06437b.
- [31] D. Yadav, R. Banerjee, A review of solar thermochemical processes, *Renew. Sustain. Energy Rev.* 54 (2016) 497–532. doi:10.1016/j.rser.2015.10.026.
- [32] R.J. Carrillo, J.R. Scheffe, Advances and trends in redox materials for solar thermochemical fuel production, *Sol. Energy*. 156 (2017) 3–20. doi:10.1016/j.solener.2017.05.032.
- [33] Y. Zhang, T. Nie, Z. Wang, J. Liu, J. Zhou, K. Cen, Splitting of CO<sub>2</sub> via the Heterogeneous Oxidation of Zinc Powder in Thermochemical Cycles, (2015). doi:10.1021/acs.iecr.5b02407.
- [34] J. Jumas, J. Olivier-fourcade, Characterization of Two-Step Tin-Based Redox System for Thermochemical Fuel Production from Solar-Driven CO<sub>2</sub> and H<sub>2</sub>O Splitting Cycle, (2014).
- [35] P. Furler, J.R. Scheffe, D. Marxer, A. Steinfeld, Solar reactors for thermochemical CO<sub>2</sub> and H<sub>2</sub>O splitting via metal oxide redox reactions, (2014).
- [36] U.W. Hartley, N. Ngoenthong, K. Cheenkachorn, T. Sornchamni, CO<sub>2</sub> to Syngas : Metal Oxides on Stainless Steel 316L for micro- channel reactor application, (n.d.) 8–11.
- [37] S. Tescari, C. Agrafiotis, S. Breuer, L. De Oliveira, M. Neises-Von Puttkamer, M. Roeb, C. Sattler, Thermochemical solar energy storage via redox oxides: Materials and reactor/heat exchanger concepts, *Energy Procedia*. 49 (2013) 1034–1043. doi:10.1016/j.egypro.2014.03.111.
- [38] Q. Jiang, Z. Chen, J. Tong, M. Yang, Z. Jiang, C. Li, Catalytic Function of IrOx in the Two-Step Thermochemical CO<sub>2</sub>-Splitting Reaction at High Temperatures, *ACS Catal.* 6 (2016) 1172–1180. doi:10.1021/acscatal.5b01774.

- [39] N. Gokon, T. Suda, T. Kodama, Oxygen and hydrogen productivities and repeatable reactivity of 30-mol%-Fe-, Co-, Ni-, Mn-doped CeO<sub>2</sub>- $\delta$  for thermochemical two-step water-splitting cycle, *Energy*. 90 (2015) 1280–1289. doi:10.1016/j.energy.2015.06.085.
- [40] T. Nakamura, Hydrogen production from water utilizing solar heat at high temperatures, *Sol. Energy*. 19 (1977) 467–475. doi:10.1016/0038-092X(77)90102-5.
- [41] M. Roeb, C. Sattler, R. Klüser, N. Monnerie, L. de Oliveira, A.G. Konstandopoulos, C. Agrafiotis, V.T. Zaspalis, L. Nalbandian, A. Steele, P. Stobbe, Solar Hydrogen Production by a Two-Step Cycle Based on Mixed Iron Oxides, *J. Sol. Energy Eng.* 128 (2006) 125. doi:10.1115/1.2183804.
- [42] L.S. Darken, R.W. Gurry, The System Iron-Oxygen. II. Equilibrium and Thermodynamics of Liquid Oxide and Other Phases, *J. Am. Chem. Soc.* 68 (1946) 798–816. doi:10.1021/ja01209a030.
- [43] M. Roeb, M. Neises, N. Monnerie, F. Call, H. Simon, C. Sattler, M. Schmecker, R. Pitz-Paal, Materials-related aspects of thermochemical water and carbon dioxide splitting: A review[1] M. Roeb et al., “Materials-related aspects of thermochemical water and carbon dioxide splitting: A review,” *Materials (Basel)*., vol. 5, no. 11, pp. 2015–2054, 2012, *Materials (Basel)*. 5 (2012) 2015–2054. doi:10.3390/ma5112015.
- [44] F.X. Chiron, G.S. Patience, Kinetics of mixed copper-iron based oxygen carriers for hydrogen production by chemical looping water splitting, *Int. J. Hydrogen Energy*. 37 (2012) 10526–10538. doi:10.1016/j.ijhydene.2012.04.052.
- [45] W. Liu, J.Y. Lim, M.A. Saucedo, A.N. Hayhurst, S.A. Scott, J.S. Dennis, Kinetics of the reduction of wüstite by hydrogen and carbon monoxide for the chemical looping production of hydrogen, *Chem. Eng. Sci.* 120 (2014) 149–166. doi:10.1016/j.ces.2014.08.010.
- [46] T. Kodama, N. Gokon, R. Yamamoto, Thermochemical two-step water splitting by ZrO<sub>2</sub>-supported Ni<sub>x</sub>Fe<sub>3-x</sub>O<sub>4</sub> for solar hydrogen production, *Sol. Energy*. 82 (2008) 73–79. doi:10.1016/j.solener.2007.03.005.
- [47] F. Liu, Cerium oxide promoted oxygen carrier development and scale modeling study for chemical looping combustion, (2013).
- [48] W.C. Chueh, S.M. Haile, A thermochemical study of ceria: exploiting an old material for new modes of energy conversion and CO<sub>2</sub> mitigation, *Philos. Trans. R. Soc. A Math. Phys. Eng. Sci.* 368 (2010) 3269–3294. doi:10.1098/rsta.2010.0114.
- [49] S. Ackermann, L. Sauvin, R. Castiglioni, J.L.M. Rupp, J.R. Scheffe, A. Steinfeld, Kinetics of CO<sub>2</sub> Reduction over Nonstoichiometric Ceria, *J. Phys. Chem. C*. 119 (2015) 16452–16461. doi:10.1021/acs.jpcc.5b03464.
- [50] S. Abanades, G. Flamant, Thermochemical hydrogen production from a two-step solar-driven water-splitting cycle based on cerium oxides, *Sol. Energy*. 80 (2006) 1611–1623. doi:10.1016/j.solener.2005.12.005.
- [51] B. Bulfin, A.J. Lowe, K.A. Keogh, B.E. Murphy, O. Lübben, S.A. Krasnikov, I. V.

- Shvets, Analytical Model of CeO<sub>2</sub> Oxidation and Reduction, *J. Phys. Chem. C*. 117 (2013) 24129–24137. doi:10.1021/jp406578z.
- [52] E.A. Kümmerle, G. Heger, The Structures of C-Ce<sub>2</sub>O<sub>3+δ</sub>, Ce<sub>7</sub>O<sub>12</sub>, and Ce<sub>11</sub>O<sub>20</sub>, *J. Solid State Chem.* 147 (1999) 485–500. doi:10.1006/jssc.1999.8403.
- [53] N. Gokon, S. Sagawa, T. Kodama, Comparative study of activity of cerium oxide at thermal reduction temperatures of 1300–1550 C for solar thermochemical two-step water-splitting cycle, *Int. J. Hydrogen Energy*. 38 (2013) 14402–14414. doi:10.1016/j.ijhydene.2013.08.108.
- [54] S. Abanades, A. Legal, A. Cordier, G. Peraudeau, G. Flamant, A. Julbe, Investigation of reactive cerium-based oxides for H<sub>2</sub> production by thermochemical two-step water-splitting, *J. Mater. Sci.* 45 (2010) 4163–4173. doi:10.1007/s10853-010-4506-4.
- [55] A. Le Gal, S. Abanades, Catalytic investigation of ceria-zirconia solid solutions for solar hydrogen production, *Int. J. Hydrogen Energy*. 36 (2011) 4739–4748. doi:10.1016/j.ijhydene.2011.01.078.
- [56] J.R. Scheffe, A. Steinfeld, Thermodynamic analysis of cerium-based oxides for solar thermochemical fuel production, *Energy and Fuels*. 26 (2012) 1928–1936. doi:10.1021/ef201875v.
- [57] Q. Jiang, G. Zhou, Z. Jiang, C. Li, Thermochemical CO<sub>2</sub> splitting reaction with C<sub>x</sub>M<sub>1-x</sub>O<sub>2-δ</sub> (M=Ti<sup>4+</sup>, Sn<sup>4+</sup>, Hf<sup>4+</sup>, Zr<sup>4+</sup>, La<sup>3+</sup>, Y<sup>3+</sup> and Sm<sup>3+</sup>) solid solutions, *Sol. Energy*. 99 (2014) 55–66. doi:10.1016/j.solener.2013.10.021.
- [58] S. Abanades, A. Legal, A. Cordier, G. Peraudeau, G. Flamant, A. Julbe, Investigation of reactive cerium-based oxides for H<sub>2</sub> production by thermochemical two-step water-splitting, *J. Mater. Sci.* 45 (2010) 4163–4173. doi:10.1007/s10853-010-4506-4.
- [59] L. Protasova, F. Snijkers, Recent developments in oxygen carrier materials for hydrogen production via chemical looping processes, *Fuel*. 181 (2016) 75–93. doi:10.1016/j.fuel.2016.04.110.
- [60] G. Voitic, V. Hacker, Recent advancements in chemical looping water splitting for the production of hydrogen, *RSC Adv.* 6 (2016) 98267–98296. doi:10.1039/C6RA21180A.
- [61] A.H. McDaniel, A. Ambrosini, E.N. Coker, J.E. Miller, W.C. Chueh, R. O’Hayre, J. Tong, Nonstoichiometric perovskite oxides for solar thermochemical H<sub>2</sub> and CO production, *Energy Procedia*. 49 (2013) 2009–2018. doi:10.1016/j.egypro.2014.03.213.
- [62] Q. Jiang, J. Tong, G. Zhou, Z. Jiang, Z. Li, C. Li, Thermochemical CO<sub>2</sub> splitting reaction with supported La<sub>x</sub>A<sub>1-x</sub>FeyB<sub>1-y</sub>O<sub>3</sub> (A=Sr, Ce, B=Co, Mn; 0 ≤ x, y ≤ 1) perovskite oxides, *Sol. Energy*. 103 (2014) 425–437. doi:10.1016/j.solener.2014.02.033.
- [63] N.L. Galinsky, Y. Huang, F. Li, Iron Oxide with Facilitated O<sub>2</sub> – Transport for Facile Fuel Oxidation and CO<sub>2</sub> Capture in a Chemical Looping Scheme, (2013). doi:10.1021/sc300177j.
- [64] D.S. Mathew, R.S. Juang, An overview of the structure and magnetism of spinel ferrite

- nanoparticles and their synthesis in microemulsions, *Chem. Eng. J.* 129 (2007) 51–65. doi:10.1016/j.cej.2006.11.001.
- [65] T.A.S. Ferreira, J.C. Waerenborgh, M.H.R.M. Mendonça, M.R. Nunes, F.M. Costa, Structural and morphological characterization of FeCo<sub>2</sub>O<sub>4</sub> and CoFe<sub>2</sub>O<sub>4</sub> spinels prepared by a coprecipitation method, *Solid State Sci.* 5 (2003) 383–392. doi:10.1016/S1293-2558(03)00011-6.
- [66] V.J. Aston, B.W. Evanko, A.W. Weimer, Investigation of novel mixed metal ferrites for pure H<sub>2</sub> and CO<sub>2</sub> production using chemical looping, *Int. J. Hydrogen Energy.* 38 (2013) 9085–9096. doi:10.1016/j.ijhydene.2013.05.078.
- [67] S. Cocchi, M. Mari, F. Cavani, J.M.M. Millet, Chemical and physical behavior of CoFe<sub>2</sub>O<sub>4</sub> in steam-iron process with methanol, *Appl. Catal. B Environ.* 152–153 (2014) 250–261. doi:10.1016/j.apcatb.2014.01.040.
- [68] KTH Royal Institute of Technology Energy Department, Different Types of Solar Concentrators, (n.d.). [http://energy.kth.se/compedu/webcompedu/webhelp/S9\\_Renewable\\_Energy/B5\\_Solar\\_Energy/C3\\_Advanced\\_Solar\\_Thermal/ID107\\_files/Different\\_Types\\_of\\_Solar\\_Concentrators.htm](http://energy.kth.se/compedu/webcompedu/webhelp/S9_Renewable_Energy/B5_Solar_Energy/C3_Advanced_Solar_Thermal/ID107_files/Different_Types_of_Solar_Concentrators.htm) (accessed June 2, 2018).
- [69] C.N.R. Rao, S. Dey, Solar thermochemical splitting of water to generate hydrogen, *Proc. Natl. Acad. Sci.* 2017 (2017) 201700104. doi:10.1073/pnas.1700104114.
- [70] C.L. Muhich, B.D. Ehrhart, I. Al-Shankiti, B.J. Ward, C.B. Musgrave, A.W. Weimer, A review and perspective of efficient hydrogen generation via solar thermal water splitting, *Wiley Interdiscip. Rev. Energy Environ.* 5 (2016) 261–287. doi:10.1002/wene.174.
- [71] N.P. Siegel, J.E. Miller, I. Ermanoski, R.B. Diver, E.B. Stechel, Factors affecting the efficiency of solar driven metal oxide thermochemical cycles, *Ind. Eng. Chem. Res.* 52 (2013) 3276–3286. doi:10.1021/ie400193q.
- [72] W.C. Chueh, M. Abbott, D. Scipio, S.M. Haile, High-flux solar-driven thermochemical dissociation of CO<sub>2</sub> and H<sub>2</sub>O using ceria redox reactions, *Science* (80-. ). 63 (2010) 2010. doi:10.1126/science.1197834.
- [73] A. Houaijia, C. Sattler, M. Roeb, M. Lange, S. Breuer, J.P. Säck, Analysis and improvement of a high-efficiency solar cavity reactor design for a two-step thermochemical cycle for solar hydrogen production from water, *Sol. Energy.* 97 (2013) 26–38. doi:10.1016/j.solener.2013.07.032.
- [74] M. Chambon, S. Abanades, G. Flamant, Thermal Dissociation of Compressed ZnO and SnO<sub>2</sub> Powders in a Moving-Front Solar Thermochemical Reactor, *AIChE J.* 57 (2011) 2264–2273. doi:10.1002/aic.
- [75] P. Furler, J.R. Scheffe, A. Steinfeld, Syngas production by simultaneous splitting of H<sub>2</sub>O and CO<sub>2</sub> via ceria redox reactions in a high-temperature solar reactor, *Energy Environ. Sci.* 5 (2012) 6098–6103. doi:10.1039/C1EE02620H.
- [76] C. Agrafiotis, M. Roeb, A.G. Konstandopoulos, L. Nalbandian, V.T. Zaspalis, C. Sattler,

- P. Stobbe, A.M. Steele, Solar water splitting for hydrogen production with monolithic reactors, *Sol. Energy*. 79 (2005) 409–421. doi:10.1016/j.solener.2005.02.026.
- [77] R.B. Diver, J.E. Miller, M.D. Allendorf, N.P. Siegel, R.E. Hogan, Solar Thermochemical Water-Splitting Ferrite-Cycle Heat Engines, *J. Sol. Energy Eng.* 130 (2008) 041001. doi:10.1115/1.2969781.
- [78] J. Kim, J.E. Miller, C.T. Maravelias, E.B. Stechel, Comparative analysis of environmental impact of S2P (Sunshine to Petrol) system for transportation fuel production, *Appl. Energy*. 111 (2013) 1089–1098. doi:10.1016/j.apenergy.2013.06.035.
- [79] T. Melchior, C. Perkins, A.W. Weimer, A. Steinfeld, A cavity-receiver containing a tubular absorber for high-temperature thermochemical processing using concentrated solar energy, *Int. J. Therm. Sci.* 47 (2008) 1496–1503. doi:10.1016/j.ijthermalsci.2007.12.003.
- [80] J. Martinek, R. Viger, A.W. Weimer, Transient simulation of a tubular packed bed solar receiver for hydrogen generation via metal oxide thermochemical cycles, *Sol. Energy*. 105 (2014) 613–631. doi:10.1016/j.solener.2014.04.022.
- [81] M. Roeb, M. Neises, J.P. Säck, P. Rietbrock, N. Monnerie, J. Dersch, M. Schmitz, C. Sattler, Operational strategy of a two-step thermochemical process for solar hydrogen production, *Int. J. Hydrogen Energy*. 34 (2009) 4537–4545. doi:10.1016/j.ijhydene.2008.08.049.
- [82] M. Roeb, J.P. Säck, P. Rietbrock, C. Prahl, H. Schreiber, M. Neises, L. de Oliveira, D. Graf, M. Ebert, W. Reinalter, M. Meyer-Grünefeldt, C. Sattler, A. Lopez, A. Vidal, A. Elsberg, P. Stobbe, D. Jones, A. Steele, S. Lorentzou, C. Pagkoura, A. Zygogianni, C. Agrafiotis, A.G. Konstandopoulos, Test operation of a 100kW pilot plant for solar hydrogen production from water on a solar tower, *Sol. Energy*. 85 (2011) 634–644. doi:10.1016/j.solener.2010.04.014.
- [83] H. Kaneko, T. Miura, A. Fuse, H. Ishihara, S. Taku, H. Fukuzumi, Y. Naganuma, Y. Tamaura, Rotary-type solar reactor for solar hydrogen production with two-step water splitting process, *Energy and Fuels*. 21 (2007) 2287–2293. doi:10.1021/ef060581z.
- [84] Y. Tamaura, A. Steinfeld, P. Kuhn, K. Ehrensberger, Production of solar hydrogen by a novel, 2-step, water-splitting thermochemical cycle, *Energy*. 20 (1995) 325–330. doi:10.1016/0360-5442(94)00099-O.
- [85] R. Müller, P. Haeberling, R.D. Palumbo, Further advances toward the development of a direct heating solar thermal chemical reactor for the thermal dissociation of ZnO(s), *Sol. Energy*. 80 (2006) 500–511. doi:10.1016/j.solener.2005.04.015.
- [86] C. Muhich, A. Steinfeld, Principles of doping ceria for the solar thermochemical redox splitting of H<sub>2</sub>O and CO<sub>2</sub>, *J. Mater. Chem. A*. 5 (2017) 15578–15590. doi:10.1039/C7TA04000H.
- [87] E. Koepf, S.G. Advani, A. Steinfeld, A.K. Prasad, A novel beam-down, gravity-fed, solar thermochemical receiver/reactor for direct solid particle decomposition: Design, modeling, and experimentation, *Int. J. Hydrogen Energy*. 37 (2012) 16871–16887.

- doi:10.1016/j.ijhydene.2012.08.086.
- [88] E.E. Koepf, M.D. Lindemer, S.G. Advani, A.K. Prasad, Experimental Investigation of Vortex Flow in a Two-Chamber Solar Thermochemical Reactor, *J. Fluids Eng.* 135 (2013) 111103. doi:10.1115/1.4024965.
- [89] J.R. Scheffe, M. Welte, A. Steinfeld, Thermal Reduction of Ceria within an Aerosol Reactor for H<sub>2</sub>O and CO<sub>2</sub> Splitting, *Ind. Eng. Chem. Res.* 53 (2014) 2175–2182. doi:10.1021/ie402620k.
- [90] N. Gokon, T. Mataga, N. Kondo, T. Kodama, Thermochemical two-step water splitting by internally circulating fluidized bed of NiFe<sub>2</sub>O<sub>4</sub> particles: Successive reaction of thermal-reduction and water-decomposition steps, *Int. J. Hydrogen Energy.* 36 (2011) 4757–4767. doi:10.1016/j.ijhydene.2011.01.076.
- [91] I. Ermanoski, N.P. Siegel, E.B. Stechel, A New Reactor Concept for Efficient Solar-Thermochemical Fuel Production, *J. Sol. Energy Eng.* 135 (2013) 031002. doi:10.1115/1.4023356.
- [92] I. Ermanoski, Cascading pressure thermal reduction for efficient solar fuel production, *Int. J. Hydrogen Energy.* 39 (2014) 13114–13117. doi:10.1016/j.ijhydene.2014.06.143.
- [93] L.F. De Diego, F. Garcí, J. Ada, A. Abad, P. Gaya, Fuel reactor modelling in chemical-looping combustion of coal: 1 . model formulation, 87 (2013) 277–293. doi:10.1016/j.ces.2012.10.006.
- [94] M.A. Schnellmann, S.A. Scott, G. Williams, J.S. Dennis, Sensitivity of chemical-looping combustion to particle reaction kinetics, *Chem. Eng. Sci.* 152 (2016) 21–25. doi:10.1016/j.ces.2016.05.028.
- [95] D.L.-S. Fan, *Chemical Looping Partial Oxidation: Gasification, Reforming, and Chemical Syntheses*, Cambridge University Press, 2017.
- [96] J.G. Yates, P. Lettieri, *Fluidized-Bed Reactors: Processes and Operating Conditions*, 2016. doi:10.1007/978-3-319-39593-7.
- [97] M. Kramp, S. Heinrich, Carbon Stripping – A Critical Process Step in Chemical Looping Combustion of Solid Fuels, (2012) 497–507. doi:10.1002/ceat.201100438.
- [98] A. Cuadrat, A. Abad, P. Gayán, L.F. De Diego, F. García-labiano, J. Adánez, Theoretical approach on the CLC performance with solid fuels : Optimizing the solids inventory, *Fuel.* 97 (2012) 536–551. doi:10.1016/j.fuel.2012.01.071.
- [99] T.A. Brown, J.S. Dennis, S.A. Scott, J.F. Davidson, A.N. Hayhurst, Gasification and Chemical-Looping Combustion of a Lignite Char in a Fluidized Bed of Iron Oxide, 44 (2010) 3034–3048. doi:10.1021/ef100068m.
- [100] K. Mahalatkar, J. Kuhlman, E.D. Huckaby, T.O. Brien, CFD simulation of a chemical-looping fuel reactor utilizing solid fuel, *Chem. Eng. Sci.* 66 (2011) 3617–3627. doi:10.1016/j.ces.2011.04.025.

- [101] Y. Zhang, Z. Chao, H.A. Jakobsen, Modelling and simulation of chemical looping combustion process in a double loop circulating fluidized bed reactor, *Chem. Eng. J.* 320 (2017) 271–282. doi:10.1016/j.cej.2017.03.046.
- [102] R. Legros, J. Chaouki, J. Paris, Simulation of circulating fluidized bed reactors using ASPEN PLUS, *77* (1998) 327–337.
- [103] N. Sadhwani, P. Li, M.R. Eden, S. Adhikari, *Process Modeling of Fluidized Bed Biomass-CO<sub>2</sub> Gasification using ASPEN Plus*, Elsevier Masson SAS, 2017. doi:10.1016/B978-0-444-63965-3.50420-7.
- [104] A. Technology, Fluidization in Aspen Plus Fluidization in Aspen Plus □ Aspen Plus fluidized bed model, (2013).
- [105] R.J. Schaefer, Steady State Behaviour of Moving Bed Reactors, *Chem. Eng. Sci.* 29 (1974) 119–127.
- [106] A. Rahimi, A. Niksiar, A general model for moving-bed reactors with multiple chemical reactions part I: Model formulation, *Int. J. Miner. Process.* 124 (2013) 58–66. doi:10.1016/j.minpro.2013.02.015.
- [107] D.R. Parisi, M.A. Laborde, Modeling of counter current moving bed gas-solid reactor used in direct reduction of iron ore, *Chem. Eng. J.* 104 (2004) 35–43. doi:10.1016/j.cej.2004.08.001.
- [108] E.D. Negri, O.M. Alfano, M.G. Chiovetta, Moving-Bed Reactor Model for the Direct Reduction of Hematite . Parametric Study, (1995) 4266–4276. doi:10.1021/ie00039a017.
- [109] B. Dussoubs, J. Jourde, F. Patisson, J.L. Houzelot, D. Ablitzer, Mathematical modelling of uranium dioxide conversion in a moving bed furnace, *128* (2002) 168–177.
- [110] B.W. Benjamin, *Great Plains ASPEN Model Development: Gasifier Model*. Final Topical Report, New York, NY, 1985.
- [111] Aspen Technology, *Aspen Plus Model for Moving Bed Coal Gasifier*, 2010.
- [112] A. Tong, L. Zeng, M. V Kathe, D. Sridhar, L. Fan, Application of the Moving-Bed Chemical Looping Process for High Methane Conversion, (2013). doi:10.1021/ef3020475.
- [113] C. He, X. Feng, K. Hoong, Process modeling and thermodynamic analysis of Lurgi fixed-bed coal gasifier in an SNG plant, *111* (2013) 742–757.
- [114] S. Mukherjee, Chemical looping combustion for solid fuels – Development and optimisation of industrial scale flowsheet models for power generation, (2015). doi:10.13140/2.1.2554.1442.
- [115] R. Porrazzo, G. White, R. Ocone, Techno-economic investigation of a chemical looping combustion based power plant, *Faraday Discuss.* 192 (2016) 437–457. doi:10.1039/C6FD00033A.

- [116] E. Gençer, D.S. Mallapragada, F. Maréchal, M. Tawarmalani, R. Agrawal, Round-the-clock power supply and a sustainable economy via synergistic integration of solar thermal power and hydrogen processes, *Proc. Natl. Acad. Sci.* 112 (2015) 15821–15826. doi:10.1073/pnas.1513488112.
- [117] O.V. Ogidiana, T. Shamim, Numerical Analysis of a Solar Assisted Chemical Looping Combustion System for CO<sub>2</sub> Capture, *Energy Procedia.* 105 (2017) 4537–4542. doi:10.1016/j.egypro.2017.03.973.
- [118] J.R. Scheffe, A.H. McDaniel, M.D. Allendorf, A.W. Weimer, Kinetics and mechanism of solar-thermochemical H<sub>2</sub> production by oxidation of a cobalt ferrite–zirconia composite, *Energy Environ. Sci.* 6 (2013) 963. doi:10.1039/c3ee23568h.
- [119] V.M. Wheeler, R. Bader, P.B. Kreider, M. Hangi, S. Haussener, W. Lipiński, Modelling of solar thermochemical reaction systems, *Sol. Energy.* 156 (2017) 149–168. doi:10.1016/j.solener.2017.07.069.
- [120] O. Levenspiel, *Chemical reaction engineering*, 1999. doi:10.1021/ie990488g.
- [121] A. Abad, J. Adánez, F. García-Labiano, L.F. de Diego, P. Gayán, Modeling of the chemical-looping combustion of methane using a Cu-based oxygen carrier, *Energy Procedia.* 1 (2009) 391–398. doi:10.1016/j.egypro.2009.01.053.
- [122] L. Chen, X. Yang, G. Li, C. Wen, X. Li, C. Snape, An Improved Form of Shrinking Core Model for Prediction of the Conversion during Reduction Process in Chemical Looping Combustion, *Energy and Fuels.* 31 (2017) 1993–2006. doi:10.1021/acs.energyfuels.6b03036.
- [123] Z. Zhao, M. Uddi, N. Tsvetkov, B. Yildiz, A.F. Ghoniem, Redox Kinetics Study of Fuel Reduced Ceria for Chemical-Looping Water Splitting, *J. Phys. Chem. C.* 120 (2016) 16271–16289. doi:10.1021/acs.jpcc.6b01847.
- [124] D. Arifin, Study of redox reactions to split water and carbon dioxide, University of Colorado, 2013. [http://scholar.colorado.edu/chbe\\_gradetds/54](http://scholar.colorado.edu/chbe_gradetds/54).
- [125] T. Ishida, N. Gokon, T. Hatamachi, T. Kodama, Kinetics of thermal reduction step of thermochemical two-step water splitting using CeO<sub>2</sub> particles: Master-plot method for analyzing non-isothermal experiments, *Energy Procedia.* 49 (2013) 1970–1979. doi:10.1016/j.egypro.2014.03.209.
- [126] M.A. Panlener, R.N. Blumenthal, J.E. Garnier, A thermodynamic and electrical conductivity study of nonstoichiometric cerium dioxide, *Solid State Ionics.* 60 (1993) 279–298. doi:10.1016/0167-2738(93)90006-O.
- [127] J.W. Dawicke, R.N. Blumenthal, Oxygen association pressure measurements on nonstoichiometric cerium dioxide, *J. Electrochem. Soc.* 133 (1986) 904–909. doi:10.1149/1.2108760.
- [128] D. Arifin, A.W. Weimer, Kinetics and mechanism of solar-thermochemical H<sub>2</sub> and CO production by oxidation of reduced CeO<sub>2</sub>, *Sol. Energy.* 160 (2018) 178–185. doi:10.1016/j.solener.2017.11.075.

- [129] I. Ermanoski, N. Siegel, E. Stechel, A New Reactor Concept for Efficient Solar-Thermochemical Fuel Production, 2013. doi:10.1115/1.4023356.
- [130] J. Adánez, F.G. Labiano, Modeling of Moving-Bed Coal Gasifiers, *Ind. Eng. Chem. Res.* 29 (1990) 2079–2088. doi:10.1021/ie00106a016.
- [131] J. Fan, L. Zhu, P. Jiang, L. Li, H. Liu, Comparative exergy analysis of chemical looping combustion thermally coupled and conventional steam methane reforming for hydrogen production, *J. Clean. Prod.* 131 (2016) 247–258. doi:10.1016/j.jclepro.2016.05.040.
- [132] CO2 Capture Project (CCP), CCS Technology Development and Demonstration Results, 2015. [http://www.co2captureproject.org/reports.html?utm\\_medium=email&utm\\_campaign=CCP](http://www.co2captureproject.org/reports.html?utm_medium=email&utm_campaign=CCP).
- [133] R.W. Breault, E.R. Monazam, J.T. Carpenter, Analysis of hematite re-oxidation in the chemical looping process, *Appl. Energy.* 157 (2015) 174–182. doi:10.1016/j.apenergy.2015.08.015.
- [134] C. Zhou, K. Shah, H. Song, J. Zanganeh, E. Doroodchi, B. Moghtaderi, Integration Options and Economic Analysis of an Integrated Chemical Looping Air Separation Process for Oxy-fuel Combustion, *Energy & Fuels.* 30 (2016) 1741–1755. doi:10.1021/acs.energyfuels.5b02209.
- [135] C. Yin, J. Yan, Oxy-fuel combustion of pulverized fuels: Combustion fundamentals and modeling, *Appl. Energy.* 162 (2016) 742–762. doi:10.1016/j.apenergy.2015.10.149.
- [136] S. Mukherjee, P. Kumar, A. Yang, P. Fennell, Energy and exergy analysis of chemical looping combustion technology and comparison with pre-combustion and oxy-fuel combustion technologies for CO<sub>2</sub> capture, *J. Environ. Chem. Eng.* 3 (2015) 2104–2114. doi:10.1016/j.jece.2015.07.018.
- [137] K. Shah, B. Moghtaderi, J. Zanganeh, T. Wall, Integration options for novel chemical looping air separation (ICLAS) process for oxygen production in oxy-fuel coal fired power plants, *Fuel.* 107 (2013) 356–370. doi:10.1016/j.fuel.2013.01.007.
- [138] I. Pfaff, A. Kather, Comparative thermodynamic analysis and integration issues of CCS steam power plants based on oxy-combustion with cryogenic or membrane based air separation, *Energy Procedia.* 1 (2009) 495–502. doi:10.1016/j.egypro.2009.01.066.
- [139] J.-P. Tranier, R. Dubettier, N. Perrin, Air Liquide, Air Separation Unit for Oxy-Coal Combustion Systems, 1st Int. Oxyfuel Combust. Conf. (2009).
- [140] B. Moghtaderi, A Novel Chemical Looping Based Air Separation Technology for Oxy-Fuel Combustion of Coal, 2014. doi:10.1115/1.802915.ch1.
- [141] A.E. Farooqui, H.M. Badr, M.A. Habib, R. Ben-Mansour, Numerical investigation of combustion characteristics in an oxygen transport reactor, *Int. J. Energy Res.* 38 (2014). doi:10.1002/er.3070.
- [142] A.E. Farooqui, M.A. Habib, H.M. Badr, R. Ben-Mansour, Modeling of ion transport

- reactor for oxy-fuel combustion, *Int. J. Energy Res.* 37 (2013). doi:10.1002/er.2923.
- [143] R. Ben-Mansour, M.A. Habib, H.M. Badr, F. Azharuddin, M. Nemitallah, Characteristics of oxy-fuel combustion in an oxygen transport reactor, in: *Energy and Fuels*, ACS Publications, 2012: pp. 4599–4606. doi:10.1021/ef300539c.
- [144] A. Skorek-Osikowska, Ł. Bartela, J. Kotowicz, Thermodynamic and ecological assessment of selected coal-fired power plants integrated with carbon dioxide capture, *Appl. Energy*. 200 (2017) 73–88. doi:10.1016/j.apenergy.2017.05.055.
- [145] C.C. Cormos, Evaluation of syngas-based chemical looping applications for hydrogen and power co-generation with CCS, *Int. J. Hydrogen Energy*. 37 (2012) 13371–13386. doi:10.1016/j.ijhydene.2012.06.090.
- [146] K. Jana, A. Ray, M.M. Majoumerd, M. Assadi, S. De, Polygeneration as a future sustainable energy solution – A comprehensive review, *Appl. Energy*. 202 (2017) 88–111. doi:10.1016/j.apenergy.2017.05.129.
- [147] R. Stanger, T. Wall, R. Spörl, M. Paneru, S. Grathwohl, M. Weidmann, G. Scheffknecht, D. McDonald, K. Myöhänen, J. Ritvanen, Oxyfuel combustion for CO<sub>2</sub> capture in power plants, *Int. J. Greenh. Gas Control*. 40 (2015) 55–125.
- [148] J. Mletzko, S. Ehlers, A. Kather, Comparison of natural gas combined cycle power plants with post combustion and oxyfuel technology at different CO<sub>2</sub> capture rates, *Energy Procedia*. 86 (2016) 2–11. doi:10.1016/j.egypro.2016.01.001.
- [149] S. Nazir, O. Bolland, S. Amini, Analysis of Combined Cycle Power Plants with Chemical Looping Reforming of Natural Gas and Pre-Combustion CO<sub>2</sub> Capture, *Energies*. 11 (2018) 147. doi:10.3390/en11010147.
- [150] Mitsubishi Heavy Industries, Gas Turbines, (n.d.). [https://www.mhi.com/products/energy/gas\\_turbine.html](https://www.mhi.com/products/energy/gas_turbine.html) (accessed May 23, 2018).
- [151] Wärtsilä, Gas Turbine for Power Generation: Introduction, (2018). <https://www.wartsila.com/energy/learning-center/technical-comparisons/gas-turbine-for-power-generation-introduction> (accessed May 29, 2018).
- [152] A. Mutuberría, J. Pascual, M. V. Guisado, F. Mallor, Comparison of Heliostat Field Layout Design Methodologies and Impact on Power Plant Efficiency, *Energy Procedia*. 69 (2015) 1360–1370. doi:10.1016/j.egypro.2015.03.135.
- [153] B. Ehrhart, D. Gill, Evaluation of annual efficiencies of high temperature central receiver concentrated solar power plants with thermal energy storage, *Energy Procedia*. 49 (2013) 752–761. doi:10.1016/j.egypro.2014.03.081.
- [154] G.P. Hammond, Engineering sustainability : thermodynamics , energy systems , and the environment, 639 (2004) 613–639. doi:10.1002/er.988.
- [155] A. Bejan, *Thermal Design and Optimization*, John Wiley, New York, 1996.
- [156] L.K. Rihko-Struckmann, P. Datta, M. Wenzel, K. Sundmacher, N.V.R.A.

- Dharanipragada, H. Poelman, V. V Galvita, G.B. Marin, Hydrogen and Carbon Monoxide Production by Chemical Looping over Iron-Aluminium Oxides, *Energy Technol.* 4 (2016) 304–313. doi:10.1002/ente.201500231.
- [157] A.I. Demidov, I.A. Markelov, Thermodynamics of interaction of iron oxides and carbon monoxide, *Russ. J. Appl. Chem.* 84 (2011) 196–198. doi:10.1134/S1070427211020054.
- [158] R. Bader, L.J. Venstrom, J.H. Davidson, W. Lipiński, Thermodynamic analysis of isothermal redox cycling of ceria for solar fuel production, *Energy and Fuels.* 27 (2013) 5533–5544. doi:10.1021/ef400132d.
- [159] P. Furler, J. Scheffe, M. Gorbar, L. Moes, U. Vogt, A. Steinfeld, Solar Thermochemical CO<sub>2</sub> Splitting Utilizing a Reticulated Porous Ceria Redox System, *Energy & Fuels.* 26 (2012) 7051–7059. doi:10.1021/ef3013757.
- [160] A. Steinfeld, P. Scherrer, P. Kuhn, J. Karni, High-Temperature Solar Thermochemistry: Production of Iron and Synthesis Gas by Fe<sub>3</sub>O<sub>4</sub>-Reduction With Methane, 18 (1993) 239–249.
- [161] E.R. Monazam, R.W. Breault, R. Siriwardane, Kinetics of magnetite (Fe<sub>3</sub>O<sub>4</sub>) oxidation to hematite (Fe<sub>2</sub>O<sub>3</sub>) in air for chemical looping combustion, *Ind. Eng. Chem. Res.* 53 (2014) 13320–13328. doi:10.1021/ie501536s.
- [162] K.S. Kang, C.H. Kim, K.K. Bae, W.C. Cho, S.H. Kim, C.S. Park, Oxygen-carrier selection and thermal analysis of the chemical-looping process for hydrogen production, *Int. J. Hydrogen Energy.* 35 (2010) 12246–12254. doi:10.1016/j.ijhydene.2010.08.043.
- [163] A. Laachir, V. Perrichon, A. Badri, J. Lamotte, E. Catherine, J.C. Lavalley, J. El Fallah, L. Hilaire, F. Normand, B. Pascal, E. Quemere, G.N. Sauvion, O. Touret, Reduction of CeO<sub>2</sub> by Hydrogen, *J. CHEM. SOC. FARADAY TRANS.*, 87 (1991) 1601–1609.
- [164] M. Welte, R. Barhoumi, A. Zbinden, J.R. Scheffe, A. Steinfeld, Experimental Demonstration of the Thermochemical Reduction of Ceria in a Solar Aerosol Reactor, *Ind. Eng. Chem. Res.* 55 (2016) 10618–10625. doi:10.1021/acs.iecr.6b02853.
- [165] V. Galvita, K. Sundmacher, Hydrogen production from methane by steam reforming in a periodically operated two-layer catalytic reactor, *Appl. Catal. A Gen.* 289 (2005) 121–127. doi:10.1016/j.apcata.2005.04.053.
- [166] V. Collins-Martinez, M. Escobedo Bretado, M. Meléndez Zaragoza, J. Salinas Gutiérrez, A.L. Ortiz, Absorption enhanced reforming of light alcohols (methanol and ethanol) for the production of hydrogen: Thermodynamic modeling, *Int. J. Hydrogen Energy.* 38 (2013) 12539–12553. doi:10.1016/j.ijhydene.2012.11.146.
- [167] P.T. Krenzke, J.R. Fosheim, J.H. Davidson, Solar fuels via chemical-looping reforming, *Sol. Energy.* 156 (2017) 48–72. doi:10.1016/j.solener.2017.05.095.
- [168] K. Otsuka, T. Ushiyama, I. Yamanaka, Partial Oxidation of Methane Using the Redox of Cerium Oxide, *Chem. Lett.* 22 (1993) 1517–1520. doi:10.1246/cl.1993.1517.
- [169] K. Otsuka, E. Sunada, T. Ushiyama, I. Yamanaka, The production of synthesis gas by

- the redox of cerium oxide, in: M. de Pontes, R.L. Espinoza, C.P. Nicolaidis, J.H. Scholtz, M.S.B.T.-S. in S.S. and C. Scurrall (Eds.), *Nat. Gas Convers. IV*, Elsevier, 1997: pp. 531–536. doi:[https://doi.org/10.1016/S0167-2991\(97\)80386-2](https://doi.org/10.1016/S0167-2991(97)80386-2).
- [170] M.M. Nair, S. Abanades, Tailoring Hybrid Nonstoichiometric Ceria Redox Cycle for Combined Solar Methane Reforming and Thermochemical Conversion of H<sub>2</sub>O/CO<sub>2</sub>, *Energy and Fuels*. 30 (2016) 6050–6058. doi:10.1021/acs.energyfuels.6b01063.
- [171] F.J. Gotor, José, M. Criado, J. Malek, N. Koga, Kinetic analysis of solid-state reactions: The universality of master plots for analyzing isothermal and nonisothermal experiments, *J. Phys. Chem. A*. 104 (2000) 10777–10782. doi:10.1021/jp0022205.
- [172] A. Khawam, D.R. Flanagan, Solid-State Kinetic Models: Basics and Mathematical Fundamentals, *J. Phys. Chem. B*. 110 (2006) 17315–17328. doi:10.1021/jp062746a.
- [173] A.E. Farooqui, A.M. Pica, P. Marocco, D. Ferrero, A. Lanzini, S. Fiorilli, J. Llorca, M. Santarelli, Assessment of kinetic model for ceria oxidation for chemical-looping CO<sub>2</sub> dissociation, *Chem. Eng. J.* 346 (2018) 171–181. doi:10.1016/j.cej.2018.04.041.
- [174] M. Galwey, AK;Brown, Chapter 3 Kinetic models for solid state reactions, in: 1999: pp. 75–115. doi:10.1016/S0167-6881(99)80004-4.
- [175] S.K. Bhatia, D.D. Perlmutter, A random pore model for fluid-solid reactions: I. Isothermal, kinetic control, *AIChE J.* 26 (1980) 379–386. doi:10.1002/aic.690260308.
- [176] J. Šesták, G. Berggren, Study of the kinetics of the mechanism of solid-state reactions at increasing temperatures, *Thermochim. Acta*. 3 (1971) 1–12. doi:10.1016/0040-6031(71)85051-7.
- [177] F. Prout, EG; Tompkins, The thermal decomposition of potassium permanganate, *Trans. Faraday Soc.* 40 (1944) 488–98.
- [178] J.D. HANCOCK, J.H. SHARP, Method of Comparing Solid-State Kinetic Data and Its Application to the Decomposition of Kaolinite, Brucite, and BaCO<sub>3</sub>, *J. Am. Ceram. Soc.* 55 (1972) 74–77. doi:10.1111/j.1151-2916.1972.tb11213.x.
- [179] S.R. Son, K.S. Go, S.D. Kim, Thermogravimetric Analysis of Copper Oxide for Chemical-Looping Hydrogen Generation, *Ind. Eng. Chem. Res.* 48 (2009) 380–387. doi:10.1021/ie800174c.
- [180] L. Zhu, Y. Lu, Reactivity and efficiency of ceria-based oxides for solar CO<sub>2</sub> splitting via isothermal and near-isothermal cycles, *Energy & Fuels*. (2017) acs.energyfuels.7b03284. doi:10.1021/acs.energyfuels.7b03284.
- [181] L.J. Venstrom, R.M. De Smith, Y. Hao, S.M. Haile, J.H. Davidson, Efficient Splitting of CO<sub>2</sub> in an Isothermal Redox Cycle Based on Ceria, *Energy & Fuels*. 28 (2014) 2732–2742. doi:10.1021/ef402492e.
- [182] S.G. Rudisill, L.J. Venstrom, N.D. Petkovich, T. Quan, N. Hein, D.B. Boman, J.H. Davidson, A. Stein, Enhanced Oxidation Kinetics in Thermochemical Cycling of CeO<sub>2</sub> through Templated Porosity, *J. Phys. Chem. C*. 117 (2013) 1692–1700.

doi:10.1021/jp309247c.

- [183] W.C. Chueh, C. Falter, M. Abbott, D. Scipio, P. Furler, S.M. Haile, A. Steinfeld, High-Flux Solar-Driven Thermochemical Dissociation of CO<sub>2</sub> and H<sub>2</sub>O Using Nonstoichiometric Ceria, *Science* (80-. ). 330 (2010) 1797–1801. doi:10.1126/science.1197834.
- [184] B. Janković, B. Adnađević, S. Mentus, The kinetic study of temperature-programmed reduction of nickel oxide in hydrogen atmosphere, *Chem. Eng. Sci.* 63 (2008) 567–575. doi:10.1016/j.ces.2007.09.043.
- [185] L. Han, Z. Zhou, G.M. Bollas, Heterogeneous modeling of chemical-looping combustion. Part 1: Reactor model, *Chem. Eng. Sci.* 104 (2013) 233–249. doi:10.1016/j.ces.2013.09.021.
- [186] Z. Zhao, M. Uddi, N. Tsvetkov, B. Yildiz, A.F. Ghoniem, Enhanced intermediate-temperature CO<sub>2</sub> splitting using nonstoichiometric ceria and ceria–zirconia, *Phys. Chem. Chem. Phys.* 19 (2017) 25774–25785. doi:10.1039/C7CP04789D.
- [187] Galwey AK; Brown ME, Kinetic background to thermal analysis and calorimetry, in: *Handb. Therm. Anal. Calorim. Vol. 1 Princ. Pract.*, 1998: pp. 147–216.
- [188] D.R. Burnham, Kenneth P., Anderson, *Model selection and multi-model inference: a practical information-theoretic approach*, 2nd ed., Springer-Verlag, New York, 2002.
- [189] A. Steinfeld, A. Frei, P. Kuhn, D. Wuillemin, Solar thermal production of zinc and syngas via combined ZnO-reduction and CH<sub>4</sub>-reforming processes, *Int. J. Hydrogen Energy.* 20 (1995) 793–804. doi:10.1016/0360-3199(95)00016-7.
- [190] X. Zhu, H. Wang, Y. Wei, K. Li, X. Cheng, Hydrogen and syngas production from two-step steam reforming of methane using CeO<sub>2</sub> as oxygen carrier, *J. Nat. Gas Chem.* 20 (2011) 281–286. doi:10.1016/S1003-9953(10)60185-5.
- [191] S.M. Nazir, O. Bolland, S. Amini, Full Plant Scale Analysis of Natural Gas Fired Power Plants with Pre-Combustion CO<sub>2</sub> Capture and Chemical Looping Reforming (CLR), *Energy Procedia.* 114 (2017) 2146–2155. doi:10.1016/j.egypro.2017.03.1350.
- [192] D.P. Harrison, Sorption-Enhanced Hydrogen Production : A Review, (2008) 6486–6501.
- [193] HYGHSPIN, Flexible use – maximum efficiency : Gentle product handling plus CIP with one and the same pump !, n.d.
- [194] M.N. Khan, T. Shamim, Influence of Specularity Coefficient on the Hydrodynamics and Bubble Statistics of an Annular Fluidized Bed Reactor, *Energy Procedia.* 105 (2017) 1998–2003. doi:10.1016/j.egypro.2017.03.573.
- [195] Politecnico di Milano - CAESER Project, European best practice guidelines for assessment of CO<sub>2</sub> capture technologies, 2011.
- [196] J. Szargut, Chemical Exergies of the Elements, *Appl. Energy.* 32 (1989) 269–286.

- [197] M.N. Khan, T. Shamim, Exergoeconomic analysis of a chemical looping reforming plant for hydrogen production, *Int. J. Hydrogen Energy*. 42 (2017) 4951–4965. doi:10.1016/j.ijhydene.2016.11.098.
- [198] J.Y. Xiang, M. Cal, M. Santarelli, Calculation for physical and chemical exergy of flows in systems elaborating mixed-phase flows and a case study in an IRSOFC plant, 115 (2004) 101–115. doi:10.1002/er.953.
- [199] T.J. Kotas, *The Exergy Method of Thermal Plant Analysis*, Butterworths, 1985.
- [200] S. Sievers, T. Seifert, M. Franzen, G. Schembecker, C. Bramsiepe, Fixed capital investment estimation for modular production plants, *Chem. Eng. Sci.* 158 (2017) 395–410. doi:10.1016/j.ces.2016.09.029.
- [201] C. Cormos, Integrated assessment of IGCC power generation technology with carbon capture and storage (CCS), *Energy*. 42 (2012) 434–445. doi:10.1016/j.energy.2012.03.025.
- [202] Y. Zhao, H. Chen, M. Waters, D.N. Mavris, Modeling and Cost Optimization of Combined Cycle Heat Recovery Generator Systems, Vol. 1 Turbo Expo 2003. (2003) 881–891. doi:10.1115/GT2003-38568.
- [203] N. Berghout, T. Kuramochi, M. van den Broek, A. Faaij, Techno-economic performance and spatial footprint of infrastructure configurations for large scale CO<sub>2</sub> capture in industrial zones. A case study for the Rotterdam Botlek area (part A), *Int. J. Greenh. Gas Control*. 39 (2015) 256–284. doi:10.1016/j.ijggc.2015.05.019.
- [204] IEA, *Executive Summary - Projected Costs of Generating Electricity*, 2015.
- [205] Eurostat, Natural gas price statistics, EU-28, (2016) 1–12. doi:http://ec.europa.eu/eurostat/statistics-explained/index.php/Natural\_gas\_price\_statistics.
- [206] M.M. Mekonnen, P.W. Gerbens-Leenes, A.Y. Hoekstra, The consumptive water footprint of electricity and heat: a global assessment, *Environ. Sci. Water Res. Technol.* 1 (2015) 285–297. doi:10.1039/C5EW00026B.
- [207] A.D. Martin, A. Delgado, A. Delgado Martin, *Water Footprint of Electric Power Generation: Modeling its use and analyzing options for a water-scarce future*, 2012. doi:10.1021/es802162x.
- [208] N. Florin, P. Fennell, CCR Land Footprint Review, IC 26, (2006) 1–30. [https://www.gov.uk/government/uploads/system/uploads/attachment\\_data/file/43615/CCR\\_guidance\\_-\\_Imperial\\_College\\_review.pdf](https://www.gov.uk/government/uploads/system/uploads/attachment_data/file/43615/CCR_guidance_-_Imperial_College_review.pdf).
- [209] M. Ishida, H. Jin, A novel chemical-looping combustor without NO<sub>x</sub> formation, *Ind. Eng. Chem. Res.* 35 (1996) 2469–2472. doi:10.1021/ie950680s.
- [210] M. Pan, F. Aziz, B. Li, S. Perry, N. Zhang, I. Bulatov, R. Smith, Application of optimal design methodologies in retrofitting natural gas combined cycle power plants with CO<sub>2</sub> capture, *Appl. Energy*. 161 (2016) 695–706. doi:10.1016/j.apenergy.2015.03.035.

- [211] U.S.D. of Energy, Capital Cost Estimates for Utility Scale Electricity Generating Plants, (2016).  
[https://www.eia.gov/analysis/studies/powerplants/capitalcost/pdf/capcost\\_assumption.pdf](https://www.eia.gov/analysis/studies/powerplants/capitalcost/pdf/capcost_assumption.pdf).
- [212] Market Observatory for Energy, Quarterly Report on on European Electricity Markets, 2017.
- [213] Z. Khorshidi, M. Soltanieh, Y. Saboohi, M. Arab, Economic Feasibility of CO<sub>2</sub> Capture from Oxy-fuel Power Plants Considering Enhanced Oil Recovery Revenues, *Energy Procedia*. 4 (2011) 1886–1892. doi:10.1016/j.egypro.2011.02.067.
- [214] E.S. Rubin, J.E. Davison, H.J. Herzog, The cost of CO<sub>2</sub> capture and storage, *Int. J. Greenh. Gas Control*. (2015). doi:10.1016/j.ijggc.2015.05.018.
- [215] J. Varghese, S. Bandyopadhyay, Targeting for energy integration of multiple fired heaters, *Ind. Eng. Chem. Res.* 46 (2007) 5631–5644. doi:10.1021/ie061619y.
- [216] C.C. Cormos, Evaluation of energy integration aspects for IGCC-based hydrogen and electricity co-production with carbon capture and storage, *Int. J. Hydrogen Energy*. 35 (2010) 7485–7497. doi:10.1016/j.ijhydene.2010.04.160.
- [217] E.S. Spang, W.R. Moomaw, K.S. Gallagher, P.H. Kirshen, D.H. Marks, The water consumption of energy production: an international comparison, (2014). doi:10.1088/1748-9326/9/10/105002.